Quantum thermodynamic properties in many-body systems out-of-equilibrium

Amy Hannah Skelt

Doctor of Philosophy

University of York

Physics

April 2020

Abstract

Relatively small many-body quantum systems are often used as hardware for quantum devices. Most of these devices will operate below the thermal limit where thermodynamics must be treated differently to account for quantum behaviours. It is therefore imperative that the thermodynamic properties of these systems are well understood, especially as they can limit the technologies but also help the fabrication and running of efficient quantum devices.

In this thesis we study quantum work and entropy production in closed many-body quantum systems out-of-equilibrium. We find that, for the systems studied, the largest average quantum work can be extracted in adiabatic weakly correlated regimes. These regimes are also seen to minimise the entropy produced, making them efficient regimes in which to operate devices based on these systems.

Adiabatic evolutions are important for many quantum devices, and so it is important that they can be accurately characterised. The validity of current methods has been questioned recently, so in this thesis we propose the use of metrics as a good quantitative measure to characterise adiabaticity. We found that the density distance (a more accessible quantity than the wavefunction and its distance measures) alone can determine adiabaticity in a range of quantum systems, even at finite temperature.

However, when calculating properties of many-body systems, there are many challenges often resulting in the need to approximate. In this thesis we propose a new style of approximation for quantum thermodynamic properties, taking inspiration from density functional theory (DFT). This new style uses the exact initial state of the system but approximates the dynamics and is seen to be computationally cheap but largely accurate. We test this with non-interacting and DFT approximated dynamics, finding that, surprisingly, the non-interacting dynamics give the most accurate results in most regimes, with the cheapest cost.

Contents

List of Tables

List of Figures

Acknowledgements

As is the case in a many-body system, so many interactions have impacted my PhD. I have been fortunate to have worked with some very talented people as well as make new friends. I am very grateful for this opportunity, and have had so many fantastic experiences and met so many wonderful people as a consequence of it.

This work would not have been possible without my supervisor, Professor Irene D'Amico, to whom I am immensely grateful. Her knowledge, insight, and guidance have been invaluable these last four years, and I am so thankful to have been given the opportunity to work on this project. And of course a thank you to the EPSRC for funding this project.

I would also like to thank Professor Rex Godby for continuing the joint supervision from my masters into the first year of my PhD, resulting in the successful publication of the work in chapter 4. His guidance and insight during this time was greatly appreciated. I must also extend my thanks to Professor Godby's group, in particular Jack Wetherell and Matthew Hodgson, who helped me understand and use the iDEA code.

My thanks also goes out to Paul Sharp, Marcela Herrera, and Vivian França, all of whom provided useful thoughts and helpful discussions at some point in this research. An extra thank you to Paul for his advice on surviving a PhD too; he was always a welcome visitor back in the office.

During the PhD, I was fortunate enough to meet and work with Krissia Zawadzki. I cannot thank her enough for all of the help and support she gave, particularly regarding her code. I feel privileged to have inherited such a well written code, as well as to collaborate with someone so driven and intelligent. On top of that, I must thank Krissia for her brigadeiro recipe and enlightening me to Roberto's Gelataria in York; the tasty treats made even the worst days better.

I would like to thank all the great friends I made in York along the way. In particular, thanks go to Alessandro Veneri and Guilherme Canella for the fun games nights and adventures into Yorkshire; to Eleanor, Iulia, and the biology group who didn't mind a physicist sneaking in for games and adventures; to Nettie and the Physics PG social committee for the great opportunities I was able to be a part of; and thanks to David Muir, who was always happy for a pint and a chat.

York has been an incredible place to be, and I feel very fortunate to have spent almost 8 years studying here. A big thank you to the Department of Physics, the University of York, and to the James College teams from 2016-2018, who all made this a great experience and helped me develop not only my knowledge but also myself.

Although being over 200 miles away, I would like to thank my friends back home, Amanda, Julia, and Lucy. Meeting up may have been infrequent but it was always fun and I could not have done this without your support and laughter.

I have a huge thank you to say to my family, whose unending support and love has been phenomenal. This would have been impossible without them. So to Lindsey, Derek, Lucy, Marilyn, and Derrick: thank you, I am truly blessed to have you all as my family.

And finally, to Frederico, meu amor, you have brightened every day, given such joy and laughter, and provided invaluable advice and insight. I cannot thank you enough for everything you do.

Declaration

I declare that this thesis is a presentation of original work and I am the sole author. This work has not previously been presented for an award at this, or any other, university. All sources are acknowledged as references.

Work in chapter 4 has been published in *Measuring adiabaticity in nonequilibrium quantum systems*, A. H. Skelt, R. W. Godby, and I. D'Amico, Physical Review A **98** 012104 (2018). I made adjustments to an existing code, developed a new code, and performed all the numerical calculations. I participated fully in discussions and wrote the first draft of the manuscript.

Work in chapters 6 and 7 has been published in *Many-body effects on the thermodynamics of closed quantum systems*, A. H. Skelt, K. Zawadzki, and I. D'Amico, Journal of Physics A: Mathematical and Theoretical **52** 485304 (2019). Krissia Zawadzki wrote the Hubbard model code. I adapted the code for the hybrid approximation, tested various approximation combinations, and performed the numerical calculations shown in the paper. I participated fully in discussions of the results and wrote the first draft of the manuscript.

Work in chapter 5 has been published in *Characterizing Adiabaticity in Quantum Many-Body Systems at Finite Temperature*, A. H. Skelt and I. D'Amico, Advanced Quantum Technologies **3** 1900139 (2020). I developed a new code for this work (using K. Zawadzki's code to initialise the Hubbard systems) and ran all calculations. I participated fully in discussions of the results and wrote the first draft of the manuscript.

Signed,

Amy Skelt

1. Introduction

Progress in modern technologies has lead to the ability to fabricate systems of only a few particles. These small systems allow for smaller technologies to be developed. These technologies often use systems consisting of only a few particles. When using a small number of particles, quantum physics dominates and strange phenomena occur such as superposition of states, quantum tunnelling, and particle entanglement. We can use these phenomena to gain advantages over classical technologies, and indeed much work is being done to try and achieve this. For example, quantum computers utilise superposition to perform some calculations faster than classical computers, and quantum key distribution uses entanglement to generate more secure communication methods than classically available [1]. Because many-body quantum systems constitute the hardware for a lot of these devices, it is imperative we have a good understanding of them.

Much work is being done looking to advance quantum technologies, including opening up the new field of quantum thermodynamics. This new field is vital to help the progression of quantum technologies as it provides a platform on which to consider energy interplays within quantum systems at finite temperature. Because zero temperature is not possible to realise experimentally, it is important to explore quantum physics at non-zero temperatures. In doing so we unlock a wealth of applications for quantum devices as well as allow for greater insight into fundamental physics. For example, recent experiments have already demonstrated the possibility of fabricating quantum engines and refrigerators [2, 3], and Batalhão *et al.* [4] used NMR techniques to study the arrow of time in a quantum system. It is therefore important to understand quantum thermodynamic properties in many-body systems out-of-equilibrium.

1.1 Quantum thermodynamics

Classical thermodynamics has been well established for many decades now, describing the interplay between work, heat, energy, and entropy. It has been used for the creation and development of many technologies. From humble beginnings in the industrial revolution with the advancement of steam and combustion engines [5, 6], it now has applications which allow us to explore the far reaches of the universe [7, 8]. For example, through thermodynamics we have been able to develop engines which power rockets with the ability to carry large satellites and telescopes into space. Combined with other major advances in physics (such as improved optics), these satellites have enabled improved communication, and the telescopes, such as the Hubble space telescope, have been able to provide insight into the far reaches of the universe [9].

However, as quantum technologies continue to progress, with quantum engines and refrigerators being experimentally realised [2, 3], it is important that thermodynamics is understood in the quantum realm. Ideas like heat, work, and temperature lose their usual (classical) meaning in this quantum world with the introduction of quantum phenomenon such as entanglement and quantum fluctuations. The rapidly growing field of quantum thermodynamics was established to develop these key thermodynamic concepts for quantum physics [10–12]. It looks at the uses and limitations of thermodynamic properties for applications to quantum technologies [10, 11, 13–15]. For example, quantum work is an important property to study because devices can be developed to extract and use this work, such as for quantum heat engines or quantum batteries [16–18]. Quantum work can also be used to understand how to optimise energy consumption in quantum devices [19, 20]. Quantum heat is another key property to understand as it is the uncontrollable energy in the system, limiting the efficiency of devices [10, 19]. The entropy of a system is also a vital quantity to understand; depending on the type of entropy one looks at, different information can be gained. For example, the irreversible work (a type of entropy) can provide information on the amount of energy required to return the system to equilibrium (such as when resetting a system after a perturbation or calculation) [4, 21], alternatively the von Neumann entropy can be used as a measure of bipartite entanglement in the system (when in a pure state) [22].

Accurately accounting for the impact of many-body interactions on quantum thermodynamic properties is still an open challenge which we will address in this thesis. It is also important to understand how these proper-

ties are affected by out-of-equilibrium dynamics since small quantum systems out-of-equilibrium at finite temperature are predominantly the hardware for quantum technologies. To do this, we must first be able to characterise out-of-equilibrium dynamics at finite temperature, identifying when an evolution is adiabatic or not.

1.2 Adiabaticity

An adiabatic evolution in terms of quantum physics[1] is an evolution which is slow enough to prevent any transitions between energy levels occurring. They are of key importance to many areas of quantum physics, with important uses and applications in quantum information, quantum computing, and quantum thermodynamics to name but a few [23–34]. For example, adiabatic evolutions can be used to avoid quantum friction when trying to maximise the quantum work extracted from a system [32, 35]. It was seen recently that in the Hubbard dimer, the largest amount of average quantum work extractable is achieved for adiabatic evolutions, whilst the entropy production is minimised [32]. Therefore it is important to know when an evolution can be considered (quasi-)adiabatic[2] to potentially develop efficient quantum devices.

By using an adiabatic evolution where no transitions occur between the eigenstates of the evolving system, one can design a protocol which accurately obtains a target eigenstate of a complex interacting Hamiltonian [36, 37]. Indeed, adiabatic dynamics via quantum annealing is the method used by the D-Wave quantum computer [38, 39]. Adiabatic dynamics is a key concept in adiabatic quantum computing, and so being able to characterise an adiabatic evolution is vital [23, 34, 40, 41].

Being able to characterise an evolution as adiabatic is also important for time-dependent density functional theory (DFT), because approximations for density functionals are currently only tailored for the quasi-adiabatic regime. This has important implications for devices comprising of many-body interacting systems, where one would need to use an accurate DFT approximation to calculate system properties.

We can see that adiabatic evolutions are important for quantum technologies, but being able to quantitatively characterise an adiabatic evolution is still open to debate [42, 43]. In this thesis we develop new methods of quan-

[1] Not to be confused with the thermodynamic definition which defines an adiabatic evolution as one in which no heat is transferred.

[2] i.e. the evolution is slow enough that it is, for all practical purposes, adiabatic.

tifying an adiabatic evolution which are not as susceptible to the criticisms of current methods. It is also important to evaluate how temperature impacts adiabaticity, given that zero temperature quantum devices are impossible to realise. Indeed it is still an open question as to how one can quantitatively characterise an adiabatic evolution in a system at non-zero temperature, and this is one of the questions we will address in this thesis.

1.3 Many-body physics

We have established that many quantum technologies require many-body systems [44–46] which have elaborate behaviours [47, 48]. However, properties of many-body systems of interacting particles are hugely challenging to calculate and often need to be approximated. The interactions between the particles lead to complex correlations and dynamics such as collective behaviours and phase transitions. This complexity increases exponentially as the number of particles in the system is increased. Because these many-body interacting systems have important applications in quantum physics at finite temperature, we need to understand them in the context of quantum thermodynamics. This allows for the progression of quantum devices and helps further knowledge of fundamental physics.

It is only in recent years that the effects of many-body interactions have begun to be investigated for quantum thermodynamics [49–58]. Previous work has not only investigated exact quantum thermodynamic properties (such as the average quantum work, and the entropy production/irreversible work) in small spin chain systems of 2 sites, but also began to develop techniques adapting DFT for approximating these properties [32, 59, 60]. This work demonstrated that DFT can be applied to quantum thermodynamics with great success for small chains of 2 electrons, and indeed detailed a method which can be applied to any chain size, as well as providing insight into the behaviour of the quantum thermodynamic properties of the exact 2 electron spin chain system. Many new quantum technologies will require systems greater than 2 sites in size, so we need to develop and test new, computationally cheap approximations and approaches for calculating the system properties for larger systems.

In this thesis, we will be bringing together important concepts from many-body physics, quantum thermodynamics, and adiabaticity to build a better understanding of how we can calculate key quantum thermodynamic properties in complex many-body systems out-of-equilibrium. From this, it is hoped

that one can determine the system parameters which maximise quantum work whilst minimising entropy production: these are the parameters which one would use to increase the efficiency of the device performing a calculation. This, in turn, could improve the fabrication, development, and use of quantum devices.

1.4 Thesis outline

This thesis aims to answer two main questions, which themselves can be divided further into more defined questions. These questions are:

1. How can we determine if a given evolution of a quantum system at finite temperature is adiabatic?
   (a) Can we characterise adiabaticity without using the quantum adiabatic criterion which has several limitations such as its base in perturbation theory, and does not have an easy extension to finite temperature?
   (b) Can we apply the characterisation method developed from answering 1a to systems at finite temperature?
2. Can we accurately approximate quantum thermodynamic properties in many-body quantum systems using simple approximations inspired by DFT?
   (a) Firstly, what do these properties look like for the Hubbard system solved numerically exactly?
   (b) How accurate are simple non-interacting-style approximations?
   (c) Can we improve the approximations from point 2b using DFT?

Chapter 2 focuses on general theory on the concepts used throughout this thesis (note that any theory used in only one results chapter will be discussed only in that chapter). The computational methods used are outlined in chapter 3, both previously established codes and codes developed during this PhD, with clear distinctions made between them.

Each results chapter aims to answer one of the research questions. Research question 1 is split across two chapters; point 1a will be addressed in chapter 4 and point 1b will be addressed in chapter 5. Research question 2

will be addressed in chapter 6 (point 2a), chapter 7 (point 2b), and chapter 8 (point 2c).

We then conclude the thesis in chapter 9, bringing together the main points from all results chapters and explaining these conclusions in terms of the wider research field. Without further ado, let us begin.

2. Theory

This thesis draws together several fields of physics in order to investigate how many-body physics impacts quantum thermodynamic properties. In this chapter we will look at the theory behind the relevant parts of each field, and in subsequent chapters we will see how they can be combined to compute and analyse thermodynamic properties by applying them to our systems of interest.

2.1 Many-body quantum physics

In quantum mechanics, all properties of an N-electron system can be determined from its wavefunction, $\Psi(x_1, x_2, \ldots x_N)$. For systems which do not interact with their environment (closed quantum systems), the dynamics of the wavefunction is determined by the time-dependent Schrödinger equation

$$i\frac{\partial}{\partial t}\left|\Psi(x_1, x_2, \ldots x_N, t)\right\rangle = \hat{H}(t)\left|\Psi(x_1, x_2, \ldots x_N, t)\right\rangle, \tag{2.1}$$

where $\hat{H}(t)$ is the time-dependent Hamiltonian of the system. Through this we can control the evolution of a quantum system, emulating physical systems and experiments such as performing a calculation on a quantum computer.

To utilise the quantum system, we need to find a way to access properties we are interested in, such as energy, momentum, position, etc. To extract the property of interest, we apply the appropriate operator to the wavefunction. Every observable (physical property) Q has an associated Hermitian operator $\hat{Q}$ which itself has a corresponding set of orthonormal eigenfunctions $\{|\phi_i(x_1, x_2, \ldots x_N)\rangle\}$ and eigenvalues $\{q_i\}$. These form the set of solutions to the operator's eigenequation,

$$\hat{Q}\left|\phi_i(x_1, x_2, \ldots x_N)\right\rangle = q_i\left|\phi_i(x_1, x_2, \ldots x_N)\right\rangle. \tag{2.2}$$

Since we can write the system wavefunction as a summation of eigenfunctions

from a different complete basis, we can express $|\Psi\rangle$ in terms of the eigenfunctions of the observable,

$$|\Psi\rangle = \sum_i c_i |\phi_i\rangle , \tag{2.3}$$

where $|c_i|^2$ is the probability of $|\Psi\rangle$ being in the state $|\phi_i\rangle$.

Expectation values are very important in quantum physics for finding physical quantities one would want to utilise. The orthonormality condition of $\{|\phi_i(x_1, x_2, \ldots x_N)\rangle\}$ implies $\langle\phi_j|\phi_i\rangle = \delta_{i,j}$, therefore we can write the expectation value of any observable as

$$\langle\hat{Q}\rangle = \langle\Psi|\,\hat{Q}\,|\Psi\rangle \tag{2.4}$$

$$= \sum_i |c_i|^2 q_i. \tag{2.5}$$

In much of this thesis we will be working with closed systems at finite temperature. At non-zero temperature, it is highly unlikely that the system will be in a pure state $|\Psi\rangle$. Instead, we will need to look at the density matrix $\hat{\rho}$, which treats pure states and mixed states in the same manner. We can write the density matrix using the set of eigenfunctions associated with the Hamiltonian of the system

$$\hat{\rho} = \sum_i p_i |\psi_i\rangle \langle\psi_i| , \tag{2.6}$$

where p_i is the probability of being in the eigenfunction $|\psi_i\rangle$, and for the ground state, zero temperature system $p_i = \delta_{1,i}$. For closed systems at finite temperature and at thermal equilibrium, we take the probability to be the Boltzmann distribution,

$$p_i = \frac{\exp\frac{-E_i}{k_B T}}{\sum_j \exp\frac{-E_j}{k_B T}} \tag{2.7}$$

where T is the temperature of the system, and E_i is the eigenenergy associated with the eigenfunction $|\psi_i\rangle$. The state $\hat{\rho}$ can also be found directly from the Hamiltonian, using

$$\hat{\rho} = \frac{\exp\left(\frac{-\hat{H}}{k_B T}\right)}{\mathrm{Tr}\left[\exp\left(\frac{-\hat{H}}{k_B T}\right)\right]}, \tag{2.8}$$

which is the Boltzmann-Gibbs (thermal) equilibrium state.

When using the density matrix (or state, as it will be commonly referred to in this thesis), we can write the expectation value of any observable Q as

$$\langle\hat{Q}\rangle = \mathrm{Tr}\left[\hat{Q}\hat{\rho}\right]. \tag{2.9}$$

One very important observable in this thesis is the density. The probability density of finding a single electron in a continuous one dimensional N-particle system can be found through

$$n(x_1) = \int \dots \int |\langle \Psi(x_1, x_2, \dots x_N) \rangle|^2 \, dx_2, dx_3 \dots dx_N. \tag{2.10}$$

For a system on a lattice, we can use the density operator $\hat{n}_i = \hat{n}_{\uparrow,i} + \hat{n}_{\downarrow,i}$ to find the density on site i. Here $\hat{n}_{\uparrow,i} = \hat{c}^\dagger_{\uparrow,i}\hat{c}_{\uparrow,i}$ and counts the number of spin up electrons in site i, and similarly for $\hat{n}_{\downarrow,i}$ counting spin down electrons. $\hat{c}^\dagger_{\uparrow,i}$ and $\hat{c}_{\uparrow,i}$ are the usual creation and annihilation operators respectively. The electron density (or site occupation) of site i is therefore written as

$$n_i = \langle \Psi | \, \hat{n}_i \, | \Psi \rangle \, , \tag{2.11}$$

or, for mixed states,

$$n_i = \mathrm{Tr} \left[\hat{n}_i \hat{\rho} \right] . \tag{2.12}$$

The density is a very important quantity because it is much simpler to use than the wavefunction or state, as we will discover in the next few sections.

2.1.1 The many-body problem

All that has been said so far is applicable to both single-electron systems as well as many-body systems. If we have a many-electron system with non-interacting electrons, it is possible to simplify the Hamiltonian and wavefunction of the system. The Hamiltonian of this non-interacting system can be written in the form

$$\hat{H}^{NI} = \hat{T} + \hat{V}, \tag{2.13}$$

where $\hat{T}$ is the kinetic energy operator, and $\hat{V}$ is the external potential operator. This Hamiltonian can be solved using the usual Schrödinger equation (now generalised to D dimensions)

$$\hat{H}^{NI} \, |\Psi(\mathbf{r}_1, \mathbf{r}_2, \dots \mathbf{r}_N)\rangle = E \, |\Psi(\mathbf{r}_1, \mathbf{r}_2, \dots \mathbf{r}_N)\rangle \, , \tag{2.14}$$

but because the system is non-interacting, equation 2.14 can be separated into N single-electron Schrödinger equations. In practice, each coordinate $\mathbf{r}_i$ of the wavefunction $|\Psi(\mathbf{r}_1, \mathbf{r}_2, \dots \mathbf{r}_N)\rangle$ is controlled by p^D parameters (where p is, for example, the spatial grid size the system is mapped over, and D is the number of dimensions of the grid) and so the non-interacting wavefunction requires

Np^D parameters to be found. Note that the corresponding density is simpler still as it depends on one variable and hence only requires p^D parameters.

In practice, the electrons in the system will interact, and so the Hamiltonian should include an interacting term, $\hat{U}$. This interacting term is often the Coulomb interaction, given by[1]

$$\hat{U} = \sum_{i<j} \frac{1}{|\mathbf{r}_i - \mathbf{r}_j|}. \tag{2.15}$$

This term cannot be separated which means the interacting Schrödinger equation cannot be separated into N single-electron Schrödinger equations, unlike its non-interacting counterpart. Therefore the interacting Schrödinger equation must be treated as a whole. As N increases, this becomes more and more challenging.

On top of this, as N increases, the interacting wavefunction increases in complexity, more so than the non-interacting wavefunction. Because of the electron-electron interactions, the number of parameters required to define the interacting wavefunction is p^{DN}. It is clear to see how the complexity increases exponentially as the number of electrons increases. For example, the wavefunction for a silicon atom, consisting of 14 electrons and stored on a very crude 3D grid of $10 \times 10 \times 10$ points, would require $10^{3\times14} = 10^{42}$ values to be stored. Therefore it is not feasible to store the wavefunction for many-body systems of more than just a few electrons.

Notice, however, that the density still only requires p^D parameters. It is easier to work with both computationally (because of its smaller size) and experimentally (because it is a measurable quantity). We will see next how this is possible using density functional theory.

2.1.2 Density Functional Theory

Density Functional Theory (DFT) is a widely used and very successful theory for calculating properties of many-body systems [61–70]. It is based on the Hohenberg-Kohn theorem which proves that there exists a one-to-one mapping between the ground state wavefunction and the ground state many-body density of any given system. The result of this is that we can reformulate the ground state wavefunction and all associated expectation values into functionals of the ground state density. This is of great importance because, as we

[1]Note that here we are using atomic units where $e = \hbar = m = 1$, e the electron charge and m the electron mass.

have already demonstrated, the density is a much more manageable quantity, and so by using it for functionals, the properties of many-body systems are, in principle, more accessible.

Another key theory associated with DFT is the Kohn-Sham theory. The Kohn-Sham theory allows for the application of DFT by providing a method of calculating the exact many-body density from complex interacting systems. It is, in principle, an exact method of finding the exact many-body density by using a fictitious non-interacting system, allowing the system to be solved by using N single-electron Schrödinger equations which are much simpler. In practice, approximations are required to find the many-body interacting density, but this has not hampered the success of these theories; they are widely used in physics, chemistry, and even biology [61, 66–69]. These original theorems have been extended to most scenarios, such as time-dependent systems (TDDFT) [71], magnetic systems (CDFT) [65], and lattice Hamiltonians (SOFT) [72, 73].

In this thesis we will use ideas from DFT, focusing on the mapping between the wavefunction and the density, and the concept of using a non-interacting system to calculate the properties of an interacting many-body system. Since we will only explicitly use DFT approximations in chapter 8, we will just briefly introduce the main concepts of DFT here, and will more explicitly describe the relevant ideas where they are used.

Hohenberg Kohn Theory

In 1964, Hohenberg and Kohn demonstrated that there is a one-to-one mapping between the ground state wavefunction $|\Psi\rangle$ and the ground state density n of any system [74]. Therefore we can write any ground state property of the system as a functional of the density, which only requires p^D parameters, compared to using the cumbersome wavefunction, which needs p^{DN} parameters.

Hohenberg and Kohn proved this one-to-one mapping very simply, by *reductio ad absurdum* [74]. Let us assume we have two potentials, $\hat{V}_1(\mathbf{r})$ and $\hat{V}_2(\mathbf{r})$, which differ by more than the addition of a constant and give rise to the same density $n(\mathbf{r})$. Each potential leads to a distinct Hamiltonian, $\hat{H}_1$ and $\hat{H}_2$, with its own ground state solution $|\Psi_1(\mathbf{r})\rangle$ and $|\Psi_2(\mathbf{r})\rangle$ respectively, which we will assume are non-degenerate and have ground state energies E_1 and E_2

respectively. From this we can write

$$\hat{H}_1 = \hat{H}_2 - \hat{V}_2(\mathbf{r}) + \hat{V}_1(\mathbf{r}), \tag{2.16}$$

$$E_1 = \langle \Psi_1(\mathbf{r}) | \, \hat{H}_1 \, | \Psi_1(\mathbf{r}) \rangle \, , \tag{2.17}$$

$$E_2 = \langle \Psi_2(\mathbf{r}) | \, \hat{H}_2 \, | \Psi_2(\mathbf{r}) \rangle \, . \tag{2.18}$$

From the variational principle [75], we know that no wavefunction can give an energy lower than the ground state wavefunction. This means

$$E_1 = \langle \Psi_1(\mathbf{r}) | \, \hat{H}_1 \, | \Psi_1(\mathbf{r}) \rangle < \langle \Psi_2(\mathbf{r}) | \, \hat{H}_1 \, | \Psi_2(\mathbf{r}) \rangle \, . \tag{2.19}$$

Using equations 2.16 and 2.18, we can rewrite equation 2.19 as

$$E_1 < \langle \Psi_2(\mathbf{r}) | \, \hat{H}_1 \, | \Psi_2(\mathbf{r}) \rangle = \langle \Psi_2(\mathbf{r}) | \left[\hat{H}_2 - \hat{V}_2(\mathbf{r}) + \hat{V}_1(\mathbf{r}) \right] | \Psi_2(\mathbf{r}) \rangle \, , \tag{2.20}$$

$$< \langle \Psi_2(\mathbf{r}) | \, \hat{H}_2 \, | \Psi_2(\mathbf{r}) \rangle + \langle \Psi_2(\mathbf{r}) | \left[\hat{V}_1(\mathbf{r}) - \hat{V}_2(\mathbf{r}) \right] | \Psi_2(\mathbf{r}) \rangle \, , \tag{2.21}$$

$$< E_2 + \langle \Psi_2(\mathbf{r}) | \left[\hat{V}_1(\mathbf{r}) - \hat{V}_2(\mathbf{r}) \right] | \Psi_2(\mathbf{r}) \rangle \, . \tag{2.22}$$

We can then repeat this process but starting from the second system, obtaining

$$E_2 = \langle \Psi_2(\mathbf{r}) | \, \hat{H}_2 \, | \Psi_2(\mathbf{r}) \rangle < \langle \Psi_1(\mathbf{r}) | \, \hat{H}_2 \, | \Psi_1(\mathbf{r}) \rangle \, , \tag{2.23}$$

$$E_2 < E_1 + \langle \Psi_1(\mathbf{r}) | \left[\hat{V}_2(\mathbf{r}) - \hat{V}_1(\mathbf{r}) \right] | \Psi_1(\mathbf{r}) \rangle \, . \tag{2.24}$$

Because we have assumed the same ground state density for both systems, we write the potentials using $\langle \hat{V} \rangle = \int \hat{V}(\mathbf{r}) n(\mathbf{r}) d(\mathbf{r})$, and so equations 2.22 and 2.24 become

$$E_1 < E_2 + \int \left[\hat{V}_1(\mathbf{r}) - \hat{V}_2(\mathbf{r}) \right] (\mathbf{r}) n(\mathbf{r}) d(\mathbf{r}), \tag{2.25}$$

$$E_2 < E_1 + \int \left[\hat{V}_2(\mathbf{r}) - \hat{V}_1(\mathbf{r}) \right] (\mathbf{r}) n(\mathbf{r}) d(\mathbf{r}) \tag{2.26}$$

respectively. Now if we add equations 2.25 and 2.26, we obtain

$$E_1 + E_2 < E_2 + E_1, \tag{2.27}$$

which is indeed absurd. This shows that two different wavefunctions cannot produce the same density, and therefore there is a one-to-one mapping between a system's ground state wavefunction and density.

This mapping allows for many properties of complex many-body systems

to be calculated. In this thesis we will investigate this mapping in metric spaces, with a focus on characterising system dynamics.

Kohn Sham theory

The Kohn-Sham theory is very useful when it comes to calculating the particle density to be used to find the other physical properties of a many-body interacting system. It maps the interacting system to a non-interacting system with the same particle density, but a different external potential: this non-interacting system has additional potentials which apply corrections that aim to include the effect of the electron-electron interactions [76]. These additional potentials are the Hartree potential, $\hat{V}_H$, and the exchange-correlation potential, $\hat{V}_{xc}$. Using this fictitious non-interacting system, one can obtain the exact many-body interacting density. One way to visualise the mapping between the exact many-body interacting system, and the Kohn-Sham system is

$$\begin{array}{ccc} \underline{\text{Exact system}} & & \underline{\text{Kohn-Sham system}} \\ N\text{-body} & & N\text{-body} \\ \text{interacting} & \longleftrightarrow & \text{non-interacting} \\ \hat{H} = \hat{T} + \hat{V}_{ext} + \hat{U} & & \hat{H}_{KS} = \hat{T} + \hat{V}_{ext} + \hat{V}_H + \hat{V}_{xc} \\ n(\mathbf{r}) & & n(\mathbf{r}) \end{array}$$

Whilst this theory is in principle exact, the exchange-correlation potential often has to be approximated as it is not usually known exactly [61, 62, 72]. Note that there are a few cases where the exchange-correlation potential is known exactly, such as for the homogeneous electron gas [76], and these systems have then been used to create approximated exchange-correlation potentials.

In chapter 7, we will use the concept of replacing the exact interacting system with a non-interacting system plus some corrections to calculate quantum thermodynamic properties. Only in chapter 8 will we use the Kohn-Sham theory itself, and it is in this chapter where we will discuss the theory further.

2.2 Metrics for quantum mechanics

Metrics are functions which give the distance between two objects in a set. They are widely used in quantum physics [77–87] particularly because they provide insight into the distinguishability between two quantum states [81, 88, 89]. From this it is possible to interpret, for example, the entanglement between the states [90], with extensions relating this to the cost of quantum

communication [80]. Metrics have also been used to give insight into the Hohenberg-Kohn mapping between the ground state wavefunction and density in small model quantum systems [77, 78, 91].

Metrics are defined by the following axioms [82, 92]:

$$D(x, y) \geq 0 \qquad \text{Separation;} \tag{2.28}$$

$$D(x, y) = 0 \iff x = y \qquad \text{Coincidence;} \tag{2.29}$$

$$D(x, y) = D(y, x) \qquad \text{Symmetry;} \tag{2.30}$$

$$D(x, z) \leq D(x, y) + D(y, z) \qquad \text{Triangle inequality.} \tag{2.31}$$

The coincidence axiom can be seen as a special case of the separation axiom, so it is often said that there are three axioms of a metric. We will also see how the triangle inequality can be used for setting thresholds for classifying an adiabatic evolution in chapters 4 and 5.

In this thesis we will demonstrate how metrics can be used to analyse the behaviour of many-body quantum systems, with a specific interest in characterising adiabatic evolutions. To do this we need to define appropriate metrics to use. We will implement the 'natural' metrics for the wavefunction and density, which were derived from conservation laws in reference [77] meaning they can have a physical interpretation.

The reason we choose to look at the wavefunction and density distances is to facilitate future exploration into the Hohenberg-Kohn theorem. We have seen that there exists a one-to-one mapping between wavefunction and density, and that the density is a much more accessible quantity in many-body quantum systems. We also know that wavefunctions of quantum systems are described in Hilbert spaces. Hilbert spaces are vector spaces, which allow us to manipulate wavefunctions using inner products and other vector space properties, but they are also metric spaces. Electron densities do not form a vector space, but they do form a metric space. Because of this, we can use metric spaces as a framework in which we can more directly compare wavefunctions and densities. Through this, one can deduce further information into the Hohenberg-Kohn theorem and how it translates into distances where there is currently no theory to suggest whether there will be a mapping between density distance and wavefunction distance in metric spaces. It has already been shown that the ground state mapping between wavefunction and density is somewhat maintained in metric spaces (i.e. there is a monotonic, quasi-linear relationship between the ground state wavefunction distance and the ground state density distance where a small distance in one also shows

a small distance in the other to some degree) for small model systems where only one parameter was varied between systems (for example, a harmonic oscillator where ω was varied from one system to the next) [77, 78, 91]. We have previously demonstrated that this mapping is indeed true for systems with random potentials, implying it could be a more general trait [85, 93]. In this thesis we exploit this quasi-mapping to provide new, graphical, density-based tools for characterising adiabaticity in quantum systems.

2.2.1 Density metric

The natural density metric was derived as [77]

$$D_n = \int |n_1(r) - n_2(r)| dr. \tag{2.32}$$

This metric has a maximum distance of $2N$, where N is the number of particles in the system (assuming system 1 and system 2 both have N particles). In this thesis we rescale D_n such that the maximum distance is 2, and therefore we can make comparisons with the ground state gradients of D_ψ (equation 2.38) against D_n found in references [77, 78]. This is important for establishing a rough relationship between D_n and D_ψ for the ground states when considering adiabaticity, as we will see in chapters 4 and 5.

2.2.2 Metrics for pure states

From the density metric, one could be tempted to write the wavefunction metric as

$$\tilde{D}_\psi = \left[\int |\psi_1 - \psi_2|^2 dr_1 \dots dr_N \right]^{\frac{1}{2}}, \tag{2.33}$$

however this has a flaw; if ψ_1 is multiplied by a phase factor $e^{i\phi}$, meaning it is physically the same wavefunction but mathematically different, the distance between ψ_1 and $\psi_2 = e^{i\phi}\psi_1$ should be 0. We can see that ψ_1 and ψ_2 should be the same in this case if we look at $|\psi_2|^2$ (i.e. the probability amplitude)

$$\begin{aligned} |\psi_2|^2 &= |e^{i\phi}\psi_1|^2 && (2.34)\\ &= \left(e^{i\phi}\psi_1\right)^* \left(e^{i\phi}\psi_1\right) && (2.35)\\ &= e^{-i\phi}e^{i\phi}\psi_1^*\psi_1 && (2.36)\\ &= |\psi_1|^2. && (2.37) \end{aligned}$$

However if we substitute $\psi_2 = e^{i\phi}\psi_1$ into equation 2.33, $\tilde{D}_\psi \left(\psi_1, e^{i\phi}\psi_1\right) \neq 0$.

By constructing the metric from conservation laws, D'Amico *et al.* [77] overcame this issue and found the natural wavefunction metric should in fact be

$$D_\psi = \left[\int |\psi_1|^2 + |\psi_2|^2 dr_1 \dots dr_N - |2\int \psi_1^* \psi_2 dr_1 \dots dr_N|\right]^{\frac{1}{2}}. \tag{2.38}$$

This coincides with the Bures distance for pure states.

2.2.3 Metrics for mixed states

The Bures distance is a distance measure for mixed states, and is given as [82, 94]

$$D_\rho^B(\sigma, \rho) = \left[2\left(1 - \sqrt{F(\sigma, \rho)}\right)\right]^{1/2}, \tag{2.39}$$

where F is the fidelity[2]

$$F(\sigma, \rho) = \left[\mathrm{Tr}\sqrt{\sqrt{\rho}\sigma\sqrt{\rho}}\right]^2. \tag{2.40}$$

The maximum value of the Bures distance is $\sqrt{2}$ when using states normalised to be one. The Bures distance allows for the similarity between two mixed states to be found, unlike D_ψ from equation 2.38 which is for pure states. The Bures distance, however, presents challenges as it requires the square root of the density matrix operators. If one can calculate these quantities, it is a very useful measure of the distance between two mixed states. It can therefore be applied to a wide range of systems, including systems at finite temperature, which we will do in this thesis.

In quantum information, a very common metric used is the trace distance, which is defined as [82]

$$D_\rho^T(\rho, \sigma) = \frac{1}{2}\mathrm{Tr}\left[|\rho - \sigma|\right] = \frac{1}{2}\mathrm{Tr}\sqrt{(\rho - \sigma)^\dagger(\rho - \sigma)}, \tag{2.41}$$

and has a maximum value of 1 when using states normalised to 1. The trace distance can also be used as a measure of distinguishability [81, 82, 89, 95], much like the Bures, but they have a few differences and the decision of which to use will depend on the quantities one has access to and the ease of calculating these.

It is possible to write a bound for the trace distance using the fidelity

[2]Note that the fidelity itself is not a metric as it does not adhere to all the axioms. However the Bures distance shows how the fidelity can be converted into a metric.

(indicative of a link between the Bures and trace distances) [88],

$$1 - \sqrt{F(\rho_1, \rho_2)} \leq D_\rho^T(\rho_1, \rho_2) \leq \sqrt{1 - F(\rho_1, \rho_2)}. \tag{2.42}$$

This shows that when the fidelity between ρ_1 and ρ_2 is 0, and hence the states are distinguishable, both the trace distance and Bures distance are maximal. Conversely, when the fidelity is maximal (equal to 1), the trace and Bures distances are minimal (equal to 0). We can interpret the trace distance to be the probability of successfully distinguishing two quantum states with one measurement [81, 88].

As previously mentioned, we will be using these metrics in this thesis to look at characterising adiabaticity in a wide variety of quantum systems, from continuous single-electron systems with random potentials at zero temperature, to many-body systems on a lattice at finite temperature. For this we must understand what it means to be adiabatic, and how adiabaticity is currently being characterised.

2.3 Adiabatic criterion

The quantum adiabatic theorem [96] defines an adiabatic evolution as one in which no transitions between energy levels occurs, and is a fundamental concept for any time-dependent quantum system. It was first proposed in 1928 by Born and Fock, and demonstrates that for a quantum system to be considered adiabatic, it must be evolved slowly enough that it remains in an instantaneous eigenstate[3], with a gap between its eigenenergy and the rest of the Hamiltonian's spectrum [96]. Later, Avron and Elgart relaxed this gap condition through a reformulation of the theorem [97]. At zero temperature, this is often interpreted mathematically with the quantum adiabatic criterion (QAC) [42, 43, 98]:

$$\epsilon(t) = \hbar \frac{\left|\langle m(t)| \dot{H}(t) |k(t)\rangle\right|}{\left(|E_k(t) - E_m(t)|\right)^2} \ll 1, \tag{2.43}$$

where $\dot{H}(t)$ is the time derivative of the Hamiltonian, $|m(t)\rangle$ and $|k(t)\rangle$ are instantaneous eigenstates of $\hat{H}(t)$ with instantaneous eigenenergies $E_m(t)$ and $E_k(t)$ respectively, and are usually taken with $|k(t)\rangle$ as the perfectly adiabatically-

[3]Note that originally it only ever considered an eigenstate, but we will work with finite temperature and mixed states so take the definition that no transitions between states occur during the evolution.

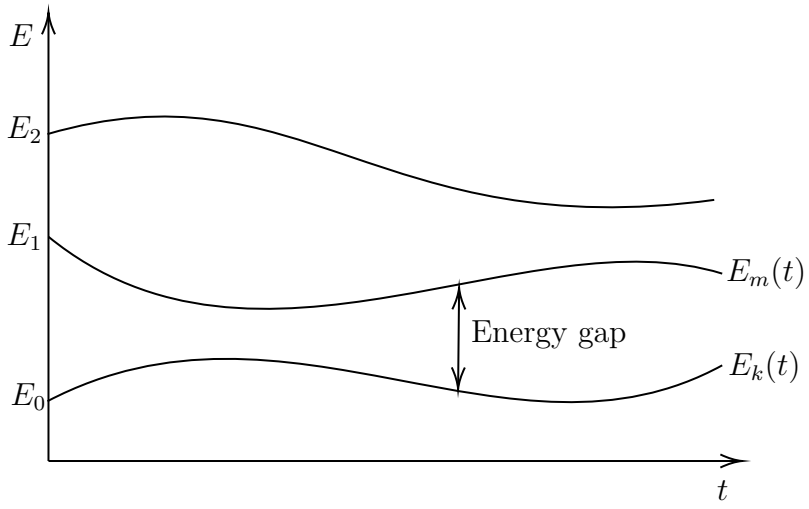

Figure 2.1: Example of energy levels with time, indicating the typical levels used to calculate ϵ in equation 2.43.

evolving original eigenstate and $|m(t)\rangle$ corresponding to another eigenstate of the instantaneous Hamiltonian, where typically $m = k + 1$ (note that in this thesis we use atomic units which sets $\hbar$ to 1). Figure 2.1 demonstrates the energy levels which ϵ typically uses, including the energy gap which is often important to consider for an adiabatic evolution.

Whilst the QAC is usually adequate at determining if an evolution is adiabatic, recent works have sparked debate into its sufficiency, necessity, and validity in certain conditions, such as when there are oscillating terms in the Hamiltonian [41–43, 99–102]. On top of this, the QAC is based on perturbation theory so may not be applicable for stronger perturbations (where it can be less accurate and result in potentially misleading conclusions), and often it only considers two eigenstates, adding to its limitations.

New approaches for characterising adiabaticity in quantum systems have been developed, where adiabaticity is analysed through comparisons between the time evolved state and the exact "adiabatic" state (usually the instantaneous ground state). Lychkovskiy *et al.* use the "adiabatic fidelity", based on the fidelity for pure states, as a figure of merit to the degree of adiabaticity [103]. The "adiabatic fidelity" is defined as

$$F_{adiab} = |\langle \psi_{GS}(t) | \psi(t) \rangle|^2 , \tag{2.44}$$

where $\psi_{GS}(t)$ is the instantaneous ground state at time t, and $\psi(t)$ is the time evolved state at time t [103]. The aim of this adiabatic fidelity is to distinguish between the evolved state and the adiabatic state to determine how close the evolution is to adiabaticity. However, the fidelity is not a metric

and is therefore a weaker method for defining the distinguishability between two states. In this thesis, we will develop a method for determining the degree of adiabaticity based on metrics[4], which provide a stronger definition of how close the two states of interest are. The closer these two states, the more adiabatic the evolution is.

This thesis also focuses on the impact of temperature on quantum systems, which can no longer be ignored when wanting to create working quantum devices. Therefore we also need to explore a method of characterising adiabaticity in systems at finite temperature, where the system state will be a mixed state and an adiabatic evolution must ensure that no transitions occur during the dynamics. For mixed states, it is no longer possible to use equation 2.43, so adaptations must be made. In chapter 5, we will address these changes and develop a new QAC for systems at finite temperature.

2.4 Quantum thermodynamics

In the previous chapter we discussed the importance of the growing field of quantum thermodynamics, especially for the development and realisation of quantum devices. In this thesis we will focus on the quantum work and entropy production, and so here we will introduce how classical work and entropy can be translated into quantum physics.

2.4.1 Quantum Work

The first law of thermodynamics describes the change in internal energy ΔU of a closed classical system as equal to the heat supplied *to* the system Q plus the work done *on* the system W:

$$\Delta U = Q + W. \tag{2.45}$$

These classical systems, however, are large enough such that any small fluctuations (i.e. on the scale of a few particles) are negligible compared to the overall energy change. This is not the case for quantum systems, where the system is too small to ignore any fluctuations or other quantum effects [11]. We therefore need a new definition of work and heat which can encapsulate these quantum effects.

[4]Reference [100] used Euclidean distances between wavefunctions to interrogate the validity of $\epsilon(t)$, but the measures used were similar to those in equation 2.33, which we know are inappropriately sensitive to physically-irrelevant overall phase changes in the state.

From equation 2.9, we know that the average energy of a quantum system described by $\hat{H}$ in state $\hat{\rho}$ can be written as

$$U(t) = \mathrm{Tr}\left[\hat{H}(t)\hat{\rho}(t)\right]. \tag{2.46}$$

Therefore, for a closed system (i.e. a system not connected to a bath) undergoing dynamics from an initial time $t = 0$ to a final time $t = \tau$, the change in average internal energy is

$$\Delta U = \mathrm{Tr}\left[\hat{H}(\tau)\hat{\rho}(\tau)\right] - \mathrm{Tr}\left[\hat{H}(0)\hat{\rho}(0)\right]. \tag{2.47}$$

By comparing equations 2.45 and 2.47, we can hope to find some interpretation of quantum work and quantum heat from the system Hamiltonian and state.

In any system, work can be defined as the *useful* energy, i.e. the energy that we have some control over. The heat, however, is the uncontrolled energy change which is usually lost to the environment [10]. In a quantum system, when considering quantum work, we can think of controlling the changes in energy with time through $\dot{H}(t)$. The change in the state with time, $\dot{\rho}(t)$, is much less controllable, and is therefore more closely related to the quantum heat.

The average quantum work done on the system is therefore defined as [10]

$$\langle W \rangle = \int_0^\tau \mathrm{Tr}\left[\dot{H}(t)\hat{\rho}(t)\right] dt, \tag{2.48}$$

and the average quantum heat supplied to the system is defined as [10]

$$\langle Q \rangle = \int_0^\tau \mathrm{Tr}\left[\hat{H}(t)\dot{\rho}(t)\right] dt. \tag{2.49}$$

From these definitions, we can see that

$$\langle Q \rangle + \langle W \rangle = \int_0^\tau \frac{d}{dt}\mathrm{Tr}\left[\hat{H}(t)\hat{\rho}(t)\right] dt. \tag{2.50}$$

We can see that equations 2.47 and 2.50 are equivalent, and therefore we can write the first law of thermodynamics for quantum systems [10]

$$\Delta U = \langle Q \rangle + \langle W \rangle. \tag{2.51}$$

For closed quantum systems, which we will be working with in this thesis, there is no heat exchange to an external bath, and therefore equation 2.51

becomes

$$\Delta U = \langle W \rangle = \mathrm{Tr}\left[\hat{H}(\tau)\hat{\rho}(\tau)\right] - \mathrm{Tr}\left[\hat{H}(0)\hat{\rho}(0)\right]. \tag{2.52}$$

Notice that whereas the internal energy is an observable, and can therefore be found directly from equation 2.46 or from a single measurement, the average quantum work is not an observable [104]; it requires two measurements to be taken, and in open systems it is also path dependent between those two measurements [10].

The average quantum work can also be calculated by looking at the probability of transitions taking place during the evolution of the system,

$$\langle W \rangle = \int P(w) dw, \tag{2.53}$$

where $P(w)$ is the work probability distribution. For closed quantum systems $P(w)$ can be written as

$$P(w) = \sum_{n,m} p_{n(0)} p_{m(\tau)|n(0)} \delta\left(w - \Delta E_{m,n}\right), \tag{2.54}$$

where $p_{n(0)} = \langle n(0)| \hat{\rho}(0) |n(0)\rangle$ is the probability of being in the n-th energy eigenstate at $t = 0$. $p_{m(\tau)|n(0)} = |\langle m(\tau)| \mathcal{U} |n(0)\rangle|^2$ is the probability of being in the m-th eigenstate at time $t = \tau$ given that the system was in the n-th eigenstate at $t = 0$, and the system was subject to the unitary time evolution operator $\mathcal{U} = \mathcal{T} e^{-i \int_0^\tau \hat{H}(t) dt/\hbar}$ where $\mathcal{T}$ is the time ordered operator. $\Delta E_{m,n} = E_m(\tau) - E_n(0)$ is the energy difference between the m-th and n-th eigenstates.

Equations 2.52 and 2.53 can be shown to be equivalent for closed systems. We will rewrite equation 2.53, substituting in equation 2.54 and the probabilities:

$$\langle W \rangle = \sum_{n,m} p_{n(0)} p_{m(\tau)|n(0)} \Delta E_{m,n} \tag{2.55}$$

$$= \sum_{n,m} \langle n(0)| \hat{\rho}(0) |n(0)\rangle \left|\langle m(\tau)| \mathcal{U} |n(0)\rangle\right|^2 (E_m - E_n) \tag{2.56}$$

$$= \sum_{n,m} \langle n(0)| \hat{\rho}(0) |n(0)\rangle \langle m(\tau)| \mathcal{U} |n(0)\rangle \langle n(0)| \mathcal{U}^\dagger |m(\tau)\rangle (E_m - E_n) \tag{2.57}$$

$$= \left(\sum_{n,m} \langle n(0)| \hat{\rho}(0) |n(0)\rangle \langle m(\tau)| \mathcal{U} |n(0)\rangle \langle n(0)| \mathcal{U}^\dagger |m(\tau)\rangle E_m \right)$$

$$- \left(\sum_{n,m} \langle n(0)| \hat{\rho}(0) |n(0)\rangle \langle m(\tau)| \mathcal{U} |n(0)\rangle \langle n(0)| \mathcal{U}^\dagger |m(\tau)\rangle E_n \right). \tag{2.58}$$

To reduce this equation, let us take one term at a time, starting with the first term:

$$\sum_{n,m} \langle n(0)| \hat{\rho}(0) |n(0)\rangle \langle m(\tau)| \mathcal{U} |n(0)\rangle \langle n(0)| \mathcal{U}^\dagger |m(\tau)\rangle E_m = \tag{2.59}$$

$$= \sum_{n,m} \langle m(\tau)| \mathcal{U} |n(0)\rangle \langle n(0)| \hat{\rho}(0) |n(0)\rangle \langle n(0)| \mathcal{U}^\dagger |m(\tau)\rangle E_m \tag{2.60}$$

We note that $\sum_n |n(0)\rangle \langle n(0)| \hat{\rho}(0) |n(0)\rangle \langle n(0)|$ can be written in terms of two identities ($\sum_n |n\rangle \langle n| = \mathbb{1}$, $\sum_s |s\rangle \langle s| = \mathbb{1}$) multiplied by the state

$$\sum_n |n(0)\rangle \langle n(0)| \hat{\rho}(0) \sum_s |s(0)\rangle \langle s(0)| . \tag{2.61}$$

This can be done if $\rho(0)$ is diagonal in the basis of $\hat{H}(0)$, and therefore $\rho(0) = \sum_{s(0)} p_s |s(0)\rangle \langle s(0)|$. From this we see equation 2.61 reduces to $\rho(0)$. Therefore the first term becomes:

$$\sum_m \langle m(\tau)| \mathcal{U} \hat{\rho}(0) \mathcal{U}^\dagger |m(\tau)\rangle E_m. \tag{2.62}$$

Now we can use $\mathcal{U}\hat{\rho}(0)\mathcal{U}^\dagger = \hat{\rho}(\tau)$ and $\hat{H}(\tau) |m(\tau)\rangle = E_m |m(\tau)\rangle$ to write

$$\sum_m \langle m(\tau)| \mathcal{U} \hat{\rho}(0) \mathcal{U}^\dagger |m(\tau)\rangle E_m = \tag{2.63}$$

$$= \sum_m \langle m(\tau)| \hat{\rho}(\tau) |m(\tau)\rangle E_m \tag{2.64}$$

$$= \sum_m \langle m(\tau)| \hat{\rho}(\tau) \hat{H}(\tau) |m(\tau)\rangle \tag{2.65}$$

$$= \mathrm{Tr}\left[\hat{\rho}(\tau)\hat{H}(\tau)\right]. \tag{2.66}$$

This is the same as the first term for the work in equation 2.52.

Let us now turn our attention to the second term. Here, the terms from $p_{m(\tau)|n(0)}$ all reduce to unity through a series of identities.

$$\sum_{n,m} \langle n(0)| \hat{\rho}(0) |n(0)\rangle \langle m(\tau)| \mathcal{U} |n(0)\rangle \langle n(0)| \mathcal{U}^\dagger |m(\tau)\rangle E_n = \tag{2.67}$$

$$= \sum_{n,m} \langle n(0)| \hat{\rho}(0) |n(0)\rangle \langle n(0)| \mathcal{U}^\dagger |m(\tau)\rangle \langle m(\tau)| \mathcal{U} |n(0)\rangle E_n \tag{2.68}$$

$$= \sum_n \langle n(0)| \hat{\rho}(0) |n(0)\rangle \langle n(0)| \mathcal{U}^\dagger \mathcal{U} |n(0)\rangle E_n \tag{2.69}$$

$$= \sum_n \langle n(0)| \hat{\rho}(0) |n(0)\rangle \langle n(0)|n(0)\rangle E_n \tag{2.70}$$

$$= \sum_n \langle n(0)| \hat{\rho}(0) |n(0)\rangle E_n. \tag{2.71}$$

Here we have used $\sum_m |m(\tau)\rangle \langle m(\tau)| = 1$ to reduce the double sum to a single sum over n, as well as $\mathcal{U}^\dagger \mathcal{U} = 1$ and $\langle n(0)|n(0)\rangle = 1$. Now we will use $\hat{H}(0)\,|n(0)\rangle = E_n\,|n(0)\rangle$:

$$\sum_n \langle n(0)|\,\hat{\rho}(0)\,|n(0)\rangle\, E_n = \tag{2.72}$$

$$= \sum_n \langle n(0)|\,\hat{\rho}(0) E_n\,|n(0)\rangle \tag{2.73}$$

$$= \sum_n \langle n(0)|\,\hat{\rho}(0)\hat{H}(0)\,|n(0)\rangle \tag{2.74}$$

$$= \mathrm{Tr}\left[\hat{\rho}(0)\hat{H}(0)\right]. \tag{2.75}$$

Putting the first and second term together, we find that the average quantum work in a closed system from the probability distribution can be written as

$$\langle W\rangle = \mathrm{Tr}\left[\hat{\rho}(\tau)\hat{H}(\tau)\right] - \mathrm{Tr}\left[\hat{\rho}(0)\hat{H}(0)\right], \tag{2.76}$$

which is indeed equation 2.52.

2.4.2 Thermodynamic entropy production

Entropy is another key thermodynamic property and introduces the concept of irreversibility in systems. It can be linked to the second law of thermodynamics, of which the common definition is that the entropy of an isolated system cannot decrease over time. In quantum physics, there has been work towards defining the second law for quantum thermodynamics [105, 106], where once again the small size of the systems means we must question the validity of the classical laws.

In general, we can formulate the second law such that the average work performed on the system is greater than the free energy, and so the free energy of the system F is reduced [10, 105, 107]

$$\langle W\rangle \geq \Delta F. \tag{2.77}$$

The change in free energy can be written as [10, 105]

$$\Delta F = \Delta U - k_B T \Delta S \tag{2.78}$$

where T is the temperature of the system (usually taken to be the temperature of a thermal bath attached to the system), and ΔS is the thermodynamic entropy production.

In quantum information theory, many use the von Neumann entropy [82]

$$S_{vN} = -\mathrm{Tr}\left[\hat{\rho}\ln\hat{\rho}\right], \tag{2.79}$$

which is the quantum extension of the Shannon entropy of probability distribution p_i

$$S_{Sh} = -\sum_i p_i \log p_i. \tag{2.80}$$

The Shannon entropy characterises the degree of uncertainty in the possible outcomes of a variable. The larger S_{Sh} is, the more uncertain the outcome is, and uniform probability distributions maximise the entropy. For example, a normal 6-sided die will have a uniform probability distribution for achieving each number on the die and so the chance of rolling the number 1 will be the same as rolling each other number, therefore the Shannon entropy is maximised as we have maximum uncertainty. Whereas a weighted die with a higher probability of rolling a 1 will increase the certainty of the outcome, and thus reduce the Shannon entropy.

The von Neumann entropy of a subsystem is commonly interpreted as a measure of entanglement between pure states [22], and gives an idea of the degree of uncertainty in a system. For equilibrium states, ΔS and ΔS_{vN} are equivalent subject to ΔS_{vN} being multiplied by the Boltzmann constant k_B [10]. For non-equilibrium states, however, there is still debate as to whether this equivalency is still true [10, 108].

The thermodynamic entropy is proportional to the "irreversible work" (there is a factor of T between the two), and is the entropy we will be using in this thesis. It describes the energy required to be dissipated for the evolved system to return to an equilibrium state [4, 32]. Figure 2.2 diagrammatically represents this thermodynamic entropy. Here a closed system initially in a thermal equilibrium state, $\rho(0)$, is subject to non-equilibrium dynamics via a unitary evolution $\mathcal{U}$ taking it from $\hat{H}(0)$ to a final system of $\hat{H}(\tau)$ (red, solid path). Through this process, work has been extracted from the system[5] $\langle W_{ext}\rangle$, and the final state $\rho(\tau)$ is now far from equilibrium. We can see the equilibrium path, where $\langle W\rangle = \Delta F$, results in the final equilibrium state $\rho_{eq.}(\tau)$ (blue, long dashed path). To get from the non-equilibrium state to the equilibrium state at time $t = \tau$, we need to dissipate some energy to the environment. This energy is encapsulated by the thermodynamic entropy, ΔS, shown by the brown dashed path (note that since we use closed systems in this

[5]Note that work could also have been performed on the system; we take work to be extracted purely as an example.

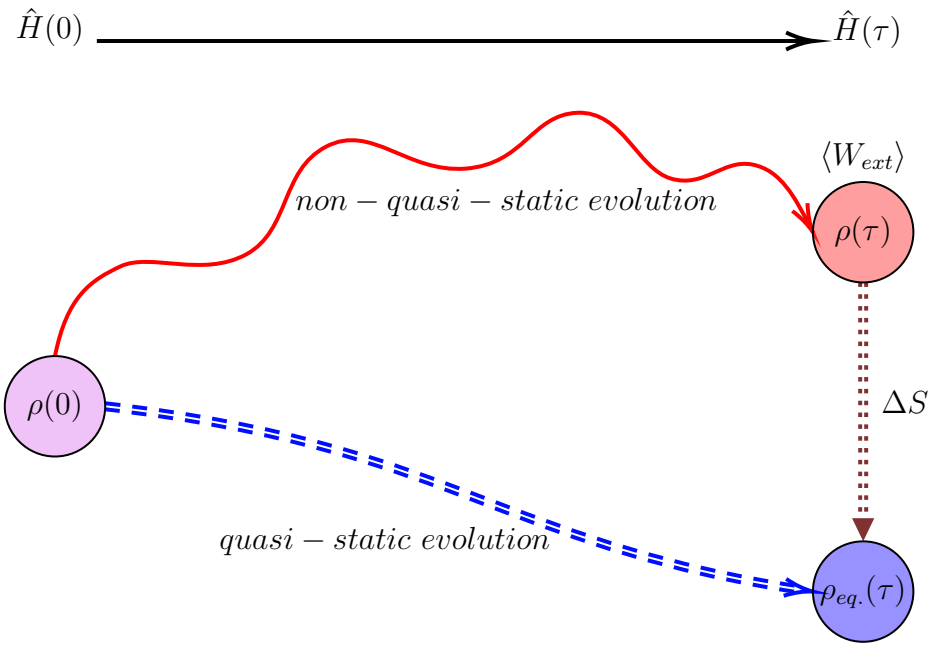

Figure 2.2: Diagram demonstrating thermodynamic entropy production in a system. It is the energy to be dissipated to the environment (brown dashed line) for the system to return to an equilibrium state after non-quasi-static dynamics (red solid line). The quasi-static evolution is where $\langle W \rangle = \Delta F$, and where the system remains in the equilibrium state at all times (blue long-dashed line).

thesis, we do not have any heat exchange and so the entropy production and entropy change are equivalent). This is a very useful entropy to understand, for example to improve knowledge of how much energy needs to be dissipated to reset a quantum system back to an equilibrium state after performing a calculation.

For a given dynamic process in a closed quantum system at temperature T, the variation in thermodynamic entropy is defined using the average work and the change in the free energy of the system [4, 11],

$$\Delta S = \beta \left(\langle W \rangle - \Delta F \right). \tag{2.81}$$

Here $\beta = 1/k_B T$ and is the inverse temperature. We use the Helmholtz free energy variation

$$\Delta F = -\frac{1}{\beta} \ln \left(\frac{Z_f}{Z_0} \right), \tag{2.82}$$

where Z_0 is the partition function at the beginning of the dynamics, $Z_0 = \mathrm{Tr}\left[\exp\left(-\beta \hat{H}(0) \right) \right]$, and Z_f is the partition function at the final time.

Now that we have discussed the main theories and concepts to be used in this thesis, it is important we address the types of systems used in this

research.

2.5 Models used

Throughout this thesis, we will explore the behaviours of one dimensional electronic systems subject to non-equilibrium dynamics. For the majority of the thesis we will use the Fermi-Hubbard model, except in chapter 4 where we will use single-electron continuous systems. Therefore we will focus on the Fermi-Hubbard model here, and will discuss the continuous systems in chapter 4 where they are pertinent.

2.5.1 Fermi-Hubbard model

The Hubbard model is a widely used model in theoretical physics because of its ability to capture some of the non-trivial behaviours of many-body systems despite its simplicity. It can depict lattice systems of weakly correlated electrons to strongly correlated electrons, and through this exhibit numerous phenomena such as the transition from a metal to a Mott insulator, antiferromagnetism, and superconductivity to name a few [83, 109–112]. The model can be used to study many physical systems, from coupled quantum dots, to molecules, to chains of atoms [113–118]. These systems are of importance to quantum technologies as they often make up the hardware of quantum devices.

For small systems consisting of a few lattice sites in the chain (up to $\sim$ 10 sites), the Hilbert space of the Hubbard model is drastically truncated meaning it is can be solved numerically exactly[6]. Despite their small size, these short Hubbard chains still show interesting non-trivial behaviours such as the precursor to the transition between the metal phase and the Mott insulator, and describes (often challenging) strongly correlated systems. For this reason it is often used as a test-bed for exploring interacting quantum systems, and any associated approximations (e.g. using DFT) [32, 59, 62, 63, 113–117, 120].

For an N-site fermionic system, the Hamiltonian of the Hubbard model

[6]Note that the Hubbard model in one dimension can be solved exactly using the Bethe ansatz, provided there is no driving term, the system is homogeneous and is an infinite chain [119], however in this work we will always be driving the system, and so it is no longer exactly solvable.

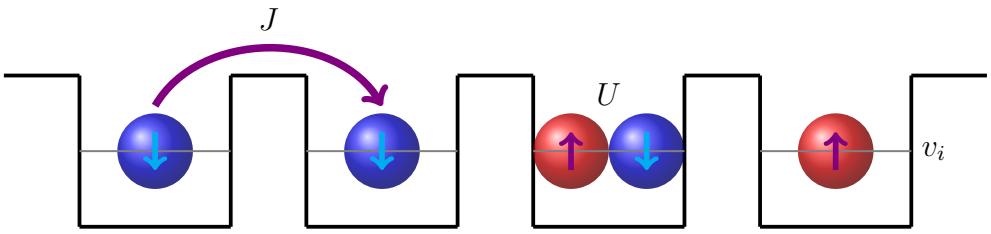

Figure 2.3: Sketch representing the 1D Fermi-Hubbard model, here showing 4 lattice sites. J shows the hopping from one site to the next; U shows the electron-electron interaction strength on-site, and v_i is the on-site potential (here pictured as uniform).

can be given as[7]

$$\hat{H}(t) = -J\sum_{i,\sigma}^{N}\left(\hat{c}^{\dagger}_{i,\sigma}\hat{c}_{i+1,\sigma} + \hat{c}^{\dagger}_{i+1,\sigma}\hat{c}_{i,\sigma}\right) + U\sum_{i}^{N}\hat{n}_{i,\uparrow}\hat{n}_{i,\downarrow} + \sum_{i}^{N}v_i(t)\hat{n}_i, \qquad (2.83)$$

where J is the hopping parameter, $\hat{c}^{\dagger}_{i,\sigma}$ ($\hat{c}_{i,\sigma}$) is the creation (annihilation) operator for a fermion with spin σ ($\sigma =\uparrow$ or $\downarrow$) on site i, U is the strength of the on-site Coulomb interaction, $\hat{n}_{i,\sigma} = \hat{c}^{\dagger}_{i,\sigma}\hat{c}_{i,\sigma}$ is the spin σ, i-site number operator, $\hat{n}_i = \hat{n}_{i,\uparrow} + \hat{n}_{i,\downarrow}$, and $v_i(t)$ is the time-dependent on-site potential. In this thesis we will be working within the dipole approximation.

Equation 2.83 is represented visually in figure 2.3. In this figure we can see a 4 site chain with on-site potential v_i represented by the grey horizontal lines within each site, the electron-electron interaction U shown on site 3, and the hopping term J from site 1 to site 2.

In chapters 5, 6, 7, and 8 we use the time-dependent inhomogeneous Fermi-Hubbard model at half filling to simulate systems at finite temperature. For this, the system is connected to a thermal bath at temperature T and allowed to thermalise from times up to $t = 0^{-}$. This ensures the initial state is a thermal state at temperature T. At $t = 0^{-}$, when the system is thermalised, it is disconnected from the bath. This now closed system in a thermal state is then evolved by a unitary operation from time $t = 0^{+}$ onward. Figure 2.4 diagrammatically represents this process (note that the configuration and size of the chain is only given as an example).

In this thesis, we focus on three types of external potential, all of which have a linear time dependence. These potentials are "zigzag", "teeth" and "slope", and each represent a type of experimentally achievable physical system. These

[7]We have set $\hbar = 1$ here, and we are taking the number of spin up and spin down electrons to be equal.

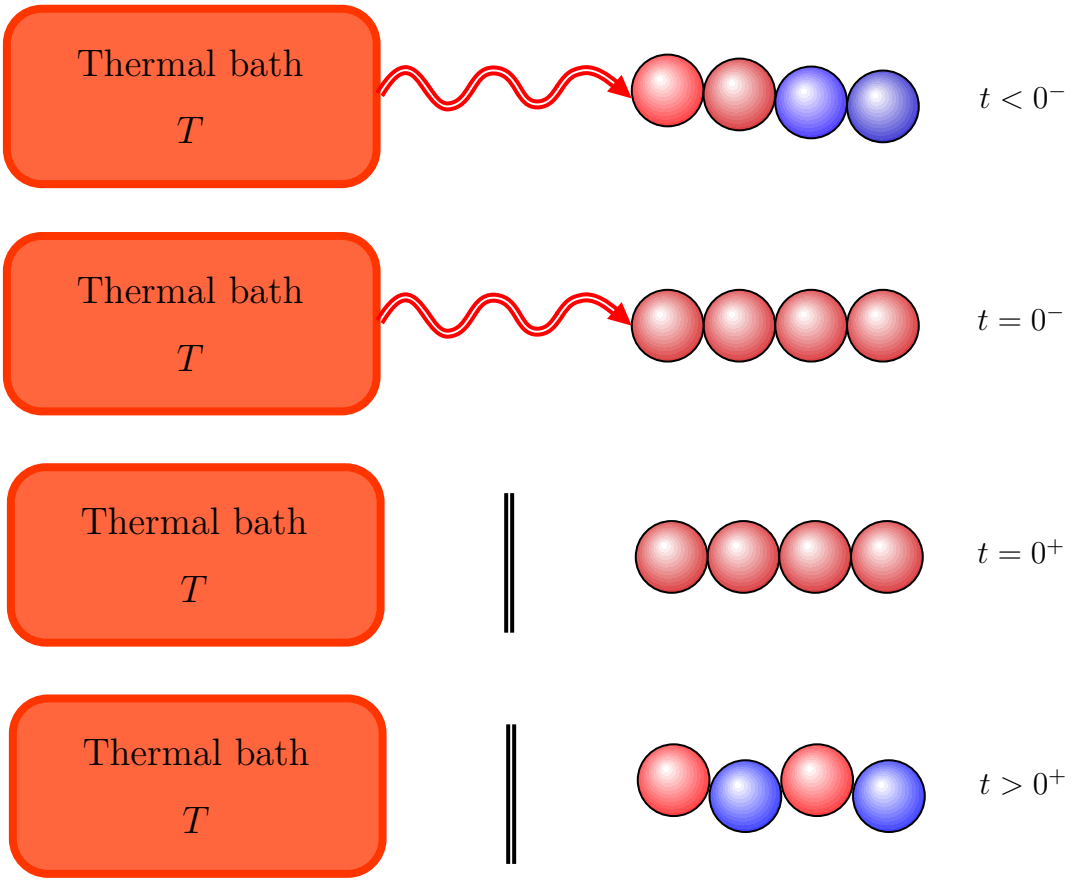

Figure 2.4: The scheme for Hubbard model: top row, we connect the Hubbard chain to a thermal bath of temperature T for times up to $t = 0^-$; second row, the system is thermalised at $t = 0^-$; third row, we disconnect the now thermalised Hubbard chain from the thermal bath; bottom row, we evolve the now closed Hubbard system by driving the external potential using a unitary operator $\mathcal{U}$.

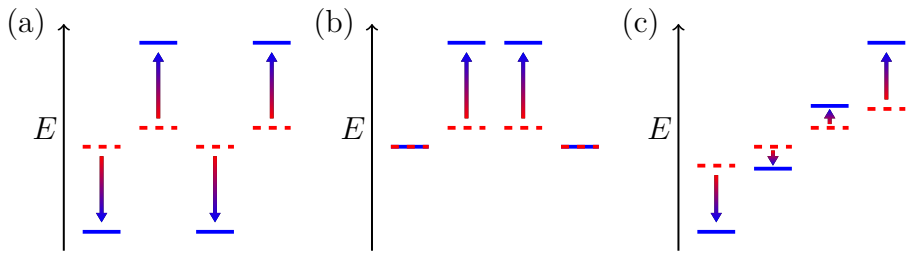

Figure 2.5: We use three driving potentials throughout this work. (a)"zigzag"; (b) "teeth"; (c) "slope".

potentials are represented in figure 2.5, where for four sites the potentials are driven from the red dashed lines to the blue solid lines linearly in time.

The "zigzag" potential [see figure 2.5(a)] pushes even number sites up and odd ones down forming a zigzag pattern. It is representative of the ionic Hubbard model [121–123] which has been used to study neutral-ionic transitions in physical systems [124]. These are transitions which occur with changes in temperature and involve the transition from a band insulator (which the Hubbard model achieves at half filling and in the atomic limit where $J \to 0$) to a Mott insulator (which the Hubbard model achieves when U is greater than the potential difference between neighbouring sites for this potential), as well as lattice dimerisation [125].

The "teeth" potential [see figure 2.5(b)] is reminiscent of the growth of a rabbit's front two teeth[8]; here the two middle sites are the only sites to be driven, all the others remain at the same on-site potential at all times. This type of potential mimics a set of impurities at the centre of the chain. It is important to understand how impurities affect quantum systems as impurity-free quantum systems are usually very challenging to manufacture.

The "slope" potential [see figure 2.5(c)] is akin to a linear electric field being applied to the chain, with the potential difference increasing with time. This type of system can give insight into molecular junctions for quantum devices [126, 127].

All of these potentials are driven linearly in time via $v_i(t) = \mu_i^0 + \mu_i^\tau t/\tau$. Here μ_i^0 and μ_i^τ are the time-independent coefficients for site i at time 0 and τ respectively. For each potential, these coefficients can be written as

- "Zigzag": for each site i, $\mu_i^0 = \mu_0(-1)^i$ at $t = 0$ and $\mu_i^\tau = \mu_\tau(-1)^i$ at $t = \tau$, where $\mu_0 = 0.5J$ and $\mu_\tau = 4.5J$.

- "Teeth": the inhomogeneity μ_i is driven only for the middle two sites

[8] Albeit here the 'teeth' grow up rather than down.

of the chain; $\mu_i^0 = 0$ for $i \neq L/2,\ (L/2)+1$ where i goes from 1 to L, and L is the chain length. For the middle two sites, $i = L/2,\ (L/2)+1$, $\mu_i^0 = 0.5J$ and $\mu_i^\tau = 10J$.

- "Slope": the sites form a linear slope from $i = 1$ to $i = L$ and are described using $\mu_i^0 = 2\mu^0/L \times i - \mu^0$ where $\mu^0 = 0.5J$, and $\mu_i^\tau = 2\mu^\tau/L \times i - \mu^\tau$ with $\mu^\tau = 10J$ in chapters 6, 7, and 8, and $\mu^\tau = 4.5J$ in chapter 5.

Writing the time dependence in this way means the final Hamiltonian of the system is independent of τ. Therefore τ gives us the time to evolve to the final Hamiltonian, and is similar to an inverse speed. A small value for τ is a fast evolution as the system rapidly reaches the final Hamiltonian, whereas a large value of τ is a slow evolution and is expected to be closer to an adiabatic dynamic.

In the next chapter, we will see how these system properties are calculated using the cited theories, established codes, and new codes developed during this PhD.

3. Computational methods

For the work presented in this thesis, we used existing computational codes, developed them for the research, and created new codes for calculating and analysing data. In this chapter we will look at these codes and how they work, explicitly addressing the changes made for this research.

The research can be split into continuous 1D systems, and 1D systems on a lattice. For systems in a continuum, we used the iDEA code [128] to solve the Schrödinger equations, calculating the wavefunctions and densities. For systems on a lattice we used Zawadzki's Exact Diagonalisation for Quantum Thermodynamics code (unpublished) coupled with the QuTiP package [129, 130] to solve the system for the states and site occupation densities. I then created and developed codes which used these outputs to investigate the properties we discuss in this research (i.e. the distances from the metrics, the quantum work approximations, and entropy production).

3.1 iDEA code

The iDEA (interacting Dynamic Electrons Approach) suite of codes developed by Hodgson *et al.* [128] has the ability to numerically exactly solve the time-dependent many-body Schrödinger equation for continuous systems of up to 3 interacting spinless electrons at zero temperature[1]. For example, the iDEA code can take the Hamiltonian of a system with two interacting electrons, written as

$$\hat{H} = -\frac{\hbar^2}{2m}\left(\frac{\partial^2}{\partial x_1^2} + \frac{\partial^2}{\partial x_2^2}\right) + V_{ext}(x_1, t) + V_{ext}(x_2, t) + u(|x_1 - x_2|). \tag{3.1}$$

where the interaction term is interpreted as $u(|x_1 - x_2|) = \frac{1}{1+|x_1-x_2|}$, which is the truncated Coulomb interaction. The Coulomb interaction is proportional to $\frac{1}{r}$, and so after the initial rapid decrease in the interaction with distance,

[1]Spinless electrons are used to increase the richness of correlations available with a given computational cost [128].

it is not worthwhile to computationally calculate the interaction, hence it is truncated. The units the iDEA code uses are Hartree atomic units, denoted by a.u.:

$$\hbar = e = m = 4\pi\epsilon_0 = 1 \tag{3.2}$$

The front end of the codes is written in python, but the main calculations are performed in fortran. The iDEA code propagates a trial wavefunction in the desired external potential through imaginary time until the ground state wavefunction ψ_{GS} of the system is found. Once ψ_{GS} is found, an electric field p is applied at $t = 0$ (i.e. representing a sudden quench) and the system is evolved to find $\psi(t)$ and the corresponding density $n(t)$. Both of these evolutions (in imaginary and real time) are performed using the Crank-Nicolson scheme [131] which is based on the trapezoid rule and is accurate to second order in time.

Chapter 4 uses two codes from the suite: SPiDEA (Single Particle iDEA) and ViDEO (a python code used to make animations of the time-dependent quantities). We use SPiDEA because we begin our study with only one electron as a proof of concept for using metrics to characterise adiabaticity in systems with random potentials. From SPiDEA we can obtain $\psi(t)$ and $n(t) = |\psi(t)|^2$ at each time step, which can then be passed to a separate code for calculating the metrics.

3.1.1 Metrics for single electron systems code

For the research performed in chapter 4, I adjusted the SPiDEA code to allow for the electric field to be applied at different speeds, and hence the applied potential then became pxt (p the final field strength, x the 1D spatial coordinate, and t the current time step divided by total number of time steps). Because the system was always run over the same time, to vary the speed at which the system is driven, p must be varied such that a large p gives fast dynamics and a small p gives quasi-adiabatic dynamics.

I also adjusted the SPiDEA code to output the necessary wavefunctions and densities [for example, we also require the instantaneous ground state wavefunctions $\psi_{GS}(t)$ and densities $n_{GS}(t)$] at given times in the evolution (e.g. SPiDEA can now save these properties for 100 times uniformly spread throughout the time steps from $t = 0$ to completion). It was also important to add the ability to calculate $\epsilon(t)$ according to the definition in equation 2.43 to provide a comparison for the metrics.

I then created a separate python code which reads in these wavefunctions

Algorithm 1: Calculating the metrics using SPiDEA	
1:	Generate random potential.
2:	Set up system parameters (grid size, time step, potential).
3:	Run SPiDEA, ensuring it saves the wavefunction and corresponding density at each time step – note it is in SPiDEA where we introduce the gradually increasing linear potential, p.
4:	Read in the saved wavefunctions and densities from SPiDEA.
5:	Calculate the 'natural' density and wavefunction metrics.
6:	Write the data to file.
7:	Repeat with different p (different driving speed, and hence different adiabaticity level).

Table 3.1: Algorithm showing how the metrics are used with the SPiDEA code.

and densities to calculate the distances between the various wavefunctions and between the various densities using equations 2.38 and 2.32 respectively. These distances are $D_\psi\left(\psi(0),\psi(t)\right)$, $D_\psi\left(\psi(0),\psi_{GS}(t)\right)$, and $D_\psi\left(\psi_{GS}(t),\psi(t)\right)$ for the wavefunction with corresponding distances for the density. These six distances are saved to file ready to be plotted in various combinations, as described in chapter 4.

The algorithm for the metrics code using SPiDEA is outlined in table 3.1.

3.2 Exact Diagonalisation for Quantum Thermodynamics code

Chapters 5, 6, 7, and 8 use the Exact Diagonalisation for Quantum Thermodynamics code developed by K. Zawadzki (unpublished). Zawadzki's suite of codes has the ability to generate the Hamiltonian of the Hubbard model (see section 2.5.1) for small one-dimensional chains up to ~ 8 sites[2], with up to ~ 8 electrons, subject to any time-dependent external potential, and with open boundary conditions. The codes can use this Hamiltonian in a variety of ways, with the main use in this thesis being exactly diagonalising the Hamiltonian to find the thermal state at any given temperature.

The concept behind this application is that the N-site Hubbard chain is connected to a heat bath of temperature T (determined by the system parameters chosen) for long enough that the system thermalises. Therefore the system state of the Hubbard chain will be the thermal state of the system, $\hat{\rho} = \frac{\exp\left(-\beta\hat{H}\right)}{Z}$ at $t = 0^-$. Once thermalised, the Hubbard chain is disconnected

[2]This is dependent on the computer's hardware.

from the heat bath, and the system is then considered to be a closed chain of N sites at thermal equilibrium at $t = 0^+$ (see figure 2.4 in section 2.5.1).

Zawadzki's codes also use the Quantum Toolkit in Python (QuTiP) [129, 130] to evolve the thermal states using any driving of the external potential. The master equation solver of QuTiP (mesolve) is used to do this, but in the absence of any collapse operators (which would indicate an open system) it evolves the system according to the unitary evolution of the Hamiltonian. For unitary dynamics, mesolve uses a usual differential equation solver for the time dependent Schrödinger equation (see equation 2.1) to evolve the states of the system and calculate a set of expectation values for operators provided [129, 130].

Through the master equation solver it is possible to calculate the quantum work via equation 2.76 or equation 2.53. Zawadzki's suite also contains modules for calculating ground state DFT approximations, including the commonly used BALDA [72] and using the reverse engineering scheme from reference [132] to find the exact ground state $\hat{V}_{xc}$ (see chapter 8 for details on these approximations).

3.2.1 Developments to the exact diagonalisation code

Throughout this PhD I have implemented changes and additions to this suite of codes, and also defined the set of parameters used to generate the Hubbard systems, allowing for the calculations in chapters 5, 6, 7, and 8. I have added the ability to calculate the entropy production from equation 2.81, and the ability to calculate the hybrid approximations developed in chapters 7 and 8. I also extended the "quantum work code" from the suite to allow for the calculation of $\langle W \rangle$ during the evolution. In this section we will look explicitly at the additions and developments made to the quantum work calculations.

Average quantum Work approximations

Zawadzki's suite already had the ability to calculate the average quantum work, and even had modules ready to apply DFT approximations to the Hamiltonian. In this thesis, I investigated various methods of applying the approximations to the quantum work calculation, trying to find the most appropriate "mixture" of exact and approximated terms to optimise a "hybrid approximation", as introduced in chapter 7.

It was found that the approximations should be in place only for the Hamiltonians (not the initial state). We approximate $\hat{H}(0)$ and $\hat{H}(\tau)$ in equa-

Algorithm 2: Approximating average quantum work	
1:	Use Zawadzki's code to formulate the Hamiltonian for a given U.
2:	Initialise the approximations.
3:	Find the exact state, $\hat{\rho}(0)$, from the exact initial Hamiltonian.
4:	Approximate the Hamiltonian for the calculation, ensuring consistent approximations for all evolution Hamiltonians, $\hat{H}^{\text{evo}}$, both in the QuTiP evolution and in the quantum work equation.
5:	Evolve the system to a given τ and calculate the quantum work from equation 2.76.
6:	Once the work is calculated, find the free energy using the same Hamiltonian as that used for $\hat{\rho}$ (see equation 2.82).
7:	Use the work and free energy to find the entropy using equation 2.81.
8:	Save all results.
9:	Repeat for all τ's and U's to be investigated.

Table 3.2: Algorithm for approximating $\langle W \rangle$ using the the exact diagonalisation code.

tion 2.76, but we also use the approximated Hamiltonian in the evolution operator used by QuTiP. The state we evolve, however, is the exact initial state.

Once the quantum work has been approximated using this hybrid technique, I then introduced the calculation of the entropy production from equation 2.81. This requires the calculation of the free energy from equation 2.82, where we now use the same Hamiltonian approximation as was used for the initial state $\hat{\rho}(0)$. The entropy production is then a simple subtraction of free energy from the average work, multiplied by the inverse temperature.

The algorithm for the hybrid approximation and the calculation of the entropy is shown in table 3.2. To generate the contour plots that will be shown in the results chapters, we choose a range of interaction strengths U and evolution times τ over which the work extracted, free energy, and entropy production are calculated. Each point in the contour plot is one run through this algorithm.

Work with time

Another major adaptation of Zawadzki's code that I implemented was the ability to calculate the accumulation of the average quantum work during the evolution of any given system. To achieve this, the evolution of $\hat{\rho}$ in QuTiP's mesolver is adjusted to record $\hat{\rho}(t)$ at each time step given in a list of time steps determined by the user. The same must also be done for the Hamiltonian, finding $\hat{H}(t)$ for each t in the time step list. The average work extracted at

Algorithm 3: Calculating the average quantum work for all time steps	
1:	Use Zawadzki's code to formulate the Hamiltonian for a specific U.
2:	Find the exact state, $\hat{\rho}(0)$.
3:	Set up the time grid (tlist) for which each $\hat{\rho}(t)$ and $\hat{H}(t)$ shall be recorded.
4:	Evolve the system to a specific τ, with $\hat{\rho}(t)$ and $\hat{H}(t)$ being recorded for each time in tlist (from 0 to τ).
5:	For each time in tlist, calculate the work as in equation 2.76, replacing τ with the current time step t.
6:	Save the results for this τ and U.
7:	Repeat for all τ's and U's to be investigated.

Table 3.3: Algorithm for finding $\langle W \rangle$ with time using the the exact diagonalisation code.

time t can then be calculated by equation 2.76, replacing $\hat{\rho}(\tau)$ and $\hat{H}(\tau)$ with $\hat{\rho}(t)$ and $\hat{H}(t)$ respectively.

The algorithm for finding the accumulation of the average quantum work extracted is shown in table 3.3. This algorithm can be used for any temperature T, any system size (subject to the limitations of the computer's memory), any external potential (defined by the user), and for a range of interaction strengths and evolution times.

3.2.2 Metrics using the exact diagonalisation code

In this section we will see how the core of Zawadzki's code (i.e. the ability to generate the Hubbard Hamiltonian for a wide range of systems) was used and added to for investigating metrics applied to systems at finite temperature. Table 3.4 gives the algorithm developed for calculating the Bures, trace, and density metrics from equations 2.39, 2.41, and 2.32 using Hubbard systems generated using Zawadzki's code.

The metrics code generates the Hubbard Hamiltonian for a given set of parameters, much in the same way as the quantum thermodynamics codes. It then finds the initial state, which is the ground state if $T = 0J/k_B$, or is the thermal state $\hat{\rho}(0) = \frac{\exp\left(-\beta\hat{H}(0)\right)}{Z(0)}$ if the system is at a finite temperature $T \neq 0J/k_B$. From this initial state, the corresponding initial density can be found using $n(0) = \mathrm{Tr}\left[\hat{\rho}(0)\hat{n}\right]$.

We then evolve the system and, much like with the work with time calculation, we ask QuTiP's mesolver to output the evolving state at every time from a list of times determined by the user. This list of times should go from $t = 0$ to $t = \tau$, and the number of times within the list corresponds to how

Algorithm 4: Finding the metrics using the exact diagonalisation code	
1:	Use Zawadzki's code to generate the system Hamiltonian for a given U.
2:	Find the initial state, $\hat{\rho}_S(0)$, which will be the ground state ($S = GS$) if at zero temperature, or the thermal state ($S = Th$) if at finite temperature.
3:	Find the density n from $\hat{\rho}(0)$ using $\mathrm{Tr}\left[\hat{\rho}(0)\hat{n}\right]$.
4:	Set up the time grid (tlist) which gives each time step at which $\hat{\rho}(t)$ shall be recorded.
5:	Evolve $\hat{\rho}$ to a given τ according to the driving potential, recording $\hat{\rho}(t)$ at each time step in tlist.
6:	Find $n(t)$ from $\hat{\rho}(t)$.
7:	At each time step, diagonalise $\hat{H}(t)$ to find the eigenstates, $\|\Psi(t)\rangle$.
8:	Use $\|\Psi\rangle$'s to find $\hat{\rho}_S(t)$ with same eigenstate populations as $\hat{\rho}_S(0)$ (see equation 5.14 from chapter 5).
9:	Find $n_S(t)$ from $\hat{\rho}_S(t)$.
10:	Calculate Bures, trace, and density metrics from equations 2.39, 2.41, and 2.32, in particular calculating $D_\rho\left(\hat{\rho}_S(0), \hat{\rho}_S(t)\right)$, $D_\rho\left(\hat{\rho}_S(0), \hat{\rho}(t)\right)$, and $D_\rho\left(\hat{\rho}_S(t), \hat{\rho}_S(t)\right)$ for the Bures and trace, and the equivalent density distances.
11:	Write the data to file.
12:	Repeat over all τ's and U's to be investigated.

Table 3.4: Algorithm for calculating the Bures, trace, and density metrics using the the exact diagonalisation code.

coarse the metric results will be (i.e. a small number of times will lead to a very coarse time grid upon which to plot the metric results but will require less memory to output the results, whereas a large number of times in the list will lead to a fine time grid but will output a larger file). For this thesis we take the time list to have 100 times ($t = 0$ and $t = \tau$ inclusive). Using the $\hat{\rho}(t)$'s from the mesolver, we can find the corresponding densities at each time step.

For each t in the time list, we then calculate the Bures, trace, and density distances, with particular focus on $D_\rho\left(\hat{\rho}_S(0), \hat{\rho}_S(t)\right)$, $D_\rho\left(\hat{\rho}_S(0), \hat{\rho}(t)\right)$, and $D_\rho\left(\hat{\rho}_S(t), \hat{\rho}_S(t)\right)$ for the Bures and trace distances, and the corresponding density distances. Here $S = GS$ for the ground state when $T = 0J/k_B$, and $S = Th$ for the thermal state when $T \neq 0J/k_B$. Notice that for these distances we also need to calculate the state which has the same populations as the initial state as this would be the perfectly evolved adiabatic state. This can be written as

$$\hat{\rho}_{Th}(t) = \sum_j \frac{\exp \frac{-E_j(0)}{k_B T}}{\sum_k \exp \frac{-E_k(0)}{k_B T}} \left|\psi_j(t)\right\rangle \left\langle\psi_j(t)\right|, \tag{3.3}$$

where $E_j(0)$ is the j-th eigenenergy at $t = 0$, and $\left|\psi_j(t)\right\rangle$ is the j-th eigenstate of the Hamiltonian at time t. We then take $n_{Th}(t)$ as the corresponding density from this state. More details on this are in chapter 5. This process is repeated for various different driving times, correlation strengths, and temperatures, building up a more complete picture of how well metrics can be used for characterising adiabaticity in lattice systems at finite temperature.

Now that we have discussed the codes being used in this PhD, how they work, and the changes that have been implemented to carry out this research, we can turn our focus to the results obtained. We begin at zero temperature, and explore system dynamics using the metrics.

4. Metrics for characterising quantum adiabaticity in continuous systems

This chapter aims to answer research question 1a: "Can we characterise adiabaticity without using the quantum adiabatic criterion which has several limitations such as its base in perturbation theory, and does not have an easy extension to finite temperature?" Adiabatic evolutions are important in many areas of quantum physics [23–31], but the criterion for adiabaticity has had several flaws exposed over the years, from not being valid or sufficient in oscillating Hamiltonians [42], to the challenge it faces when handling degenerate systems [133]. We therefore look for a method to characterise adiabaticity which does not succumb to these issues, in particular taking inspiration from references [77–79, 132] who look at the use of metrics for studying ground state properties of many-body quantum systems.

The 'natural' metrics mentioned in section 2.2, derived in reference [77], are used in this chapter to study time-dependent (TD) systems, in particular demonstrating their ability to characterise out-of-equilibrium quantum dynamics. Work in this chapter has been published in the Journal of Physics A: Mathematical and Theoretical, see reference [93].

4.1 Introduction

Recall from section 2.3, the adiabatic theorem developed by Born and Fock in 1928 [96]. The key point from their theorem is that a system initially prepared in its ground state will remain in its instantaneous ground state when evolved slowly enough. This is important for many aspects of quantum physics, in particular for adiabatic quantum computing and for achieving target states [23–31]. For example, say one has a hard-to-diagonalise target Hamiltonian

for which one wishes to find the ground state, this ground state can be known as the target state. By taking a readily diagonalisable Hamiltonian where the ground state is known, and adiabatically evolving the system to the target system, the target state can be achieved.

As we can see, adiabatic evolutions are important in quantum technologies. The question becomes how can we determine if an evolution is adiabatic? The previously mentioned quantum adiabatic theorem (QAT) [96] states that for a Hamiltonian varying slowly enough, a system initially at equilibrium will remain in an eigenstate of the instantaneous Hamiltonian, $\hat{H}$. Quantification of the adiabatic theorem is traditionally based on the criterion seen in equation 2.43 [42, 43, 98]. In recent years, debate has opened up about the validity and sufficiency of the quantum adiabatic criterion, with some conclusions showing it to break down for specially crafted systems with oscillating terms in the Hamiltonian [42, 43, 99]. However the question remains open [100]. Furthermore this criterion is derived from perturbation theory which may not be applicable for stronger perturbations.

In addressing research question 1a, we introduce the use of 'natural' metrics [77, 78] for characterising adiabaticity in quantum systems[1]. This has the advantage over the QAC that a) the metrics are not based on perturbation theory and therefore in effect consider all eigenstates of the system, b) can be used to interrogate system dynamics more completely than the QAC, and c) are efficient, simple, and graphical tools for looking into systems. We will demonstrate these points in the rest of the chapter.

4.2 Brief reminder of theory

In chapter 2 we discussed several metrics. We shall be using the metrics derived in references [77] and [78], where the concept of 'natural' metrics – directly arising from conservation laws – was introduced. These 'natural' metrics which measure the distance between two N-particle wavefunctions (normalised to N), or two N-particle densities, were described in chapter 2 and are equations 2.38 and 2.32 respectively [77].

These metrics are of particular interest because the Hohenberg-Kohn theorem from Density Functional Theory (DFT) [74] states there is a one-to-one mapping between the ground state wavefunction and density of any system

[1]Euclidean distances between wavefunctions have previously been used [100] to study the validity of $\epsilon(t)$, but are inappropriately sensitive to a physically-irrelevant overall phase-change of the state; the metrics used here are tailored to avoid this shortcoming [77].

meaning the information contained in the (commonly inaccessible) wavefunction is also contained in the more manageable density. From this, and seen in previous work [77, 78, 134], the Hohenberg-Kohn theorem implies there is the same information in the density distance as there is in the wavefunction distance. Understanding how the relationship of the wavefunction and density behaves in metric space may give useful insight into DFT [77–79, 132]. For this work, however, we shall focus on the time-dependent behaviours of systems and adiabaticity, and not worry about DFT.

4.3 Previous work

The work published in reference [93] begins with findings from my masters project [134], before going on to new research performed during the PhD. In this section we will review the previous work from the masters project, which is important for understanding the PhD work.

This previous work establishes the systems used in the study, and provides the main conclusion from looking at ground state systems: there is a quasi-linear relationship between the ground state density distance and ground state wavefunction distance[2]. This conclusion is vital for the time-dependent study done in the PhD.

4.3.1 Systems used

Initially we consider a family of single electron harmonic oscillators. We explore the mapping between ground state particle densities and the corresponding wavefunctions for single-particle systems, beginning with the harmonic oscillators before moving onto more complex, randomly generated systems. We compare 23 simple harmonic oscillators, which have a range of frequencies (ω) from 0.05 to 2.20 a.u.[3], to a reference oscillator for which $\omega = 0.1$. This yields the green circles in figure 4.1 (main panel) which are well described by a straight line with gradient 1.43.

By inserting the analytic ground states of two harmonic oscillators into

[2]Note that previous work had observed this quasi-linear relationship and had alluded to it being general across different quantum systems [77, 78, 132], but the work in this section and in reference [93] demonstrated this explicitly.

[3]We use atomic units, $\hbar = m = 1$.

equations 2.38 and 2.32, the ratio of the metrics may be written exactly as

$$\frac{D_n\left(n_1,n_2\right)}{D_\psi\left(\psi_1,\psi_2\right)}=\frac{2\left[\operatorname{erf}\left(\sqrt{\frac{\nu\ln(\nu)}{2(\nu-1)}}\right)-\operatorname{erf}\left(\sqrt{\frac{\ln(\nu)}{2(\nu-1)}}\right)\right]}{\sqrt{2-\frac{2^{3/2}\nu^{1/4}}{(\nu+1)^{1/2}}}}, \tag{4.1}$$

where $\nu=\omega_1/\omega_2$ is the ratio of the frequencies of the two oscillators. Expanding this about $\nu=1$, we obtain $D_n\left(n_1,n_2\right)/D_\psi\left(\psi_1,\psi_2\right)=4/\sqrt{e\pi}+O(v-1)^2$ where e is the base of natural logarithms, demonstrating a linear relationship with gradient $4/\sqrt{e\pi}\approx 1.37$ when $\omega_1\approx\omega_2$. The numerical results confirm the quasi-linear relationship even for $|\nu|\gg 1$.

The mapping between ground state wavefunction distance to ground state density distance found in reference [77], and indeed demonstrated above, indicates the possibility of using distances to characterise adiabatic evolutions, in particular it hints at the ability to use just the density (via the metric) as a measure of adiabaticity. However, the systems used to calculate the distances in reference [77] and shown previously with the harmonic oscillator were very similar, varying only by a single parameter (such as by varying ω in Hooke's atom or in the harmonic oscillator). Therefore we need to test whether or not the ground state distance mapping is a more general trait across systems which vary by more than one parameter. A Fourier series allows us to randomly generate a wide range of potentials which vary by more parameters (here we will vary by 6 parameters between each system), and give a range of physical characteristics, from strongly localised electrons, to delocalised electrons spread across the entire potential.

The systems we consider will have continuous, smooth, random, confining potentials. These are generated using a truncated Fourier series with random coefficients, together with an x^{10} potential to gently confine the electrons overall:

$$V_{ext}(x)=\frac{x^{10}}{10^{11}}+\Lambda\sum_{n=1}^{3}\left(a_n\cos\frac{n\pi x}{L}+b_n\sin\frac{n\pi x}{L}\right). \tag{4.2}$$

Here L is half the system size, and the random numbers a_n and b_n are drawn from a uniform distribution between $-\frac{L}{3}$ and $\frac{L}{3}$. The scaling factor Λ is used to adjust the confining strength of the potential microwells, allowing different regimes of electron localisation to be explored (see figure 4.1, lower inset, for example potentials).

4.3.2 Ground state conclusions

Figure 4.1 (lower inset) shows examples of two random potentials. For the ground state study we used a family of ten random potentials with $\Lambda = 0.1$ and $L = 15$ a.u. We solve the Schrödinger equation for our systems using the SPiDEA code[4] to obtain the exact ground state wavefunctions and densities, from which D_ψ and D_n are calculated using equations 2.38 and 2.32. Figure 4.1 (main panel) shows D_n against D_ψ for all 45 pairs of systems in the family (black crosses). The points lie close to a straight line through the origin with gradient 1.59, deviating slightly to reach the combination of the maximum values of D_n and D_ψ (2 and $\sqrt{2}$ respectively, top right-hand corner of the graph).

Reference [77] found a similar quasi-linear relationship between D_n and D_ψ for three families of systems, with the gradient depending on the number of particles, N. There, the families of systems were each generated by varying a single parameter in the Hamiltonian (e.g. the confining frequency for Hooke's atoms), while here a diverse range of systems are explored for $N = 1$ [5].

4.4 Time-dependent systems

The time-dependent work was performed during the PhD, building on the linear relationship found in the ground state systems, and using the random potentials developed in the masters project.

The quasi-linear relationship of $D_n(n_1, n_2)$ and $D_\psi(\psi_1, \psi_2)$ for ground states may become a tool to identify whether the time dependence of a quantum system is adiabatic[6]. Looking at the distances between densities versus the distance between wavefunctions, if an evolution is adiabatic then we will be comparing two ground state distances and therefore the trajectory of the distances during the evolution will lie upon the line of $D_n = mD_\psi$. Here m is the gradient of the quasi-linear relationship, and for $N = 1$ we take this relationship to be 1.5 as an average of the harmonic systems and random systems. We can then use this relationship to test whether D_n holds the same information as D_ψ, and therefore try to develop a measure of adiabaticity that

[4] J. Wetherell, unpublished; subsequently incorporated into the iDEA code suite [128].

[5] Further results for random potentials with N=2 also show a quasi-linear relationship [85].

[6] For the evolution of ground states this quasi-linear relationship indicates both equilibrium and adiabaticity; reference [79] suggests that a similar relationship may hold also for excited states, hence the proposed method could be extended to any eigenstate.

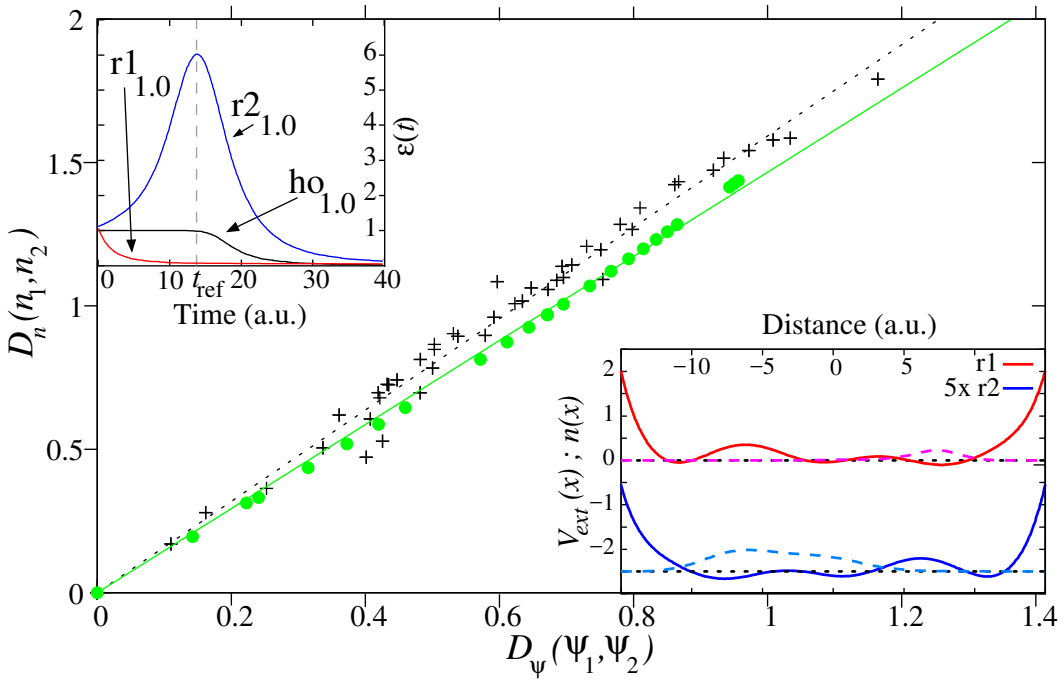

Figure 4.1: *Main panel:* Metrics D_n vs D_ψ for 10 random single electron systems (black crosses) and 23 simple harmonic oscillator systems (green circles) in their ground states. D_n/D_ψ is approximately linear with similar gradients of 1.59 and 1.43 respectively. *Inset (lower):* Two examples of the random potentials (solid lines) and their ground state densities (dashed lines). These are used for the TD study: system r1 (red, $\Lambda = 0.5$) and system r2 (blue, $\Lambda = 0.1$, the spatial reflection of r1 divided by five); the curves are displaced vertically so that the ground state energies lie at 0 and -2.5 on the vertical axis, respectively. *Inset (upper):* TD adiabaticity parameter $\epsilon(t)$ (equation 2.43) for the three time-dependent systems (r1, r2 and a harmonic oscillator, ho) corresponding to $\epsilon(0) = 1.0$. The vertical grey dashed line shows the reference time, t_{ref}, used in figures 4.5 and 4.6.

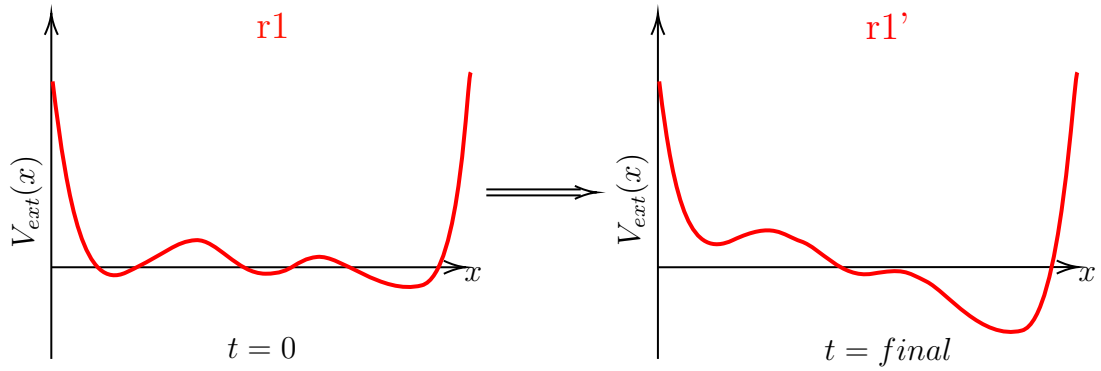

Figure 4.2: Representation of potential r1 at the initial time and at the final time, demonstrating how the linear perturbation affects the potential. Potential r2 will look very similar in these times with the exception that it is the spatial reflection of r1 in the $y-$axis, and is 5 times smaller than r1.

only uses the density and not the wavefunction. This would be useful for many-body systems where the density is a much more accessible quantity.

To explore adiabaticity, we use the SPiDEA code to turn on a uniform electric field increasing linearly with time with a rate p, making the Hamiltonian of our systems $\hat{H}(x,t) = -\frac{1}{2}\frac{\partial^2}{\partial x^2} + V_{ext}(x) - ptx$.

We evaluate the distances between a system's initial ground state, $\psi(0)$, instantaneous ground state, $\psi_{GS}(t)$, and time-dependent state, $\psi(t)$; we obtain $D_\psi(\psi(0),\psi(t))$, $D_\psi(\psi(0),\psi_{GS}(t))$ and $D_\psi(\psi_{GS}(t),\psi(t))$ from equation 2.38, and corresponding expressions for the density from equation 2.32.

We focus on three initial systems, r1, r2 (both seen in figure 4.1), and a harmonic oscillator with $\omega = 0.2$ (ho). Each system is perturbed at two different rates and figure 4.2 demonstrates how the perturbation described above affects the r1 potential at the initial and final times (where we have named the potential at the final time r1' to distinguish it from the initial time and from r2). We choose the perturbation rates p so that the initial adiabaticity parameter $\epsilon(0)$ (from equation 2.43) takes the same two values for all three initial potentials. For $\epsilon(0) = 0.01$, the values of p are 2.530, 0.15 and 0.025 for the ho, r1 and r2 systems, respectively, while for $\epsilon(0) = 1.0$ the values of p are 100 times greater. The six systems span a rich spectrum of behaviours, showing the transition from the harmonic system, ho, through the random potential r1, with a harmonic-like microwell which also allows for mild tunnelling into the neighbouring well, to the random potential r2, with a ground state delocalised over multiple microwells (note that $\epsilon(0)$ is given in the label subscripts). See **Skelt_108001277_animation_r2.mp4** for an animation of the density in r2 when $\epsilon(0) = 0.1$, demonstrating the

delocalisation of the electron[7]. The electron density initially spreads over several microwells, but as the perturbation is applied, the density moves to the right[8].

By definition, if an adiabatic regime is reached, these systems should remain in the ground state of the instantaneous Hamiltonian at every time step. From the findings in figure 4.1, we then expect the dynamics in metric space of such systems to be described by a linear relationship between $D_n(n(0), n(t))$ and $D_\psi(\psi(0), \psi(t))$. By using three types of graphs, we will study how such a regime is entered/exited and, in general, characterised in metric space. These graphs deliver complementary perspectives on the systems' time evolution and adiabaticity. We choose these three types of graph to develop a range of tools for characterising adiabaticity which depend on the properties one has access to, whilst also checking that a consensus between each method exists. For example we use the previously mentioned ground state relationship in the distances as a guide for an adiabatic evolution when comparing $D_n(n(0), n(t))$ against $D_\psi(\psi(0), \psi(t))$. Whilst the measure of $D_\psi(\psi_{GS}(t), \psi(t))$ is an intuitive mathematical interpretation of the quantum adiabatic theorem, there are several circumstances in which one may not have access to $\psi(t)$ or $\psi_{GS}(t)$, for example in many-body systems. Therefore we can also use this relationship as encouragement for exploring the possibility of a density only adiabaticity measure, since the density distance has a relationship to the wavefunction distance but is a more accessible quantity. The possibility of using the density as a method of characterising adiabaticity will then be explored further in the next chapter using many-body systems at finite temperature.

4.4.1 Density distance against wavefunction distance using the evolved state

The first type of graph is $D_n(n(0), n(t))$ against $D_\psi(\psi(0), \psi(t))$, shown in figure 4.3. Here adiabaticity is identified without the direct involvement of the instantaneous ground state. It is for this graph that the gradient from figure 4.1 is used. The ratio D_n/D_ψ of the distances between any two ground states is approximately given by this gradient of 1.5, and hence it can be used to characterise adiabaticity in figure 4.3.

The systems in the inset of figure 4.3 follow the "adiabatic line", showing

[7]Animations submitted alongside the thesis.

[8]In this animation we see oscillations about the instantaneous ground state, however they are not as obvious compared to those seen in ho for this value of $\epsilon(0)$, discussed later. We found, though, that the metrics showed this subtle dynamic clearly.

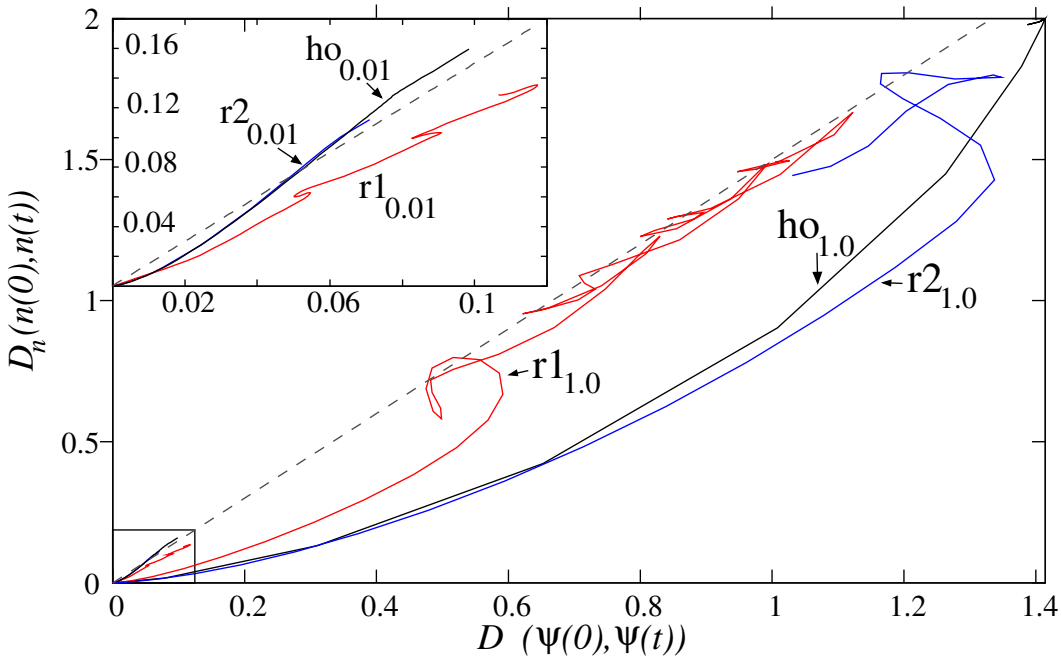

Figure 4.3: Metric distances between the initial ground state and the subsequent TD state (n vs. ψ): adiabatic behaviour corresponds to proximity to the adiabatic (GS) line (grey dashed). Subscripts denote the value of $\epsilon(0)$. Inset: zoom to boxed area.

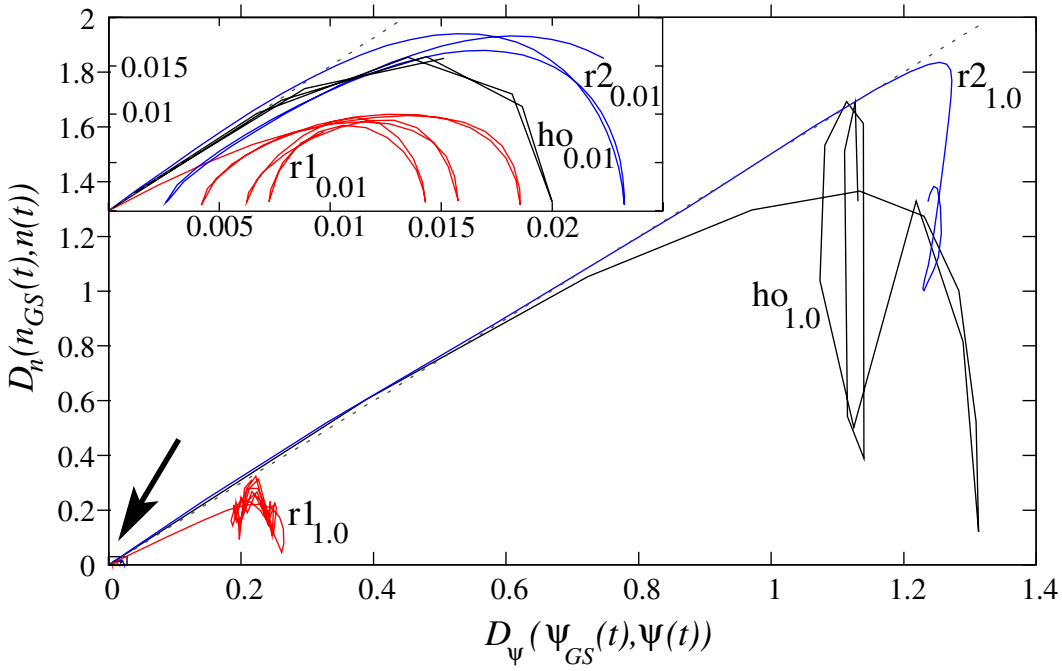

Figure 4.4: Distances between instantaneous ground states and TD states (n vs. ψ): these should remain at the origin for exactly adiabatic evolution. Inset: zoom to area denoted by arrow.

them to be adiabatic in agreement with the corresponding $\epsilon(0)$. Interestingly, after a transient, $r1_{1.0}$ (main panel) is also seen to follow the adiabatic line, despite the related value $\epsilon(0) = 1.0$ suggesting non-adiabaticity. In fact the metric graph shows the evolution to be initially non-adiabatic before returning to the adiabatic line, in agreement with $\epsilon(t)$ which drops to ~ 0.3 in the upper inset of figure 4.1 [9]. For r2, figure 4.3 suggests a degree of non-adiabaticity similar to ho, whereas $\epsilon(t)$ in the upper inset of figure 4.1 shows r2 to have a much greater degree of non-adiabaticity than ho.

4.4.2 Density distance against wavefunction distance using the instantaneous ground state

The second type of graph is $D_n(n_{GS}(t), n(t))$ against $D_\psi(\psi_{GS}(t), \psi(t))$ (figure 4.4). Here, the measure of adiabaticity comes from proximity to the origin. We can clearly see that for $\epsilon(0) = 1.0$ (denoted in the label subscripts), ho and r2 are non-adiabatic, as $\epsilon(0)$ would suggest. However, r1 is much closer to adiabaticity as it lies a lot closer to the origin. Systems ho and r2 display once more a similar degree of non-adiabaticity in the metrics, unlike their $\epsilon(t)$ values which displays them as markedly different with $\epsilon(t)$ of r2 much greater than $\epsilon(t)$ of ho (figure 4.1, upper inset). From this we are able to see how $\epsilon(t)$ does not always fully describe the degree of adiabaticity of the system.

We note that $D_\psi(\psi_{GS}(t), \psi(t))$ provides a quantitative measure of the degree of adiabaticity, with $D_\psi(\psi_{GS}(t), \psi(t)) = 0$ indicating perfect adiabaticity and $D_\psi(\psi_{GS}(t), \psi(t)) = \sqrt{N}$ corresponding to maximum non-adiabaticity [where $\psi(t)$ is either orthogonal to or completely non-overlapping with $\psi_{GS}(t)$]. This means an absolute percentage deviation of the dynamic distance from the maximum distance can be attributed at any instant in time.

This measure provides useful information beyond the degree of adiabaticity; figure 4.4 displays oscillating "arches" for the adiabatic systems (inset), where ho has the clearest arches. For ho this is seen for all values of $\epsilon(0)$ up to 1.0, where the arch is disrupted by the distortion of the harmonic well when reaching the edge of the system ($L = 15$ a.u.). The frequency of the oscillating arches is ω in the wavefunction, and 2ω for the density. The random potentials also display this oscillatory behaviour when adiabatic, but with a frequency not as clearly dependent on the trapping microwells' frequency. These arches

[9] These results suggest that, by combining the requirements of a dynamic ratio $D_n(n(0), n(t))/D_\psi(\psi(0), \psi(t))$ following a line, with the fact the distances do not explore the upper triangle above the line, adiabatic behaviour could be assessed even when the ground state gradient D_n/D_ψ is unknown.

reveal a peculiar feature of the dynamics of adiabatic states: they oscillate about the instantaneous ground state but never really adjust to it, maintaining this "inertia" no matter how slowly-varying the perturbation is.

An animation for the density of $\mathrm{ho}_{0.1}$ was produced to demonstrate the oscillations about the instantaneous ground state, see **Skelt_108001277_animation_ho.mp4** for the animation. Here $\epsilon(0) = 0.1$ was used as these dynamics can be seen clearer than for $\epsilon(0) = 0.01$, but the oscillating arches appear in both cases. The animation shows that the dynamic state remains superimposed to the initial ground state for a while (about t =5 a.u., or ∼2 seconds into the animation) after the perturbation has been applied, demonstrating inertia, before it begins to move. Once the dynamic state is moving, it catches up with the instantaneous ground state but due to the momentum, it continues past the instantaneous ground state until it is stopped by the potential at a time of ∼30 a.u (or ∼9 seconds animation time) where the maximum of the density has clearly overcome the minimum of the instantaneous potential, and then again at about 60 a.u.. This causes the oscillations about the instantaneous ground state, which are seen in figures 4.4, 4.5, and 4.6 (particularly in the insets). This inertia of the dynamic state gives rise to the "ramp-up" phase, which precedes the oscillations seen for all three families of systems (see inset of figures 4.5 and 4.6).

Figures 4.3 and 4.4 suggest a restricted behaviour for the dynamics of quantum systems in metric space, with the region above the adiabatic line remaining largely unexplored. This would imply that, on average, non-adiabaticity affects the wavefunctions more than the related densities, both when measured as a distance from the instantaneous eigenstate (figure 4.4) or from the initial state (figure 4.3)[10]. This behaviour sheds new light on the dynamic wavefunction-density mapping of TDDFT: when observed in metric space this mapping does not explore the entire space, and is limited to the lower triangle of our figures; also, in contrast to the ground state mapping of DFT [77], it maps, on average, close densities to less close wavefunctions. This can be partly understood by noting that distant densities must be non-overlapping (since n cannot be negative) and therefore imply distant wavefunctions, whereas the converse is not true.

[10]Preliminary results on a strongly driven, ionising system also confirm this restricted metric space (A. Schild, H. Gross and I. D'Amico, private communication).

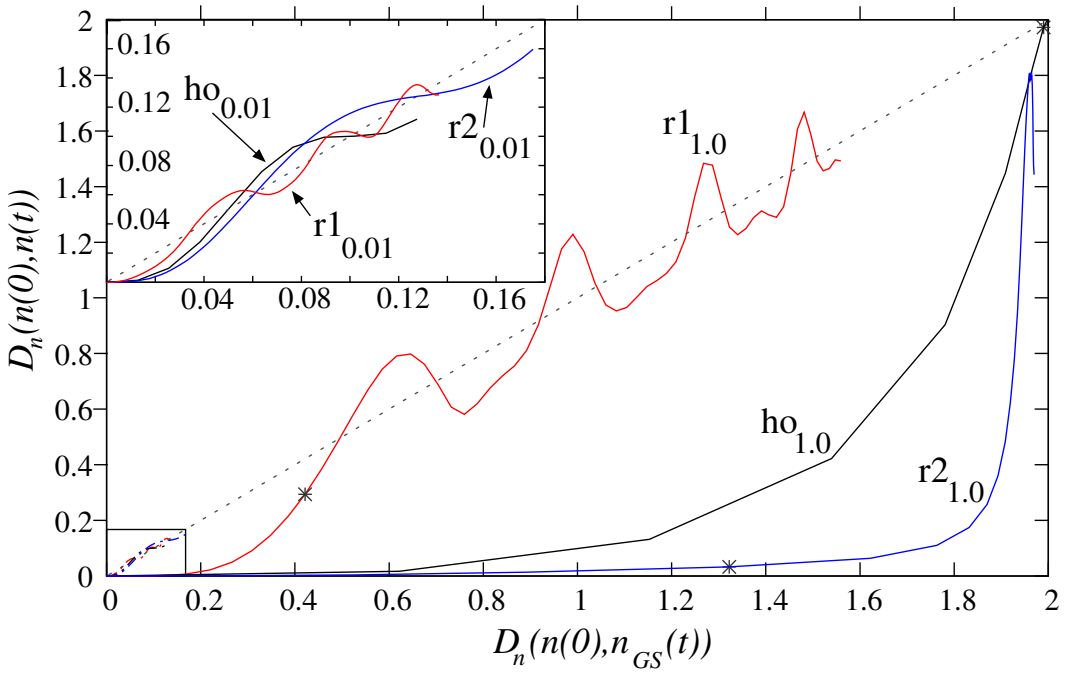

Figure 4.5: Comparing the instantaneous ground state and the TD state with the initial ground state for n. The black stars indicate the reference time t_{ref} as seen in figure 4.1 (upper inset). Inset: zoom to boxed area, with adiabatic systems following the adiabatic line (dashed).

4.4.3 Graphs of density distances and wavefunction distances

The third type of graph is shown in figure 4.5 and figure 4.6: it focuses solely on either densities (figure 4.5) or wavefunctions (figure 4.6). For an adiabatic system $\psi(t) = \psi_{GS}(t)$, and so $D_\psi(\psi(0), \psi(t)) = D_\psi(\psi(0), \psi_{GS}(t))$. By comparing $D_\psi(\psi(0), \psi(t))$ with $D_\psi(\psi(0), \psi_{GS}(t))$ (or similarly with the density), the adiabaticity of the system is discerned through the proximity to the adiabatic line $y = x$. The density and wavefunction graphs are very similar, and this suggests it should be possible to determine adiabaticity using the density alone, e.g. conveniently calculated using DFT. It must be noted that $D_\psi(\psi(0), \psi(t))$ and $D_n(n(0), n(t))$ are not directly linked to the QAT, and therefore one would not necessarily expect them to characterise adiabaticity. However, they are compared to $D_\psi(\psi(0), \psi_{GS}(t))$ and $D_n(n(0), n_{GS}(t))$ respectively, which indirectly compares the evolved state with the adiabatic state, indicating the degree of adiabaticity of the evolution. Indeed one could use $D_\psi(\psi(t), \psi_{GS}(t))$ to directly compare these values (similarly for the density), which is what we will do in the next chapter, but here we are exploring the different methods of using metrics for characterising adiabatic evolutions, ex-

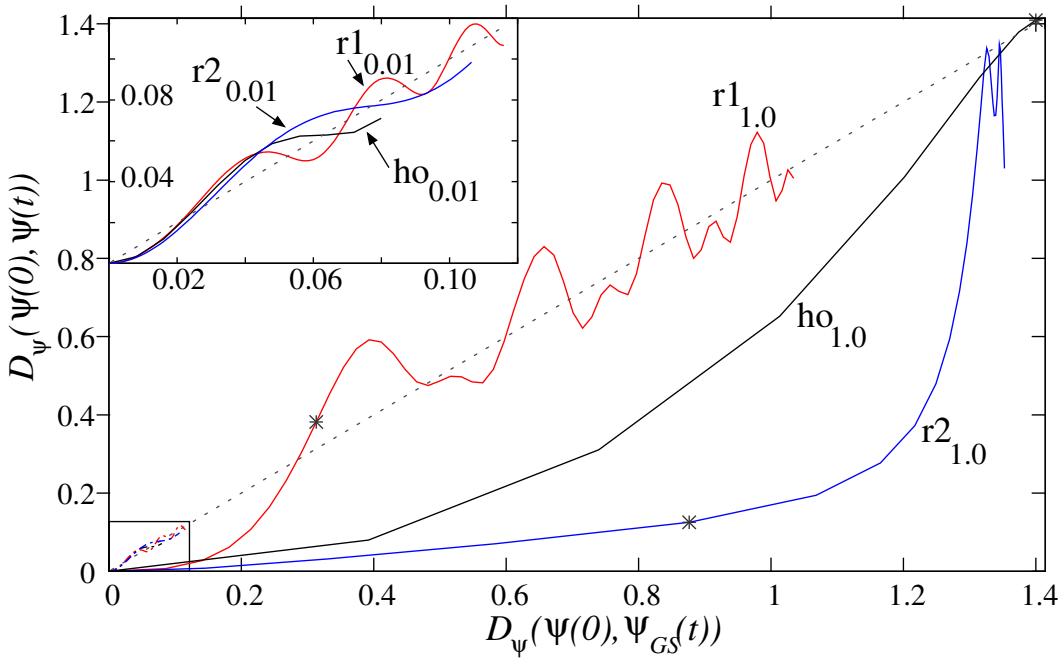

Figure 4.6: Comparing the instantaneous ground state and the TD state with the initial ground state for ψ. The black stars indicate the reference time t_{ref} as seen in figure 4.1 (upper inset). Inset: zoom to boxed area, with adiabatic systems following the adiabatic line (dashed).

ploring different combinations of metrics (both wavefunction and density) to give greater understanding of how they can characterise a system's dynamics.

The systems for $\epsilon(0) = 0.01$ are indeed adiabatic and oscillate about the adiabatic line. These oscillations always begin below the adiabatic line as the dynamic state lags behind the instantaneous ground state, in agreement with the arches seen in figure 4.4 and showing again the "inertia" felt by the dynamic system.

The region above the adiabatic line is barely explored, once more suggesting a restriction for the dynamics of quantum systems in metric space. For figure 4.5, this may be understood using the triangle inequality obeyed by metrics, which here takes the form $D_\psi(\psi(0),\psi(t)) \leq D_\psi(\psi_{GS}(t),\psi(t)) + D_\psi(\psi(0),\psi_{GS}(t))$[11]. Since $D_\psi(\psi_{GS}(t),\psi(t))$ becomes smaller for increasing adiabaticity, this means that $D_\psi(\psi(0),\psi(t)) \approx D_\psi(\psi(0),\psi_{GS}(t))$ to an increasingly better approximation, limiting the vertical excursion of curves in figure 4.5. The more adiabatic a system, the smaller the amplitude of the oscillations about the adiabatic line. This also holds true for the density. For ho and r2, when $\epsilon(0) = 1.0$, the region below the adiabatic line is explored

[11]The triangle inequality has also been used to develop limits on adiabatic time in many-body systems [135].

considerably, demonstrating their non-adiabatic nature.

The black stars on the $\epsilon = 1.0$ curves in figures 4.5 and 4.6 indicate t_{ref} (an arbitrary reference time chosen to indicate interesting dynamics) from figure 4.1 (upper inset). It is clear that r2 remains non-adiabatic at this time, however r1 has come closer to adiabaticity, and oscillates about the adiabatic line as a result of the spreading and contracting of the density in a "breathing" motion[12] (explained later).

This move towards an adiabatic regime is clearly seen in the metrics and in $\epsilon(t)$, yet the metrics, due to their non-perturbative nature, reveal a lot more about the dynamics of the system, such as the oscillations and the initial ramp-up phase due to the inertia. They also reveal that $\text{r1}_{1.0}$ is definitely not as adiabatic as $\epsilon(t) \to 0.03$ (from figure 4.1 upper inset) would suggest.

An animation of the density of $\text{r1}_{1.0}$ was produced to demonstrate the breathing motion (see **Skelt_108001277_animation_r1.mp4** for the animation). From the beginning the electronic ground state is mainly confined by the asymmetric right-hand microwell and the perturbation ($-pxt$) pushes the electron closer to the confining potential as the microwell deepens. Starting at about 30 a.u. (or $\sim$10 seconds into the animation) we observe a "breathing" motion, with the density widening with the amplitude reducing, followed by it tightening with the amplitude increasing. This is combined with a sideways oscillation. This complex motion is caused by a combination of oscillations about the instantaneous ground state caused by inertia (similar to that mentioned previously) combined with the reflection of the wave packet by each side of the microwell in turn, an overall motion that is reminiscent of water oscillating sideways in a basin. Each density maxima corresponds to one of the maxima of the metric oscillations observed for $\text{r1}_{1.0}$ in figure 4.5: the higher metric maxima correspond to the density maxima close to the system boundary, while the secondary metric maxima correspond to the density maxima close to the less steep left border of the microwell.

4.5 Conclusion

To conclude, the answer to research question 1a "can we characterise adiabaticity without using the quantum adiabatic criterion?", is yes; by utilising metrics for wavefunction and density, we have proposed three types of metric graphs as tools to assess adiabaticity, which all agree on the character of

[12]Whereas Dobson's harmonic potential theorem [136] shows the propensity for "breathing" of a time-evolving wavefunction to be suppressed in the harmonic oscillator.

the dynamic evolutions considered. These tools provide both quantitative and qualitative estimates of the degree of adiabaticity in the dynamics of a quantum system, and show how the ground state linear relationship between D_n and D_ψ is related to adiabatically-evolving time-dependent systems. All the numerical results, including additional intermediate perturbations not shown here, for these three types of graph support the conjecture that the behaviour is indeed general.

We have demonstrated that the metric-space approach can be used to assess the character of the dynamics of quantum systems, in an accurate and appealingly visual way. The metric approach studied here is also applicable to many-particle systems, for which the characterisation of the degree of adiabaticity using metrics based on densities alone is particularly convenient (we shall study this in the next chapter). This method could therefore be used to predict parameters for experiments requiring adiabaticity, and experimentally measured local densities could be used in the density metrics to determine the degree of adiabaticity achieved.

The ability to use metrics based purely on densities or wavefunctions also allows for their use in situations where only the wavefunctions or only the densities are known. An example in which the exploration of the wavefunction metric dynamics could be informative is the case of quantum phase transitions.

These results show that quantum dynamics, even for systems strongly far from equilibrium, appears to be restricted in metric space with distances above the adiabatic line not being seen. This sheds light on the density-wavefunction mapping at the core of TDDFT.

Importantly, the metric graphs do not suffer from the same limitations as the currently widely used adiabatic criterion, $\epsilon(t)$, and hence provide a more robust indication of the degree of adiabaticity, as well as a greater insight into the system dynamics. This establishes the metric space approach to quantum mechanics as a versatile and sensitive probe of adiabaticity.

Next we shall look at applying this technique to many-body systems, and explore the effects of temperature on characterising adiabaticity.

5. Characterising adiabaticity in quantum many-body systems at finite temperature

In chapter 4, we developed a method to characterise adiabaticity in single-electron systems at zero temperature using distance measures, which do not have the same issues as the commonly used quantum adiabatic criterion. However, many quantum devices consist of more than one electron, and in practice they must be operated at non-zero temperature. It is therefore important to look at these methods for many-body interacting systems working at finite temperature. In this chapter, we aim to answer research question 1b: "Can we apply the characterisation method developed from answering 1a to systems at finite temperature?".

To answer this, we will consider small many-body systems on a one-dimensional lattice using the Hubbard model. The Hubbard model is exactly solvable for small chains but has non-trivial behaviours making it a good test-bed for a wide range of many-body applications, including, as we will see, analysing the use of metrics for characterising adiabaticity. Work in this chapter has been published in Advanced Quantum Technologies, see reference [137].

5.1 Introduction

Adiabatic evolutions are important in many areas of quantum physics, such as quantum computation, quantum thermodynamics, and quantum field theory [23–31]. One particularly important application of adiabatic evolutions is achieving specific (target) states, e.g. in adiabatic quantum computation, where the target state is known to be the ground state of the final Hamiltonian. Other important applications of adiabatic evolutions are for quantum thermodynamic cycles, where, for example, they may yield the highest extractable

quantum work [32, 138].

5.1.1 Metrics for the adiabatic theorem

In our approach the adiabatic theorem is written in terms of two distance measures (metrics), namely the Bures and the trace distances. The Bures distance is connected to the fidelity (which itself is not a proper distance), and at zero temperature one could use the "adiabatic fidelity" as a figure of merit for adiabaticity in time-dependent systems [103]. Importantly, the Bures distance can be derived from conservation laws [77, 78] so that it can provide relevant information on the physics of the many-body system [77–79, 86].

Within quantum information processing, the trace distance is considered the best measure to operationally distinguish two quantum states [95], so we also look at using the trace distance in place of the Bures, and find that both the trace and Bures can be used to determine the degree of adiabaticity.

To provide a comparison with a somewhat more familiar quantity, we propose an extension of the QAC to finite temperatures, and discuss its limitations. All of these methods broaden the choice of adiabatic measures to best suit one's needs.

At zero temperature, the Bures distance for pure states has already been demonstrated to characterise adiabaticity in single electron systems (see previous chapter) [93], and in previous work we saw its potential for characterising adiabaticity in two-electron systems [85]. Here we consider many-body systems (formally of any size, then testing on systems with a small number of electrons) described over a lattice, at zero and finite temperatures. Computationally, as the system size increases, the cost of the calculation increases exponentially. Therefore we apply the aforementioned methods to many-body systems up to 6 electrons on a discrete lattice which can be solved numerically exactly (giving us a test-bed on which to analyse these methods).

Taking inspiration from DFT, we ask: "can metrics based on the particle density alone give quantitative guidance to the level of adiabaticity of a system?" We ask this because the density is, in principle, experimentally observable and much easier to estimate, e.g. by density functional methods, than the corresponding many-body state. Therefore the density would be a preferable quantity to use in a tool for characterising adiabatic evolutions. By demonstrating that this question has a positive answer, we will provide a manageable way to measure and track adiabaticity in many-body systems, even at finite temperature.

This analysis aims to help guide those wanting an adiabatic evolution (either experimentally or computationally) in many-body systems at any temperature towards achieving an understanding of the degree of adiabaticity of their system. A guideline threshold for considering an evolution adiabatic is also presented with discussion of the factors which impact this threshold and the important quantities to consider when deciding a threshold for one's system.

5.2 Proposal for a temperature-dependent quantum adiabatic criterion

Recall the quantum adiabatic theorem first proposed by Born and Fock in 1928 [96], described in section 2.3, where we rephrase its definition to be: an adiabatic evolution is one in which no transitions between energy levels occur. We have rephrased this so that when we extend our system to finite temperatures, and are therefore no longer in the ground state even at equilibrium, we still have a working definition of the adiabatic theorem. The requirement for quantum adiabaticity at finite temperature[1] that there are no transitions between eigenstates of the system as it evolves [139] practically implies that the population of the various eigenstates should not change with time.

When it comes to accurately characterising an adiabatic evolution, there are many challenges, such as the complexity of calculations involving many-body systems and defining the criterion at finite temperature. Recently, the validity and sufficiency of this QAC for certain systems have been questioned [42, 43, 98], and new approaches for characterising adiabaticity have also come to light, where chapter 4 and reference [103] look at comparing the time evolved state of the system with the "adiabatic" state, i.e. the instantaneous ground state. It was demonstrated in chapter 4 that metrics can be used to characterise adiabaticity through a variety of approaches to best suit the quantities one has at hand [93]. All of these approaches only consider quantum adiabaticity for pure states at zero temperature. The issue of tracking adiabaticity both at finite temperature and for many-body systems remains outstanding. Here we introduce a new expression for characterising adiabaticity in systems at finite temperature, which are described by mixed states.

As a comparison between the metrics and a more familiar quantity, we

[1] Since temperature is being introduced, there are two definitions of adiabaticity; quantum and thermal. Thermal adiabaticity looks at the heat loss of the system, which is zero for this investigation as the system is closed. Therefore it only makes sense to look at the quantum adiabaticity, especially when considering applications to quantum systems.

propose the following extension of the QAC, equation 2.43, valid at any temperature T:

$$\epsilon(t) = \max_{n,m} \left\{ \hbar \frac{\left| \langle m(t)| \dot{H}(t) |n(t)\rangle \right|}{\left(|E_n(t) - E_m(t)|\right)^2} \right\}, \tag{5.1}$$

with

$$E_n(t) - E_0(t) < s k_B T, \tag{5.2}$$

$$E_m(t) - E_0(t) < s' k_B T, \tag{5.3}$$

$$s' > s \geq 1. \tag{5.4}$$

Here $E_0 \leq E_1 \leq \ldots \leq E_n$, $m \neq n$, k_B is the Boltzmann constant, $\hbar$ is Planck's constant and is taken to be 1 for this work (using atomic units), and s and s' are used to practically limit the energy levels considered, based on the temperature. In the calculations presented here, we use $s = 1$ and do not cap s'. For adiabaticity to hold, we still required that $\epsilon(t) \ll 1$. Also note that the criterion is adapted for degenerate states following Rigolin and Ortiz [133], so that the maximum distance between the degenerate subspaces and other levels is considered to calculate $\epsilon(t)$.

5.3 Metrics for density and quantum state

As seen in the previous chapter, metrics provide a useful quantitative measure in the distance between two elements in a set [92, 140]. The use of metrics for investigating the relationship between wavefunctions and corresponding particle densities was developed in references [77–79, 141] where the chosen metrics were derived from conservation laws (referred to as 'natural' metrics [77, 78]) to ensure that they could provide physical insights. In chapter 4, we introduced a method of using these metrics for characterising adiabaticity in single electron systems at zero temperature [93]; other works [77, 78, 85, 141] support the possibility of developing this metric-based method to characterise adiabaticity in many-body systems. All these works considered pure states, but since the focus in this chapter is on finite temperature, the 'natural' metrics must be extended to mixed states.

The 'natural' metric for the wavefunction developed in reference [77] is in fact the Bures metric at the zero temperature limit. So for mixed states we use the Bures metric, equation 2.39, from chapter 2, remembering it has a maximum value of $\sqrt{2}$ ready for forming adiabatic thresholds later. We also

saw in chapter 2 another metric which is widely used in the quantum technology community as a measure of distinguishability between quantum states: the trace distance [95, 140], defined in equation 2.41, and with a maximum value of 1 for states normalised to 1. We will also consider the trace distance in this chapter, and compare the results to the Bures. The Bures and trace distances are related by bounds [95, 140] (as seen in section 2.2 of chapter 2) and, at least for the systems and dynamics discussed in this work, they provide very similar conclusions. Therefore we can suggest that the decision of which metric to use be based on which quantities are more readily available, e.g. if the fidelity is easy to obtain, then the Bures distance should be chosen.

The 'natural' density metric is unaffected by the type of state, and remains

$$\tilde{D}_n\left(n_1, n_2\right) = \frac{1}{N}\int \left|n_1(\mathbf{r}) - n_2(\mathbf{r})\right| d^3\mathbf{r}, \tag{5.5}$$

with $n_j(\mathbf{r})$ the particle density of system j at position $\mathbf{r}$. However, because we will be applying these metrics to a lattice system, the density metric can be adapted for the site occupation by replacing the integration with a summation,

$$D_n\left(n_1, n_2\right) = \frac{1}{N}\sum_{i=1}^{L} \left|n_{1,i} - n_{2,i}\right|, \tag{5.6}$$

where $n_{j,i}$ is now the site occupation of system j at site i in the system of length L. In this chapter, we know that systems 1 and 2 will have the same number of particles, N, and consequently rescale the metric in equation 5.6 so that the maximum distance is 2 (much like in reference [77]).

We propose using the density metric to characterise adiabaticity because it is much simpler to calculate, and yields similar results to the state distances (seen later, in section 5.5). The motivation to use the density distance relies on the Runge-Gross theorem [64, 71] for continuous systems, and on its extension to lattice Hamiltonians [63, 142]. At zero temperature, these theorems provide a one-to-one correspondence between the driven many-body state and the corresponding particle density. This allows us to shift the attention from the system's quantum states to the corresponding particle densities (continuum) and site occupations (lattice Hamiltonians), objects which are much simpler to calculate, e.g. by density functional methods [63, 64]. We therefore also test the ability to use only the density distance to characterise adiabaticity of many-body systems (specifically of the Hubbard model) at finite temperature, and find it to be successful.

Using the metrics in equations 2.39, 2.41, and 5.6, we will address re-

search question 1b, more explicitly asking "could suitable metrics be used to characterise adiabaticity at finite temperature and for complex interacting many-body systems which are difficult to handle?". To answer these questions, we will propose an operative definition of adiabaticity based on an 'adiabatic threshold' (see section 5.4), and monitor the distance between the time-dependent state and its adiabatic counterpart.

5.4 Introducing an adiabatic threshold

In practice, a system can be considered adiabatic when it remains close enough to its adiabatic state during the dynamics. In this section, we will quantify the concept of 'close enough' by developing an 'adiabatic threshold' based on conclusions from the previous chapter [93]. We exploit the fact that the chosen metrics have well-defined maximum values, D_ρ^{max}, and so it is possible to quantify an adiabatic threshold, Δ_ρ, as a percentage of these maxima. It is taken that for a state $\rho(t)$ to be considered adiabatic, it obeys

$$D_\rho(\rho_S(t), \rho(t)) \leq \Delta_\rho, \tag{5.7}$$

where $\rho_S(t)$ is the instantaneous ground state for $T = 0J/k_B$ ($S = GS$), or instantaneous transitionless state for finite temperature ($S = Th$, where the system began in the thermal state, and no transitions between energy levels have occurred during the evolution)[2]. Equation 5.7 looks at the distance between the instantaneous adiabatic state, and the evolved state; if these quantities are very similar, then the system is adiabatic (within an error/threshold) and the distance is small.

For this work, we take $\Delta_\rho = 0.1 D_\rho^{max}$, but this threshold can be adjusted based on the accuracy or constraints of the experiment or calculation being performed. For example, we note that as the temperature increases, $k_B T$ becomes the dominant energy scale so the same external driving affects the system less, meaning for the same drive but increased temperature, $\rho(t)$ will remain closer to the adiabatic state throughout the evolution. Therefore one could choose a tighter adiabatic threshold in this case, to improve appreciation of the effect of the driving.

[2]For $T \to 0$, $S = Th$ becomes $S = GS$.

5.4.1 Densities and the adiabatic line

In references [77–79, 85, 93] it was shown that there is a monotonic relationship between ground state wavefunction distances and their corresponding density distances. This relationship is quasi-linear up to relatively large distances $\approx (2/3)D_{\rho}^{B,max}$ [3], with reference [79] indicating this relationship may also hold for higher order eigenstates and corresponding densities. The results from this chapter show the same behaviour at finite temperatures (see figure 5.2 which demonstrates that the relationship between $D_{\rho}(\rho(0), \rho_{GS})$ and $D_n(n(0), n_{GS}(t))$ can be extended to finite temperatures, and will be discussed further in section 5.5.2). We also note that the mapping between thermal ensembles and densities exists in the flavour of DFT known as 'Thermal DFT' [143, 144]. Therefore we can be confident that the relationship between $D_{\rho}(\rho(0), \rho_{GS})$ and $D_n(n(0), n_{GS}(t))$ is maintained at finite temperature. We refer to this quasi-linear relationship as the 'adiabatic line' as defined in chapter 4[4] [93]. The adiabatic line for a given time-dependent process can be written as

$$D_n(n_S(0), n_S(t)) \approx m D_{\rho}(\rho_S(0), \rho_S(t)). \tag{5.8}$$

We can then extend this relation to the maximum distances, multiplied by a small parameter δ which gives the fraction for the threshold[5] so that the quasi-linear relationship remains valid,

$$\delta D_n^{max} \approx m \delta D_{\rho}^{max}. \tag{5.9}$$

We note that δD_n^{max} and δD_{ρ}^{max} are the thresholds, and so we convert them to Δ_n and Δ_{ρ}:

$$\Delta_n = \delta D_{n,\max} \approx m \delta D_{\rho,\max} = m \Delta_{\rho}, \tag{5.10}$$

$$\Delta_n \approx m \Delta_{\rho}. \tag{5.11}$$

This further restricts the threshold in the density metric, which we will see is necessary as the density distances are affected much less during the system evolution. Without this scaling, the density distance would often classify evolutions as adiabatic where the state distance shows they are not adiabatic.

[3] For example, see figure 2 in reference [77].

[4] We use the Bures metric to find the adiabatic line, but one could use the trace distance. If using the trace distance though, note that the gradient will be different to those reported in table 5.1. One must be consistent with their use of the trace or Bures metric when finding the adiabatic line to then use the gradient for Δ_n described later.

[5] Here we use $\delta = 0.1$, so the adiabatic threshold is 10% of the maximum distance.

k_BT	U	N	Gradient	N	Gradient	N	Gradient
$0J$	$0J$	2	1.33294	4	0.647511	6	0.450959
$0J$	$5J$	2	0.91163	4	0.411435	6	0.2779
$0J$	$10J$	2	0.502006	4	0.218927	6	0.237795
$0.2J$	$0J$	2	0.924189	4	0.647354	6	0.45059
$0.2J$	$5J$	2	0.911343	4	0.409499	6	0.278244
$0.2J$	$10J$	2	0.619401	4	0.210794	6	0.205762
$2.5J$	$0J$	2	0.924189	4	0.57114	6	0.444165
$2.5J$	$5J$	2	0.744725	4	0.473781	6	0.389355
$2.5J$	$10J$	2	0.48877	4	0.231146	6	0.179414

Table 5.1: Gradients m of the adiabatic line (using the Bures metric) for the driven Hubbard model with the slope potential considered in this chapter for three temperatures (k_BT), correlation strengths (U), and electron numbers (N).

The gradient of the linear relationship, m, depends on N, U, and T, as well as the type of driving and driving strength. Table 5.1 gives the gradients for three different coupling strengths, temperatures, and site numbers. In practice, the gradient m can be estimated by calculating $D_n(n_S(0), n_S(t))$ and $D_\rho(\rho_S(0), \rho_S(t))$ at 2-3 times. For these chosen times, D_ρ should be less than $(2/3)D_\rho^{max}$ where the linear relationship holds better, and the origin should be included in the fit because of the coincidence axiom, equation 2.29. Estimating m then requires the exact or approximate diagonalisation of the system Hamiltonian at 2-3 instants in time[6].

In principle a more accurate (and more computationally expensive) estimate of m could be achieved by using a polynomial fitting to the plot of $D_n(n_S(0), n_S(t))$ versus $(D_\rho(\rho_S(0), \rho_S(t)))$, but we find that the linear approximation in equation 5.8 and the simple method described above is sufficient for achieving good results, as we will see next.

5.5 Numerical results

While the methods proposed here can be applied to both continuous and lattice systems, we will illustrate them using the iconic model for strongly correlated many-body quantum systems on a lattice: the Hubbard model. We shall do this firstly at zero temperature and then move on to look at finite temperatures.

[6]Table 5.1 can be used as a guideline to the type of expected values for m in a few different circumstances.

5.5.1 Hubbard model and system drive

We consider the out-of-equilibrium dynamics of the inhomogenous 1D Hubbard model at half filling to demonstrate the properties of the methods for characterising adiabaticity proposed in this work. The Hubbard model is used to simulate various physical systems of interest to quantum technologies [113–118], and the inhomogeneous Hubbard model is often used as a test-bed for developing techniques for strongly correlated many-body systems [32, 59]. This is because it displays non-trivial properties such as the metal to Mott insulator transition, antiferromagnetism, and superconductivity, even for small chains [32, 62, 115, 138, 145] where it can be solved (numerically) exactly, meaning it can push approximations to their limits and compare them against exact results (as we will see in chapters 7 and 8). The dynamics used in this study can be used to represent transient electronic currents along a chain of atoms or nanostructures, like coupled quantum dots, because of the application of a time-dependent electric field across the chain, driving the system.

The corresponding Hubbard Hamiltonian for a system of N fermions and N sites with nearest-neighbour hopping is

$$\hat{H} = -J\sum_{i,\sigma}^{N}\left(\hat{c}^{\dagger}_{i,\sigma}\hat{c}_{i+1,\sigma} + \hat{c}^{\dagger}_{i+1,\sigma}\hat{c}_{i,\sigma}\right) + U\sum_{i}^{N}\hat{n}_{i,\uparrow}\hat{n}_{i,\downarrow} + \sum_{i}^{N}v_i\hat{n}_i, \tag{5.12}$$

where J is the hopping parameter for an electron with spin σ, and $\sigma =\uparrow$ or $\downarrow$, U is the on-site electron-electron interaction strength, and v_i is the external potential at site i. We also note that $\hat{c}^{\dagger}_{i,\sigma}$ and $\hat{c}_{i,\sigma}$ are the usual creation and annihilation operators for a spin-σ fermion on site i, and $\hat{n}_i = \hat{n}_{i,\uparrow} + \hat{n}_{i,\downarrow}$ is the number operator, with $\hat{n}_{i,\sigma} = \hat{c}^{\dagger}_{i,\sigma}\hat{c}_{i,\sigma}$.

To drive the system out-of-equilibrium, we will use a time-dependent v_i simulating a uniform electric field linearly increasing with time from a potential difference of $1J$ to a potential difference of $10J$ across the chain of 6 sites. For the change in potential to be linear in time, the on-site potential is written as

$$v_i(t) = \mu_i^0 + \mu_i^{\tau}t/\tau \tag{5.13}$$

where μ_i^0 and μ_i^{τ} are time independent coefficients of site i at $t = 0$ and $t = \tau$ respectively. Then to achieve a linear electric field across the sites, the coefficients are written as $\mu_i^0 = (2\mu^0/L \times i) - \mu^0$ where $\mu^0 = 0.5J$, and $\mu_i^{\tau} = (2\mu^{\tau}/L \times i) - \mu^{\tau}$ with $\mu^{\tau} = 4.5J$.

From this way of forming the time dependence, the final Hamiltonian does

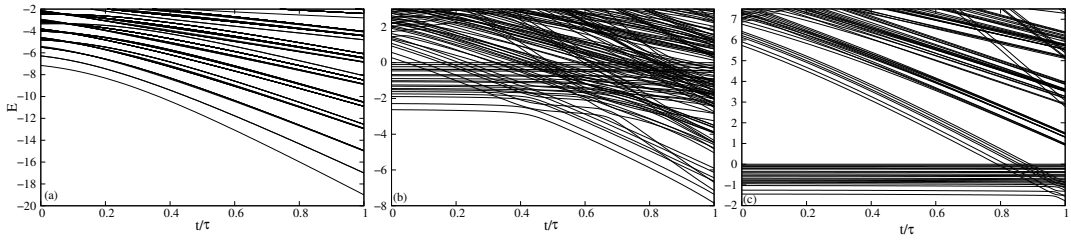

Figure 5.1: A zoom into the low-mid section of the instantaneous spectrum versus t/τ of the time-dependent Hubbard Hamiltonian considered in this work (6 sites, half filling). Panel (a) corresponds to zero on-site Coulomb interaction ($U = 0J$), (b) to $U = 5J$, and (c) to $U = 10J$. Note the different energy scales on the y-axis.

not depend on τ, and therefore τ denotes the evolution time, or inverse speed, of the evolution. We can relate ϵ to tau such that $\epsilon \propto (\tau(\Delta E)^2)^{-1}$ where ΔE is the minimum spectral gap. Therefore, the larger τ is, the smaller ϵ will be (remembering that $\epsilon \ll 1$ is considered adiabatic), and hence closer to adiabaticity the system is expected to be.

In this chapter we analyse the dynamics of short inhomogeneous Hubbard chains of $N = 2$, 4, and 6 sites, driven at different rates ($\tau = 0.5/J$, $5/J$, and $50/J$), for 3 different interaction strengths ($U = 0J$, $5J$, and $10J$). We will only explicitly look at $N = 6$ here but similar qualitative conclusions can be drawn for all N studied[7] (with the understanding that there will be quantitative differences due to the adiabatic line varying with N, as discussed previously). This system has 400 eigenstates leading to a very complex spectrum (see figure 5.1), which we will see greatly impacts the dynamics.

Instantaneous eigen-energies of the Fermi-Hubbard Hamiltonian

Figure 5.1 shows the low-mid section of the instantaneous spectrum of the driven Hubbard Hamiltonian described in section 5.5.1 as it is driven (for (a) $U = 0J$, (b) $U = 5J$, and (c) $U = 10J$). For $U = 10J$ [figure 5.1(c)], the Coulomb repulsion for states which include double occupation of sites leads to the grouping of energy levels, separated with large gaps where no energy levels occur. The lowest two groupings start crossing when the applied external potential is of the order of U, around $t \approx 0.8\tau$. For $U = 5J$ the gap between the lowest two energy groups is just starting to form, and the two groups start crossing for $t \approx 0.05\tau$. We will see the impact of these groups on the adiabaticity in the coming sections.

[7] See appendix A for results with 2 and 4 sites.

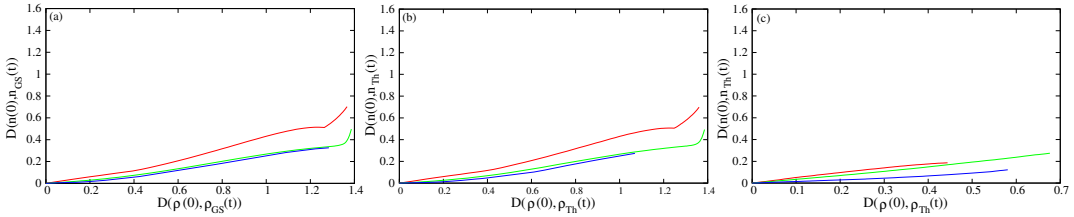

Figure 5.2: Curves of $D_n(n_S(0), n_S(t))$ versus $D^B_\rho(\rho_S(0), \rho_S(t))$ for 3 interaction strengths: $U = 0J$ in red, $U = 5J$ in green, and $U = 10J$ in blue; and 3 temperatures, $T = 0J/k_B$ ($S = GS$, left) $T = 0.2J/k_B$ ($S = Th$, middle), $T = 2.5J/k_B$ ($S = Th$, right). Note that $n(0) = n_S(0)$ and $\rho(0) = \rho_S(0)$.

5.5.2 Adiabatic threshold for the density

Figure 5.2 shows the adiabatic line ($D_n(n_S(0), n_S(t))$ versus $D^B_\rho(\rho_S(0), \rho_S(t))$) for three temperatures [(a) $k_BT = 0J$, $S = GS$; (b) $k_BT = 0.2J$, $S = Th$; (c) $k_BT = 2.5J$, $S = Th$] using the set up described previously. This is the line whose gradient determines the scaling of the density threshold, Δ_n, as described in section 5.4.1. By increasing U (from red to green to blue), or increasing the temperature (panels from left to right), the gradient of the adiabatic line decreases. This is also seen in the gradients given in table 5.1, whose values give m to be used in equation 5.11. Note that here we have used the linear approximation described in section 5.4.1, and used this to calculate Δ_n for the density thresholds used in the results.

5.5.3 Zero temperature

At zero temperature, the initial system is in its ground state, and during an adiabatic evolution it would remain in its instantaneous ground state. The results for the zero temperature system are shown in figure 5.3. We consider different rates of dynamics ($\tau = 0.5/J$, red, 'fast' dynamics; $\tau = 5/J$, green, 'intermediate' dynamics; $\tau = 50/J$, blue, 'slow' dynamics, closer to adiabaticity), and three interaction strengths ($U = 0J$, left, no interaction; $U = 5J$, middle, medium interaction; $U = 10J$, right, strong interaction). We choose $U = 0J$ as it sits in the metallic side of the Hubbard model's metal-Mott insulator transition, and it also allows for a comparison to the single electron results from chapter 4. We then choose $U = 5J$ as it sits at the transition from a metal to Mott insulator, and then $U = 10J$ as it sits in the Mott insulator phase. One would anticipate behaviour far from adiabaticity from the red curves, the blue curves showing behaviour closer to adiabaticity, and the green curves demonstrating behaviour somewhere in between. In figure 5.3, we

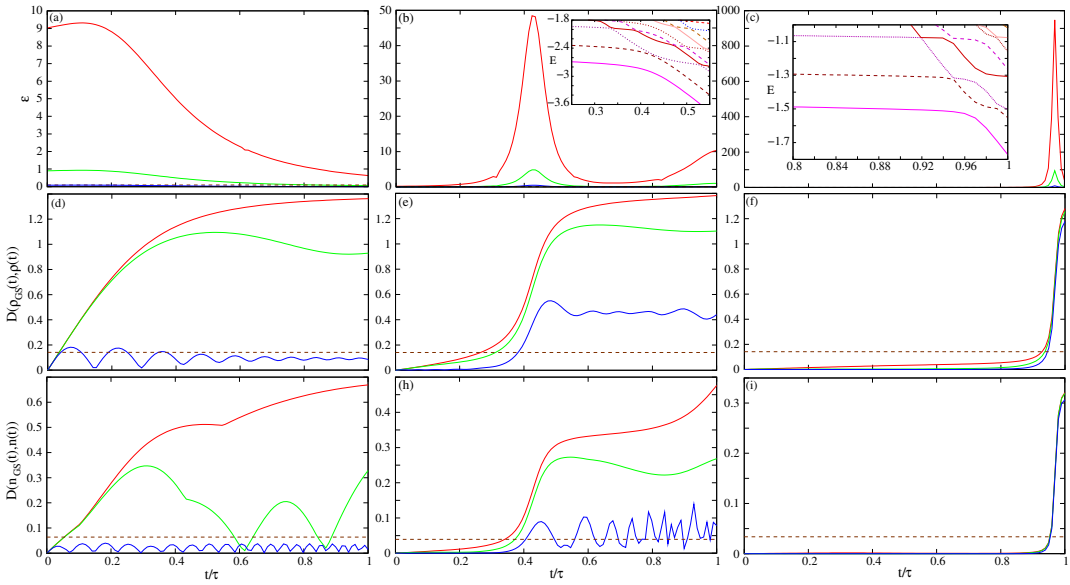

Figure 5.3: Zero temperature results. Red lines: $\tau = 0.5/J$ dynamics; green lines: $\tau = 5/J$ dynamics; blue lines: $\tau = 50/J$ dynamics. Panels show: $\epsilon(t)$ [(a)-(c)], $D_\rho^B(\rho_{GS}(t), \rho(t))$ [(d)-(f)], and $D_n(n_{GS}(t), n(t))$ [(g)-(i)] versus t/τ. Three interaction strengths are considered: $U = 0J$ (left), $U = 5J$ (middle), and $U = 10J$ (right). In all panels the horizontal dashed lines indicate the corresponding adiabatic threshold. Insets of panel (b) and (c): low energy spectrum of the instantaneous Hamiltonian versus t/τ for $U = 5$ [panel (b)] and $U = 10$ [panel (c)].

then compare the conclusions of $\epsilon(t)$ [panels (a)-(c)], the Bures metric [panels (d)-(f)], and the density metric [panels (g)-(i)].

Predictions from $\epsilon(t)$

Figure 5.3 (a)-(c) shows $\epsilon(t)$ from equation 5.1 with respect to time in units of τ. For $U = 0J$ [panel (a)], $\epsilon(t)$ indeed follows the expected results for each value of τ initially, with the red curve being far from adiabaticity, the blue curve being adiabatic at $\epsilon(t) > 0.1$, and the green curve showing behaviour in between the two. $\epsilon(t)$ then shows behaviour getting closer to adiabaticity as the evolution progresses and the instantaneous eigen-energies separate [see figure 5.1(a)], with the $\tau = 5/J$ dynamics becoming adiabatic for $t \lesssim 0.9\tau$.

For $U = 5J$ [figure 5.3(b)], many-body interactions become important as at this interaction strength the static system is undergoing the transition between a metal and a quasi-Mott insulator [62, 77, 138]. This means that states with double occupation become less favourable, and dynamics begin to stiffen for small driving potentials. The result of this is the system being less receptive to the drive, and so transitions are less likely to happen meaning the system

remains adiabatic for longer. At $t \approx 0.4\tau$, the driving potential becomes large enough to create an avoided crossing in the low energy spectrum [see inset of figure 5.3(b)], which $\epsilon(t)$ captures by spiking into non-adiabatic behaviour for $\tau = 0.5/J$ and $5/J$. The non-adiabatic behaviour is quickly dropped as $\epsilon(t)$ is Markovian by construct, meaning it holds no memory of previous events or times (it is based on instantaneous quantities). Therefore, as the spectrum separates again after $t \approx 0.45\tau$, $\epsilon(t)$ returns to adiabaticity. However the populations of the eigenstates could have changed in this period, meaning the system may not be adiabatic any more[8].

When $U = 10J$ [figure 5.3(c)], the system is fully into the regime of being a quasi-Mott insulator. This means the system is 'frozen' because the interaction strength dominates over all other energy scales and prevents any hopping between neighbouring sites. In this regime the system is clearly adiabatic for all values of τ, where no transient dynamics can take place, no matter the speed of the dynamics. At $t \approx 0.95\tau$, however, the driving potential becomes too large to be negligible in comparison to the interaction strength. At this time, transient dynamics can occur, and we see avoided crossings in the spectrum [inset of figure 5.3(c)]. This leads to sudden peaks in $\epsilon(t)$ as the system breaks out of its adiabatic evolution. Once again, because $\epsilon(t)$ is Markovian, it drops quickly after the crossings have occurred.

Note that the original QAC assumes the system is non-degenerate and there is a sufficient gap between concurrent energy levels to prevent a transition [97]. Also remember that the original QAC has been shown to be insufficient, with Marzlin and Sanders igniting the recent debate [42], particularly concerning oscillating Hamiltonians. Others then went on to further demonstrate the necessity but insufficency and lack of validity of the QAC for non-degenerate Hamiltonians [98, 133, 146]. Even though Avron and Egart reformulated the original QAC to avoid the gap condition, and Rigolin and Ortiz developed a QAC for degenerate systems, the QAC is still not shown to be necessary and sufficient[9] and so it is unsurprising that our adapted version has issues for this challenging setup.

[8]It may not be adiabatic when compared to the initial system, however it could be 'instantaneously' adiabatic, where no transitions have occurred from the last time step to the current, however this is not a useful classification for many applications involving adiabatic evolutions, such as adiabatic quantum computing.

[9]Rigolin and Ortiz developed a necessary condition and a *separate* sufficient condition in reference [133].

Adiabatic and non-adiabatic behaviour according to the metrics

Figure 5.3 shows $D_\rho^B(\rho_{GS}(t), \rho(t))$ versus time in panels (d)-(f), and in panels (g)-(i) $D_n(n_{GS}(t), n(t))$ versus time, all for the same parameters as $\epsilon(t)$ in panels (a)-(c)[10]. The horizontal dashed lines indicate the threshold Δ_ρ for the state distances in panels (d)-(f) and the corresponding threshold Δ_n for the density distances in panels (g)-(i).

For $U = 0J$ with $\tau = 0.5/J$ and $5/J$ (red and green curves respectively), $D_\rho^B(\rho_{GS}(t), \rho(t))$ and $D_n(n_{GS}(t), n(t))$ (panels (d) and (g) respectively) are in striking contrast to $\epsilon(t)$ in panel (a). For short times, the metrics correctly predict adiabatic behaviour as the (initial) ground state takes time to mix with the excited states. This means the system begins adiabatic then as the transitions occur it loses the adiabatic behaviour. However, $\epsilon(t)$ erroneously predicts a return to adiabaticity for these driving times. The system state for dynamics far-from-equilibrium is highly affected by the trajectory at previous times, and hence can be considered non-Markovian. Therefore, taking a non-Markovian measure of adiabaticity, such as the proposed metrics, is vital for avoiding false characterisations.

For slow dynamics with $U = 0J$ ($\tau = 50/J$, blue curves in panels (d) and (g) for D_ρ^B and D_n respectively), the behaviour is always adiabatic, which is also seen for $\epsilon(t)$. We can therefore safely characterise this evolution as adiabatic, and in this case any of the three methods proposed here could be used. The oscillations seen in these results are due to the inertia of the system, as discussed in section 4.4.2 in chapter 4.

When many-body interaction strengths are non-zero, i.e. $U = 5J$ (panel (e) for D_ρ, or panel (h) for D_n) or $U = 10J$ (panel (f) for D_ρ, or panel (i) for D_n), both $D_\rho^B(\rho_{GS}(t), \rho(t))$ and $D_n(n_{GS}(t), n(t))$ respond to the avoided crossings ($t \approx 0.4\tau$ for $U = 5J$, and $t \approx 0.95\tau$ for $U = 10J$). Unlike $\epsilon(t)$, they show the system remaining non-adiabatic afterwards, even as the energy levels begin to separate again. This demonstrates the importance of memory effects on the adiabaticity of a system, and hence the necessity for a non-Markovian characterisation method.

$D_\rho^B(\rho_{GS}(t), \rho(t))$, as distance between the system quantum state and its adiabatic counterpart, can be readily associated to the definition of adiabaticity. This is not the case for $D_n(n_{GS}(t), n(t))$ because the densities are just a function of position and time, and might not be expected to be as sensitive to system details, such as the energy spectrum, dynamic changes, or memory

[10]Corresponding results for the trace distance will be discussed in section 5.5.5.

effects. However because of the Runge-Gross theorem [71], and the corresponding lattice adaptation [142], the density should contain the same information as the state. Therefore we speculate that both the metrics employed here can be used as successful measures of adiabaticity. This was indeed confirmed for single electron systems in chapter 4, and here for many-body systems. This leads to the possibility of characterising the adiabaticity using only the density, a much more accessible quantity than the state. We have seen this is the case for zero temperature systems, now let us see if the same can be said for finite temperature systems.

5.5.4 Finite temperature

A thermal bath at temperature T is now connected to the Hubbard chain, to thermalise the system. Once thermalised, the bath is disconnected at $t = 0^-$ and the now closed system is evolved from $t = 0^+$ to τ. Therefore, the initial state is now a thermal state, with a corresponding thermal density. We no longer look at the distance between the dynamic state, $\rho(t)$, and the instantaneous ground state, but instead must compare $\rho(t)$ to the "transitionless" state. This is the state which has the same populations as the initial thermal state, and is therefore the state if the evolution was exactly adiabatic. This is written as

$$\rho_{Th}(t) = \sum_j \frac{\exp \frac{-E_{j,0}}{k_B T}}{\sum_k \exp \frac{-E_{k,0}}{k_B T}} \left|\psi_{j,t}\right\rangle \left\langle\psi_{j,t}\right|, \tag{5.14}$$

where $E_{j,0}$ is the j-th eigenenergy of the Hamiltonian at $t = 0$, and $|\psi_{j,t}\rangle$ is the j-th eigenstate of the instantaneous Hamiltonian at time t. The corresponding density $n_{Th}(t)$ is used in the density distance $D_n(n_{Th}(t), n(t))$.

For this finite temperature work, we consider two temperatures: a low temperature of $T = 0.2J/k_B$, and a high temperature of $T = 2.5J/k_B$.

Low temperature

Figure 5.4 shows the results for $\epsilon(t)$, the Bures distance, and the density distance when $T = 0.2J/k_B$. At this temperature, $k_B T \ll E_1 - E_0$ for most cases, and so the results are very similar to the zero temperature ones as access to the higher energy states is still strongly limited. However a notable difference occurs for $U = 10J$ at $0.9 < t/\tau < 1$. Here the inset of figure 5.3(c) shows the occurrence of four low-energy avoided crossings. Due to the finite-temperature state mixing, both metrics signal the four crossings with corresponding steps in the distances, while $\epsilon(t)$ remains sensitive only to the crossing occurring at

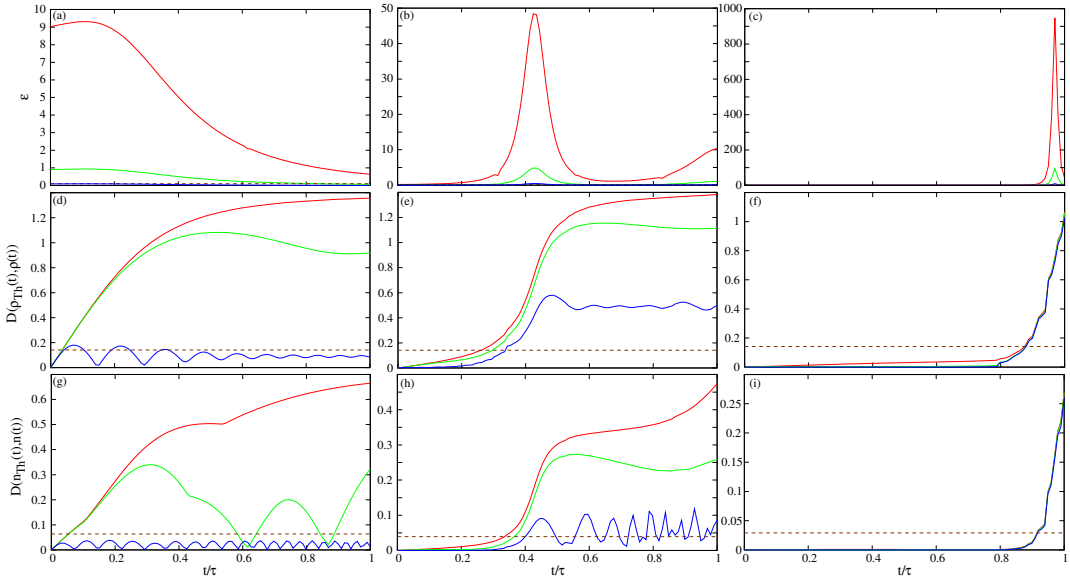

Figure 5.4: Low temperature ($T = 0.2J/k_B$) results. Red lines: $\tau = 0.5/J$ dynamics, green lines: $\tau = 5/J$ dynamics, blue lines: $\tau = 50/J$ dynamics. Panels show: $\epsilon(t)$ [(a)-(c)], $D^B_\rho(\rho_{Th}(t), \rho(t))$ [(d)-(f)], and $D_n(n_{Th}(t), n(t))$ [(g)-(i)] versus t/τ. Three interaction strengths are considered: $U = 0J$ (left), $U = 5J$ (middle), and $U = 10J$ (right). In all panels the horizontal dashed lines indicate the corresponding adiabatic threshold.

$t/ \approx 0.96\tau$ between ground and first excited state.

These results suggest that for low temperatures, $k_B T \ll J$, the density could be used as a good indicator to characterise adiabaticity, much like at zero temperature.

High temperature

At this higher temperature of $T = 2.5J/k_B$, more eigenstates of the initial Hamiltonian will be populated, strongly impacting the system evolution and highlighting the impact of many-body interactions. Figure 5.5 shows $\epsilon(t)$ in the top row, $D^B_\rho(\rho_{Th}(t), \rho(t))$ in the middle row, and $D_n(n_{Th}(t), n(t))$ in the bottom row, all versus t/τ. The columns give the interaction strengths: $U = 0J$ in the left column, $U = 5J$ in the middle column, and $U = 10J$ in the right column.

For $U = 0J$ [figure 5.5, panels (a), (d), and (g)], $\epsilon(t)$ and the metrics are qualitatively similar to the low temperature and zero temperature results. The quantitative distance of the metrics is reduced, however, because the potential driving has less of an impact on the system due to the increased temperature. Also note the oscillations in the slowest evolution are less regular than the lower temperatures due to thermal fluctuations in the system. Another important

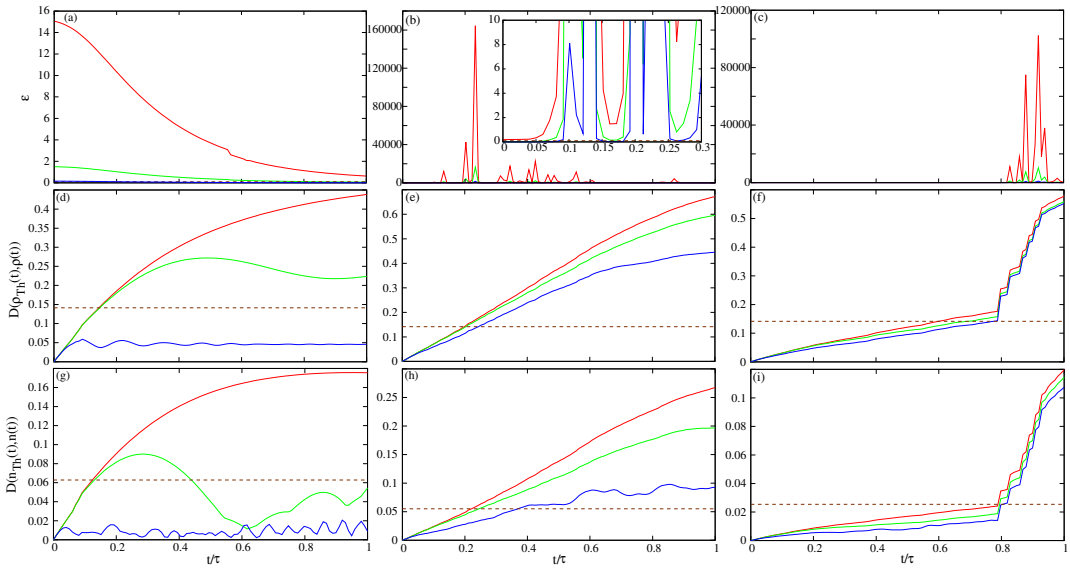

Figure 5.5: High temperature ($T = 2.5J/k_B$) results. Red lines: $\tau = 0.5/J$ dynamics; green lines: $\tau = 5/J$ dynamics; blue lines: $\tau = 50/J$ dynamics. Panels show: $\epsilon(t)$ [(a)-(c)], $D_\rho^B(\rho_{Th}(t), \rho(t))$ [(d)-(f)], and $D_n(n_{Th}(t), n(t))$ [(g)-(i)] versus t/τ. Three interaction strengths are considered: $U = 0J$ (left), $U = 5J$ (middle), and $U = 10J$ (right). In all panels the horizontal dashed lines indicate the corresponding adiabatic threshold. Inset of panel (b): zoom into short times of main panel.

aspect of this non-interacting system is that the lower part of the energy spectrum, below k_BT, has no crossings [see figure 5.1 panel (a)]: we will see that crossings in the spectrum have a large impact on the results.

The impact of many-body interactions and avoided crossings is clear for $U = 10J$ [figure 5.5, panels (c), (f), and (i)], where there are distinct groupings of energy levels in the spectrum [figure 5.1(c)]. The gap (due to on-site repulsion) between the lowest band of 20 eigenstates and the next band up (consisting of 6 eigenstates) at $t = 0$ is much larger than k_BT meaning only the lower band is populated. For all τ's, the insulating behaviour of the quasi-Mott insulator due to large U is seen, with all driving speeds showing mostly adiabatic behaviour until $t \approx 0.8\tau$. At this point in the evolution, the upper band of 6 eigenstates "meets" the lower band and causes avoided crossings. There are 6 steps clearly visible in both metrics, and there are 6 states in the upper band causing the crossings. Each of the steps in the metrics signal each of the upper states beginning to cross into the lower band.

For each of the eigenstates in the upper band, the avoided crossings after the initial avoided crossing are much less (if at all) noticeable in the metrics. This can be attributed to the populations of the states involved with the crossing. When the upper states first descend, they are unoccupied, so as soon

as they cross the occupied lower band, the populations of each state drastically change. This causes a very clear difference when compared to the adiabatic state, where no transitions would have occurred. This, in turn, gives rise to the sudden jumps in the Bures distance. However, as these now populated "upper" states descend further into the lower band, any transitions between states will be much smaller and less noticeable. Both the Bures metric *and* the density metric capture this behaviour faithfully.

When we look at $\epsilon(t)$ for $U = 10J$ [figure 5.5, panel (c)], a series of peaks are presented in the region where the energy groups cross, but without distinction between avoided crossings at the top of the lower band, or deeper within the lower band structure. The avoided crossings affecting $\epsilon(t)$ are not necessarily the ones expected to greatly change the system (e.g. due to large population differences between states involved in the avoided crossing)[11]. As with the lower temperatures, the peaks also decline rapidly after the crossings, again due to $\epsilon(t)$'s Markovian nature.

This issue of $\epsilon(t)$ inappropriately signalling the avoided crossings is even more evident for $U = 5J$ [figure 5.5, panels (b), (e), and (h)]. In this system, the next band up from the lowest band begins to cross the lowest band almost immediately, at $t \approx 0.05\tau$ [figure 5.1(b)]. Since the system begins with almost no gap between the lowest two groupings, the top states of the lower band and the bottom states of the upper band will be similarly populated. This means that the avoided crossings should not cause such a drastic increase in non-adiabatic behaviour (compared to $U = 10J$). Both metrics capture this well, and gradually increase out of the adiabatic threshold into non-adiabatic behaviour. However $\epsilon(t)$ shows many peaks throughout the evolution, as well as signalling the initial avoided crossing at $t \approx 0.05\tau$ (see figure 5.5, panel (b) inset).

Although in this work the degenerate form of QAC was adapted for finite temperature, the results show that it is still not well suited for high T. On the other side, the metrics, which naturally include degeneracy and non-Markovianity, can be seen to cope well with the temperature increase[12].

[11] In fact $\epsilon(t)$ often appears to use unexpected eigenstates, as it is the sudden switch in the instantaneous eigenstates used which leads to the small jump for $U = 0J$ at $t \approx 0.55\tau$.

[12] Note that for the high temperature, there is a reduction of the distances for all U's and τ's in all metrics. This is because the system is less susceptible to the same driving when at the higher temperature, and so one may wish to tighten the adiabatic threshold for the metrics.

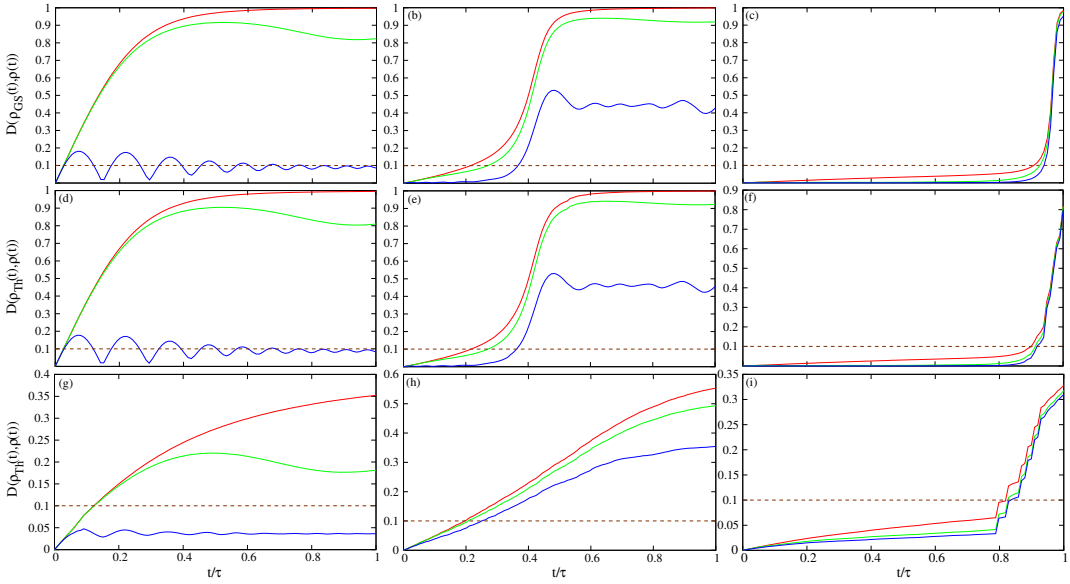

Figure 5.6: All figures here show the trace distance $D_\rho^T(\rho_{GS(Th)}(t), \rho(t))$ against t/τ. Interaction strengths: $U = 0J$ (left), $U = 5J$ (middle), and $U = 10J$ (right); red lines corresponds to $\tau = 0.5/J$, green lines to $\tau = 5/J$, and blue lines to $\tau = 50/J$. Panels (a)-(c) show the zero temperature results, $T = 0J/k_B$; (d)-(f) show the low temperature results, $T = 0.2J/k_B$; (g)-(i) show the high temperature results, $T = 2.5J/k_B$.

5.5.5 Comment on the trace distance

Having seen how the Bures metric characterises adiabaticity in these many-body systems at finite temperature, we turn to look at the trace distance and compare the results.

Beginning at zero temperature, we compare figure 5.6 (a)-(c) to figure 5.3 (d)-(f). For low temperature we compare figure 5.6 (d)-(f) to figure 5.4 (d)-(f). And for the high temperature, we compare figure 5.6 (g)-(i) to figure 5.5 (d)-(f). With respect to its own adiabatic threshold[13], the trace distance results are quantitatively close to the Bures distance, including the signalling of avoided crossings via steps in the distance. This means that the trace distance can be used as an alternative quantitative measure of adiabaticity.

5.6 Conclusion

In this chapter we have introduced methods for characterising adiabaticity in many-body systems at finite temperature, tracking how the degree of adiabaticity evolves with time. Not only did we see that both the Bures metric

[13]Remember that the maximum value of the trace distance is 1 for normalised states, therefore the numerical values of the distance will be different to those of the Bures distance.

and the trace metric give similar conclusions, but thanks to the Runge-Gross theorem (fundamental to time-dependent density functional theory) [71, 142], the density metric alone was able to characterise adiabaticity. This is important as the density may be estimated more accurately and simply than the corresponding many-body state. It is also experimentally measurable, opening up new applications of this method.

Given that, in practice, achieving a perfectly adiabatic evolution is extremely challenging, we use the finite maximum values of the metrics to design a practical 'adiabatic threshold'. We have related the threshold for the state metrics to an upper bound for the threshold for the density metric, which is tight enough along most parts of the time evolutions analysed. It is also relatively easy to estimate the density threshold, even for large systems, and future work can look into improving this estimate (i.e. by using more complex fits to the adiabatic line).

We also propose a method of extending the QAC to degenerate many-body systems at finite temperature. While this is a useful adaptation, it highlights the importance of including memory effects when characterising adiabaticity. By construction, a measure based on the QAC is basically Markovian, because, at most, the instantaneous Hamiltonian time derivative is included. Our results show that this leads to false readings as highly out-of-equilibrium dynamics may be reported as adiabatic. This adapted QAC can also characterise quasi-adiabatic passages as non-adiabatic because it is overly sensitive to avoided crossings where the actual many-body state may not necessarily change significantly, giving rise to different false readings. One could propose a cumulative measure of adiabaticity by integrating ϵ over time to try and combat some of these Markovian issues, e.g. $\int_0^\tau \epsilon(t)dt$. This would lead to a non-Markovian measure but there is the potential issue of the method being unable to characterise returns to adiabaticity. In a similar vein, one could then take a rolling average of ϵ which would be "less Markovian" (i.e. considers the history of the evolution more) than the adapted QAC (although "more Markovian" than the integrated QAC), and also more open to returns to adiabaticity. Also note that a similar adjustment could be performed for the density distance to combat its erroneous returns to adiabaticity.

We have seen how the energy scales of the temperature, interaction strength, and driving potential have also all had an impact on the dynamics. The metrics have allowed us to analyse these behaviours more thoroughly, including alluding to a temperature dependence required for the adiabatic threshold, which can be studied in future work.

To summarise, the Bures metric is a mathematical interpretation of the quantum adiabatic theorem so can be thought of as an accurate measure of the degree of adiabaticity (especially as it is non-Markovian). The adapted QAC for finite temperature that we have proposed is a useful adaptation of the QAC, but still has some faults (for example, it is Markovian and also struggles in accurately capturing avoided crossings, which leads to false readings about the adiabatic nature of the evolution). The density metric follows the state metrics well, and as the density is a more accessible quantity, this method could be the most useful of all proposed here for characterising adiabatic evolutions, even at finite temperature. Therefore the density metric could be used as a mathematical interpretation of the quantum adiabatic theorem, especially for many-body systems where the state is hard to calculate and evolve.

We have looked intensively at the dynamics of many-body systems, and added temperature to the system. Let us now use these systems to further explore the impact of temperature on many-body systems.

6. Many-body effects on the thermodynamics of closed quantum systems

Now that we have explored methods of interrogating many-body system dynamics at finite temperature, we can turn our focus to other aspects of these systems. Since we are at finite temperature, it makes sense to look at the thermodynamic properties of the systems, especially because quantum thermodynamics is a rich and growing field with many applications [10, 12, 13, 28–30]. One very important quantum thermodynamic property is the quantum work. It is able to inform us of energy costs for quantum technologies, as well as opening up the possibility to generate technologies which can utilise it, such as quantum batteries and quantum heat engines.

In this chapter we address research question 2a; "what do these [quantum thermodynamic] properties look like for the Hubbard system solved numerically exactly?" This work will prepare us for question 2b "how accurate are simple non-interacting-style approximations?", to be addressed in chapter 7 and question 2c "can we improve the approximations from point 2b using DFT?" to be addressed in chapter 8. Work in this chapter has been published in Journal of Physics A: Mathematical and Theoretical [138].

6.1 Introduction

We discussed previously how progress on applications of quantum technologies is linked to acquiring deeper understanding of the out-of-equilibrium thermodynamic properties of small quantum systems, particularly at finite temperature and away from the thermodynamic limit. We know that quantum thermodynamic properties, such as the extracted average quantum work and thermodynamic entropy production, are important for quantum technolo-

gies. A remaining challenge, however, is properly understanding the effects of many-body interactions on quantum thermodynamic properties. Because these many-body interactions are so important to new and existing technologies, we need to develop new approximations for quantum thermodynamic properties in many-body interacting systems. First, however, we need to understand the exact results, and create an appropriate test-bed for the new approximations.

Here we present a systematic study of the out-of equilibrium thermodynamics of many-body quantum systems subject to a set of qualitatively different potentials. For each type of potential, we consider dynamic regimes from sudden quench, to quasi-adiabatic (denoted by τ, the system driving time); for each dynamic regime we consider different interaction strengths, from non-interacting to strongly correlated systems (characterised by U, the Coulomb strength). We also consider different temperatures: low ($T = 0.2k_B/J$), intermediate ($T = 2.5k_B/J$) and high temperature ($T = 20k_B/J$). For all cases considered, we calculate and discuss the average quantum work extracted and entropy produced. This systematic study allows us to uncover some important dependencies of work and entropy on the systems' correlation and dynamic regimes, which are seen across the different potentials.

We also look at the accumulation of the average quantum work extraction throughout the duration of the driving for these parameters to further understand how the system and quantum thermodynamic properties respond whilst being driven. This provides insight into how the parameters impact the accumulation of average quantum work extraction, and in some cases show potential application limits when using quantum technologies.

6.2 Theory

6.2.1 Hubbard model

We will continue to use the time-dependent, inhomogeneous, one-dimensional Hubbard model, described in section 2.5.1, as we now progress on to investigating the aforementioned quantum thermodynamic properties in many-body systems. Because the Hubbard model presents non-trivial dynamics but is exactly solvable numerically for small chains, it is a great test-bed for exploring and understanding these properties, developing approximations, and testing them. The model parameters to be used in our systematic study are outlined next, in section 6.2.2.

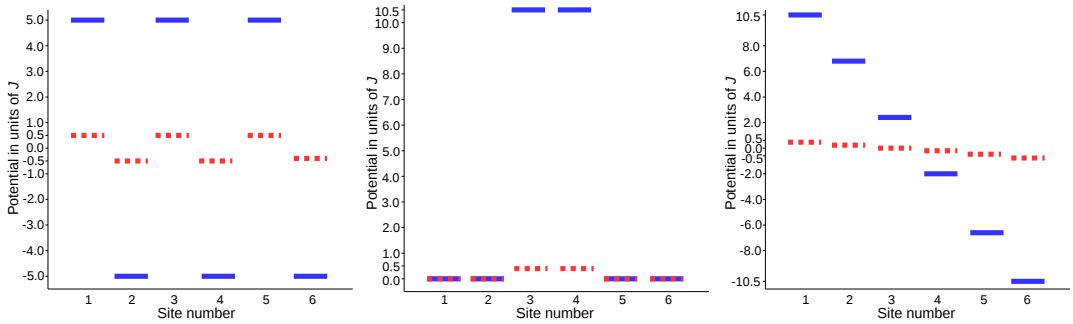

(a) Zigzag dynamics. (b) Teeth dynamics. (c) Slope dynamics.

Figure 6.1: On-site potentials versus site number for a 6 site chain; red dashed lines show the potentials at $t = 0$, and blue solid lines show the potentials at $t = \tau$.

6.2.2 System parameters

Because the inhomogeneous Hubbard Hamiltonian is non-integrable and not analytically solvable, to understand quantum thermodynamic properties and their approximations in a more general sense, we must explore a wide range of parameters. Therefore we shall calculate the work extracted and entropy produced for different potentials at different temperatures undergoing a variety of dynamic regimes with various interaction strengths.

We will consider Hubbard chains of 2, 4, and 6 sites, at half-filling and under open boundary conditions, and explore low ($T = 0.2J/k_B$), medium ($T = 2.5J/k_B$), and high ($T = 20J/k_B$) temperatures. For each system size and temperature, we will explore regimes from non-interacting ($U = 0J$) all the way to strongly correlated ($U = 10J$), and dynamics from almost sudden quench ($\tau = 0.5/J$) all the way to quasi-adiabatic ($\tau = 10/J$).

For each parameter combination, we will consider three types of potential[1], where each potential is driven linearly via $v_i(t) = \mu_i^0 + \mu_i^\tau t/\tau$, with t the time, τ the final time, and μ_i^0 and μ_i^τ the time-independent coefficients for site i at time 0 and τ respectively. With this choice, the character of the dynamics will depend on τ, while the final Hamiltonian $\hat{H}_f$ will be independent of it. These potentials were outlined in section 2.5.1 and are "zigzag", "teeth", and "slope" (remembering that μ_i^τ is now $10J$ for slope). The initial (red; dashed) and final (blue; solid) potentials for a six-site Hubbard chain are illustrated in figure 6.1.

[1]We note that for the 2 site chain slope and zigzag are the only relevant dynamics, and are equivalent with appropriate values of μ_i^0 and μ_i^τ.

6.2.3 Average quantum work and entropy production

Recall from chapter 2, section 2.4, that in a closed system at temperature T, the average quantum work can be calculated as [10]

$$\langle W \rangle = \mathrm{Tr}\left[\hat{\rho}_f \hat{H}_f\right] - \mathrm{Tr}\left[\hat{\rho}_0 \hat{H}_0\right], \tag{6.1}$$

with $\hat{\rho}_t$ the system state at time t (0 for initial, and f for final), and $\hat{H}_t$ Hamiltonian at time t (again with 0 for initial and f for final).

From this work, and using the change in free energy, we can define the variation in thermodynamic entropy for a given dynamic process as

$$\Delta S = \beta \left(\langle W \rangle - \Delta F\right), \tag{6.2}$$

where $\beta = 1/k_B T$ [4, 11]. The free energy variation is

$$\Delta F = -\frac{1}{\beta} \ln\left(\frac{Z_f}{Z_0}\right), \tag{6.3}$$

with Z_t the partition function at time t of the dynamics (again with 0 for initial and f for final), given by $Z_t = \mathrm{Tr}\left[\exp\left(-\beta \hat{H}_t\right)\right]$. This thermodynamic entropy can be considered a measure of the degree of irreversibility of the system dynamics. In fact it captures an uncompensated heat which would need to be dispersed to the environment for the system to return to thermodynamic equilibrium at the end of the driven process [4, 32].

6.3 Exact results

As mentioned previously, before we can assess the accuracy of the approximations for quantum thermodynamic properties (addressed in chapters 7 and 8), we first need to understand how the exact system behaves. To do this, we will consider the system to be in thermal equilibrium at time $t = 0^-$, at which point the coupling with the thermal bath of temperature T is switched off. The closed system is then driven by a time-dependent external potential from the initial Hamiltonian, $\hat{H}_0$, to the final Hamiltonian, $\hat{H}_f$, in a time τ. The extracted work, $\langle W_{ext} \rangle$, from this driving is calculated using equation 6.1, where $\langle W_{ext} \rangle = -\langle W \rangle$.

We stress that with each of the driven dynamics described in section 6.2.2 the final Hamiltonian is independent of τ. This means τ controls the rate of driving to the final Hamiltonian. Therefore, the larger τ is, the slower the

system has evolved and hence the more adiabatic the evolution.

For each set of the many-body system parameters, we will consider driving times of $0.5 \leq \tau \times J \leq 10$ and electron correlation strengths of $0 \leq U/J \leq 10$. Due to the sheer number of results from all the combination of parameters[2], we will only explicitly show results for 6 site chains, and comment on the rest in the chapter. The results for the parameters not shown here can be found in appendix B.

6.3.1 Exact average quantum work extraction

Figure 6.2 shows the exact average quantum work extracted from a 6 site chain driven via "slope" (right column), "zigzag" (middle column), and "teeth " (left column) potentials at temperatures of $T = 0.2J/k_B$ (first row), $T = 2.5J/k_B$ (second row), and $T = 20J/k_B$ (third row). Each panel shows a wide range of regimes: from non-interacting to strongly correlated systems as U increases along the y-axis; and from sudden quench towards adiabaticity as τ increases along the x-axis. A lighter shade of colour corresponds to higher extracted work.

The same data from figure 6.2 is shown in figure 6.3 but with each colour showing a specific value of the work across all the panels. This better highlights the trends in the work extraction between the potentials and temperatures, whereas figure 6.2 better demonstrates the trends across the parameter space for a given potential and temperature.

The general trend we find with these data is that most extractable work (in our parameter space for any given potential and temperature) is in the adiabatic regime and at low-medium correlation strengths. This is also seen as N varies (see appendix B for examples), where qualitatively the figures look the same, but quantitatively more work is extracted as N increases. As temperature increases, we still see most work extracted in the adiabatic regime, however the value of this work reduces. Now let us analyse the plots with more scrutiny to explain some of these trends.

At all temperatures, the largest work is extracted using a slope potential (figure 6.2, right column). The slope systems have the largest final drive, so they are able to convert this energy to extractable work. $\langle W_{ext} \rangle$ is minimum for the teeth potential, with work needing to be done *on* the system because

[2]A necessity due to the non-integrable Hamiltonian, meaning exact analytical solutions are not possible. However this also shows the behaviours of the thermodynamic properties in complex non-integrable systems with finite time dynamics, something not often done due to its complexity.

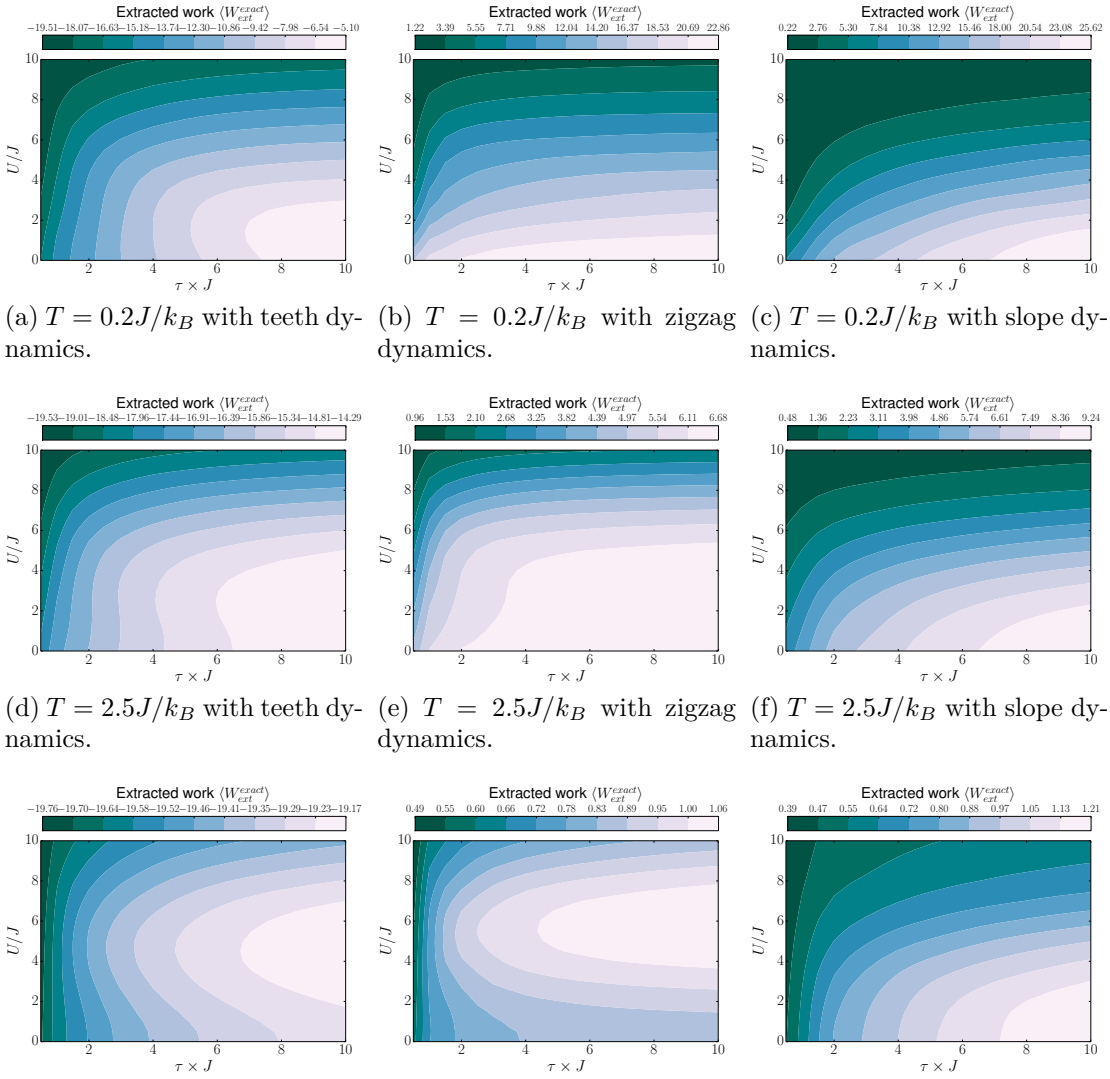

(a) $T = 0.2J/k_B$ with teeth dynamics.

(b) $T = 0.2J/k_B$ with zigzag dynamics.

(c) $T = 0.2J/k_B$ with slope dynamics.

(d) $T = 2.5J/k_B$ with teeth dynamics.

(e) $T = 2.5J/k_B$ with zigzag dynamics.

(f) $T = 2.5J/k_B$ with slope dynamics.

(g) $T = 20J/k_B$ with teeth dynamics.

(h) $T = 20J/k_B$ with zigzag dynamics.

(i) $T = 20J/k_B$ with slope dynamics.

Figure 6.2: (a)-(i) Exact extracted average quantum work versus total dynamics time τ (x-axis) and interaction strength U (y-axis). Data are presented for 6 site Hubbard chains driven by teeth, zigzag, and slope potentials, and at low, medium, and high temperatures, as indicated. The lighter the colour shade, the more work is extracted, compatible with the respective work range indicated over each panel.

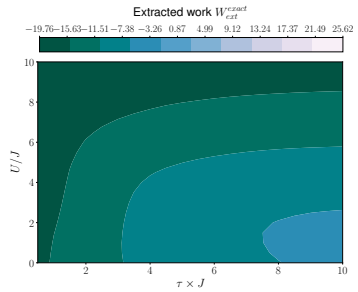

(a) $T = 0.2J/k_B$ with teeth dynamics.

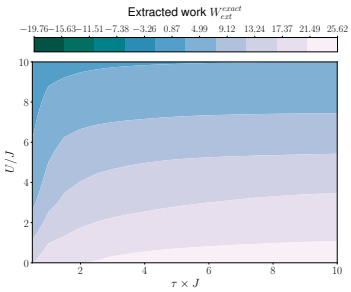

(b) $T = 0.2J/k_B$ with zigzag dynamics.

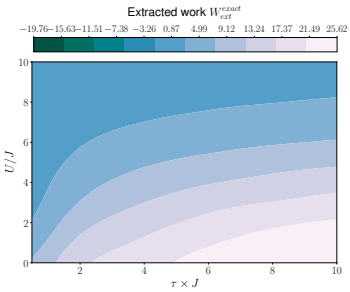

(c) $T = 0.2J/k_B$ with slope dynamics.

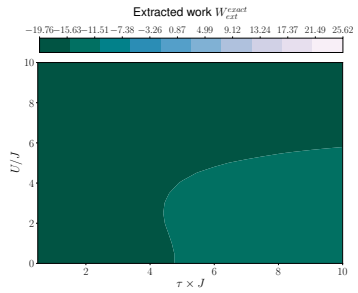

(d) $T = 2.5J/k_B$ with teeth dynamics.

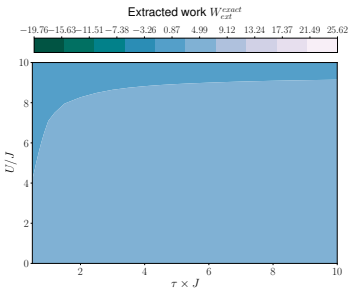

(e) $T = 2.5J/k_B$ with zigzag dynamics.

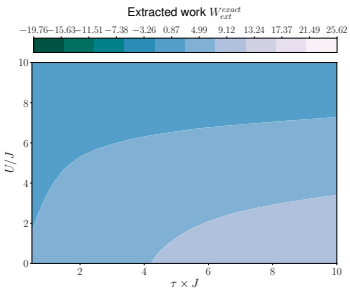

(f) $T = 2.5J/k_B$ with slope dynamics.

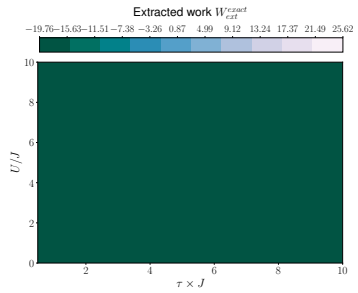

(g) $T = 20J/k_B$ with teeth dynamics.

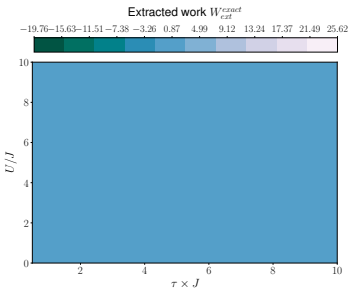

(h) $T = 20J/k_B$ with zigzag dynamics.

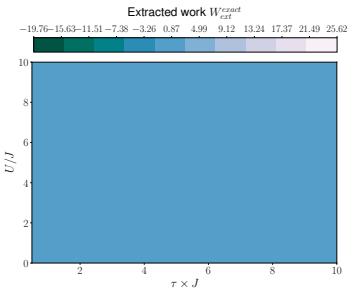

(i) $T = 20J/k_B$ with slope dynamics.

Figure 6.3: (a)-(i) Exact extracted average quantum work versus total dynamics time τ (x-axis) and interaction strength U (y-axis). This figure shows the same data as figure 6.2, but here each colour represents a specific value for the work across all panels. This enables easier comparison between panels.

the middle two sites are being driven up[3]. Because the work extracted spans a wide range of values, even from positive to negative, we can feel confident that the parameters and potentials chosen are a good test bed for understanding work extraction in systems representable by Hubbard chains. This is especially important because our system is non-integrable, and ensures that we will have a good test-bed on which to develop approximations for quantum thermodynamic properties to be used when exact solutions (i.e. for larger chains) are unobtainable.

For all potentials, increasing the temperature decreases the maximum extractable work and also decreases the range of extracted work over our parameter space. This is because as the temperature increases, it becomes the dominant energy; at $t = \tau$, the potential differences across the chains are $\sim 10J$ for zigzag and teeth, and $\sim 20J$ for slope, and the highest temperature is $T = 20J/k_B$. With the temperature as a dominant energy, the system becomes less sensitive to the applied field and so less work is extracted.

For all temperatures and potentials, the maximum work extracted occurs at large τ's where the system approaches adiabaticity. Here the dynamic state adjusts better to the driving and prefers low potential sites (T and U allowing), which increases the average work extracted. This behaviour has been seen not only for the results shown in figure 6.2, but also for 2 and 4 site chains (see appendix B). So although the precise region and quantity of largest average work extracted will be affected by N, we would anticipate the largest average work extraction to occur with adiabatic regimes for all N in these systems[4].

When increasing U for the slope potential at all temperatures (figure 6.2, right column), hopping between sites is hampered which reduces the transient current dynamics. This reduces the work extracted, and so we see the largest work extracted is for non-interacting to weakly interacting regimes. As U increases, the Hubbard chain experiences the precursor to the phase transition to a Mott insulator which 'freezes' the system preventing work extraction.

Now looking at the zigzag potential (figure 6.2, middle column), at the low temperature the results are qualitatively similar to the slope potential, but as the temperature increases the region of largest average work extraction moves to regimes with larger many-body interactions. Indeed for the highest temperature, the maximum work extraction moves to a medium/strong U regime ($4 \lesssim U/J \lesssim 8$). This is due to the high temperature having approximately

[3]If the middle two sites were driven down, $\langle W_{ext} \rangle$ would be positive and hence work could be extracted from the system.

[4]It would be surprising if the region of largest extracted work suddenly 'jumped' from an adiabatic region to a quench region as N increases.

twice the energy of the potential difference between neighbouring sites ($\sim 10J$ at $t = \tau$), and so some repulsion is required to depopulate the high energy sites completely and maximise work extraction.

For the teeth potential (figure 6.2, left column), the work extracted is negative meaning work must be performed on the system to achieve the final state. The drive raises the middle two sites, making them less and less favourable for occupation, and after the two middle sites have been depleted of electrons no more work can be produced by the system. Throughout the parameter space used, the sites continue to be raised after the middle sites have been depleted, so work must be performed on the system resulting in the work performed on the system greatly outweighing any work produced by the system. As with the zigzag potential, we see the region of largest average work extraction moves to regimes of larger U as the temperature increases. This is for a similar reason, as a small amount of repulsion is required to completely depopulate the middle high energy sites allowing for maximum work extraction, especially as the temperature increases and the thermal energy encourages the electrons up to the higher energy sites.

To briefly summarise, for all potentials and temperatures we see the largest average work extracted in the adiabatic regime, however we see how the temperature and potentials themselves cause large differences in the average work extraction. Here we see how the most average work extracted is achieved using the slope potential at a low temperature, and the least is using the teeth potential at a high temperature. However, also note the strengths of these driven potentials because these energies are in competition with the temperature and interaction strength, and therefore impact the work extraction. Overall we see that the most average work extraction is in the adiabatic regime, but the energy scales of the potential, temperature, and interaction strength impact the quantitative value and, to a lesser extent, the qualitative result.

6.3.2 Average quantum work extracted with time

We have now seen how the average quantum work extracted behaves in a wide range of τ's and U's, noting we most often get more work extracted in the weak-medium coupling regime, and for adiabatic evolutions. But how does this average work extraction accumulate as the Hamiltonian evolves from $\hat{H}_0$ to $\hat{H}_f$? Let us look at a few examples to explore this[5].

[5]Note that although only the results for 6 sites are discussed here, 2 and 4 sites chains have also been calculated, and are in qualitative agreement with the 6 site results, (see appendix B).

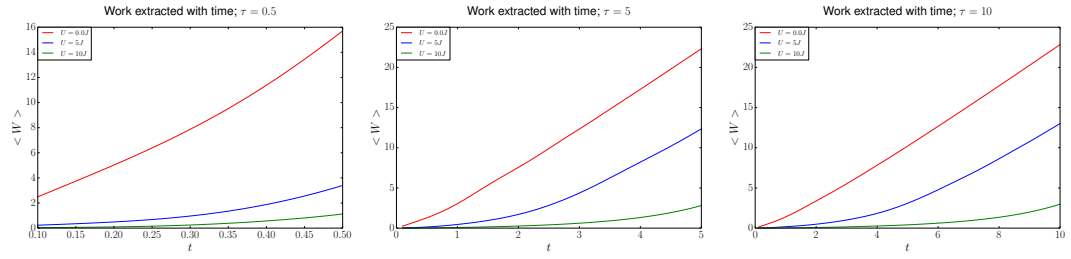

(a) $T = 0.2J/k_B$; $\tau = 0.5$. (b) $T = 0.2J/k_B$; $\tau = 5$. (c) $T = 0.2J/k_B$; $\tau = 10$.

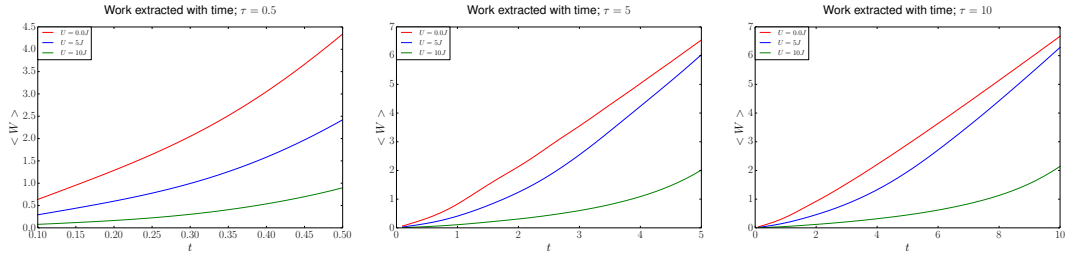

(d) $T = 2.5J/k_B$; $\tau = 0.5$. (e) $T = 2.5J/k_B$; $\tau = 5$. (f) $T = 2.5J/k_B$; $\tau = 10$.

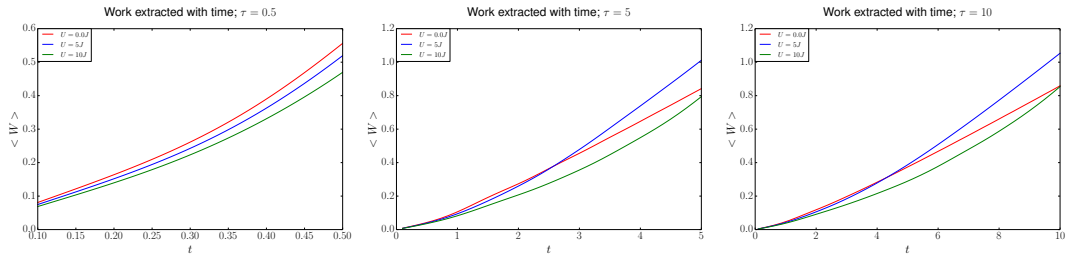

(g) $T = 20J/k_B$; $\tau = 0.5$. (h) $T = 20J/k_B$; $\tau = 5$. (i) $T = 20J/k_B$; $\tau = 10$.

Figure 6.4: (a)-(i) The average quantum work extracted versus time for 6 sites with zigzag potentials. Three temperatures are shown, low ($T = 0.2J/k_B$) in the top row, medium ($T = 2.5J/k_B$) in the middle row, and high ($T = 20J/k_B$) in the bottom row. The columns correspond to the values of τ with $\tau = 0.5/J$ in the left column, $\tau = 5/J$ in the middle column, and $\tau = 10/J$ in the right column. Each figure has 3 values of U: $U = 0J$ in red, $U = 5J$ in blue, and $U = 10J$ in green.

Figure 6.4 shows the average extracted work accumulation with time for 6 sites with a zigzag potential. For the three temperatures used previously, we explore three values of τ ($\tau = 0.5/J$ in the left column, $\tau = 5/J$ in the middle column, and $\tau = 10/J$ in the right column), each showing three values of U ($U = 0J$ in red, $U = 5J$ in blue, and $U = 10J$ in green).

In general we see a quasi-linear accumulation of the work after an initial ramp-up phase. When $T \gg U$, the work extracted is almost completely linear in time for all potentials [unless the system saturates in work, such as with the teeth potential shown in figure 6.6(a)], and so the ramp-up phase is very short. The ramp-up phase is longest for the highest U where we do not even see the linear relationship before the final time, and indeed the work extraction for high U is always lower than for the smaller interaction strengths. This can be attributed to the fact that at high U the system is approaching the precursor to the phase transition leading to the Mott-insulator. This means the system 'freezes' with the repulsion being so strong it greatly hampers hopping between sites and results in little work being extracted.

For the zigzag potential, we can see that the work extracted becomes more linear in time as $\tau \gg U$. We also note that for all potentials, when $T \ll 20J/k_B$, lower U's give more work extraction.

At the highest temperature the work extracted is greatly reduced and remains relatively similar for all three values of U. There are several crossings evident between the $U = 0J$ and $U = 5J$ results for the longer τ's [figure 6.4(h) and (i)]. These crossings show the regime of largest $\langle W_{ext} \rangle$ transitioning from low U to medium U (compare, for example, the regions of maximum work extraction in figure 6.2(e) where the maximum work is with low U, to figure 6.2(h) where the maximum work extracted is with medium U; although these are the final time results, they highlight the type of transition to which these crossings allude). As the driving takes place, there reaches a point where some repulsion is advantageous for work extraction[6]. This is because the repulsion encourages electrons to remain in the rising sites longer than they would in a non-interacting zigzag system, allowing for more work to be extracted. Hints of a crossing are also seen for the teeth potential (see figure 6.6 and appendix B), which also has a large difference between neighbouring sites and hence repulsion to encourage electrons to remain in the upper sites longer is beneficial. The slope potential (see figure 6.5 and appendix B) does not have such a stark difference between neighbouring site energies, and so it does not

[6]We do not want U to be too strong otherwise the system behaves more like an insulator so less work is extracted, as described earlier.

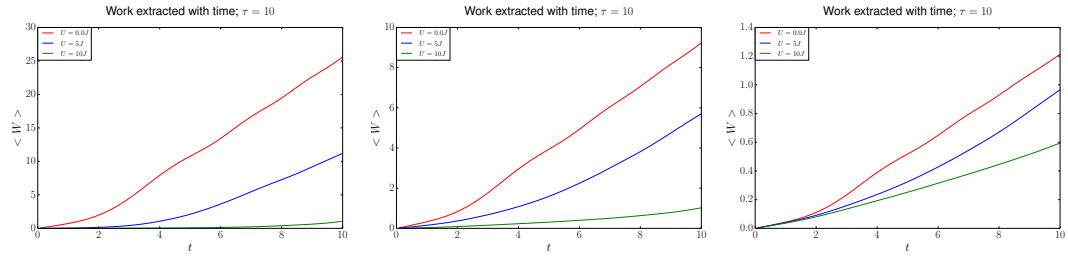

(a) $T = 0.2J/k_B$. (b) $T = 2.5J/k_B$. (c) $T = 20J/k_B$.

Figure 6.5: (a)-(c) The average quantum work extracted versus time for 6 sites with slope potentials driven with $\tau = 10/J$. Three temperatures are shown, low [$T = 0.2J/k_B$, (a)], medium [$T = 2.5J/k_B$, (b)], and high [$T = 20J/k_B$, (c)]. Each figure has 3 values of U: $U = 0J$ in red, $U = 5J$ in blue, and $U = 10J$ in green.

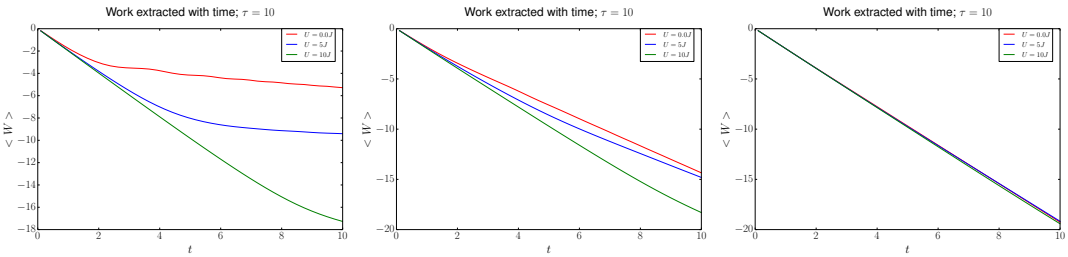

(a) $T = 0.2J/k_B$. (b) $T = 2.5J/k_B$. (c) $T = 20J/k_B$.

Figure 6.6: (a)-(c) The average quantum work extracted versus time for 6 sites with teeth potentials driven with $\tau = 10/J$. Three temperatures are shown, low [$T = 0.2J/k_B$, (a)], medium [$T = 2.5J/k_B$, (b)], and high [$T = 20J/k_B$, (c)]. Each figure has 3 values of U: $U = 0J$ in red, $U = 5J$ in blue, and $U = 10J$ in green.

show any crossings of this nature. In addition, at the high temperature (bottom row of figure 6.4), the system is less sensitive to both U and the potential, with T being the dominant energy. It is because of this lack of sensitivity to U that the work extraction curves remain relatively close to one another. This clustering of the curves also means crossings from a low U maximum to a medium U maximum are easier than for lower temperatures where there are larger differences between the curves.

Calculations for both teeth and slope potentials have also been performed with some results being shown in figures 6.5 and 6.6 (the complete set are displayed in appendix B). A key feature seen with teeth and slope potentials, but not seen with zigzag potentials, is a modulation of the work extraction with time [for example, $U = 0J$ in figure 6.5 and figure 6.6(a)]. It is pre-

dominantly seen with small U, where the system is more sensitive to changes in the potential and hopping between sites is more likely as the electrons do not have the restricted movement which is associated with high U[7]. This is seen particularly for the slope potential, where the modulations occur in most parameter sets for $U = 0J$. The modulations are clearer for longer τ's as the system has more time to adjust to the driving and more hopping between sites can occur.

For the teeth potential, the modulations are mainly seen for low temperature with $U = 0J$ because it is at the low temperature where the system is more affected by the interaction strength and potential driving. It is also worth noting that, in both teeth and slope potentials, the modulations are seen more for 6 site chains than for 2 and 4 site chains. We speculate it is because there are more degrees of freedom in the 6 site chains.

For the teeth potential (figure 6.6), there is another interesting feature which the other potentials do not have: the work extraction reaches a plateau for low T. If we think about the potential, two sites rising in the middle of the chain whilst the rest remain unchanged, then this plateau indicates the point at which the middle sites are depopulated and therefore no more work can be done. This gives us an idea as to the timescale for driving a device in this manner: a run-time which goes into the plateau will be inefficient and will not gain anything further. We can therefore use this to increase efficiency in any device which uses this type of potential. It is also worth noting that the plateau occurs at larger τ's because the system has time to adjust to the potential. The plateau is also reached quicker in the low temperature case because the dominant energies are the potential and interaction strength. As the temperature is increased we do not reach the plateau in figure 6.6, panels (b) and (c), because the temperature becomes an important energy and this thermal energy helps keep the middle island populated.

Also note that at the high temperature for the teeth potential [figure 6.6(c)], there is very little distinction between the different interaction strengths, again because the temperature is the dominant energy. This is also seen in figure 6.2 (g), which shows the contour plot of the average extracted work for the teeth potential, and from the scale we can see there is little change in work across the parameter space.

[7]As the system approaches an insulating phase, it 'freezes', as discussed earlier.

6.3.3 Entropy production

As mentioned before, the average work extracted can be related to the entropy (or irreversible work). This entropy corresponds to the heat which the system would have to disperse to the environment to return to thermodynamic equilibrium at the end of the dynamics. Let us examine the exact results for this entropy, ΔS from equation 6.2, using the exact work results in section 6.3.1. Apart from the average quantum work, the other key ingredient for ΔS is the free energy variation, ΔF, calculated using equation 6.3. Since our final Hamiltonians are independent of τ, the free energy only depends on U and T (via the inverse temperature, β).

Figure 6.7, panels (a)-(c), shows the variation of free energy as U varies at each of the temperatures considered (green line for low, blue for medium, and red for high temperature) and for each of the potentials. At low temperatures and, to a lesser extent, at medium temperatures ΔF significantly changes with the interaction strength. At high temperatures though, ΔF is weakly dependent on U. This is further evidence that the system behaves more like a non-interacting system as the temperature increases[8], which will be important for the approximations addressed in chapters 7 and 8.

The exact entropy production for all potentials and temperatures is shown in figure 6.7, second to fourth rows: left column for teeth, middle for zigzag, and right for slope. ΔS increases as the colour shade becomes lighter; note, however, that the same shade corresponds to different values in different panels, as the overall entropy range significantly changes according to both temperature and type of potential.

The temperature affects the entropy production drastically; compare the ranges of ΔS (above the contour plots) between the second and last rows of figure 6.7, where ΔS is consistently greater for the low temperature than it is for the high temperature. This can be understood by comparing energy scales of T, U, and the potential differences. By the end of the dynamics, our potentials reach the maximum energy difference of $10J$ for zigzag, $10.5J$ for teeth, and $21J$ for slope. For the low temperature $k_BT = 0.2J$ in the range of parameters explored, both the interaction strength U and the potentials can be much bigger than the thermal energy, and so they have a large impact on the system evolution. This means the system can change quite drastically leading to the possibility of large entropy production (and large work extraction, as

[8]Earlier in section 6.3 we discussed how energy scales impact the system, and a high temperature dominates over U. This results in the system at high temperature behaving as if it is a non-interacting system.

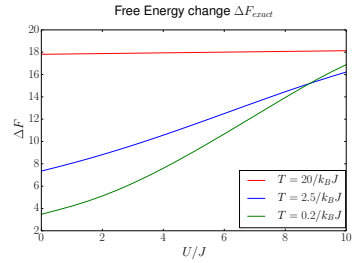

(a) Free energy – teeth potential.

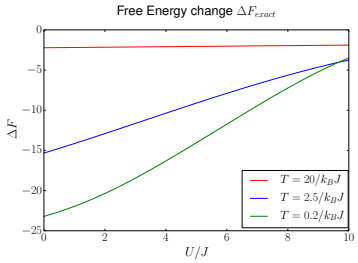

(b) Free energy – zigzag potential.

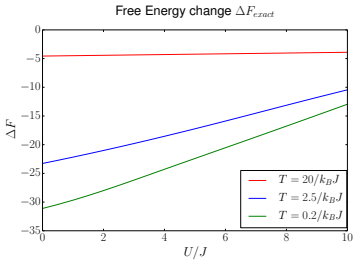

(c) Free energy – slope potential.

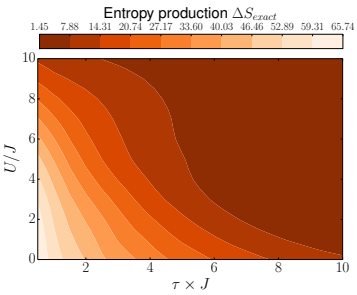

(d) $T = 0.2J/k_B$ with teeth potential.

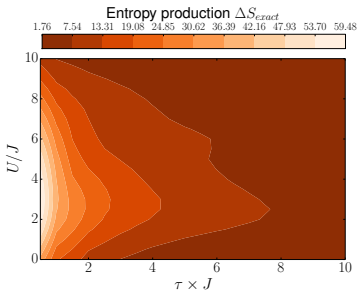

(e) $T = 0.2J/k_B$ with zigzag potential.

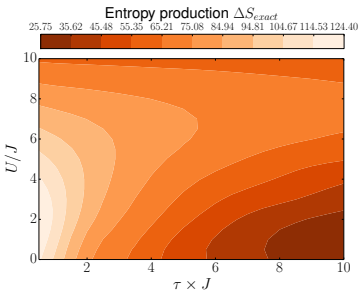

(f) $T = 0.2J/k_B$ with slope potential.

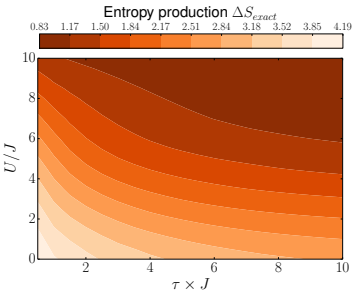

(g) $T = 2.5J/k_B$ with teeth potential.

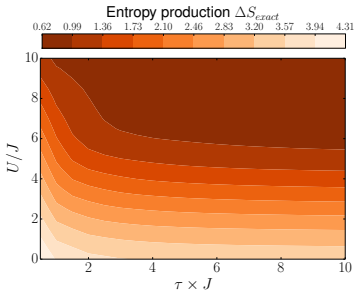

(h) $T = 2.5J/k_B$ with zigzag potential.

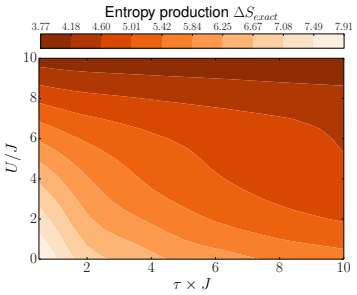

(i) $T = 2.5J/k_B$ with slope potential.

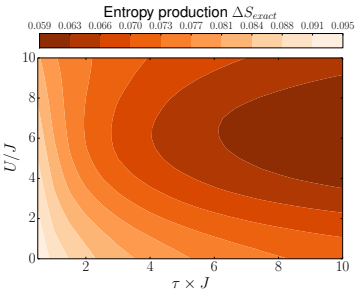

(j) $T = 20J/k_B$ with teeth potential.

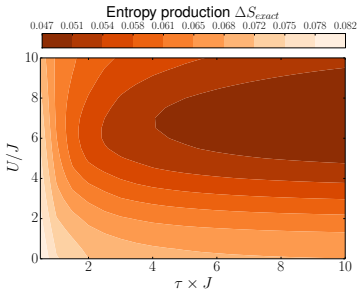

(k) $T = 20J/k_B$ with zigzag potential.

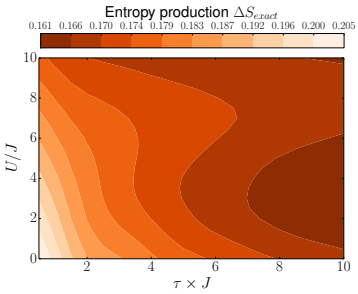

(l) $T = 20J/k_B$ with slope potential.

Figure 6.7: (a)-(c) Variation of free energy ΔF versus U for 6 site chains at low (green), medium (blue), and high (red) temperatures and for the three potential (as indicated). (d)-(l) Exact entropy production ΔS versus τ (x-axis) and U (y-axis), for 6 site chains, with teeth (left column), zigzag (middle) and slope (right column) potential; temperatures as indicated. Darker colour shades correspond to lower entropy production, whilst lighter to higher entropy production.

seen previously). However, at high temperature $k_BT = 20J$ the interaction strength and potential are, at most, comparable to the thermal energy. The system is therefore not as receptive to being driven. This results in it remaining closer to its thermal state, and hence the energy required to be dispersed to return to equilibrium (i.e. the entropy that we are considering here) will be much less.

In general (and seen most clearly at the lowest temperature) the sudden quench with weak-medium interaction strength region corresponds to very high ΔS values, while a dramatic reduction in entropy is seen moving towards the adiabatic regime. Given the correspondence between ΔS and the heat to be dispersed at the end to recover equilibrium, it stands to reason that a sudden quench would require a larger dissipation of energy to return to an equilibrium state compared to an adiabatic evolution, which remains closer to an equilibrium state at all times.

We note that systems subject to slope potential show, at low T, a relatively larger entropy production in the strongly-coupled regime and $\tau \approx 10/J$ than systems subject to zigzag and teeth potentials. The level of adiabaticity reached for the same value of τ differs with potential. Indeed the dynamic induced by slope at $U \gtrsim 6J$ and $\tau \approx 10/J$ is less adiabatic than the ones by teeth or zigzag, as can be observed by comparing panel (c) to panels (a) and (b) of figure 6.2[9]. This leads to a larger amount of entropy production occurring with slope even in this strongly-coupled large-τ region.

6.4 Conclusion

To conclude, we have presented a comprehensive study of the extracted average quantum work and entropy production in complex many-body systems subject to a wealth of potentials and dynamic regimes. By understanding the regimes which maximise the average work extraction, and minimise the entropy production, efficient protocols for quantum technologies can be developed.

In general, for a quantum technologist developing a device which requires a lot of work production and can be based on the Hubbard model, these results have demonstrated that they should look at using a suitably low temperature,

[9]If adiabaticity is reached, the work extracted will plateau as τ increases because no more work can be extracted as the system is fully adiabatic, no matter how much more slowly it is driven. In panel (c) of figure 6.2, the work has not plateaued fully yet, and so the system is not yet completely adiabatic.

keeping interactions small, and evolving the system slowly in order to maximise the work output. They should also be very careful with the type of potential they use, with a teeth-like potential where sites are raised requiring energy to be put into the system, whilst a slope-like potential improving the energy output. They should be aware of the balance between temperature, interaction strength, evolution time, and potential type/strength, and the impact these have on the work and entropy i.e. a temperature that is much greater than the interaction strengths considered will limit the amount of work that could be produced compared to a temperature more comparable to the interaction strength.

We have discussed in detail the effects of the interplay between the different energy scales governing the systems – potentials, many-body interactions, and thermal energy – on $\langle W \rangle$ and ΔS. We have also compared results as many-body correlations are increased up to the strongly coupled regime and as the dynamic regime is continuously changed from sudden quench to quasi-adiabatic. By using finite time processes and a system which is far from integrability, we shed light onto how thermodynamic properties behave in this challenging regime.

For all potentials at low to intermediate temperatures, medium to strong Coulomb repulsion decreases work extraction by making the system less responsive to the external drive. At weak Coulomb correlations, more work can be extracted as the system becomes adiabatic, while with stronger many-body interactions the work production becomes independent of the overall driving time τ much sooner. For the same parameter sets at high temperatures, work extraction is greatly reduced both in absolute values and in variation range.

We have seen how the average work extraction accumulates whilst the system is being driven, and analysed the effects of the energy scales. In general the work accumulates in a quasi-linear manner, with more work being extracted for low-medium correlation strengths. This gives an idea as to the parameters to be used for more efficient quantum technology applications. The impact of temperature is seen clearly, with the work extraction declining and the effect of U drastically reducing as temperature increases. The type of potential also gives rise to interesting features, with modulations being seen in non-interacting slope and teeth systems, and a plateau showing an effective end-point to any technological application run-times for systems with the teeth potential.

At low temperatures the entropy production presents a behaviour somewhat more dependent on the potential applied. We observe a general tendency

of lower ΔS values for intermediate to large τ's, but the onset of an adiabatic-like entropy dynamics varies considerably with the potential at intermediate coupling strengths. For a zero temperature, open-boundary, finite, homogeneous Hubbard chain, intermediate coupling strengths correspond to the precursor of a transition between metallic and insulating behaviour (precursor to a Mott insulator transition). The behaviour observed at intermediate coupling strengths may be a signal of how the different potentials affect this transition.

Similarly to the extracted average quantum work, entropy production decreases with temperature in both absolute value and range of variation, as the system becomes less and less responsive to the applied potential.

Now that we have analysed $\langle W \rangle$ and ΔS, and confirmed that the parameter set provides a wide variety of situation and results, we can develop some approximations for these many-body systems and test them against these exact results. The hope for this is that the approximations can then be used for larger systems where exact results are currently unobtainable, and that we can provide an indication of the regimes in which the approximations are highly accurate.

7. Developing a hybrid approximation for quantum thermodynamic properties

In this chapter, we will begin to look at methods of approximating quantum thermodynamic properties in many-body interacting systems, applying these general methods to the Hubbard model. Many-body interacting systems are of great importance, being key systems for advancing of quantum devices and developing understanding of fundamental physics [50, 51, 54–56, 147–149]. However the difficulty in computationally calculating properties of many-body interacting systems increases exponentially with system size. The many-body interactions are often approximated to allow for computationally viable calculations. Here we will be addressing research question 2b: "how accurate are simple non-interacting-style approximations [for quantum thermodynamic properties]?" Because we analysed the exact average work extraction and entropy production in the previous chapter, we can use those results to quantify the accuracy of the non-interacting-style approximations developed in this chapter.

Work in this chapter has been published in Journal of Physics A: Mathematical and Theoretical [138].

7.1 Introduction

We saw from chapter 6 that many-body systems are of key importance to the progress on applications of quantum technologies, and indeed the need to understand the role of thermodynamics in these systems has become more apparent [10, 11, 13, 32, 59, 150]. In this respect, there have been recent works studying out-of-equilibrium thermodynamics of many-body systems such as quantum harmonic oscillator chains and spin chains [49–58].

However, wherever there are many-body interactions, the computational cost increases as the size of a many-body interacting system increases, exponentially so. Therefore, solving large many-body systems (over $\sim$10 electrons for evolving systems) exactly is almost impossible with current hardware[1]. To bypass this issue, approximations for the interactions are often used. This brings us to Density Functional Theory (DFT), concepts of which have lead to the Kohn-Sham theorem where many-electron systems are approximated using their non-interacting counterpart plus some approximation for the interaction (explained later in chapter 8).

We will not use DFT in this chapter (that will come in chapter 8), but we will take inspiration from it; we will look at approximating our Hubbard system from chapter 6 with its non-interacting counterpart, and then add some effects of the interactions. This approximation will be applied to the average quantum work and entropy production. This will enable the calculation of these important quantum thermodynamic quantities for larger many-body systems, hopefully leading to more energy efficient devices and even new applications.

A proposal for a density-functional-theory-based set of approximations for the quantum work, which is in principle applicable to systems of high complexity, has already been seen and proven successful [32, 59], numerically considering a system of 2 electrons. In this chapter, however, we numerically consider larger systems and develop a new, hybrid, approximation which is computationally cheap but has great accuracy in many parameter regimes.

As alluded to before, in this chapter we consider two quite drastic approximations for the same parameter set used in chapter 6, and compare them with the exact results. The first is the completely non-interacting approximation, where many-body interactions are set to zero in all phases of the thermodynamic processes considered. The second approximation assumes knowledge of the initial interacting many-body state, but completely neglects interactions afterwards for the driven dynamics. We find that including interactions through just the initial state yields surprisingly accurate results for the times used in our parameter set. Of course, as the time of the evolution is extended, the effect of the interactions will become greater and so a non-interacting approximation will become less favourable (for example, we will see later in figure 7.2(f) the accuracy is decreasing at larger τ's for intermediate interac-

[1]It is possible to find highly accurate results for larger systems using techniques such as DMRG, but here we are referring to exactly diagonalising the Hamiltonian for systems on a lattice.

tion strengths). However, once the system reaches adiabaticity, no more work can be extracted (i.e. when the work extracted plateaus with τ in our figures) and the impact of the interactions during the larger τ's is reduced. Therefore, the accuracy of a non-interacting-based approximation would be expected to reduce at longer timescales until adiabaticity is reached when the accuracy should remain relatively constant as τ is increased further. We also compare how this hybrid approximation impacts the different methods of calculating the quantum work[2].

7.2 Recapitulation of system parameters

Having investigated the exact average work extraction and entropy production in chapter 6, and established the range of parameters used as a good test-bed, we will use those parameters for the approximated systems. This allows us to directly compare the approximations with the exact results, and hence determine the accuracy and suitability of the approximations in various regimes.

We therefore continue to use the time-dependent, inhomogeneous, one-dimensional Hubbard model at half filling with three potentials (zigzag, slope, and teeth) at three temperatures [low ($T = 0.2J/k_B$), medium ($T = 2.5J/k_B$), and high ($T = 20J/k_B$)] with a range of driving times ($0.5 \leq \tau \times J \leq 10$) and interaction strengths ($0 \leq U/J \leq 10$). This is our test-bed for the average quantum work extraction and entropy production for the non-interacting-based approximations discussed in this chapter.

7.3 Developing the hybrid approximation

The most basic approximation to make to a many-body interacting system is to assume that there are no interactions, also known as the "tight-binding approximation". It is with the interactions that the calculation becomes exponentially more challenging as system size N increases, and so by taking a non-interacting approximation we reduce our calculation down to N single-electron problems. Such a dramatic approximation is not expected to accurately capture the system when U is a dominant factor.

To keep the computational requirement small, but increase the accuracy of the results, we here propose to use a hybrid approximation composed of

[2]Discussed in section 2.4.1 of chapter 2: $\langle W \rangle$ can be found using the probability distribution or the change in internal energy (for closed systems).

the exact initial system and non-interacting dynamics. By taking the exact initial system, we are providing some knowledge of the interactions to help guide the approximation. However, because the evolution is still taken to be non-interacting, the calculation is still computationally cheap at its most challenging point.

7.3.1 Average quantum work approximations

The type of approximations we consider for the average quantum work are of the form:

$$\langle W^{is+\text{evo}} \rangle = \text{Tr}\left[\hat{\rho}_f^{is+\text{evo}} \hat{H}_f^{\text{evo}}\right] - \text{Tr}\left[\hat{\rho}_0^{is} \hat{H}_0^{\text{evo}}\right]. \tag{7.1}$$

Here is (initial system) refers to the approximation used to derive the system state at $t = 0$, $\hat{\rho}_0^{is} = \exp\left(-\beta \hat{H}_0^{is}\right) / \text{Tr}\left[\exp\left(-\beta \hat{H}_0^{is}\right)\right]$, and evo is the approximation used for the evolution operator $\mathcal{U}_{\text{evo}} = \mathcal{T} e^{-i \int_0^\tau \hat{H}_t^{\text{evo}}(t) dt}$ where $\mathcal{T}$ is the time-ordered operator. The final state is then $\hat{\rho}_f^{is+\text{evo}} = \mathcal{U}_{\text{evo}} \hat{\rho}_0^{is} \mathcal{U}_{\text{evo}}^\dagger$. We note that $\hat{H}_0^{\text{evo}} = \hat{H}_t^{\text{evo}}(t = 0)$. In the approximation where is and evo are the same, only one acronym shall be written. As equation 7.1 indicates, all Hamiltonians must use the same approximation[3], otherwise the mismatch in eigenstates leads to spurious oscillations in the work production (see appendix C).

We will consider two approximations, as described in table 7.1. The first, $\langle W^{NI} \rangle$, corresponds to a completely non-interacting system, the one obtained by setting $U = 0$ in the Hubbard Hamiltonian. The second approximation, $\langle W^{exact+NI} \rangle$, uses the exact many-body initial state, but approximates the Hamiltonian for the evolution of the system to be non-interacting, in accordance with the notation previously introduced[4].

7.3.2 Entropy production approximations

When approximating the entropy, we use $\langle W^{is+\text{evo}} \rangle$, while the free energy is estimated using the same assumptions as $\hat{\rho}^{is}$. This is because both $\hat{\rho}^{is}$ and Z_t (in the free energy) have a similar computational cost: they include $\exp\left(-\beta \hat{H}_t\right)$ and this term requires a computationally diagonalisable Hamiltonian. In the NI approximation, diagonalising $\hat{H}^{NI}$ is relatively easy, but then the free energy is a constant. For $\Delta S_{exact+NI}$, the exact free energy is then used (see

[3] Note that we are *not* referring to the Hamiltonian used to find $\hat{\rho}$.

[4] Although this can be considered a quench in U which has an associated work cost, we are proposing this as an approximation not a protocol, and therefore define the approximation without this cost. If one wished to implement this as a protocol, they would have to consider this work.

Acronym	NI	exact + NI
Approx.	$\langle W^{NI} \rangle$	$\langle W^{exact+NI} \rangle$
$\hat{H}^{\text{evo}}$	$\hat{H}^{NI} = - J \sum_{i\sigma}^{N} \left(\hat{c}^{\dagger}_{i,\sigma} \hat{c}_{i+1,\sigma} + h.c. \right) + \sum_{i}^{N} v_i \hat{n}_i$	$\hat{H}^{NI} = - J \sum_{i\sigma}^{N} \left(\hat{c}^{\dagger}_{i,\sigma} \hat{c}_{i+1,\sigma} + h.c. \right) + \sum_{i}^{N} v_i \hat{n}_i$
Initial state	$\hat{\rho}_0^{NI} = \exp\left(-\beta \hat{H}_0^{NI}\right) / Z^{NI}$	$\hat{\rho}_0^{exact} = \exp\left(-\beta \hat{H}_0^{exact}\right) / Z^{exact}$

Table 7.1: Types of approximations with their Hamiltonians and initial states.

figure 6.7 (a)-(c) in chapter 6) as this uses the same assumption made for calculating the initial thermal state, that the system Hamiltonian can be exactly – or very accurately – diagonalised.

7.4 Approximated results

We will firstly approximate the many-body system with a non-interacting system and use this to estimate quantum thermodynamic quantities. Afterwards we will extend this approach to include some memory of the electron-electron interaction through the system's initial state.

7.4.1 Non-interacting approximation for average quantum work

Clearly, for non-interacting (NI) systems, the average work extracted $\langle W_{ext}^{NI} \rangle$ has no dependence on U. This is shown in the upper panels of figure 7.1, where we plot $\langle W_{ext}^{NI} \rangle$ for a zigzag potential, with low (left), intermediate (middle), and high (right) temperatures. The horizontal red line shows the temperature $k_B T$ as a comparison with the interaction strength, noting how (for the exact results) the most work is extracted when the interaction strength is comparable to, or less than, the temperature. For the highest temperature, $k_B T = 20J$ is above our parameter space so the red line cannot be seen in the figures. We show the zigzag potential results as they correspond to an accuracy of the results consistently in-between those of the slope and teeth potentials (see appendix D for all results).

The lower panels of figure 7.1 show the corresponding relative error of the

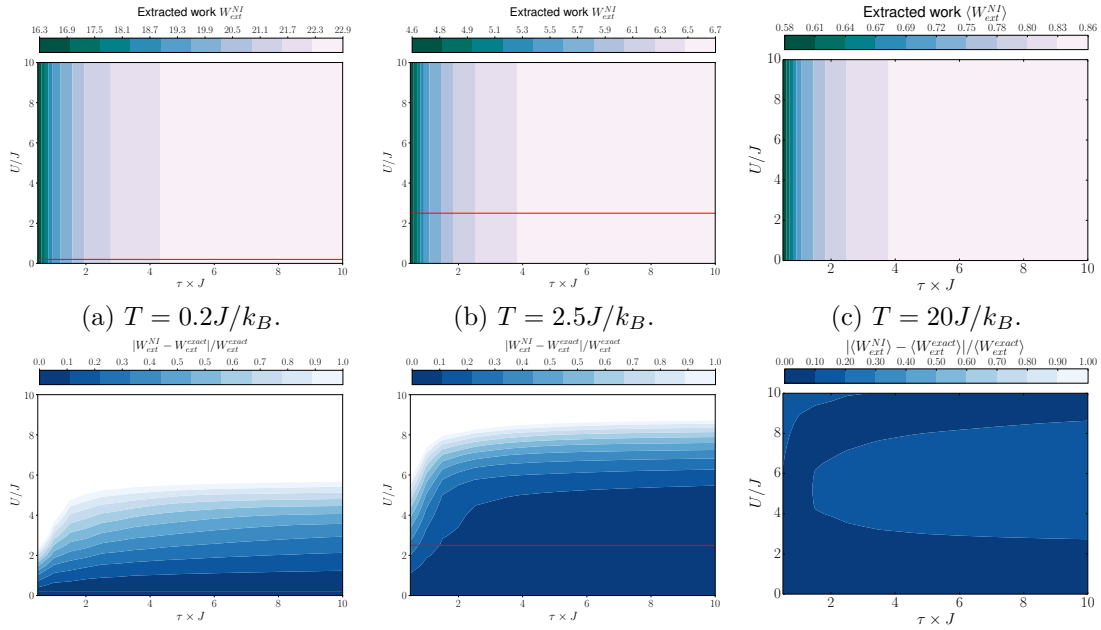

(a) $T = 0.2J/k_B$. (b) $T = 2.5J/k_B$. (c) $T = 20J/k_B$.

(d) $T = 0.2J/k_B$. (e) $T = 2.5J/k_B$. (f) $T = 20J/k_B$.

Figure 7.1: Panels (a) to (c): Work extracted in the NI approximation for 6 site chains driven by the zigzag potential. Considered regimes go from non-interacting to strongly coupled along the y-axis, and from sudden quench to nearly adiabatic along the x-axis. The lighter the colour shade, the more work is extracted, compatible with the respective value ranges indicated above each panel. Temperature increases from left to right, as indicated.
Panels (d) to (f): Relative error for $\langle W_{ext}^{NI} \rangle$ with respect to the exact results for the same parameters as the upper panels. The darker the colour, the more accurate the approximation is in that regime. The red horizontal lines show the value of $k_B T$, where for the highest temperature $k_B T = 20J$ is beyond the parameter space.

NI approximation, where the darker the blue, the more accurate the approximation is in that regime. This approximation accurately captures the work extraction only in the parameter regions where interactions are weak compared to the other energy scales. These regions include higher values of U as the temperature increases (see related discussion in section 6.3.1 in chapter 6). At the high temperature, U becomes less of an important energy scale meaning the system behaves more like a non-interacting system. Therefore we see the NI approximation becomes more accurate as temperature increases for most of the parameters sets. The range of $\langle W_{ext}^{NI} \rangle$ over the parameter space decreases with temperature (see colour scale above each panel), and at high temperature there is also very little work extracted because the thermal energy is comparable to the driving potential rendering the driving less effective. We find a similar accuracy pattern with increasing temperature for 2 site[5] and 4 site chains.

We saw in chapter 6, figure 6.2, that the smallest average work extraction occurs at high U, where the system 'freezes' and becomes a Mott insulator. Since the non-interacting approximation does not give accurate results for large U's, we see it greatly overestimating the minimum work that can be extracted. To see this, compare the range of extracted work (indicated over each panel by the colour scale) for the mid column of figure 6.2 to the corresponding upper panels of figure 7.1.

In contrast, the largest average work extraction is quantitatively captured well by the non-interacting approximation because the regions of largest work extraction are commonly found in the weak U regimes, for these systems. However the parameter regions of the largest work extraction are not captured accurately, with the non-interacting approximation struggling to encapsulate the effect of τ to a high accuracy. For example, compare the shape of the light-shade areas of the mid-column panels of figure 6.2 to the corresponding areas of the upper panels of figure 7.1. Despite this mismatch in large work extraction regions, the non-interacting approximation is still within 10% of the exact result for these small U's.

With the teeth potential, shown in appendix D, the non-interacting approximation performs better than for the zigzag potential because U only becomes a dominant energy at larger values (as discussed in section 6.3.1 of chapter 6). Therefore the non-interacting potential can accurately capture the dynamics better for a larger parameter region. As a consequence, for 6 site chains the

[5]See references [32] and [59] for 2 site chain examples, and especially [32] for 2 site non-interacting results.

teeth potential results in 10% accuracy (or better) for $U \lesssim 3J$ at low temperatures, for $U \lesssim 7J$ at intermediate temperatures, and for all regimes at high temperatures. Recall, though, that at the highest temperature the thermal energy dominates so that the system is not as sensitive to parameter changes and little work is extracted across all regimes.

The slope potential, also shown in appendix D, gives rise to results less accurate than the zigzag and teeth potentials. The improvement in accuracy as temperature increases is also not as great as that seen for zigzag and teeth potentials. With the slope potential, there is not a large potential difference between neighbouring sites (unlike the other potentials), and so U still remains relevant and is a dominating energy over the potential. Therefore, with U still very much a key ingredient in the system, the non-interacting approximation is bound to struggle and fail at smaller U's than for zigzag and teeth potentials. Indeed we see this even at high temperatures, where we get an accuracy of 10% only for $U \lesssim 3J$ in the 6 site chain.

7.4.2 'Exact initial + NI' approximation for average quantum work

As explained previously, to try and improve the estimate of the work extracted, we shall continue to implement a non-interacting evolution, but this time starting from the exact many-body initial state. The rationale is that a many-body evolution is, in general, a more challenging part of the calculation (and hence here it is approximated), while an accurate estimate for the initial state would be more readily available. This approximation is referred to as $\langle W^{exact+NI} \rangle$ in table 7.1.

Indeed this simple approximation leads to a striking improvement in the accuracy. Results are presented in figure 7.2 with $\langle W_{ext}^{exact+NI} \rangle$ in the upper three panels, and its relative error with respect to the exact results in the lower panels. The parameters are the same as in figure 7.1, and again the higher the accuracy, the darker the blue of the relative difference in the second row.

By comparing $\langle W_{ext}^{exact+NI} \rangle$ to the corresponding exact results in panels (b), (e), and (h) of figure 6.2 we see that including interactions just through the initial state is sufficient to recover the qualitative (and in great part quantitative) behaviour at low and intermediate temperatures. The greatest improvement is seen at the low temperature, where $\langle W^{exact+NI} \rangle$ recaptures the correct work to 10-20% for most regimes up to $U \approx 9J$ (unlike before where $\langle W^{NI} \rangle$ was only able to capture this accuracy for regimes up to $U \approx 2J$).

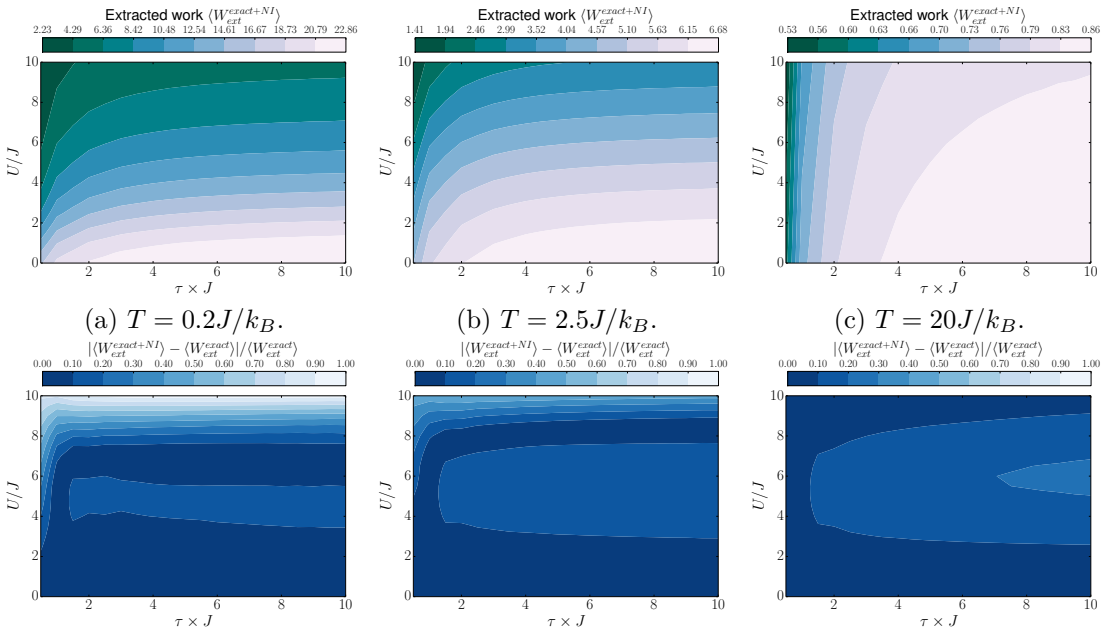

(a) $T = 0.2J/k_B$. (b) $T = 2.5J/k_B$. (c) $T = 20J/k_B$.

(d) $T = 0.2J/k_B$. (e) $T = 2.5J/k_B$. (f) $T = 20J/k_B$.

Figure 7.2: Panels (a) to (c): Work extracted in the 'exact + NI' approximation for 6 site chains driven by the zigzag potential. Considered regimes go from non-interacting to strongly coupled along the y-axis, and from sudden quench to nearly adiabatic along the x-axis. The lighter the colour shade, the more work is extracted, compatible with the respective value ranges indicated above each panel. Temperature increases from left to right panel, as indicated. Panels (d) to (f): Relative error for $\langle W_{ext}^{exact+NI} \rangle$ with respect to the exact results for the same parameters as the upper panels. The darker the colour, the more accurate the approximation is in that regime.

At the high temperature the qualitative behaviour is not recovered, but, as the work extracted varies only slightly at this temperature, quantitatively the approximation remains good overall. It reproduces rather well the overall range in the work extraction (compare the colour scale limits of figures 6.2 (b), (e), and (f) with figures 7.2 (a), (b), and (c) respectively). In general, at all temperatures the 'exact + NI' approximation significantly improves the minimum extracted average work accuracy compared to the NI value.

A similar pattern is seen in all the other systems considered, i.e. for 2 and 4 site chains, and for the teeth and slope potentials (see appendix D), demonstrating the scalability and versatility of this approximation. The $\langle W^{exact+NI} \rangle$ approximation handles weak to medium correlated systems well in all regimes and temperatures, from adiabatic to sudden quench, and from low to high temperatures. This is a vast improvement over the purely non-interacting approximation, and for still a relatively cheap computation. The success of this approximation indicates that the approximation of the work is far more sensitive to the initial conditions than it is to the evolution or final conditions.

7.4.3 'Exact + NI' using probability distributions.

We have now developed and tested this hybrid approximation, however, as section 2.4.1 in chapter 2 demonstrated, there is more than one way to calculate the average quantum work for closed systems. Because this hybrid approximation moulds together two different systems (a non-interacting one, with the exact), it is important to investigate how it could be implemented using the other method of calculating $\langle W \rangle$ (calculated using the probabilities, see equation 2.53 in chapter 2). This is especially important given the sensitivity of the results to the placement of the approximation for the evolution (especially for the Hamiltonian), found during the development of this hybrid approximation (mentioned in section 7.3.1, and demonstrated in appendix C).

We demonstrated in section 2.4.1 that, for closed quantum systems, equations 2.76 and 2.53 are equivalent. To understand the impact of the hybrid approximation, we will begin from equation 2.76 with the 'exact + NI' conditions, and by following the steps in section 2.4.1 we will see how equation 2.53 changes. The 'exact + NI' work is

$$\langle W \rangle = \mathrm{Tr}\left[\hat{\rho}_\tau^{exact+NI} \hat{H}_\tau^{NI}\right] - \mathrm{Tr}\left[\hat{\rho}_0^{exact} \hat{H}_0^{NI}\right]. \tag{7.2}$$

Now let us expand the second term, writing the trace as a sum over the non-

interacting Hamiltonian eigenstates,

$$\mathrm{Tr}\left[\hat{\rho}_0^{ex}\hat{H}_0^{NI}\right] = \sum_n \langle n_0^{NI}|\,\hat{\rho}_0^{ex}\hat{H}_0^{NI}\,|n_0^{NI}\rangle \tag{7.3}$$

$$= \sum_n \langle n_0^{NI}|\,\hat{\rho}_0^{ex}\,|n_0^{NI}\rangle\, E_{0,n}^{NI}. \tag{7.4}$$

Because we know we want to be able to write $p_{m(\tau)|n(0)}$ in some form, we can introduce the identity $\sum_m |\langle m(\tau)|\,\mathcal{U}\,|n(0)\rangle|^2 = 1$ and use $p_{n(0)} = \langle n(0)|\,\hat{\rho}(0)\,|n(0)\rangle$ and $p_{m(\tau)|n(0)} = |\langle m(\tau)|\,\mathcal{U}\,|n(0)\rangle|^2$;

$$\mathrm{Tr}\left[\hat{\rho}_0^{ex}\hat{H}_0^{NI}\right] = \sum_n E_{0,n}^{NI}\,\langle n_0^{NI}|\,\hat{\rho}_0^{ex}\,|n_0^{NI}\rangle \sum_m \langle n_0^{NI}|\,\mathcal{U}_{NI}^\dagger\,|m_\tau^{NI}\rangle\,\langle m_\tau^{NI}|\,\mathcal{U}_{NI}\,|n_0^{NI}\rangle \tag{7.5}$$

$$= \sum_{n,m} p_{n^{ex+NI}} p_{m^{NI}(\tau)|n^{NI}(0)} E_{0,n}^{NI}, \tag{7.6}$$

where $p_{n^{ex+NI}}$ is the probability of the exact state being in the n-th non-interacting eigenstate $|n_0^{NI}\rangle$ at $t = 0$.

Now turning our attention to the first term of equation 7.2, we can write

$$\mathrm{Tr}\left[\hat{\rho}_\tau^{NI+ex}\hat{H}_\tau^{NI}\right] = \sum_m \langle m_\tau^{NI}|\,\hat{\rho}_\tau^{NI+ex}\hat{H}_\tau^{NI}\,|m_\tau^{NI}\rangle \tag{7.7}$$

$$= \sum_m \langle m_\tau^{NI}|\,\hat{\rho}_\tau^{NI+ex}\,|m_\tau^{NI}\rangle\, E_{\tau,m}^{NI} \tag{7.8}$$

$$= \sum_m \langle m_\tau^{NI}|\,\mathcal{U}_{NI}\hat{\rho}_0^{ex}\mathcal{U}_{NI}^\dagger\,|m_\tau^{NI}\rangle\, E_{\tau,m}^{NI}. \tag{7.9}$$

We can now introduce the identities $\sum_n |n\rangle\langle n| = \mathbb{1}$ and $\sum_s |s\rangle\langle s| = \mathbb{1}$ to try and obtain some form of $p_n p_{m(\tau)|n(0)}$;

$$= \sum_m \langle m_\tau^{NI}|\,\mathcal{U}_{NI}\sum_n |n\rangle\langle n|\hat{\rho}_0^{ex}\sum_s |s\rangle\langle s|\mathcal{U}_{NI}^\dagger\,|m_\tau^{NI}\rangle\, E_{\tau,m}^{NI}. \tag{7.10}$$

These identities, highlighted in green, show where an issue arises; $|n\rangle$ and $|s\rangle$ need to be non-interacting to allow $\left|\langle m_\tau^{NI}|\,U_{NI}\sum_n |n_0^{NI}\rangle\right|^2 = p_{m^{NI}(\tau)|n^{NI}(0)}$ and so to match the probability in the second term. However, even if they are non-interacting, we cannot reduce the equation further towards equation 7.2 (because $\langle n_0^{NI}|\,\hat{\rho}_0^{ex}\,|s_0^{NI}\rangle \neq p_{n^{ex+NI}}$). To reduce it further, we would need to take $|n\rangle$ and $|s\rangle$ as exact eigenstates.

Let us continue with $|n\rangle$ and $|s\rangle$ as exact eigenstates (so the orthogonality of $|n\rangle$ and $|s\rangle$ can be utilised, resulting in $\langle n_0^{ex}|\,\hat{\rho}_0^{ex}\,|s_0^{ex}\rangle = \delta_{n^{ex},s^{ex}} p_{n^{ex}}$) to see

how different the result is from equation 7.2:

$$\sum_m \langle m_\tau^{NI}| \mathcal{U}_{NI} \sum_n |n_0^{ex}\rangle \langle n_0^{ex}| \hat{\rho}_0^{ex} \sum_s |s_0^{ex}\rangle \langle s_0^{ex}| \mathcal{U}_{NI}^\dagger |m_\tau^{NI}\rangle E_{\tau,m}^{NI} \tag{7.11}$$

$$= \sum_{n,m} \langle m_\tau^{NI}| \mathcal{U}_{NI} |n_0^{ex}\rangle \langle n_0^{ex}| \hat{\rho}_0^{ex} |n_0^{ex}\rangle \langle n_0^{ex}| \mathcal{U}_{NI}^\dagger |m_\tau^{NI}\rangle E_{\tau,m}^{NI} \tag{7.12}$$

$$= \sum_{n,m} p_{n^{ex}} p_{m^{NI}(\tau)|n^{ex}(0)} E_{\tau,m}^{NI}. \tag{7.13}$$

And now putting the first and second terms together gives

$$\langle W \rangle = \sum_{n,m} p_{n^{ex}} p_{m^{NI}(\tau)|n^{ex}(0)} E_{\tau,m}^{NI} - p_{n^{ex+NI}} p_{m^{NI}(\tau)|n^{NI}(0)} E_{0,n}^{NI}. \tag{7.14}$$

Highlighted in green are the terms which prevent us from factorising this formalism into one similar to equation 2.55.

So from the trace form of the average work hybrid approximation (equation 7.2), we cannot achieve the probability distribution form. However, let us try to see how the probability distribution expression would look, both mathematically and graphically. The closest equivalent form of equation 2.55 is

$$\langle W \rangle = \sum_{n,m} p_{n^{ex+NI}} p_{m^{NI}|n^{NI}} \left(E_{\tau,m}^{NI} - E_n^{0,NI} \right). \tag{7.15}$$

Figure 7.3 (a) gives the exact result for the 2 site Hubbard model at $k_B T = 2.5 J/k_B$ with the zigzag potential. Panel (b) shows the result of equation 7.15 and panel (c) shows the relative error when compared with the exact work. The results from the trace expression for these parameters are shown in panels (d) and (e). We can see when comparing figure 7.3 (b) and (c) with figure 7.3 (d) and (e) respectively that the trace method yields larger regions of higher accuracy and qualitatively captures the exact work better for this parameter set.

Now let us try to identify the difference mathematically. Expanding equation 7.15, the second term (from $E_{0,n}^{NI}$) becomes $\mathrm{Tr}\left[\hat{\rho}_0^{ex} \hat{H}_0^{NI}\right]$, but the first term (from $E_{\tau,m}^{NI}$) cannot be reduced beyond

$$\sum_{n,m} \langle m^{NI}| \mathcal{U}_{NI} |n^{NI}\rangle \langle n^{NI}| \hat{\rho}_0^{ex} |n^{NI}\rangle \langle n^{NI}| \mathcal{U}_{NI}^\dagger |m^{NI}\rangle E_{\tau,m}^{NI} \tag{7.16}$$

where the green terms highlight the difference with equation 7.10 and where $\langle n^{NI}| \hat{\rho}_0^{ex} |n^{NI}\rangle$ cannot be used to factorise into the trace expression.

The difference between the trace calculation and the $P(w)$ calculation can

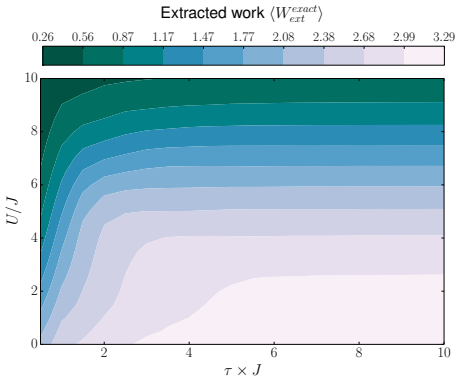

(a) The exact average quantum work extraction, $\langle W_{ext}^{exact} \rangle$.

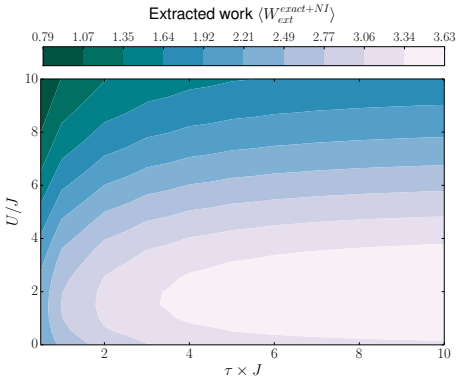

(b) $\langle W_{ext}^{exact+NI} \rangle$ using the $P(w)$ method.

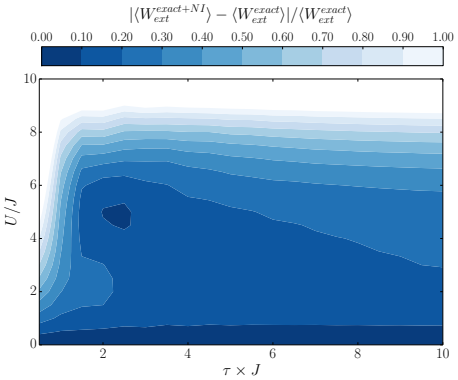

(c) Relative difference between the exact work and $\langle W_{ext}^{exact+NI} \rangle$ using the $P(w)$ method.

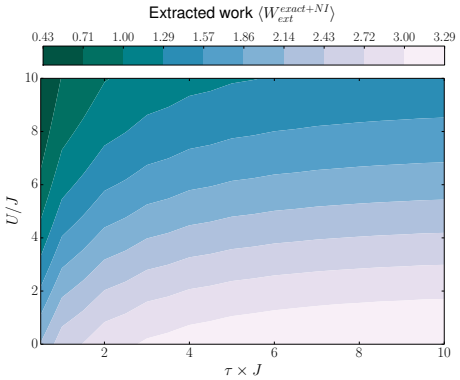

(d) $\langle W_{ext}^{exact+NI} \rangle$ using the trace method.

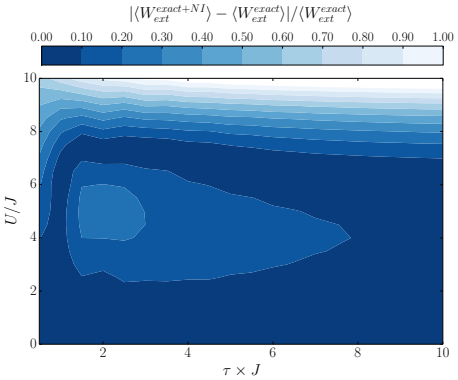

(e) Relative difference between the exact work and $\langle W_{ext}^{exact+NI} \rangle$ using the trace method.

Figure 7.3: (a) The exact average quantum work extraction for a 2 site chain with zigzag potential at $T = 2.5J/k_B$. (b) The average work extracted using $P(w)$ (from equation 2.53) for the same parameters. (c) The relative difference with the exact work for the work in (b).
(d) The average work extracted using the trace expression (from equation 2.76) for the same parameters as (a). (e) The relative difference of panel (d) with the exact work.

be written as

$$\sum_{n,m} E^{NI}_{\tau,m} \Big[\langle m^{NI}_\tau | \mathcal{U}_{NI} | n^{ex}_0 \rangle \langle n^{ex}_0 | \hat{\rho}^{ex}_0 | n^{ex}_0 \rangle \langle n^{ex}_0 | \mathcal{U}^\dagger_{NI} | m^{NI}_\tau \rangle - \langle m^{NI}_\tau | \mathcal{U}_{NI} | n^{NI}_0 \rangle \langle n^{NI}_0 | \hat{\rho}^{ex}_0 | n^{NI}_0 \rangle \langle n^{NI}_0 | \mathcal{U}^\dagger_{NI} | m^{NI}_\tau \rangle \Big] \quad (7.17)$$

where the green terms highlight why the equation cannot be reduced to the trace form. Note that the initial, $t = 0$, term cancels.

The difficulty appears when handling the initial states in the term which includes $E_{\tau,m}$: it seems challenging to match the initial probabilities in both the initial and final terms without being very careful with where the approximations are made.

And so we can see that for the hybrid approximation, care must be taken with where the approximation is applied and as to which method of calculating the work is used, as equations 2.76 and 2.53 are no longer equivalent. Certainly for closed systems, the trace method (equation 7.2) should be used as it is seen to be more accurate.

One potential explanation as to why the trace calculation is more accurate could be down to the $\langle n^{ex}_0 | \hat{\rho}^{ex}_0 | n^{ex}_0 \rangle$ term in equation 7.17. This term stems from the trace calculation and shows the initial state matches with the basis of the eigenstates. The other terms, $\langle m^{NI}_\tau | \mathcal{U}_{NI} | n^{ex}_0 \rangle$ and $\langle n^{ex}_0 | \mathcal{U}^\dagger_{NI} | m^{NI}_\tau \rangle$ do not match bases, however we have already seen (particularly in appendix C) that it is matching the initial state which is important for a more accurate approximation. When we look at the term from the $P(w)$ calculation, we see that $\hat{\rho}^{ex}_0$ does not match the non-interacting basis of $|n^{NI}\rangle$ but the evolution operator $\mathcal{U}_{NI}$ does. So although in the evolution the basis is matched, the fact the initial state is not matched once again seems to be key to it's reduced accuracy.

7.4.4 Entropy production

Using the approximated work, we can now approximate the entropy production. As seen from equation 6.2 in chapter 6, the free energy is required for the entropy. The free energy is dependent only on U, not τ, and must be approximated using the same assumptions used in the quantum work; mainly whether or not the Hamiltonian is computationally exactly diagonalisable, and therefore if the exact partition function can be used.

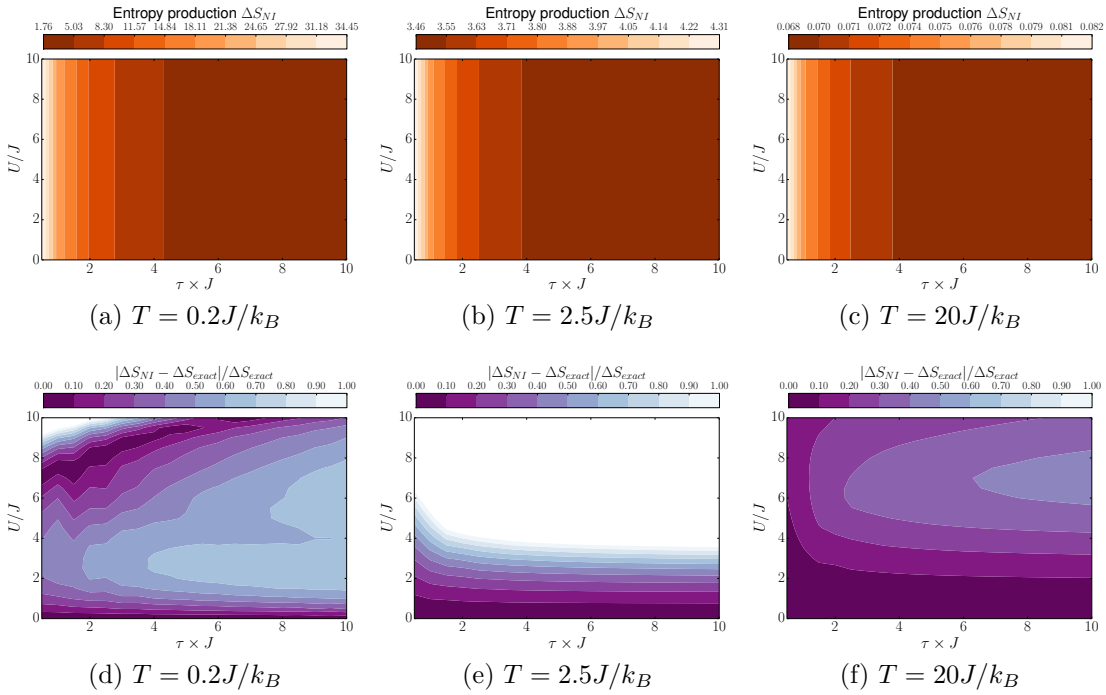

(a) $T = 0.2J/k_B$ (b) $T = 2.5J/k_B$ (c) $T = 20J/k_B$

(d) $T = 0.2J/k_B$ (e) $T = 2.5J/k_B$ (f) $T = 20J/k_B$

Figure 7.4: Upper panels: Non-interacting entropy production versus τ (x-axis) and U (y-axis) for 6 site chains with a zigzag potential. Lower panels: Non-interacting entropy production relative difference for the same parameters as the upper panels.

Non-interacting approximation

For the non-interacting approximation, we do not assume the exact Hamiltonian can be readily diagonalised and therefore we must use the non-interacting Hamiltonian in the free energy. This means the free energy no longer depends on U and is simply a constant added to the work ($U = 0J$ values are the y-intercept in figure 6.7, panels (a)-(c), in chapter 6).

Figure 7.4 presents the ΔS_{NI} results for 6 sites with zigzag potential, and increasing temperature (left to right). The upper panels show the non-interacting entropy production, and the lower ones the relative difference with the exact entropy production (the darker the purple, the more accurate the approximation is in that region).

For each given temperature, the entropy ΔS_{NI} is just $\langle W_{ext}^{NI} \rangle$ with an added constant (from the free energy). So, much like the non-interacting work, for all driving times this approximation is unable to qualitatively describe the exact entropy produced.

Comparing with the accuracy of the non-interacting approximation for the work, the overall quantitative accuracy of the entropy is in general reduced for all three temperatures. This is to be expected since we are severely approxi-

mating the free energy as well as approximating the work. As U increases we are exploring highly correlated systems, but these Coulomb correlations are completely neglected by the non-interacting approximation.

The NI approximation works better for the slope potential than for the zigzag potential at all temperatures. It gives a 10% accuracy (or better) for $U \lesssim 1.5J$ at low and intermediate temperatures and for almost all regimes at high temperatures. For the teeth potential, the accuracy of the results is comparable to the zigzag potential (see appendix D).

Overall we see that with this extra error coming from the free energy, the entropy is not as accurately captured. It is only accurately calculated in very weakly coupled systems, and cannot qualitatively describe the exact entropy.

Exact initial state with non-interacting evolution

Let us now see how considering the exact initial state affects the estimate of the entropy production. Initially the entropy $\Delta\tilde{S}_{exact+NI}$ is calculated from equation 6.2 using $\langle W^{exact+NI}\rangle = -\langle W_{ext}^{exact+NI}\rangle$ and the exact free energy variation. When using the 'exact + NI' approximation, we can assume the exact Hamiltonian can be readily diagonalised at both $t = 0$ and $t = \tau$ [6], and so we can use the exact free energy (see figure 6.7(a)-(c) in chapter 6) in the calculation of the entropy[7].

However we note that, with the implementation described above, this approximation could lead to the nonphysical occurrence of negative entropy. The two contributions to the entropy have opposite sign, and since the work has been approximated, the occurrence of a negative sign cannot be excluded. We therefore further impose that $\Delta S_{exact+NI} = \max\{\Delta\tilde{S}_{exact+NI}, 0\}$ to correct for it. At least for the systems at hand, in the regions where the further restriction is imposed, and the regions leading up to them, the accuracy of the approximation is so poor that it would not be worthwhile to use this approximation for those parameters anyway.

Related results are plotted in figure 7.5 for 6 sites with a zigzag potential, and increasing temperature (left to right). By comparing the upper panels of figure 7.5 to the upper panels of figure 7.4 and to the corresponding ones in the mid column of figure 6.7 (in chapter 6), we note a marked improvement in the qualitative behaviour of the approximation. As with the work, we can

[6] We are already assuming that we can diagonalise the initial Hamiltonian to get the exact initial state, we then make the same assumption for H_f, as this operation would have the same calculation costs/difficulties.

[7] Note that since the free energy depends on U, the entropy produced is not a simple translation of the work.

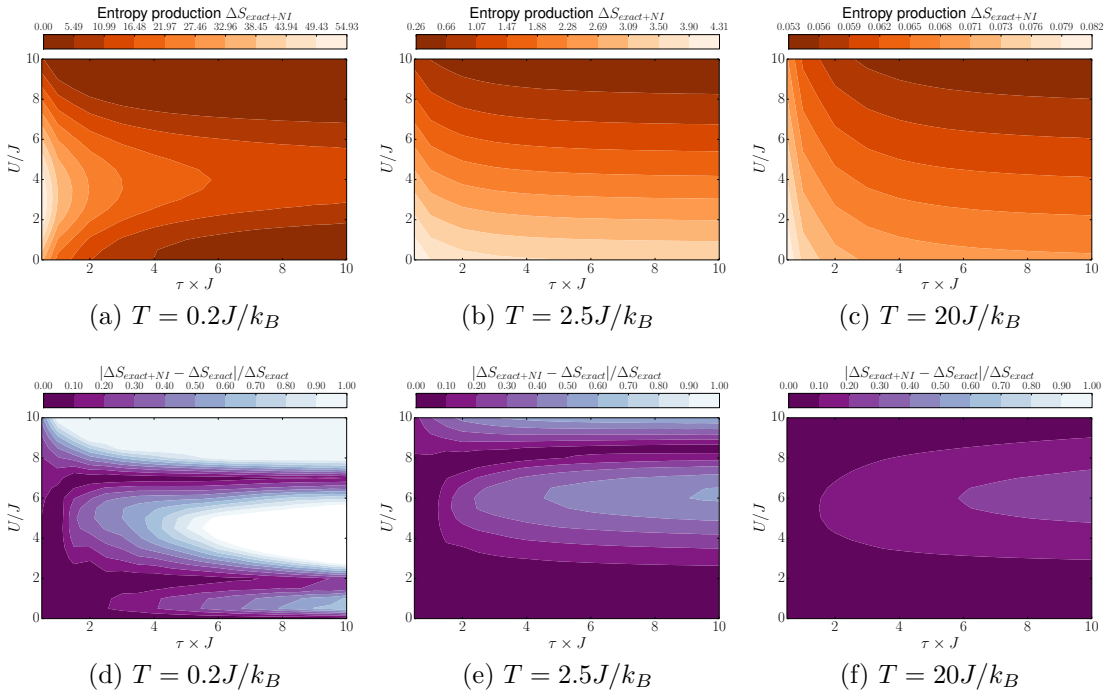

(a) $T = 0.2J/k_B$ (b) $T = 2.5J/k_B$ (c) $T = 20J/k_B$

(d) $T = 0.2J/k_B$ (e) $T = 2.5J/k_B$ (f) $T = 20J/k_B$

Figure 7.5: Upper panels: 'Exact + non-interacting' entropy production versus τ (x-axis) and U (y-axis) for 6 site chains with zigzag potential. Lower panels: 'Exact + non-interacting' entropy production relative difference for the same parameters as the upper panels.

see an improvement also in the quantitative results. The high temperature accuracy is very much akin to that of the work, and is accurate within 30% for all regimes. However, as the temperature decreases, the quantitative accuracy also decreases, with the low temperature approximation only being good in a small area at short driving times with weak interactions. This inaccuracy comes into the entropy calculations through the approximation of the average work, so the regimes of greater/lesser accuracy fairly mirror those of the work.

Results for the other two potentials (teeth and slope) confirm these trends and are shown in appendix D. Similarly to the zigzag potential, the 'exact + NI' approximation with the teeth and slope potentials recovers to a good extent the qualitative behaviour of ΔS_{exact} for low and intermediate temperatures. For high temperatures the qualitative behaviour is recovered only for $U \lesssim 2J$. Quantitatively, the areas of worse performance are related to the areas of worse performance for the corresponding $\langle W_{ext}^{exact+NI} \rangle$, however the approximation performs worse for $\Delta S_{exact+NI}$ than $\langle W_{ext}^{exact+NI} \rangle$ for teeth, and better for slope. In general the approximation improves its quantitative performance with temperature as it reproduces well the limits of the entropy production range, and especially so at high temperature.

Overall the approximation improves its quantitative performance compared

to the NI approximation, and while the results are not as accurate as for the work, they are still accurate in a wide span of regimes, increasing in accuracy as the temperature increases. The limits of entropy produced are also captured well by the approximation.

7.5 Conclusion

In this chapter we have studied simple non-interacting style approximations for quantum work and entropy production in many-body interacting systems. Although the basic non-interacting approximation has very limited regions of high accuracy in our parameter space, we have demonstrated that when the initial state is taken to be exact and the evolution is crudely approximated with the non-interacting system, the results are markedly improved in their accuracy. This computationally cheap but surprisingly accurate hybrid approximation could potentially be used to find better and more efficient operational regimes for systems where the exact solutions are inaccessible, particularly for Hubbard-like devices working at correlation strengths less than or comparable to the temperature.

The purely non-interacting approximation highlights the strong effect of the Coulomb interaction on the extracted average quantum work. By comparing exact results to the corresponding non-interacting approximations, apart from the obvious independence on U for all regimes, this approximation strongly overestimates the smallest average work extracted from a system. This is because it cannot reproduce the freezing of the system dynamics which is a result of the strong many-body correlations. On the other hand, the largest average work extracted is well captured, although it is often attributed to the wrong parameter regions (mainly in τ).

Including many-body interactions exactly for complex systems is often a hopeless task. In this work we have proposed a relatively simple approximation which relies on being able to provide an accurate approximation for the system's initial state, while interactions are completely neglected in the dynamics. This approximation provides accurate results in a wide range of parameters, although it may not always be accurate at low temperatures or with comparatively high interaction strengths for quantum devices (see table 7.2 below for valid ranges).

Compared to the non-interacting approximation, we found that this hybrid approximation behaves surprisingly well. By including interactions just through the initial state, the qualitative (and in great part quantitative) be-

haviour is recovered at low and intermediate temperatures for all regimes, potentials, and system sizes considered. The greatest improvement is seen at low temperatures; for example, when considering the zigzag potential, the 'exact + NI' approximation reproduces the exact work within 10-20% up to very strong interactions ($U \approx 9J$) for most regimes, whereas the non-interacting approximation only manages this accuracy for weak interactions ($U \approx 2J$). At all temperatures, the 'exact + NI' approximation reproduces reasonably well the range of the average extracted quantum work across the parameter space (see colour scales above the related figures). In particular it significantly improves the minimum value compared to the non-interacting approximation.

We also compared the two methods of calculating the average work extraction outlined in chapter 2. This hybrid approximation results in these two methods no longer being equivalent. Therefore care must be taken when applying the 'exact + NI' approximation to a closed system, where we recommend the use of the trace method over the probabilities method, as it has been seen to yield much higher accuracy in most regions.

When looking at the entropy, using the approximated work, the fully non-interacting approximations strongly under-perform, both qualitatively and quantitatively. However, at high temperatures the exact entropy production range becomes very small, and the quantitative non-interacting approximation is crudely correct due to the decreased influence of many-body interactions. As a result, at high temperatures even the non-interacting approximation gives reasonable quantitative (but not qualitative) results.

When we extend the 'exact + NI' approximation to the entropy production, we find qualitative improvements similar to the work extraction, with the behaviour for low and intermediate temperatures largely recovered. Quantitatively this approximation significantly improves over the non-interacting approximation, albeit not as strikingly as for the average quantum work. For example, at high temperature and with a teeth potential, this approximation would reproduce exact results within 10% for all parameter ranges, in contrast to the performance by the non-interacting approximation which gives such an accuracy only for $U \lesssim 3J$. Overall the 'exact + NI' approximation improves its quantitative performance with temperature, and it captures the entropy production range well.

In general we can summarise the regions in which it would be suitable to use the approximations through table 7.2. Here we take 20% as a good approximation, and look at the zigzag potential.

Our results show that, even when taking a very crude approximation for

Approx.	T	U	τ
$\langle W^{NI} \rangle$	low T	low; $U \leq 1J$	all τ's
$\langle W^{NI} \rangle$	mid T	low-mid; $U \leq 5J$	all τ's
$\langle W^{NI} \rangle$	high T	all U	all τ's
$\langle W^{ex+NI} \rangle$	low T	low-high; $U \leq 8J$	most; $\tau > 0.75/J$
$\langle W^{ex+NI} \rangle$	mid T	low-high; $U \leq 9J$	all τ's
$\langle W^{ex+NI} \rangle$	high T	all U bar $U \approx 6J$ at long τ	all bar $\tau > 7/J$ for mid U
ΔS_{NI}	low T	low; $U \leq 1J$	all τ's
ΔS_{NI}	mid T	low; $U \leq 1J$	all τ's
ΔS_{NI}	high T	low-mid; $U \leq 4J$	all τ's
ΔS_{ex+NI}	low T	low; $U \leq 2J$	short; $\tau < 3/J$
ΔS_{ex+NI}	mid T	low-mid; $U \leq 4J$	all τ's
ΔS_{ex+NI}	high T	all U bar $U \approx 6J$ at long τ	all bar $\tau > 6/J$ for mid U

Table 7.2: Table summarising the regions where the approximations would be valid for work extraction and entropy production in systems with a zigzag-like potential.

the evolution operator, starting from an accurate initial state is sufficient for greatly improving the estimate of thermodynamic quantities such as the average quantum work and the corresponding entropy production for the wide range of potentials, temperatures, and a great part of the interaction and dynamic regimes considered.

Let us now try to make this hybrid approximation more sophisticated, and take inspiration from DFT to consider the evolution more accurately.

8. Density Functional Theory approaches to quantum thermodynamic properties

Given the success of the hybrid approximation developed in the previous chapter, we now aim to develop a more sophisticated hybrid approximation. To do this we turn back to density functional theory (DFT) to (cheaply) include knowledge of the initial interactions within the evolution. Therefore we can address research question 2c: "Can we improve the approximations from point 2b using DFT?" in this chapter.

8.1 Introduction

From previous chapters, we have seen why many-body systems are of vital importance to the progression of quantum technologies as well as for developing the understanding of fundamental physics. We have also seen that as the size of a many-body interacting system increases, the computational cost in the calculation increases exponentially. Methods of addressing these many-body systems have been alluded to in previous chapters (namely DFT) but it is in this chapter where we will explicitly use DFT to develop approximations for quantum thermodynamic properties. Previous work has demonstrated the applicability of DFT to quantum thermodynamics [32, 59], but here we take DFT approximations, combine them with the hybrid approach from chapter 7 [138], and explore the resulting approximations for many-body systems, up to 6 sites. This proposal for a DFT-based set of approximations is, ideally, applicable to systems of higher complexity.

DFT is, in principle, an exact method of calculating properties of many-body systems, and was proposed by Hohenberg and Kohn in 1964 [74]. They demonstrated that any property of a ground state system can be, in theory,

calculated through the ground state density. This means that properties of complex many-body systems, for which the wavefunction is too large to handle, can be found using their density, which is a much simpler quantity both computationally and experimentally.

To find the ground state density of a given system, Kohn and Sham developed a method which mapped the interacting system to a fictitious non-interacting system whose potential is adjusted in such a way to reproduce the many-body interacting ground state density [76]. In practice, finding the density of the many-body system through this Kohn-Sham system usually requires some approximation to be made. This has led to a plethora of DFT approximations, each one designed to suit a given set of parameters [61, 63, 151, 152]. One of the most commonly used approximations is the local density approximation (LDA), which is often used to represent slowly varying continuous systems close to a homogeneous electron gas [76, 153]. An extension of the LDA, away from the homogeneous electron gas to other model systems, is the Bethe Ansatz LDA (BALDA) developed by Lima *et al.*, who originally used the Hubbard model in place of the homogeneous electron gas [72]. In this work we shall use BALDA to approximate quantum thermodynamic properties in many-body systems out-of-equilibrium.

The other DFT approximation we shall use is to take the exact initial Kohn-Sham system by reverse engineering the exact density at the initial time to find the Kohn-Sham potential. The reverse engineering scheme we use was developed in reference [132] for ground state lattice systems at zero temperature. Other work has begun to explore reverse engineering the thermal density to find the Kohn-Sham system at low temperatures (where the temperature is much less than the electron-electron interaction strength) [60, 154, 155]. They found that the exact Kohn-Sham system at low temperatures is remarkably similar to the ground state (zero temperature) Kohn-Sham system. Therefore in this chapter we will use the well established ground state reverse engineering scheme to find the exact $T = 0J/k_B$ Kohn-Sham system, which we will then use to approximate the dynamics of the system when calculating the quantum thermodynamic properties at $T \neq 0J/k_B$.

Much like in chapter 7, we will use the parameter set from section 6.2.2 to test these DFT-hybrid approximations against the exact results from chapter 6. The BALDA-based approximations give us a rough lower bound to the accuracy of approximating the quantum work and entropy production in this manner, whilst the exact Kohn-Sham-based approximations give an estimate of the upper bound.

8.2 Theory

8.2.1 Density Functional Theory

We saw in chapter 2 that DFT is extremely useful for enabling calculations of properties of many-body interacting systems which otherwise would be practically unachievable. One of the key aspects of DFT is the Hohenberg-Kohn theorem, which demonstrates there is a one-to-one mapping between a system's ground state wavefunction, its ground state density, and its external potential [74]. From this density we can then, in theory, find all other properties of the ground state system. We can then ask: how can one find this ground state density in the first place? This is where the other key idea in DFT becomes relevant: the Kohn-Sham theory.

Kohn-Sham theory

The Kohn-Sham theory shows that by using a fictitious non-interacting system with an adjusted potential (the Kohn-Sham system), one can achieve the same ground state density as the fully interacting system [76]. This is important because it reduces the hard-to-solve many-body interacting system to a system of N single electrons, which is less complex.

The Kohn-Sham system takes the fully interacting Hamiltonian

$$\hat{H} = \hat{T} + \hat{U} + \hat{V}_{ext}, \tag{8.1}$$

removes the interaction $\hat{U}$ and replaces the external potential $\hat{V}_{ext}$ with a corrected potential which partially includes the effect of the interactions. This means the Kohn-Sham Hamiltonian is

$$\hat{H}_{KS} = \hat{T} + \hat{V}_{KS}, \tag{8.2}$$

where $\hat{T}$ is the same kinetic energy operator, and

$$\hat{V}_{KS} = \hat{V}_{ext} + \hat{V}_H + \hat{V}_{xc}. \tag{8.3}$$

Here we have introduced two new potentials which correct the external potential so the final potential incorporates some effects of the original many-body interactions, enough to obtain the same ground state particle density. The first potential is the Hartree potential, $\hat{V}_H$, which introduces an average, direct electron-electron Coulomb repulsion. The second potential is the

exchange-correlation potential, $\hat{V}_{xc}$, which includes corrections due to all other many-body interaction effects (for example the Pauli exclusion principle).

Although DFT is, in principle, exact, when it is put into practice approximations must be made. The exchange-correlation potential of the Kohn-Sham system is often not known exactly, and so one must take an appropriate approximation for $\hat{V}_{xc}$. Despite this need for approximations, DFT is widely used not only in physics but also in chemistry and biology [61, 66–69]. Because of its widespread use, there is a sea of formulations of DFT, each adaptation allowing the application of DFT to a wide range of systems (for example, one can use time-dependent DFT (TDDFT) for time-dependent systems [71], or current DFT (CDFT) for systems with a magnetic field [65]).

Given that in this chapter we will continue to use the Hubbard model, the flavour of DFT we will use is the site-occupation functional theory (SOFT) [72, 73]. SOFT replaces the continuous density with the site occupation $n_i = \langle \sum_\sigma \hat{c}^\dagger_{i,\sigma} \hat{c}_{i,\sigma} \rangle$ for site i in the lattice. The Hartree potential is then written as $\hat{V}_H = \sum_i \hat{v}_{H,i} = \sum_i U\hat{n}_i/2$, and is an average electron-electron on-site interaction [62].

Each formulation of DFT comes with its own ever-increasing choice of approximations[1]. In this work we will focus on the Bethe-Ansatz LDA (BALDA), and on using a reverse engineering scheme to find the exact exchange-correlation potential.

BALDA

The Bethe Ansatz LDA (BALDA) uses the same principle as the LDA, looking at local densities assuming the system is locally homogeneous, rather than including any gradients or derivatives of the density like the generalised gradient approximation [61, 157]. However, instead of taking the homogeneous electron gas as the model system, it shifts the focus to other model systems, looking at systems on a lattice. These other model systems still allow the approximation to assume a locally homogeneous density, but they take into account the correlations that would be present in the corresponding inhomogeneous system [72]. Therefore BALDA assumes the density does not change too rapidly across the chain, allowing it to identify small volumes of uniform density. To

[1]Reference [156] points out that there is a lack of approximations for the exchange-correlation potential at finite temperature, and derives conditions for creating these approximations. So although we only use ground state (zero temperature) approximations for $\hat{V}_{xc}$ in this thesis (shown to be appropriate up until a critical temperature by references [60, 155]), there is the hope that appropriate approximations for $\hat{V}_{xc}$ at finite temperature will be generated and future work can then look at implementing them in this scheme.

approximate $\hat{V}_{xc}$ using BALDA, where we take $\hat{V}_{xc} \approx \hat{V}_{BALDA} = \sum_i v_{BALDA,i}$, we write

$$v_{BALDA,i} = 2\cos\left(\frac{\pi n_i}{\zeta(U)}\right) \tag{8.4}$$

where $\zeta(U)$ for any given value of U is found from

$$-\frac{2\zeta}{\pi}\sin\left(\frac{\pi}{\zeta}\right) = -4\int_0^\infty \frac{J_0(x)J_1(x)}{x\left[1+\exp\left(Ux/2\right)\right]}dx \tag{8.5}$$

with J_0 and J_1 the zero and first order Bessel functions respectively [72].

The systems we use in this study present many challenges to BALDA, mainly testing the handling of strongly non-uniform densities. We use short chain systems where the boundary conditions impact the system to a greater extent than in longer chains, and the potential we apply across the system is non-uniform, often strongly so. Both of these factors reduce the homogeneity of the system. Further to this, BALDA was developed upon the exact Bethe Ansatz solution to the Hubbard model in the thermodynamic limit [72] so it cannot be expected to perform well in small systems. On top of these factors, we increase the coupling strength U so the systems are very strongly correlated; a regime in which all approximations of $\hat{V}_{xc}$ struggle. BALDA particularly struggles beyond intermediate coupling regimes at half filling due to the discontinuity in the exchange-correlation potential. This discontinuity is an important feature for $\hat{V}_{xc}$ as it captures the transition from the metal phase to the Mott insulator with increasing correlation strength [62].

The combination of all these factors makes our systems incredibly hard for BALDA to accurately capture. Therefore we take BALDA as a poor approximation to the $\hat{V}_{xc}$ in our systems, providing an estimate to the lower bound of the accuracy of the approximations for the quantum thermodynamic properties. Let us now look at an approximation which can act as an upper bound to the accuracy.

Inversion scheme for $\hat{V}_{xc}$

The systems we have looked at so far in this thesis have all been numerically exactly solvable, primarily to enable us to test the approximations we formulate. However there is another benefit of having the exact solution to the system; we can reverse engineer the density to find the exact exchange-correlation potential at the initial time [60, 132, 154, 158]. By finding the exact $\hat{V}_{xc}$, we can gain an indication of the upper bound to the accuracy of

the approximation style presented[2].

The reverse engineering scheme we follow in this work was developed by Coe *et al.* in reference [132]. The scheme is an iterative process which begins with an initial guess of the density[3] and takes the initial $\hat{V}_{xc} = 0$. In this way the initial Kohn-Sham Hamiltonian is $\hat{H}^0_{KS} = \hat{T} + \hat{V}_{ext} + \hat{V}_H$, where the initial guess of the density is used to calculate the Hartree potential. This Kohn-Sham Hamiltonian is then solved to give new estimates of the ground state energy, E, and density. We take the Kohn-Sham potential to be $\hat{V}_{KS} = \sum_i v_{KS,i}\hat{n}_i$. The next iteration $(j+1)$ of the potential is then found by

$$v^{j+1}_{KS,i} = \xi v^j_{KS,i} + (1-\xi)\,\frac{\left(n^j_i - n^{exact}_i\right)|E^j|}{n^{2,j}_i}, \tag{8.6}$$

where j gives the iteration step, i gives the site number in the lattice, and ξ is the mixing parameter between new and old potentials to reduce the chance of numerical instabilities[4]. Here we have written $n^j_i = \langle\Psi^j|\,\hat{n}_i\,|\Psi^j\rangle$ and $n^{2,j}_i = \langle\Psi^j|\,\hat{n}^2_i\,|\Psi^j\rangle$. Note that $\hat{H}^j_{KS}\,|\Psi^j\rangle = E^j\,|\Psi^j\rangle$. This process is repeated until it has converged such that $v^{j+1}_{KS,i} = v^j_{KS,i}(\pm$ convergence limit): we set a numerical threshold for the convergence, for example 10^{-6} was used for these results, and if the difference between the new potential and the previous potential is below this limit we say the calculation has converged. This potential is therefore the one which gives the target ground state density when using the many-body Schrödinger equation [132][5]. A graphical representation of this scheme is shown in figure 8.1.

The reverse engineering code for finding the exact $\hat{V}_{xc}$ was written by K. Zawadzki as part of her suite of codes outlined in chapter 3. Implementing the exact $\hat{V}_{xc}$ and corresponding hybrid approximation in the quantum work code was done by myself.

Other works have also shown the ability to reverse engineer the exact density of lattice systems to find the exact $\hat{V}_{xc}$ [60, 154]. Indeed reference [60] demonstrated the ability to reverse engineer the density to find the exact $\hat{V}_{xc}$

[2]By approximation style, we mean using a ground state, time-independent, DFT approximation for the initial potential used in the driving Hamiltonian, then combined with the exact initial state in the calculation of the quantum work. Note that the only time-dependent term in the driving Hamiltonian is the external potential $\hat{V}_{ext}$.

[3]This parameter is chosen by the user, and alongside the convergence limit and new-old mixing parameters, gives us variables we can adjust to achieve the exact $\hat{V}_{xc}$.

[4]Typically we use $0.8 \leq \xi \leq 0.9995$, where for some cases the mixing must be this small because the systems are very sensitive.

[5]Note that the final $\hat{V}_{KS}$ is the full system potential which contains the external potential, $\hat{V}_{ext}$, the Hartree potential, $\hat{V}_H$, and the exact exchange correlation potential, $\hat{V}_{xc}$. To then find explicitly the exact $\hat{V}_{xc}$, one must subtract $\hat{V}_{ext}$ and $\hat{V}_H$ from $\hat{V}_{KS}$ (see equation 8.3).

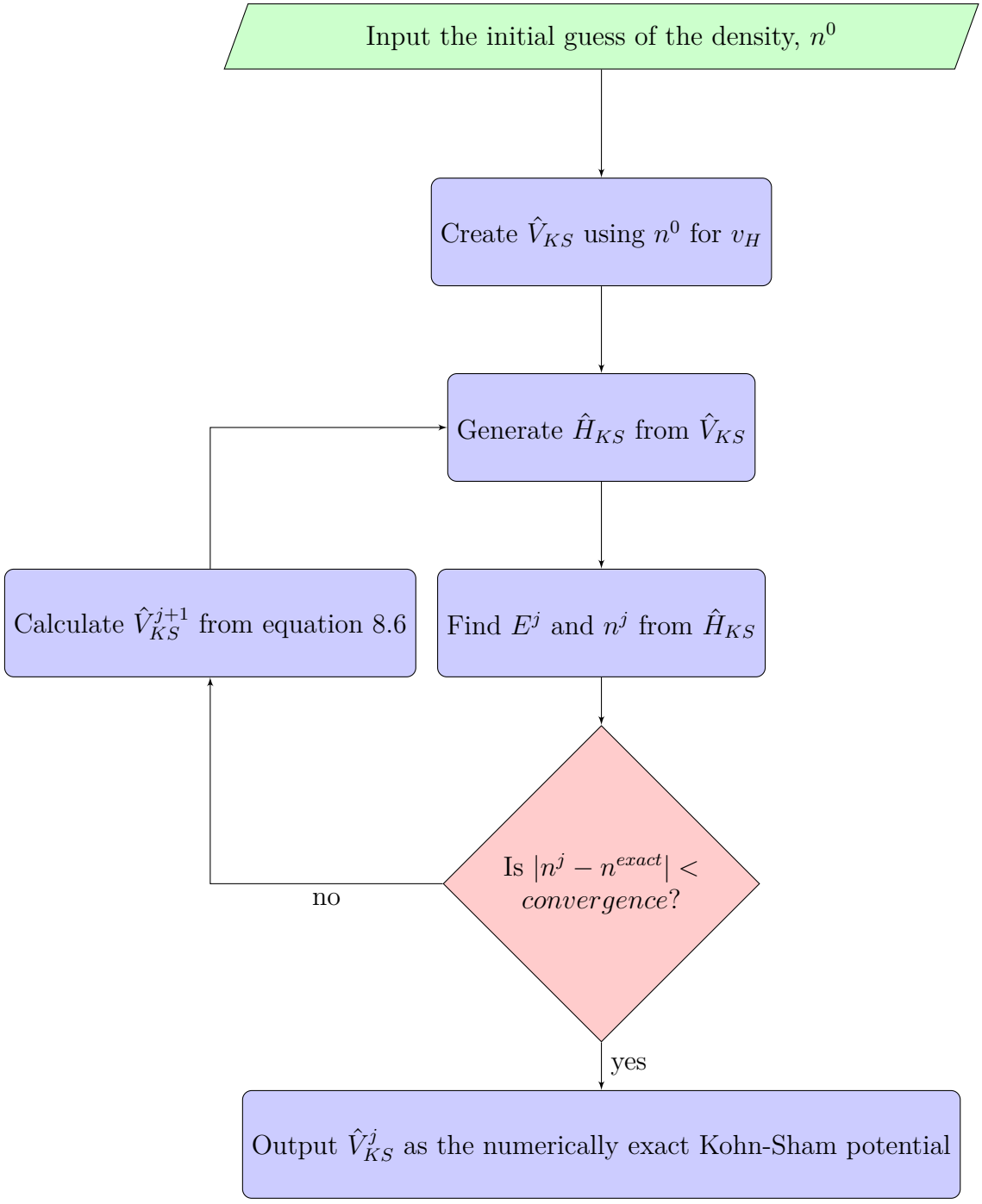

Figure 8.1: Flow chart demonstrating the reverse engineering scheme detailed in reference [132].

for a weakly correlated Hubbard dimer (2 sites) at low to medium temperatures. In fact both reference [60] and [155] found that the exchange-correlation potential for systems below a critical temperature $T_c \ll U$ matched remarkably well with the exact ground state $\hat{V}_{xc}$. Therefore, although the reverse engineering scheme we are implementing here is for the ground state system, we can use it for low temperatures with confidence, and even stretch it to medium temperatures. The high temperature system is not expected to be accurately calculated by the Hamiltonian with the exact ground state $\hat{V}_{xc}$, but we will use this temperature with the exact ground state $\hat{V}_{xc}$ approximations (see table 8.1, v_{xc} and 'exact + v_{xc}' columns) to test this approximation style further.

8.2.2 Applying DFT to the hybrid approximation for quantum thermodynamics

Our aim in this chapter is to create more sophisticated approximations in the same style as the hybrid approximation developed in chapter 7. We shall do this by applying the DFT approximations described in the previous section to the driving Hamiltonian at $t = 0$. By doing this, we are partly incorporating interactions into the evolution of the system (via this driving Hamiltonian), but we are keeping the calculation "cheap" because the DFT calculations are included only at the ground state level and at the initial time. This is therefore still a crude approximation of the interacting dynamics, but we can still analyse the impact of considering some interactions for the dynamics versus not considering them at all, like the NI approximation, or only including them through the initial state like the 'exact + NI' approximation.

In line with the previous chapter, to calculate the average quantum work we will consider the DFT-style approximations purely by themselves, and afterwards we shall introduce the exact initial state (as described in section 7.3 of chapter 7). The application of the DFT approximations to the quantum work is via the driven Hamiltonian. This means that $\hat{H}^{\text{evo}}(t)$ used in the evolution operator $\mathcal{U}$, and in the calculation of the average quantum work extraction (equation 7.1) at $t = 0$ and $t = \tau$ becomes

$$\hat{H}^{\text{evo}}(t) = -J \sum_{i\sigma}^{N} \left(\hat{c}^{\dagger}_{i,\sigma} \hat{c}_{i+1,\sigma} + h.c. \right) + \sum_{i}^{N} v_{KS,i}(t) \hat{n}_i, \tag{8.7}$$

with

$$v_{KS,i}(t) = v_{ext,i}(t) + v_{H,i} + v_{xc,i}. \tag{8.8}$$

Note that the only time-dependent part of the Hamiltonian is the external potential. The $v_{xc,i}$ and $v_{H,i}$ are only calculated for the initial time as derived from the ground state theory.

For the BALDA calculations, $v_{xc,i}$ is approximated using BALDA as defined in equation 8.4, and for the exact $\hat{V}_{xc}$ [6], $v_{xc,i}$ is calculated using the reverse engineering scheme outlined before. Table 8.1 shows the approximations to the quantum work addressed in this chapter, their abbreviations, Hamiltonians, and initial state.

Acronym	BALDA	exact + BALDA
Approx.	$\langle W^{BALDA} \rangle$	$\langle W^{exact+BALDA} \rangle$
$\hat{H}^{\text{evo}}$	$\hat{H}^{BALDA} = - J \sum_{i,\sigma}^{N} \left(\hat{c}_{i,\sigma}^{\dagger} \hat{c}_{i+1,\sigma} + h.c. \right) + \sum_{i}^{N} \left(v_{ext,i} + v_{H,i} + v_{BALDA,i} \right) \hat{n}_i$	$\hat{H}^{BALDA} = - J \sum_{i,\sigma}^{N} \left(\hat{c}_{i,\sigma}^{\dagger} \hat{c}_{i+1,\sigma} + h.c. \right) + \sum_{i}^{N} \left(v_{ext,i} + v_{H,i} + v_{BALDA,i} \right) \hat{n}_i$
Initial state	$\hat{\rho}_0^{BALDA} = \frac{\exp\left(-\beta \hat{H}_0^{BALDA}\right)}{Z^{BALDA}}$	$\hat{\rho}_0^{exact} = \frac{\exp\left(-\beta \hat{H}_0^{exact}\right)}{Z^{exact}}$
Acronym	v_{xc}	exact + v_{xc}
Approx.	$\langle W^{v_{xc}} \rangle$	$\langle W^{exact+v_{xc}} \rangle$
$\hat{H}^{\text{evo}}$	$\hat{H}^{v_{xc}} = - J \sum_{i,\sigma}^{N} \left(\hat{c}_{i,\sigma}^{\dagger} \hat{c}_{i+1,\sigma} + h.c. \right) + \sum_{i}^{N} \left(v_{ext,i} + v_{H,i} + v_{xc,i} \right) \hat{n}_i$	$\hat{H}^{v_{xc}} = - J \sum_{i,\sigma}^{N} \left(\hat{c}_{i,\sigma}^{\dagger} \hat{c}_{i+1,\sigma} + h.c. \right) + \sum_{i}^{N} \left(v_{ext,i} + v_{H,i} + v_{xc,i} \right) \hat{n}_i$
Initial state	$\hat{\rho}_0^{v_{xc}} = \frac{\exp\left(-\beta \hat{H}_0^{v_{xc}}\right)}{Z^{v_{xc}}}$	$\hat{\rho}_0^{exact} = \frac{\exp\left(-\beta \hat{H}_0^{exact}\right)}{Z^{exact}}$

Table 8.1: The types of approximations addressed in this chapter with their evolution Hamiltonians and initial states. Z^{BALDA} is the partition function calculated using $\hat{H}^{BALDA}$, and similarly $Z^{v_{xc}}$ uses $\hat{H}^{v_{xc}}$, and Z^{exact} uses $\hat{H}^{exact}$.

We will also address the entropy production results found using these approximations, using the same technique as described in section 7.3 of chapter 7.

[6] Denoted simply by v_{xc} when referred to in the approximated quantum thermodynamic properties, and not to be confused with the hybrid approximation of 'exact + v_{xc}'.

Again we will use the approximated quantum work extraction for the entropy production, but this time the free energy will use the Hamiltonian with the corresponding DFT approximation for the BALDA and v_{xc} calculations. For the 'exact + evo' calculations, the exact free energy will be used, using the same logic as in section 7.3, i.e. that if we can use the exact initial state, the Hamiltonian must be computationally diagonalisable, and therefore the exact partition function can be found for the free energy.

8.3 Approximated quantum work results

Much like in chapter 7, we will focus on 6 site chains with the zigzag potential and use the same parameter set as outlined in section 6.2.2 (see appendix D for the full set of results, including the 'teeth' and 'slope' potentials). This then allows us to directly compare not only these DFT-inspired results, but also to compare the approximations themselves. From this we will be able to determine if including interactions via DFT techniques indeed improves the accuracy of the hybrid approximation.

8.3.1 BALDA work extraction

As discussed, by using BALDA to approximate this system, we can assess a lower limit to these types of techniques for approximating quantum thermodynamic properties.

Figure 8.2 shows the average quantum work (top row) extracted across our parameter set for the three temperatures used when implementing BALDA as described in section 8.2.2. We compare these results to panels (b), (e), and (h) of figure 6.2 to get the relative differences shown in the bottom row.

As mentioned before, BALDA assumes a slowly varying system, which we do not have here, and as U increases, double site occupation is discouraged, forcing the electrons into the higher energy sites. This exacerbates the non-uniformity of the density across the system. Indeed we see that BALDA is only able to quantitatively capture the work accurately at low U, performing well for a metallic system with an accuracy up to $\sim 20\%$. However, as soon as the precursor to the phase transition is reached at $U \approx 4J$, the accuracy reduces greatly for most τ's at all temperatures. As U increases further to $U \gtrsim 6J$, work then needs to be performed *on* the system to achieve the driven dynamics for all temperatures.

Due to this negative work extraction at higher U's, the exact minimum

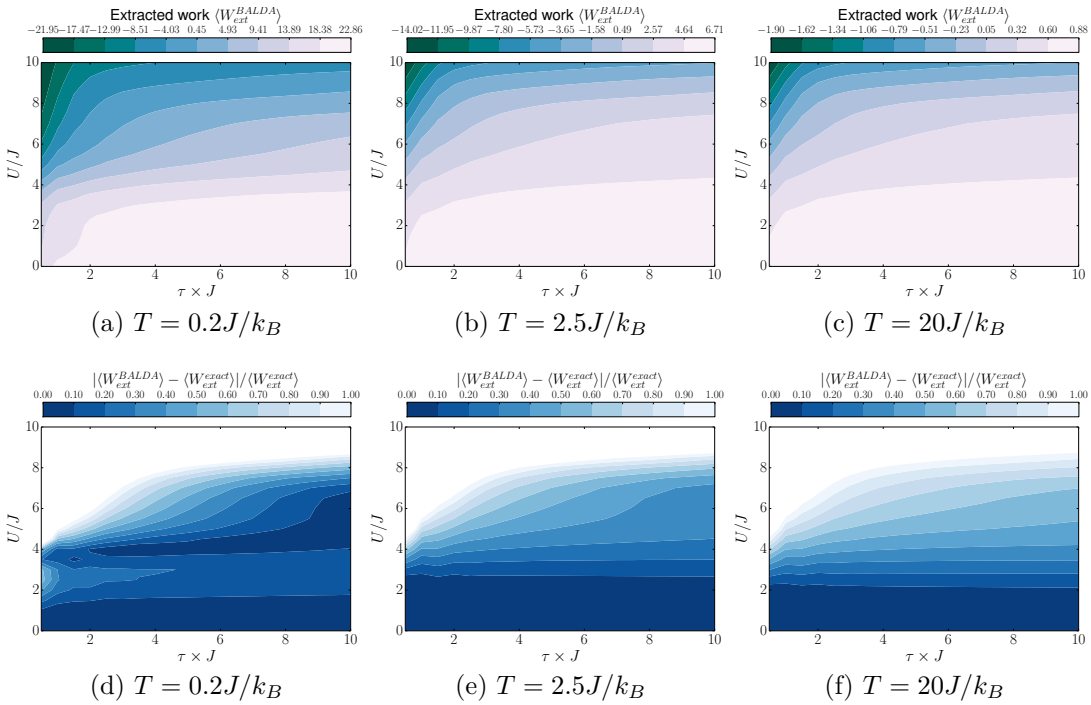

(a) $T = 0.2J/k_B$ (b) $T = 2.5J/k_B$ (c) $T = 20J/k_B$

(d) $T = 0.2J/k_B$ (e) $T = 2.5J/k_B$ (f) $T = 20J/k_B$

Figure 8.2: Upper panels: Work extracted using BALDA for $0.5 \leq \tau \times J \leq 10$ (x-axis) and $0 \leq U/J \leq 10$ (y-axis) for 6 site chains with zigzag potential, increasing temperature from left to right (the lighter shade corresponds to greater work extracted). Lower panels: Relative difference between the BALDA work and the exact results for the same parameters as the upper panels (the darker shade corresponds to higher accuracy).

work extraction across this parameter set is not captured well by BALDA (see the colour bar above each panel). However, the maximum work extracted is approximated accurately with BALDA. As we saw in chapter 6, the maximum work extracted is achieved for very weakly correlated systems, and so all of the approximations studied in this thesis capture the maximum work extraction well.

For low temperatures, BALDA shows an improvement over the completely non-interacting approximation from chapter 7, but this improvement is lost as the temperature increases. This could be attributed to the fact that BALDA is a ground state (and hence zero temperature) approximation, whereas when the temperature increases higher energy states are populated and so a ground state approximation is less reliable. Therefore BALDA would be more appropriate at a lower temperature than a higher temperature, especially in comparison to the non-interacting system which is closer to the exact behaviour of the high temperature system.

For all temperatures, BALDA is consistently quantitatively accurate within 20% of the exact results for $U \lesssim 3J$. Let us now see if including the exact initial state through the hybrid approximation outlined in table 8.1 improves the accuracy in more regions.

8.3.2 'Exact + BALDA' work extraction

Figure 8.3 shows the results for the average work extracted using the 'exact + BALDA' approximation (top row), and the relative difference (bottom row) for our parameter set. By including the exact initial state, the quantitative accuracy is similar across all temperatures, however we do not see the improvement in the accuracy that was seen when going from the non-interacting to 'exact + NI' approximations. Still, for the quasi-sudden quench regime, the accuracy is improved for higher correlation strengths (10% accuracy up to $U \approx 4J$ compared to up to $U \approx 2J$ for BALDA).

The qualitative accuracy has improved for 'exact + BALDA', and the minimum work extraction is also better captured than with just BALDA, though the minimum work in the parameter space is still negative. Surprisingly the 'exact + BALDA' approximation, with interactions now being considered somewhat in the evolution Hamiltonian, performs worse than the 'exact + NI' approximation, which has no consideration of interactions in the evolution Hamiltonian. On top of this, the improvement from BALDA to 'exact + BALDA' is modest, especially when comparing it to the improvement seen

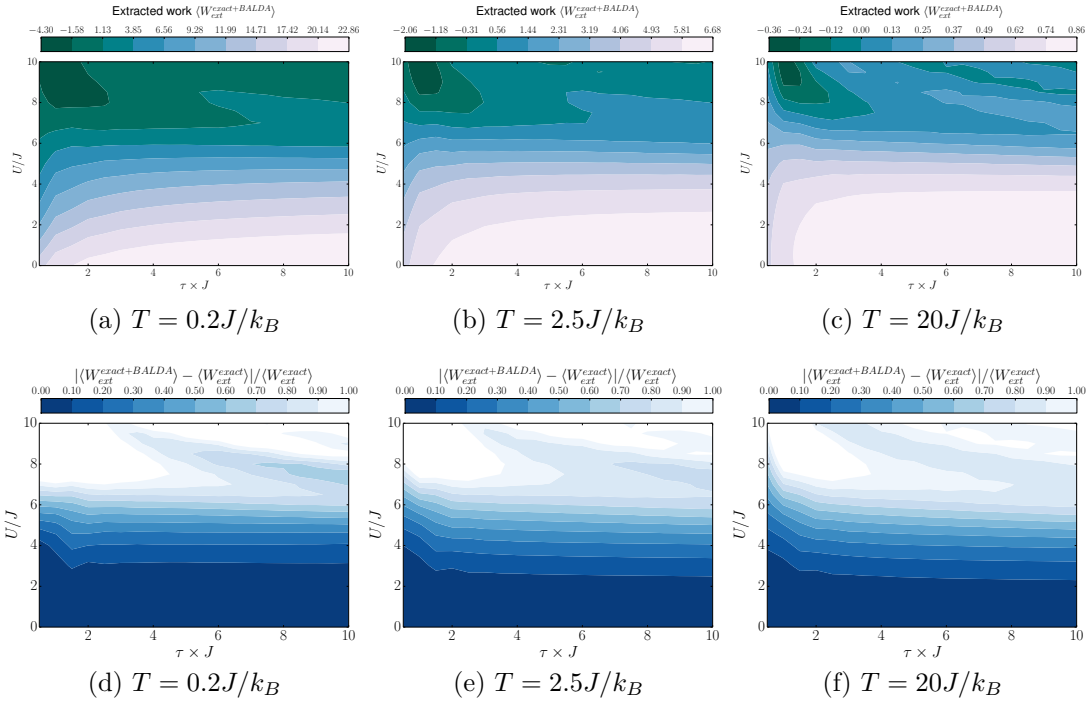

(a) $T = 0.2J/k_B$ (b) $T = 2.5J/k_B$ (c) $T = 20J/k_B$

(d) $T = 0.2J/k_B$ (e) $T = 2.5J/k_B$ (f) $T = 20J/k_B$

Figure 8.3: Upper panels: Work extracted using 'exact + BALDA' approximation for $0.5 \leq \tau \times J \leq 10$ (x-axis) and $0 \leq U/J \leq 10$ (y-axis) for 6 site chains with zigzag potential, increasing temperature from left to right, as stated. Lower panels: Relative difference between the 'exact + BALDA' work and the exact results for the same parameters as the upper panels.

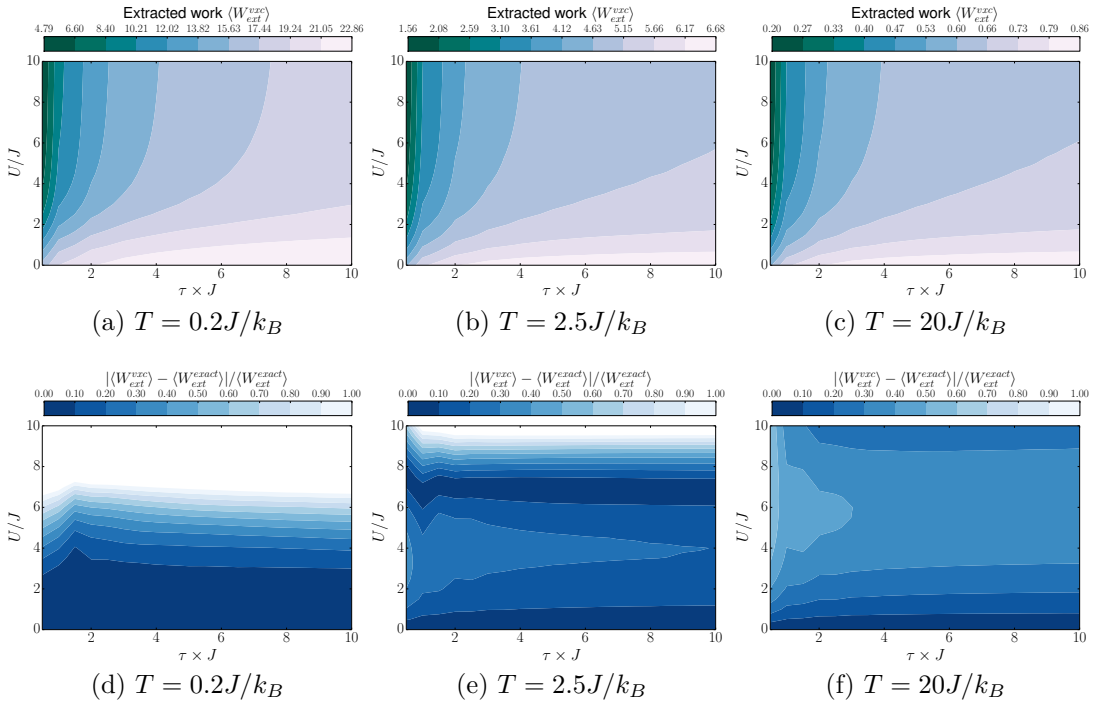

(a) $T = 0.2J/k_B$ (b) $T = 2.5J/k_B$ (c) $T = 20J/k_B$

(d) $T = 0.2J/k_B$ (e) $T = 2.5J/k_B$ (f) $T = 20J/k_B$

Figure 8.4: Upper panels: Work extracted using the exact v_{xc} for $0.5 \leq \tau \times J \leq 10$ (x-axis) and $0 \leq U/J \leq 10$ (y-axis) for 6 site chains with zigzag potential, increasing temperature from left to right. Lower panels: Relative difference between the exact v_{xc} work and the exact results for the same parameters as the upper panels.

between NI and 'exact + NI' in chapter 7. This seems to imply that when wanting to incorporate electron-electron interactions of some DFT form into the evolution Hamiltonian, it is important to use a DFT approximation which is appropriate for the system, otherwise not including any knowledge of the interactions in the evolution Hamiltonian is actually better. Let us now look at the exact ground state $\hat{V}_{xc}$ to understand a potential upper limit in the accuracy of this approximation method.

8.3.3 Exact ground state exchange-correlation potential, v_{xc}, work extraction

The approximation based on the exact ground state $\hat{V}_{xc}$, found using the reverse engineering scheme described in section 8.2.1 and denoted by 'v_{xc}' in all figures and approximation names, gives the results shown in figure 8.4 for the average work extraction (top row), and for the relative difference when compared to the exact work (bottom row).

The qualitative results are very similar to the non-interacting results for

medium to large interaction strengths. However, at low U's the impact of the corrections to interactions is apparent, with the behaviour of the exact results being somewhat regained for low and medium temperatures.

The quantitative results yield regions of higher accuracy than the non-interacting approximation, between $U \approx 1J$ and $U \approx 5.5J$, for the lowest temperature. The accuracy at this temperature is also improved over the BALDA results for the region between $U \approx 1J$ and $U \approx 3J$ for all τ's.

As the temperature increases, the regions of medium to high accuracy ($\lesssim 40\%$ difference to the exact) also increase to larger interaction strengths. However accuracy is reduced to within $\sim 50\%$ of the exact result for the majority of U's and τ's as the temperature reaches $T = 20J/k_B$, which is actually worse than the completely non-interacting approximation. Remember, though, that at this high temperature the system predominantly behaves as if it is non-interacting because $U \ll T$ and so interactions are almost negligible for regions up to $U \approx 5J$. Also, v_{xc} is found using an inversion scheme developed for the ground state, and therefore would naturally have difficulty in accurately representing systems at high temperature. That being said, v_{xc} performs better than both BALDA and 'exact + BALDA', particularly at the medium and high temperatures. It also captures the minimum work extracted over the parameter set much more accurately than either BALDA approximation; there is no negative work extraction in the v_{xc} results for the zigzag potential at 6 sites, much like in the exact results.

Let us now see how the results from v_{xc} are impacted when the calculation considers the exact initial state.

8.3.4 'Exact + v_{xc}' work extraction

Figure 8.5 shows the average work extracted using the 'exact + v_{xc}' approximation (top row) detailed in section 8.2.2, and the relative difference to the exact results (bottom row).

There is a huge qualitative *and* quantitative improvement in the accuracy over the other three approximations shown in this chapter. The regions of medium-high accuracy (within 20-30% of the exact results) spread over most regimes for all temperatures. Both the minimum and maximum values of average work extraction across the parameter set are captured well, usually within 20% of the exact value, by the 'exact + v_{xc}' approximation.

The results from 'exact + v_{xc}' are in fact comparable to those of 'exact + NI'. They show very similar patterns in the work and the relative error, but

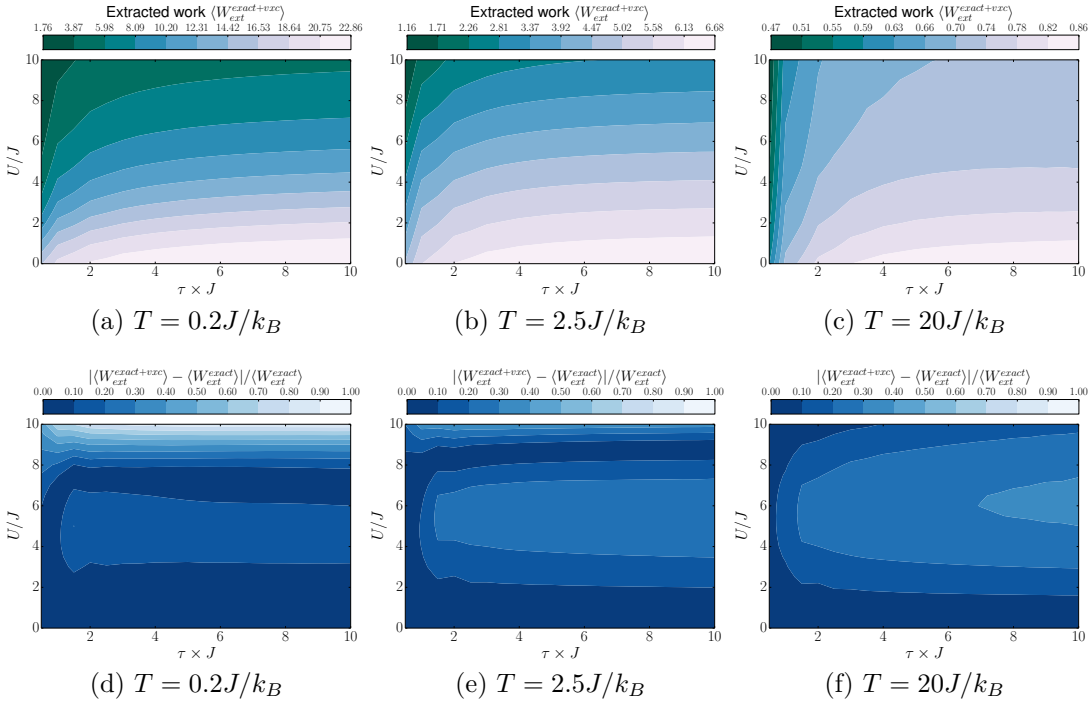

(a) $T = 0.2J/k_B$ (b) $T = 2.5J/k_B$ (c) $T = 20J/k_B$

(d) $T = 0.2J/k_B$ (e) $T = 2.5J/k_B$ (f) $T = 20J/k_B$

Figure 8.5: Upper panels: Work extracted using the 'exact + v_{xc}' approximation for $0.5 \leq \tau \times J \leq 10$ (x-axis) and $0 \leq U/J \leq 10$ (y-axis) for 6 site chains with zigzag potential, increasing temperature from left to right, as stated. Lower panels: Relative difference between the 'exact + v_{xc}' average work and the exact results for the same parameters as the upper panels.

'exact + v_{xc}' captures the very strongly correlated systems in the quasi-sudden quench regime more accurately than 'exact + NI' (particularly for the low and medium temperatures). At the other end, 'exact + NI' captures the adiabatic regime for medium interaction strengths at high temperature more accurately. These differences can be attributed to the dominant energy at play in each situation: in very strongly correlated systems at low and medium temperatures, U will be a dominant energy and so the inclusion of the $\hat{V}_{xc}$ will help capture these interactions to provide more accurate results, however at high temperature, T dominates over U resulting in the non-interacting approximation better representing the dynamics leading to more accurate results than using the v_{xc}.

Overall, we can see how a good/appropriate $\hat{V}_{xc}$ approximation can yield good results for weak to medium interaction strengths, even when only using a ground state time-independent $\hat{V}_{xc}$ approximation. It is important to choose an appropriate approximation for the $\hat{V}_{xc}$ because, as we saw with BALDA, a poor approximation will result in accuracy worse than the non-interacting approximation.

When including the exact initial state with a good (ground state) $\hat{V}_{xc}$, we gain great accuracy for most regimes, including the very challenging strongly correlated systems during a quasi-sudden quench. If a good approximation for $\hat{V}_{xc}$ cannot be found, highly accurate results can still be found using the 'exact + NI' approximation, which is actually computationally cheaper. In fact, given that the exact $\hat{V}_{xc}$ is almost impossible to find for most systems[7], and that the 'exact + NI' approximation is of similar accuracy in the majority of regimes, we can use the computationally cheap 'exact + NI' approximation to calculate the average quantum work extraction. The exception to this is of course at high U for lower temperatures, where the 'exact + v_{xc}' would be preferable, but with a more appropriate approximation to $\hat{V}_{xc}$ than BALDA.

8.4 Approximated entropy production results

As with chapters 6 and 7, we will also look at the entropy produced (irreversible work). We will apply the approximations to the entropy using the same logic as described in section 7.4.4, i.e. the approximation of the free energy will match the approximation of the initial state of the system.

[7]Because the system we are using is exactly solvable, we have been able to find and use the exact ground state $\hat{V}_{xc}$ to provide an approximate upper bound to the accuracy achievable by these techniques.

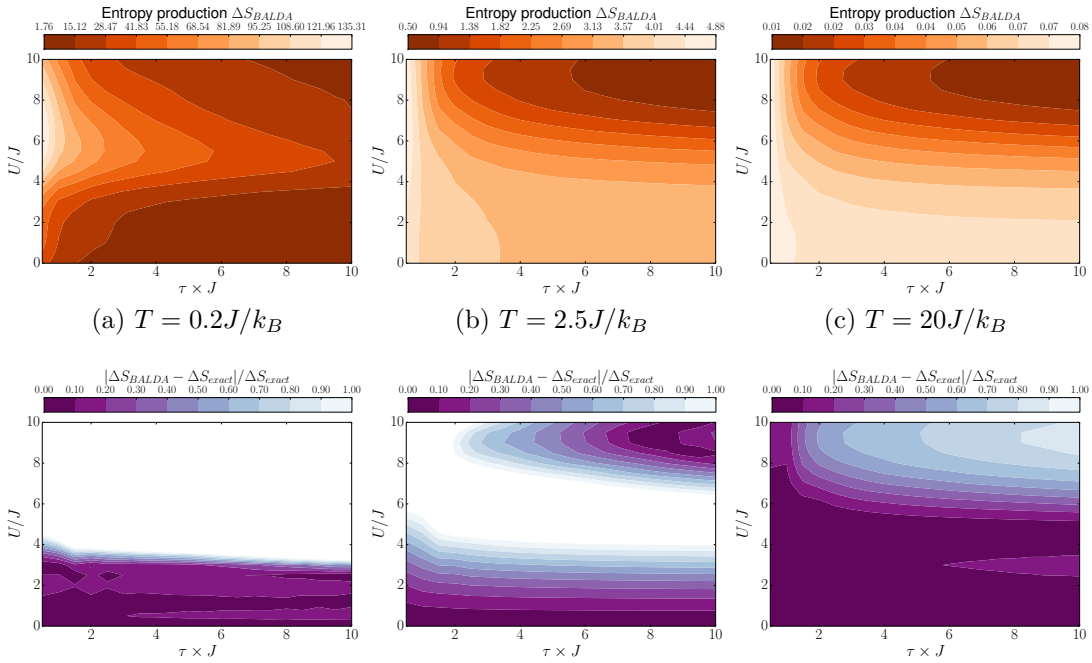

(a) $T = 0.2J/k_B$ (b) $T = 2.5J/k_B$ (c) $T = 20J/k_B$

(d) $T = 0.2J/k_B$ (e) $T = 2.5J/k_B$ (f) $T = 20J/k_B$

Figure 8.6: Upper panels: Entropy produced using BALDA for $0.5 \leq \tau \times J \leq 10$ (x-axis) and $0 \leq U/J \leq 10$ (y-axis) for 6 site chains with zigzag potential, increasing temperature from left to right. Lower panels: Relative difference between the BALDA entropy production and the exact results for the same parameters as the upper panels.

8.4.1 BALDA entropy production

With the entropy approximated using BALDA, the free energy will be calculated using $\hat{H}^{BALDA}$ in the partition function. Figure 8.6 shows ΔS_{BALDA} (top row) and the relative error with the exact entropy production (bottom row) for our parameter set. Recall the darker the orange shade, the less entropy is produced, and the deeper the purple shade, the more accurate the quantitative results are.

For all temperatures, this approximation calculates the minimum entropy production accurately (to one decimal place for low and high temperatures, and is within 0.12 of the medium temperature result). This is largely because the accuracy of the small entropy production is helped by having an accurate maximum for the average quantum work extracted (as we saw in the previous section). The BALDA approximation struggles to accurately capture the maximum entropy production though, particularly at low temperature where it overestimates the amount of entropy produced to be almost double the exact entropy production. The region of largest entropy production corresponds

to the sudden quench with strong interactions, a system which BALDA is not suited for, and so it is unsurprising that the maximum entropy production is not accurately calculated here.

As the temperature increases, the quantitative accuracy improves between the low and high temperatures, but the medium temperature loses accuracy at weak/medium interaction strengths whilst gaining accuracy at strongly correlated systems evolved adiabatically. At this medium temperature, we see accuracy gained in the regions where ΔS_{BALDA} is small. A small ΔS corresponds to a large $\langle W_{ext} \rangle$, which we saw was calculated accurately by $\langle W_{ext}^{BALDA} \rangle$.

At the low temperature, the qualitative results capture the general shape of the contour plot, particularly the high entropy region for sudden quenches and with the protrusion of regions of larger entropy production at medium correlation strengths. However qualitatively it is less accurate than the work. Here, though, we have also approximated the free energy, which adds a new error into the system.

The high temperature result is more accurate than for the other temperatures, and indeed more accurate than the work but notice that not much entropy is produced. In contrast to the medium temperature results, accuracy has been lost in the strongly correlated adiabatic region. Qualitatively the parameter region of smallest entropy production is incorrect compared to the exact result, which leads to this loss of accuracy in the upper-right section of the parameter space. At this high temperature, there is not much entropy produced across the parameter space and the system behaves more like a non-interacting system, possibly making corrections to interactions easier.

8.4.2 'Exact + BALDA' entropy production

The entropy production using the 'exact + BALDA' approximation is shown in the top row of figure 8.7. The relative difference is shown in the bottom row. Since we are using the exact initial state, the free energy will be calculated using the exact (fully interacting) Hamiltonian.

The quantitative error is very similar to the 'exact + BALDA' work, but this is unsurprising as the work is the main source of error in this calculation. Qualitatively, however, the 'exact + BALDA' entropy struggles to capture the exact entropy production, noticeably more so than the BALDA entropy.

The value of the maximum entropy production at the low temperature, however, is captured much more accurately using the 'exact + BALDA' approximation than just BALDA (within 1% of the exact for the low and medium

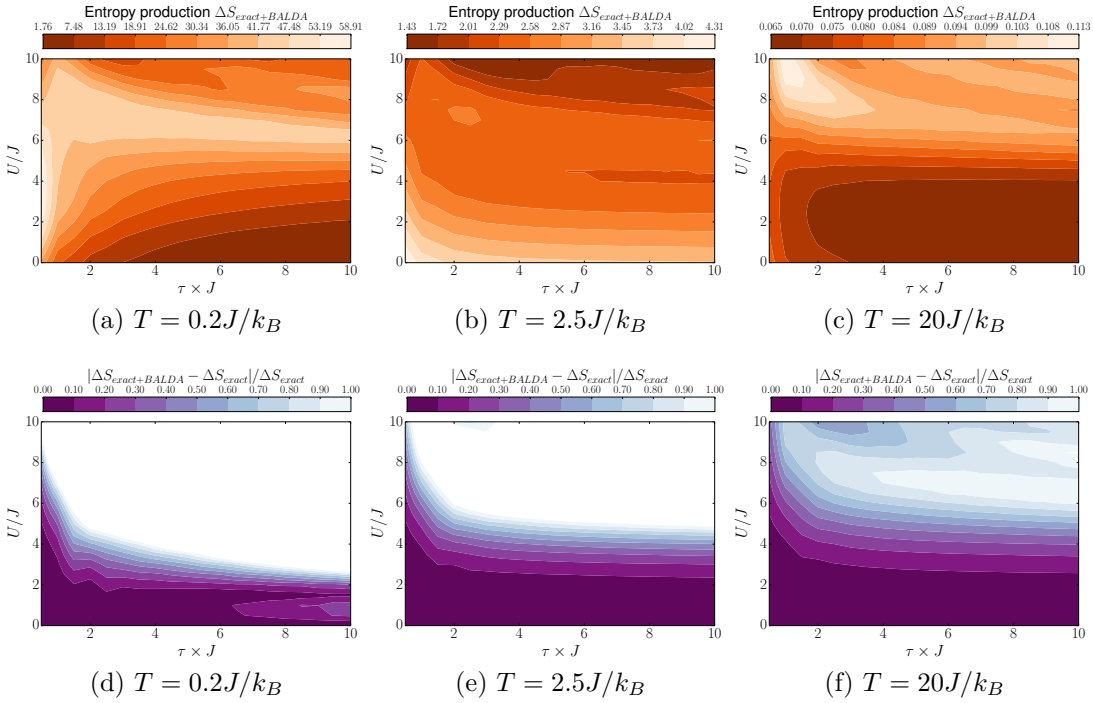

(a) $T = 0.2J/k_B$ (b) $T = 2.5J/k_B$ (c) $T = 20J/k_B$

(d) $T = 0.2J/k_B$ (e) $T = 2.5J/k_B$ (f) $T = 20J/k_B$

Figure 8.7: Upper panels: Entropy produced using 'exact + BALDA' for $0.5 \leq \tau \times J \leq 10$ (x-axis) and $0 \leq U/J \leq 10$ (y-axis) for 6 site chains with zigzag potential, increasing temperature from left to right. Lower panels: Relative difference between the 'exact + BALDA' entropy production and the exact results for the same parameters as the upper panels.

temperatures). The region of maximum entropy production (sudden quench at medium interaction strengths) is closer to the exact region, but the approximation then incorrectly extends this region of large entropy production further into larger τ's.

Much like with the work, we do not see a great improvement when using the hybrid approximation with BALDA, compared to the pure BALDA approximation. Using BALDA for the $\hat{V}_{xc}$ to give a lower bound to the accuracy of this method of approximating shows accurate results (within $\sim 10\%$ of the exact) for weakly correlated systems ($U \lesssim 3J$) for all temperatures and most τ's (up to $\tau \approx 6/J$ for the lowest temperature).

8.4.3 Exact ground state exchange-correlation potential, v_{xc}, entropy production

Figure 8.8 shows the entropy production results when using the exact v_{xc} found using the inversion scheme outlined in section 8.2.1. Here the free energy is approximated using the Hamiltonian which has the numerically-exact ground state $\hat{V}_{xc}$.

At low and medium temperatures, the results are less accurate than the approximated work. Here we have a further error coming in through the free energy, increasing the overall error in the entropy. The high temperature results are accurate within 30% of the exact ones for most regimes, but very little entropy is produced here and the range of entropy produced across the parameter space is very small.

Qualitatively, the exact ground state v_{xc} struggles to accurately represent the exact results, demonstrating behaviour closer to a non-interacting system for large U's. The v_{xc} does not show much, if any, quantitative improvement over the non-interacting approximation for the low and medium temperatures. Indeed the v_{xc} shows a small reduction in the quantitative accuracy compared to both BALDA and 'exact + BALDA' for the low and medium temperatures. At the high temperature, however, the accuracy is more consistently improved across the parameter space.

8.4.4 'Exact + v_{xc}' entropy production

Using the exact initial state alongside the exact ground state $\hat{V}_{xc}$ in the driving Hamiltonian, we see an improvement in the results for low and medium temperatures (figure 8.9, panels (a) and (b) for 'exact + v_{xc}' entropy production at

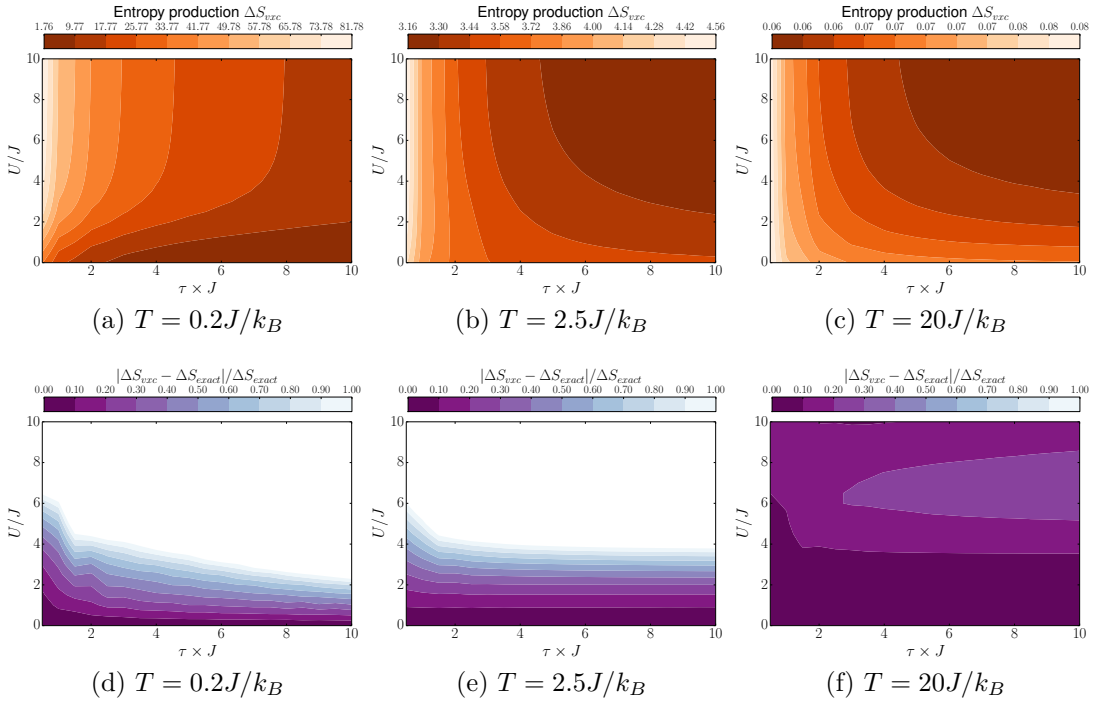

(a) $T = 0.2J/k_B$ (b) $T = 2.5J/k_B$ (c) $T = 20J/k_B$

(d) $T = 0.2J/k_B$ (e) $T = 2.5J/k_B$ (f) $T = 20J/k_B$

Figure 8.8: Upper panels: Entropy production using the exact v_{xc} for $0.5 \leq \tau \times J \leq 10$ (x-axis) and $0 \leq U/J \leq 10$ (y-axis) for 6 site chains with zigzag potential, increasing temperature from left to right. Lower panels: Relative difference between the exact v_{xc} entropy produced and the exact results for the same parameters as the upper panels.

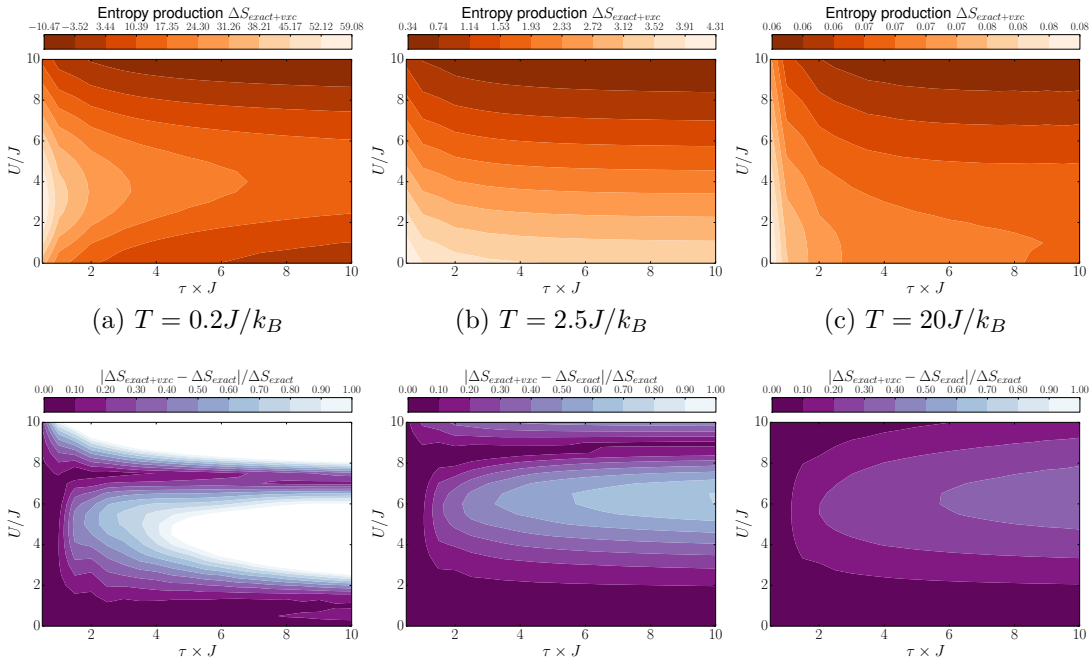

(a) $T = 0.2J/k_B$ (b) $T = 2.5J/k_B$ (c) $T = 20J/k_B$

(d) $T = 0.2J/k_B$ (e) $T = 2.5J/k_B$ (f) $T = 20J/k_B$

Figure 8.9: Upper panels: Entropy produced using 'exact + v_{xc}' for $0.5 \leq \tau \times J \leq 10$ (x-axis) and $0 \leq U/J \leq 10$ (y-axis) for 6 site chains with zigzag potential, increasing temperature from left to right. Lower panels: Relative difference between the 'exact + v_{xc}' entropy production and the exact results for the same parameters as the upper panels.

$T = 0.2J/k_B$ and $T = 2.5J/k_B$ respectively, and panels (d) and (e) for the relative errors). The high temperature ($T = 20J/k_B$, figure 8.9 panel (c) for the entropy production, and panel (f) for the relative error) shows large accuracy over most of the parameter space, but the accuracy is reduced compared to the v_{xc} approximation for systems slower than the quasi-sudden quench where $\tau \gtrsim 1/J$ [compare with figure 8.8(f)].

As with the work, both the quantitative [figure 8.9, panels (d) to (f)] and qualitative [see the general shapes in figure 8.9 panels (a) to (c)] results of the 'exact + v_{xc}' approximation are very similar to the 'exact + NI' results. Again, the main differences are seen in strongly correlated systems under a quasi-sudden quench, where the 'exact + v_{xc}' performs better, and at high temperature, where the 'exact + NI' performs better. This reinforces the preference of 'exact + NI' over any of the other ground state DFT-style approximations for quantum thermodynamic properties in the majority of regimes addressed in this thesis.

Overall, these approximations were designed with the average quantum work extraction in mind, and so the drop in accuracy seen when translating

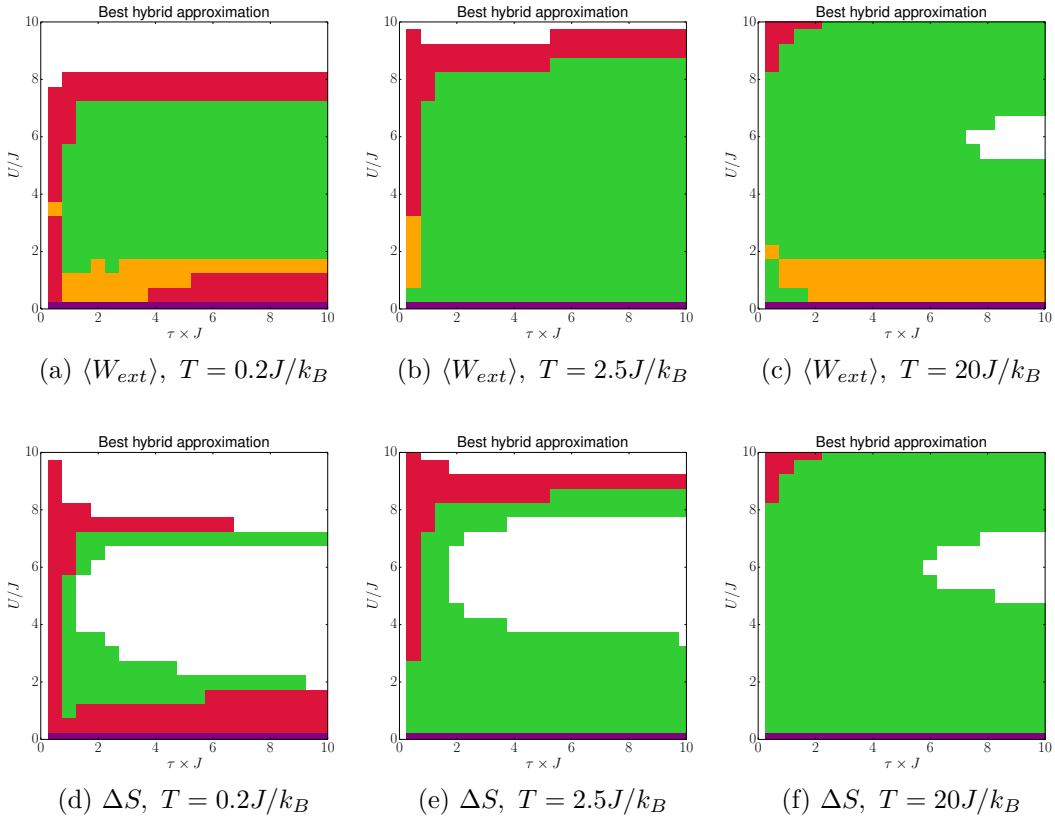

(a) $\langle W_{ext} \rangle,\ T = 0.2J/k_B$ (b) $\langle W_{ext} \rangle,\ T = 2.5J/k_B$ (c) $\langle W_{ext} \rangle,\ T = 20J/k_B$

(d) $\Delta S,\ T = 0.2J/k_B$ (e) $\Delta S,\ T = 2.5J/k_B$ (f) $\Delta S,\ T = 20J/k_B$

Figure 8.10: Upper panels: Figures showing which hybrid approximation is most accurate (up to 20%) for the quantum work in each region (6 sites, zigzag). Lower panels: Figures showing which hybrid approximation is most accurate (up to 20%) for the associated entropy production.
The colours representing the approximations are all, 'exact + NI', 'exact + BALDA', and 'exact + v_{xc}', seen here. See text for full list (including approximations which are not the most accurate in any regime).

them to the entropy production implies that an entropy specific approximation should be considered. That being said, we have still shown regions where these approximations can be useful and accurate, albeit there are fewer of these regions than for the work.

8.5 Diagrammatic summary of all approximations

Figure 8.10 shows the best hybrid approximation(s) in each region of our parameter set. The colour codes for each hybrid approximation are:

- All

- ‘exact + NI’ and ‘exact + v_{xc}’
- ‘exact + NI’
- ‘exact + NI’ and ‘exact + BALDA’
- ‘exact + BALDA’
- ‘exact + BALDA’ and ‘exact + v_{xc}’
- ‘exact + v_{xc}’
- Otherwise the error in all is over 20%

The top row shows the outcome for the average quantum work for the three temperatures when we have a 6 site chain with a zigzag potential. The bottom row shows the corresponding results for the entropy production.

These figures confirm that the ‘exact + NI’ approximation is the best performing approximation in the majority of parameter regimes. The ‘exact + v_{xc}’ outperforms the ‘exact + NI’ primarily in the strongly correlated and quasi-sudden quench regimes. Unsurprisingly all approximations are equally accurate for the non-interacting system, but ‘exact + BALDA’ is able to occasionally perform the best for the work when in weakly coupled regimes at the low and high temperatures.

For when one does not have access to the exact initial state, figure 8.11 demonstrates the best non-hybrid approximation across the regimes. BALDA and the exact ground state v_{xc} are seen to be the best in more regions than for the hybrid approximations, but the non-interacting approximation still performs well, particularly for the quantum work at medium and high temperatures.

8.6 Conclusion

Using the success of the hybrid approximation from chapter 7, we applied DFT-style approximations to the driven Hamiltonian with the aim of creating more sophisticated, but still computationally cheap, approximations to quantum thermodynamic properties. We introduced the hybrid versions of BALDA (‘exact + BALDA’) and of the exact (reverse-engineered) ground state $\hat{V}_{xc}$ (‘exact + v_{xc}’) for the quantum work and entropy production. We compared these hybrid approximations to their equivalent non-hybrid approximations

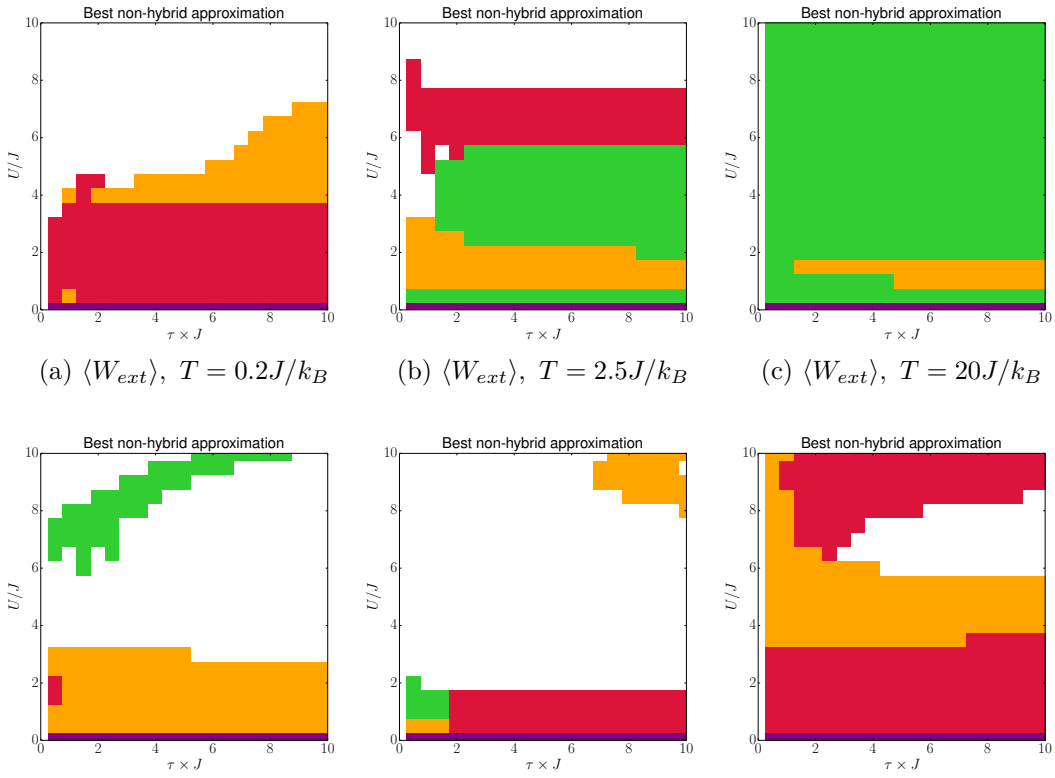

(a) $\langle W_{ext} \rangle,\ T = 0.2J/k_B$ (b) $\langle W_{ext} \rangle,\ T = 2.5J/k_B$ (c) $\langle W_{ext} \rangle,\ T = 20J/k_B$

(d) $\Delta S,\ T = 0.2J/k_B$ (e) $\Delta S,\ T = 2.5J/k_B$ (f) $\Delta S,\ T = 20J/k_B$

Figure 8.11: Upper panels: Figures showing which non-hybrid approximation is most accurate (up to 20%) for the quantum work in each region (6 sites, zigzag). Lower panels: Figures showing which non-hybrid approximation is most accurate (up to 20%) for the associated entropy production.
The colours representing the approximations are all, non-interacting, BALDA, and v_{xc}.

(BALDA and v_{xc}), as well as comparing the results to the non-interacting approximations from chapter 7.

The BALDA and 'exact + BALDA' results gave us an indication of the lower bound to the accuracy one can expect from these approximation styles for both the quantum work extraction and entropy production. Regions of high accuracy were only seen for weakly coupled regimes, and almost no improvement was found when using the hybrid approximation. In fact, almost everywhere the hybrid non-interacting approximation performed better than either BALDA based approximation, and as it is computationally cheaper, it would be preferable over a bad approximation to the Kohn-Sham system.

When using the numerically exact ground state v_{xc}, an estimate of the upper bound to the accuracy of this method of approximating the quantum work and entropy production can be found. We see regions of high accuracy for weak to medium coupled systems, with great improvements in both the quantitative and qualitative accuracy when using the hybrid approximation. The results for 'exact + v_{xc}' are strikingly similar to the 'exact + NI' results seen in chapter 7, with minor differences at strong correlations, and at the high temperature.

Therefore, we suggest that it is preferable to use the 'exact + NI' approximation, unless one has very strongly correlated systems, where $U \gtrsim 9J$, when 'exact + v_{xc}' with an appropriate $\hat{V}_{xc}$ would be more accurate. The improvements gained from using ground state DFT approximations in the driven Hamiltonian are not large enough to warrant the extra computational cost. In cases where the exact (or highly accurate) initial state cannot be found, it was seen here that an appropriate DFT approximation for the $\hat{V}_{xc}$ should be used. Otherwise higher accuracy can be gained for more regions just by using the hybrid non-interacting approximation, which again is computationally cheaper.

To improve the quantum thermodynamic approximations further, it would be recommended to include dynamic corrections i.e. by using TDDFT in the driven Hamiltonian $\hat{H}^{\text{evo}}$, such as in reference [59] who found that TDDFT improved the accuracy of the work approximations (even without including the exact initial state), however it is a more computationally expensive scheme. Alternatively one could develop a general reverse engineering scheme for the $\hat{V}_{xc}$ in thermal systems using the Mermin-Kohn-Sham theorem (which is the extension of the Kohn-Sham theory to thermal systems) [159].

9. Conclusion

This thesis looked at quantum many-body systems at finite temperature, which are commonly used as the hardware of quantum devices, and aimed to answer the questions:

1. How can we determine if a given evolution of a quantum system at finite temperature is adiabatic?

2. Can we accurately approximate quantum thermodynamic properties in many-body quantum systems using simple approximations inspired by DFT?

To do this, we have pulled together several theories from different fields, outlined in chapter 2. We have taken inspiration from DFT both in searching for simpler characterisations of adiabaticity through the electron density using distance measures, and in taking non-interacting systems as a basis for approximating quantum thermodynamic properties. To calculate the accuracy of these approximations, we have also explored exact quantum thermodynamic properties in many-body systems out-of-equilibrium, addressing how various temperatures, driving speeds, and correlation strengths impact the work extraction and entropy production.

Question 1 was addressed in chapters 4 and 5. We introduced the use of natural metrics as a method of characterising adiabaticity in many-body quantum systems, both at zero and finite temperature. We initially studied single-electron systems with random potentials at zero temperature in chapter 4, showcasing the various combinations of distances that can be used. All of these combinations agreed in general with the degree of adiabaticity of an evolution. Each combination gave its own insight into the dynamics, for example $D(\psi_{GS}(t), \psi(t))$ versus $D(n_{GS}(t), n(t))$ demonstrated oscillating arches due to the system inertia. We therefore recommend these metrics as a method of characterising adiabaticity in out-of-equilibrium systems at zero temperature.

It is in chapter 5 where we explore applying these metrics to many-body systems at finite temperature, focusing now on how the state distance $D(\rho_S(t), \rho(t))$

and the density distance $D(n_S(t), n(t))$ vary in time. We find that the metrics can be used to characterise adiabaticity, even at finite temperature. Interestingly, the Bures and trace distances give very similar qualitative results, and hence either can be used as a measure of adiabaticity. However, it is the particle density distance which gives the key result for both chapter 4 and 5. We demonstrated the ability to characterise adiabaticity using only the system densities. This is a very important result for many-body systems where the wavefunction or density matrix are complex and hard to access. This has the potential to be applied to quantum devices, allowing for better characterisation of adiabatic evolutions, and the conditions under which they can be best achieved.

By using the metrics, we have studied the dynamics of several systems in different conditions. The interplay between energies in the system is hugely important when wanting to achieve an adiabatic evolution. For example, we showed how distances are reduced when T or U dominate over the other energies in the system. We even saw the transition to a Mott insulator in the metrics, when U increased.

Because this research was performed with computational and experimental applications in mind, we have developed a threshold for adiabaticity and shown which system properties affect it. The threshold is seen to be affected by U, N, and T, however further work is needed to develop a refined threshold explicitly dependent on these values.

In answering question 1, we also investigated the quantum adiabatic criterion, which is commonly used to characterise adiabaticity for systems at zero temperature. We found the metrics give a fuller picture of the system dynamics (for example, the oscillations arising from the system's inertia), and they are not susceptible to the same limitations as the QAC: i.e. the metrics are not based on perturbation theory, and consider all states of the system so can be readily extended to finite temperature. Using the definition from the quantum adiabatic theorem, we proposed a new QAC which can be applied to systems at finite temperature. It is with the finite temperature QAC that we see the need for a non-Markovian method of characterising adiabaticity; memory effects are needed to ensure the adiabaticity measure does not mistakenly reclassify an evolution as adiabatic after it has left adiabaticity, unless the measure is able to positively identify that the correct populations of each eigenstate have been re-established. Therefore the metrics are preferable over the QAC because they can identify if an evolution is adiabatic with respect to the initial system, whereas the QAC is only able to identify an adiabatic

evolution with respect to the previous time step. A possibility of negating this issue in the QAC is to develop a cumulative QAC, such as $\int_0^\tau \epsilon(t)dt$, to include previous times. This could have the draw back of being less sensitive to returns to adiabaticity, and so smaller integration windows could be used, or a rolling average. A similar measure could be developed for the density distance to help reduce the possibility of the density characterising part of the evolution as adiabatic when the state shows it is not.

Research question 2 was addressed in chapters 6, 7, and 8. We wanted to look at quantum thermodynamic properties in many-body quantum systems because a better understanding of quantum thermodynamics can improve the fabrication and performance of quantum devices. However, properties of many-body systems are very challenging to calculate computationally, so to perform simulations of new quantum devices, we need to find accurate approximations for the quantum thermodynamic properties.

Before we could test any approximation, we needed to find the exact results. The exact quantum work and entropy production were shown in chapter 6, and gave interesting insights into the quantum thermodynamics of the many-body inhomogeneous Hubbard system. It was seen that most work is extracted in the adiabatic regime with weak correlations. As the temperature increased, the extractable work was seen to reduce. Overall we saw that the energy scales of U, T, and potential difference between sites are important, as well as the type of potential. We also saw the lowest entropy production in adiabatic regimes, so for Hubbard-type systems, we would recommend a weakly correlated adiabatic regime in which to operate quantum devices, maximising efficiency (work output versus entropy production).

We saw from reference [32] that DFT methods can be applied to quantum work for the Hubbard dimer, where the method proposed could be applied to any length chain. Here we explore new methods of approximating quantum thermodynamic properties, testing them in larger many-body Hubbard systems, and using the concept of a non-interacting system as the basis of an approximation. In chapter 7, we developed a hybrid approximation which considers the exact initial state but then uses the non-interacting Hamiltonian for the evolution. By including interactions just in the initial state, there is a large increase in accuracy when approximating the quantum work (compared to the purely non-interacting approximation), and an increase in the accuracy of approximating the entropy production (albeit a smaller increase). The 'exact + NI' hybrid approximation was developed with the quantum work in mind, and was rather simply extended to the entropy production. The drop in accuracy

from the quantum work to the entropy implies that the entropy may benefit from a tailored approximation, rather than an extension of the quantum work approximation. That being said, there were large parameter regions in both quantum work and entropy where the 'exact + NI' was accurate, despite it being a crude and computationally cheap approximation.

We then extended this hybrid approximation method in chapter 8 to try and develop more sophisticated approximations. To do this, we applied DFT approximations to the evolution Hamiltonian. We looked at a lower bound to the accuracy of this DFT method by taking a commonly used DFT approximation, BALDA, for which our system would be extremely challenging, and an upper bound by using the exact ground state $\hat{V}_{xc}$. Surprisingly neither of these DFT hybrid approximations consistently increased the accuracy of the results over the 'exact + NI' approximation. In fact the only increase was seen for highly correlated systems with sudden quench dynamics, and that was when using the (usually unknown) exact ground state $\hat{V}_{xc}$. Therefore we can see that it is the initial state which must be accurately found, and not the evolution, when approximating the quantum work. The (time-independent) approximation for the driving has much less of an impact in this method. So if one wishes to keep the computation cheap, one may simply use non-interacting dynamics.

One can use the hybrid 'exact + NI' approximation to calculate the expected work output of a system. One could also use it to find the system parameters which maximise the work and minimise the entropy production, much as we did in chapter 6 where we found regions of maximum work extraction and minimum entropy production for adiabatic evolutions at low temperature with weak correlations. From this, it could be possible to test the viability of new closed many-body systems for quantum devices; for example we saw the teeth potential required work to be inputted into the system, and so it would not be useful to use this potential when fabricating a quantum device for performing work. In these many-body systems, it can be almost impossible to exactly calculate the quantum thermodynamic properties, but with the hybrid approximation, one may be able to accurately approximate the possible work that can be extracted from their proposed system/device.

In general we always saw good accuracy in the 'exact+NI' approximation at low to medium interaction strengths, with most evolution times. We saw the region of highest accuracy increase in U when the temperature increased, and also as the number of sites increased (see appendix D), therefore we could see this trend continue with longer chains giving more regions where 'exact+NI'

could be accurate. Therefore, even when using different potentials, this approximation could be confidently recommended for low to medium U's at low temperatures and short chains, and up to higher U's for longer chains and at higher temperatures. We could also increase the confidence in the accuracy of 'exact+NI' at higher U's when the potential used has large differences between neighbouring sites, i.e. more like zigzag or teeth, and unlike slope, as the interactions have less of an impact compared to site-to-site energy difference.

Overall in this thesis we have developed new methods of characterising adiabaticity and approximating quantum thermodynamic properties. The methods for characterising adiabaticity can be used in quantum technologies where an adiabatic evolution is important, for example for an adiabatic quantum computation device which may wish to begin in a thermal state; the final density of the system can be experimentally measured and compared to the expected density using the metric to see if an adiabatic evolution was achieved. The approximation for quantum thermodynamic properties can be used in quantum technologies, for example when designing a device or trying to find the parameters which maximise work output or increase efficiency. The approximation enables the calculation of work and entropy in large Hubbard-like systems (such as coupled quantum dots) where exact calculations cannot be performed, and in turn could highlight better conditions in which to run the device. It could even be used to assess whether certain physical conditions are worth adjusting for the gain in work extracted; for example determining if it is worth trying to reduce the temperature for the amount of extra work extraction that could be gained from the device.

9.1 Future work

This research has uncovered some interesting conclusions with important implications for quantum devices, yet it can still be taken further. We have already alluded to some of the possible directions this research can take, but let us discuss them more thoroughly here.

We saw in chapter 4 that there is a quasi-linear relationship between ground state wavefunction distances and density distances. We took this to be a linear relationship when characterising adiabaticity, and in chapter 5 we used it for mapping the state adiabatic threshold to the density adiabatic threshold. Whilst this worked well, the density adiabatic threshold was still more lenient than the state adiabatic threshold when characterising an evolution as adiabatic. Remember, it is the state distance that is based on the quantum

adiabatic theorem (QAT), and we have been able to use concepts from DFT to show the density distance can be used even though it is not strictly related to the QAT. Therefore, to improve the use of the density distance for characterising adiabaticity, a more accurate mapping between the state distance and density distance would be beneficial. This would provide a tighter, and more accurate, threshold in the density.

To achieve a more accurate mapping, we recommend using a non-linear fit which can encapsulate the 'bend' in the adiabatic line [i.e. the plots of $D(\rho_S(0), \rho(t))$ versus $D(n_S(0), n(t))$] where the distances approach their maximums. This will lead to a more precise mapping from state distance to density distance, reducing the error and tightening the density adiabatic threshold.

We also noted that the adiabatic line is dependent on the correlation strength, the number of electrons, and the temperature of the system. However we have not found an analytical link between these quantities and the gradient of the adiabatic line. It would be interesting to try and find a more quantifiable relationship between these quantities and the gradient. From this one could then identify an adiabatic evolution from a single or very few measurements, comparing the measurement result to the anticipated adiabatic result from the analytical relationship. Again, a better understanding of the adiabatic line gradient will also improve the mapping from the state threshold to the density threshold, further promoting the use of the density distance as a measure of adiabaticity.

With regards to research question 2, there are a few lines of enquiry which could prove fruitful. The focus is on developing more sophisticated approximations which could potentially be applied to a wider range of systems and parameters. It would also be useful to test the hybrid approximation predictions against experimental results. One could even use the approximation to try and find the best parameter set for the experiment with regards to maximising work and minimising entropy.

To create the next generation of these approximations, there are two promising paths to follow: use a time-dependent approximation to the driven Hamiltonian $\hat{H}^{\text{evo}}$, or to find the truly exact (thermal) $\hat{V}_{xc}$ for systems at finite temperature. It is anticipated that the former would be the more fruitful line of research, and indeed reference [59] has already demonstrated the use of a time-dependent approximation for quantum work, using the adiabatic LDA (ALDA). One could therefore combine the approximations from reference [59] and chapter 7 to create a hybrid time-dependent approximation for quantum thermodynamic properties. It would be interesting to see if there is

any improvement in the accuracy of the results when using a time-dependent approximation, and if the exact initial state is as important as it was seen to be in chapters 7 and 8. This, in turn, can give us further insight into the impact of interactions and dynamics on the average quantum work.

The other path would be to use a more appropriate 'exact' $\hat{V}_{xc}$, i.e. one that is tailored to the thermal state, and not the ground state. For this, we need to develop a reverse engineering scheme which can take the exact many-body thermal density and find the $\hat{V}_{xc}$ which produces this density. The usual Kohn-Sham theory is only applicable to ground state systems, and cannot guarantee that there is a one-to-one mapping between thermal density and state. However, Mermin was able to extend the Kohn-Sham theory to finite temperatures and show that this mapping exists in thermal systems [159]. Therefore a reverse engineering scheme using the Mermin-Kohn-Sham theory could be found, and from this we can use the thermal $\hat{V}_{xc}$ to test a new upper bound to the accuracy of the hybrid approximation[1].

Overall we have introduced the ability to characterise adiabaticity using only the system densities, and we have developed a computationally cheap but surprisingly accurate approximation for quantum thermodynamic properties. In this process we have been able to interrogate system dynamics and the impact of various parameters on the system, providing insight into key influences on these many-body quantum systems out of equilibrium.

[1]Note that reference [60] has already demonstrated the ability to reverse engineer for the $\hat{V}_{xc}$ at finite temperature, however the scheme they used here is only applicable to a system of 2 sites and is not scalable.

A. Characterising adiabatic evolutions in the Hubbard model with $N = 2$ and 4

A.1 Bures and density distances for $N = 2$

This section shows the Bures distance $D_\rho^B(\rho_S(t), \rho(t))$ and density distance $D_n(n_S(t), n(t))$ with time (as outlined in chapter 5) for the 2 site system with slope potential. Figure A.1 gives the results for zero temperature, figure A.2 gives the results for $T = 0.2J/k_B$, and figure A.3 gives the results for $T = 2.5J/k_B$.

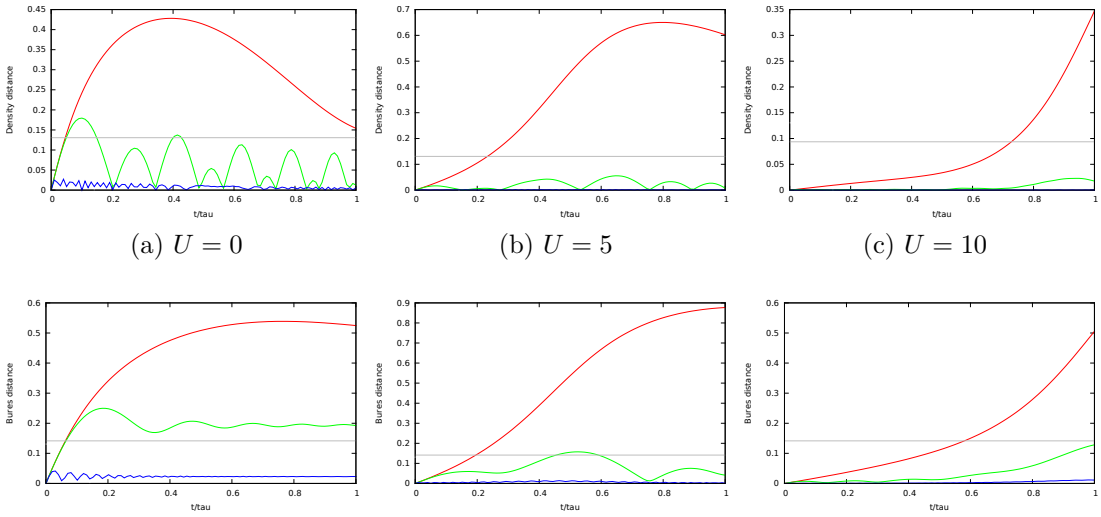

(a) $U = 0$ (b) $U = 5$ (c) $U = 10$

(d) $U = 0$ (e) $U = 5$ (f) $U = 10$

Figure A.1: Top row: $D_\rho^B(\rho_S(t), \rho(t))$ against time t/τ for $U = 0J$ (left), $U = 5J$ (middle), and $U = 10J$ (right).
Bottom row: $D_n(n_S(t), n(t))$ against time t/τ for $U = 0J$ (left), $U = 5J$ (middle), and $U = 10J$ (right).

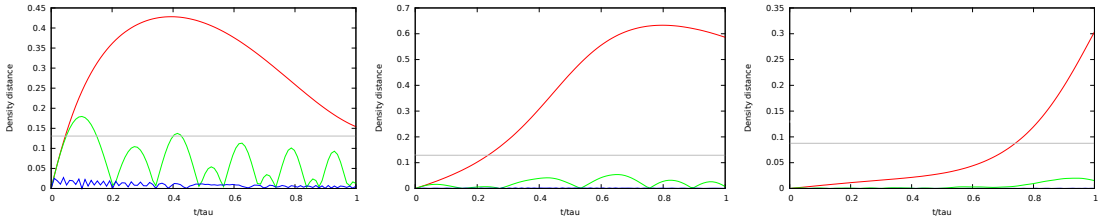

(a) $U = 0$ (b) $U = 5$ (c) $U = 10$

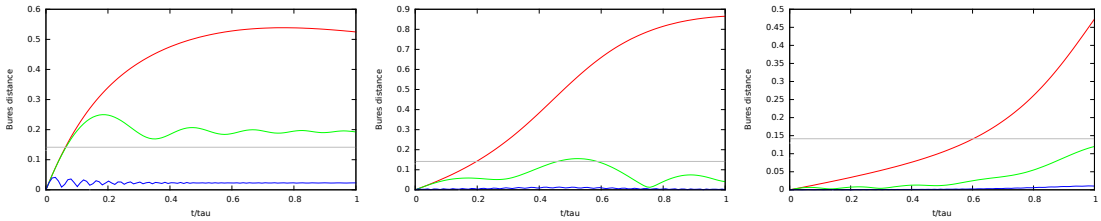

(d) $U = 0$ (e) $U = 5$ (f) $U = 10$

Figure A.2: Top row: $D_\rho^B(\rho_S(t), \rho(t))$ against time t/τ for $U = 0J$ (left), $U = 5J$ (middle), and $U = 10J$ (right).
Bottom row: $D_n(n_S(t), n(t))$ against time t/τ for $U = 0J$ (left), $U = 5J$ (middle), and $U = 10J$ (right).

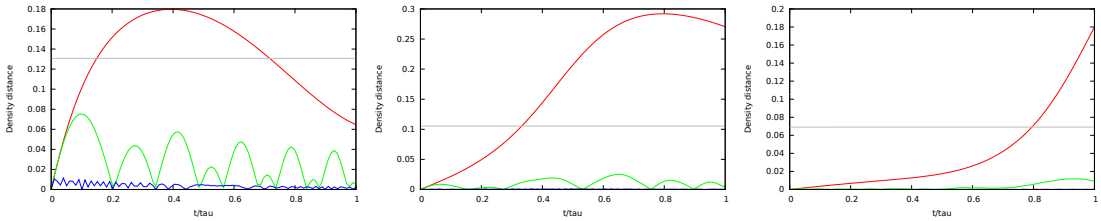

(a) $U = 0$ (b) $U = 5$ (c) $U = 10$

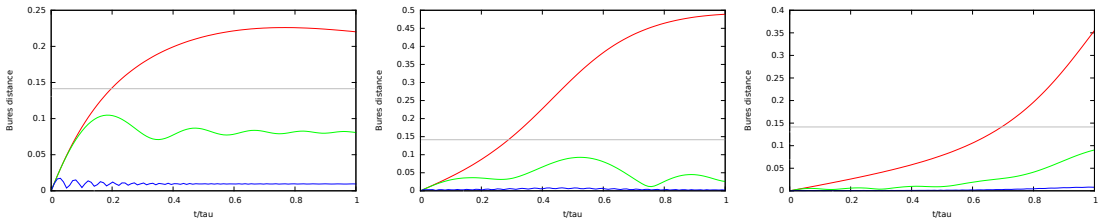

(d) $U = 0$ (e) $U = 5$ (f) $U = 10$

Figure A.3: Top row: $D_\rho^B(\rho_S(t), \rho(t))$ against time t/τ for $U = 0J$ (left), $U = 5J$ (middle), and $U = 10J$ (right).
Bottom row: $D_n(n_S(t), n(t))$ against time t/τ for $U = 0J$ (left), $U = 5J$ (middle), and $U = 10J$ (right).

A.2 $N = 4$

This section shows the Bures distance $D_\rho^B(\rho_S(t), \rho(t))$ and density distance $D_n(n_S(t), n(t))$ with time for the 4 site system with slope potential. Figure A.4 gives the results for zero temperature, figure A.5 gives the results for $T = 0.2J/k_B$, and figure A.6 gives the results for $T = 2.5J/k_B$.

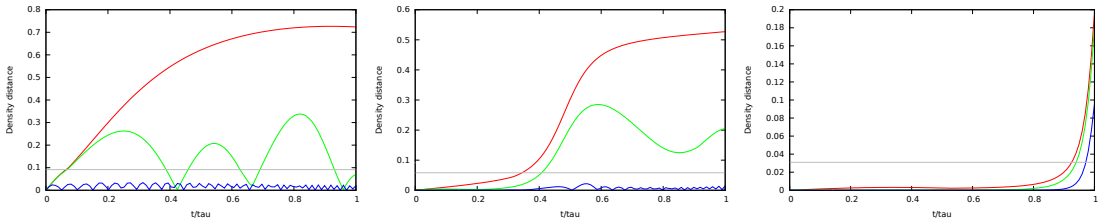

(a) $U = 0$ (b) $U = 5$ (c) $U = 10$

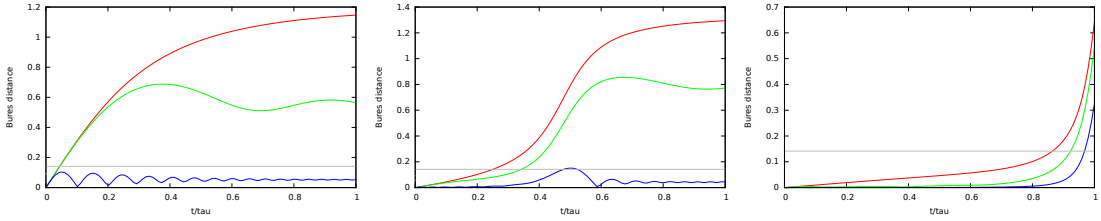

(d) $U = 0$ (e) $U = 5$ (f) $U = 10$

Figure A.4: Top row: $D_\rho^B(\rho_S(t), \rho(t))$ against time t/τ for $U = 0J$ (left), $U = 5J$ (middle), and $U = 10J$ (right).
Bottom row: $D_n(n_S(t), n(t))$ against time t/τ for $U = 0J$ (left), $U = 5J$ (middle), and $U = 10J$ (right).

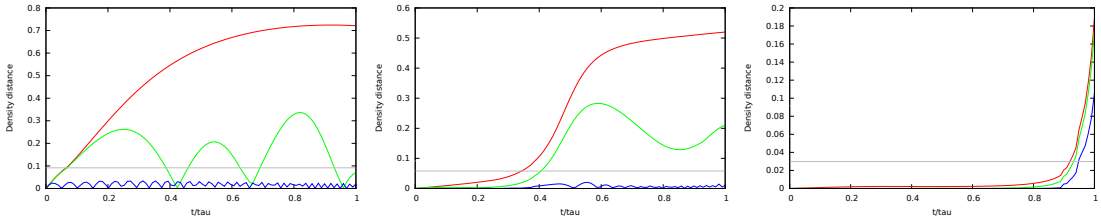

(a) $U = 0$ (b) $U = 5$ (c) $U = 10$

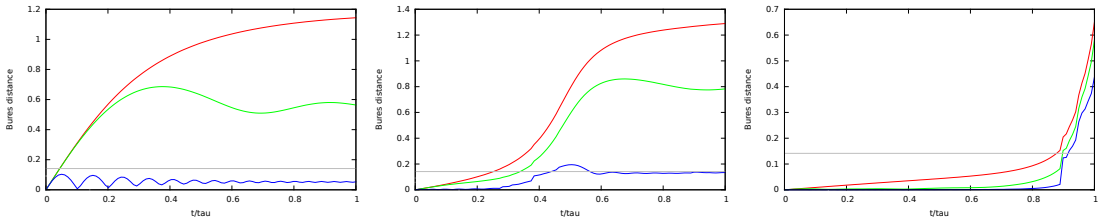

(d) $U = 0$ (e) $U = 5$ (f) $U = 10$

Figure A.5: Top row: $D_\rho^B(\rho_S(t), \rho(t))$ against time t/τ for $U = 0J$ (left), $U = 5J$ (middle), and $U = 10J$ (right).
Bottom row: $D_n(n_S(t), n(t))$ against time t/τ for $U = 0J$ (left), $U = 5J$ (middle), and $U = 10J$ (right).

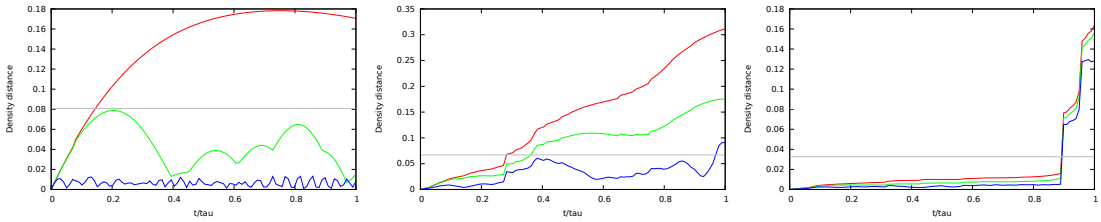

(a) $U = 0$ (b) $U = 5$ (c) $U = 10$

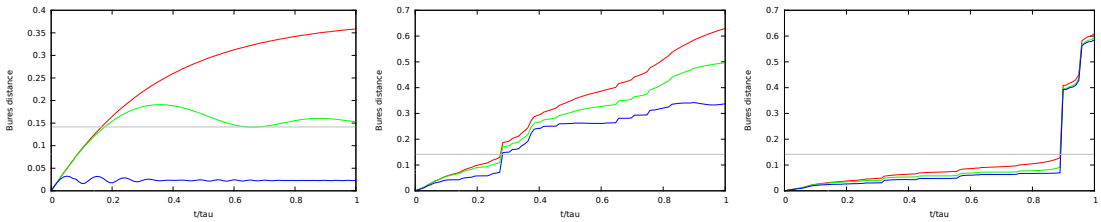

(d) $U = 0$ (e) $U = 5$ (f) $U = 10$

Figure A.6: Top row: $D_\rho^B(\rho_S(t), \rho(t))$ against time t/τ for $U = 0J$ (left), $U = 5J$ (middle), and $U = 10J$ (right).
Bottom row: $D_n(n_S(t), n(t))$ against time t/τ for $U = 0J$ (left), $U = 5J$ (middle), and $U = 10J$ (right).

B. Complete set of results for exact quantum thermodynamic properties

B.1 Exact quantum thermodynamic results

In this section, we will display the exact quantum work (as calculated using equation 2.76) and entropy production (as calculated using equation 2.81) for the complete parameter set (i.e. 2, 4, and 6 sites, with zigzag, teeth, and slope potentials, for $T = 0.2J/k_B$, $T = 2.5J/k_B$, and $T = 20J/k_B$) showing $0 \leq U/J \leq 10$ along the y-axis and $0.5 \leq \tau \times J \leq 10$ along the x-axis.

B.1.1 Exact work

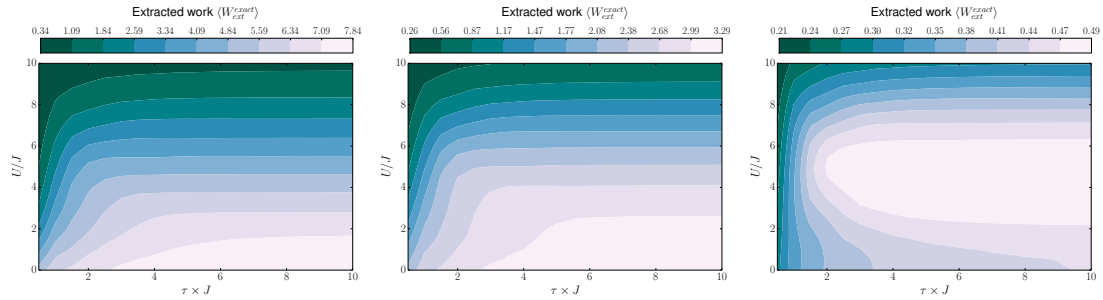

(a) $T = 0.2J/k_B$ (b) $T = 2.5J/k_B$ (c) $T = 20J/k_B$

Figure B.1: Exact work for 2 sites with zigzag potential at the three temperatures.

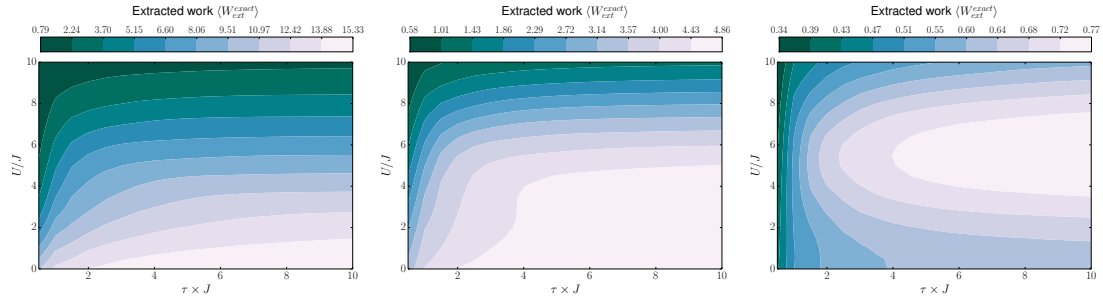

(a) $T = 0.2J/k_B$ (b) $T = 2.5J/k_B$ (c) $T = 20J/k_B$

Figure B.2: Exact work for the 4 sites zigzag at the three temperatures.

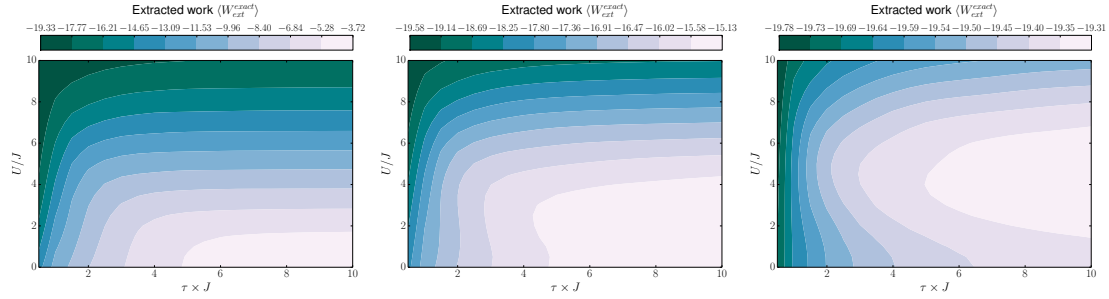

(a) $T = 0.2J/k_B$ (b) $T = 2.5J/k_B$ (c) $T = 20J/k_B$

Figure B.3: Exact work for the 4 sites teeth at the three temperatures.

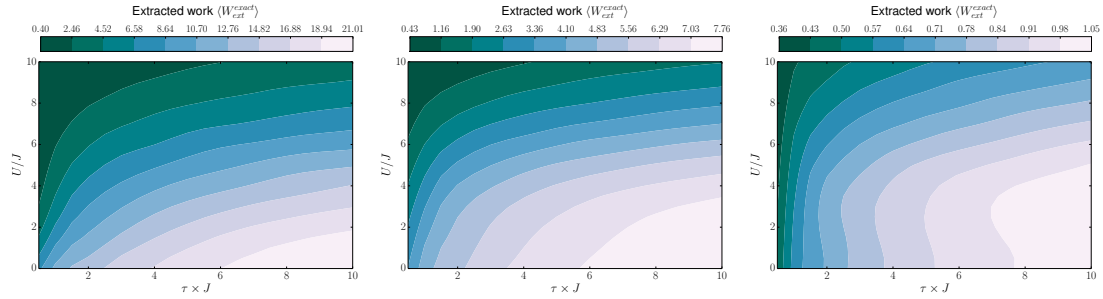

(a) $T = 0.2J/k_B$ (b) $T = 2.5J/k_B$ (c) $T = 20J/k_B$

Figure B.4: Exact work for the 4 sites slope at the three temperatures.

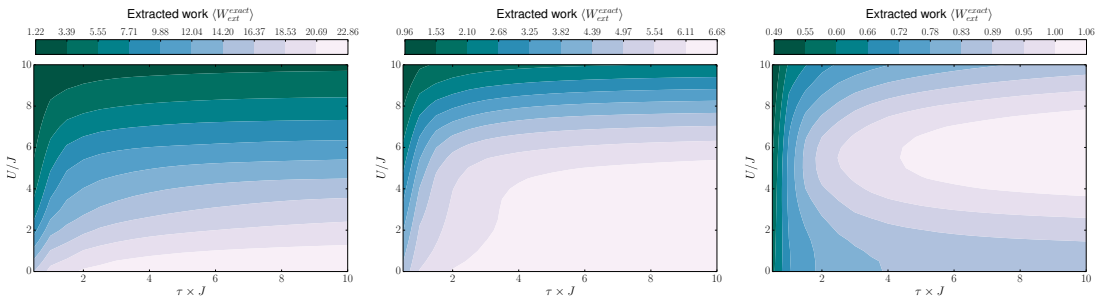

(a) $T = 0.2J/k_B$ (b) $T = 2.5J/k_B$ (c) $T = 20J/k_B$

Figure B.5: Exact work for the 6 sites zigzag at the three temperatures.

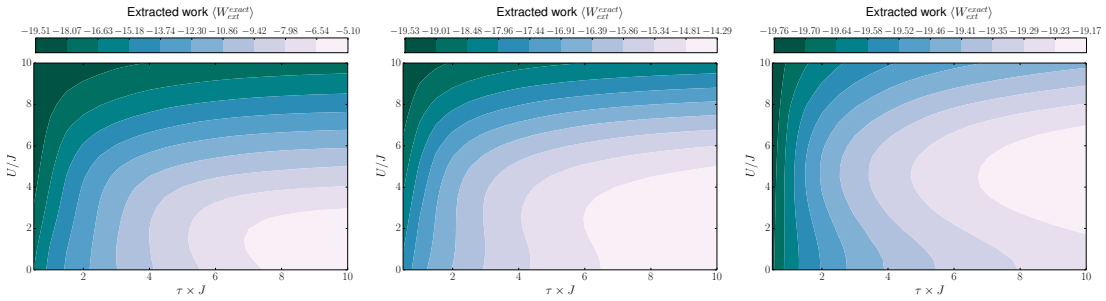

(a) $T = 0.2J/k_B$ (b) $T = 2.5J/k_B$ (c) $T = 20J/k_B$

Figure B.6: Exact work for the 6 sites teeth at the three temperatures.

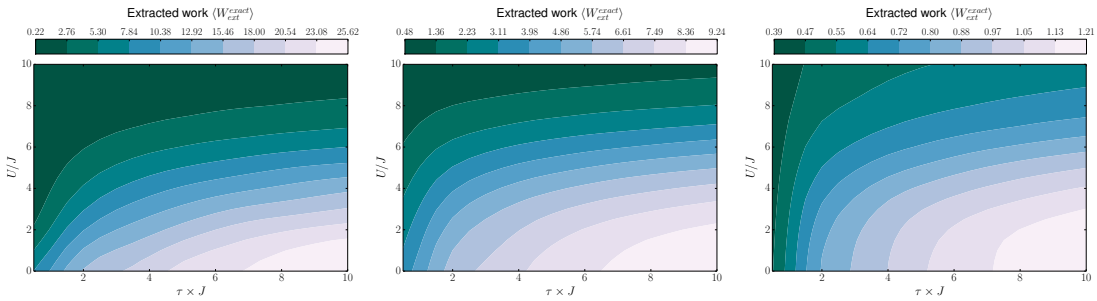

(a) $T = 0.2J/k_B$ (b) $T = 2.5J/k_B$ (c) $T = 20J/k_B$

Figure B.7: Exact work for the 6 sites slope at the three temperatures.

B.1.2 Exact entropy

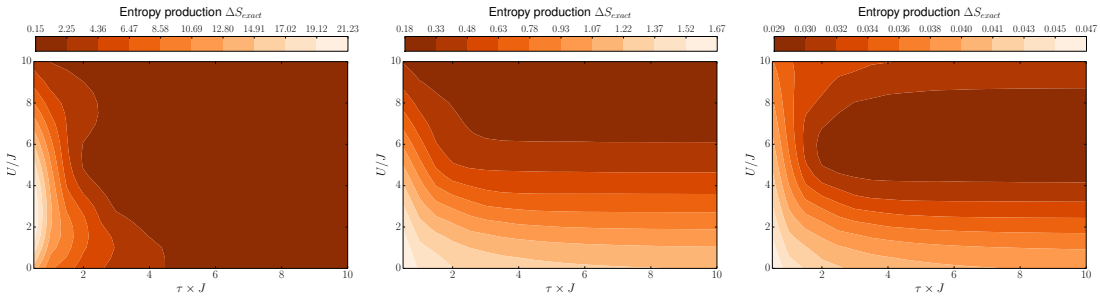

(a) $T = 0.2J/k_B$ (b) $T = 2.5J/k_B$ (c) $T = 20J/k_B$

Figure B.8: Exact entropy for the 2 sites zigzag at the three temperatures.

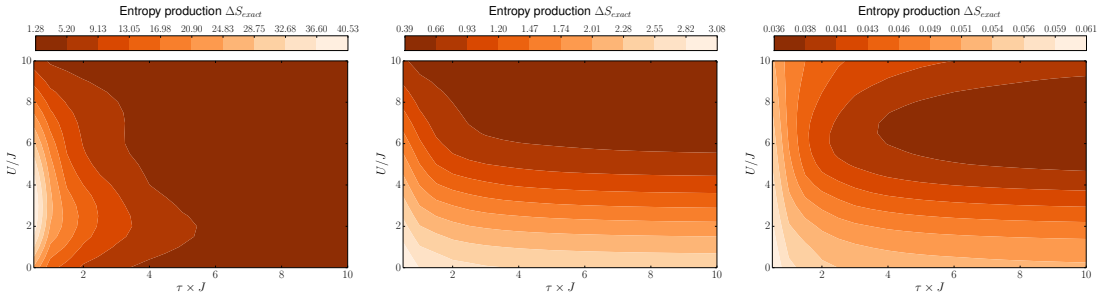

(a) $T = 0.2J/k_B$ (b) $T = 2.5J/k_B$ (c) $T = 20J/k_B$

Figure B.9: Exact entropy for the 4 sites zigzag at the three temperatures.

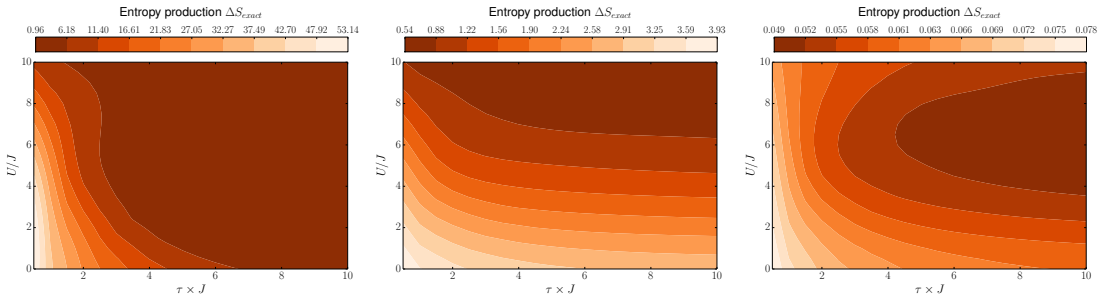

(a) $T = 0.2J/k_B$ (b) $T = 2.5J/k_B$ (c) $T = 20J/k_B$

Figure B.10: Exact entropy for the 4 sites teeth at the three temperatures.

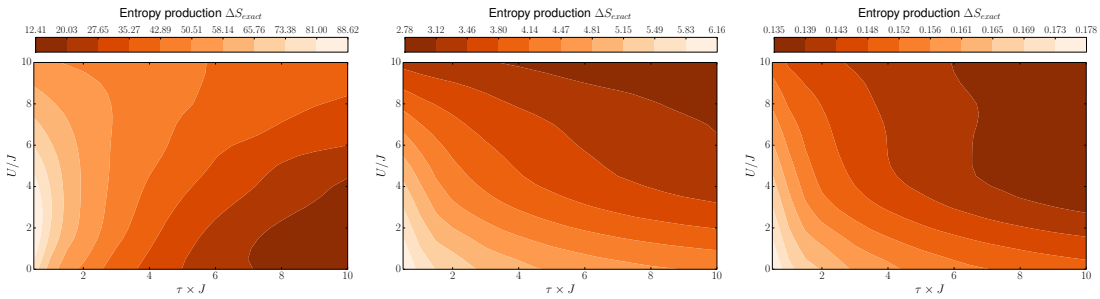

(a) $T = 0.2J/k_B$ (b) $T = 2.5J/k_B$ (c) $T = 20J/k_B$

Figure B.11: Exact entropy for the 4 sites slope at the three temperatures.

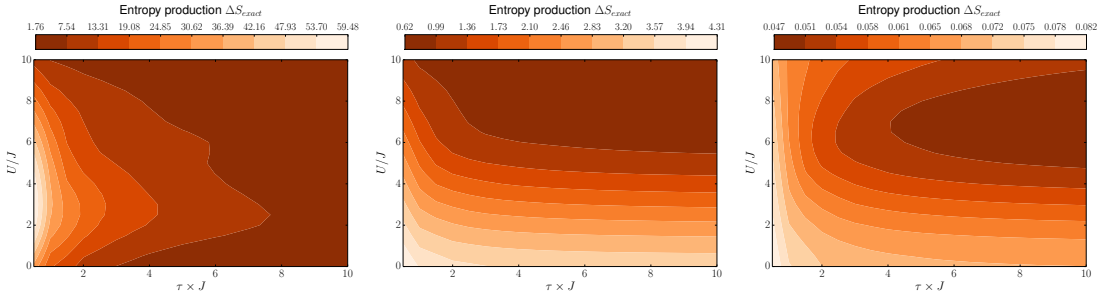

(a) $T = 0.2J/k_B$ (b) $T = 2.5J/k_B$ (c) $T = 20J/k_B$

Figure B.12: Exact entropy for the 6 sites zigzag at the three temperatures.

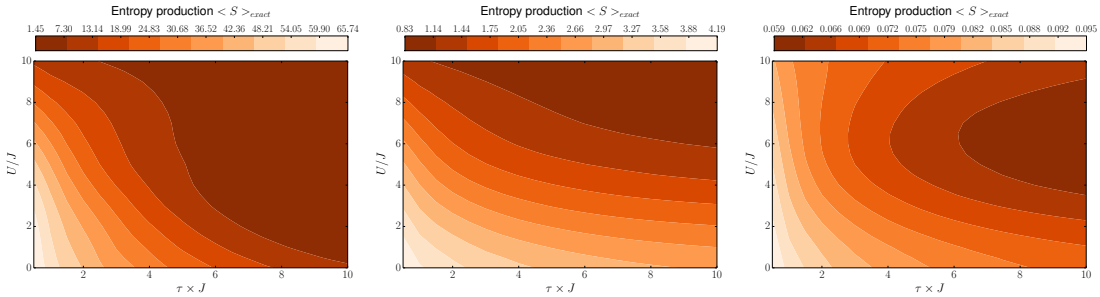

(a) $T = 0.2J/k_B$ (b) $T = 2.5J/k_B$ (c) $T = 20J/k_B$

Figure B.13: Exact entropy for the 6 sites teeth at the three temperatures.

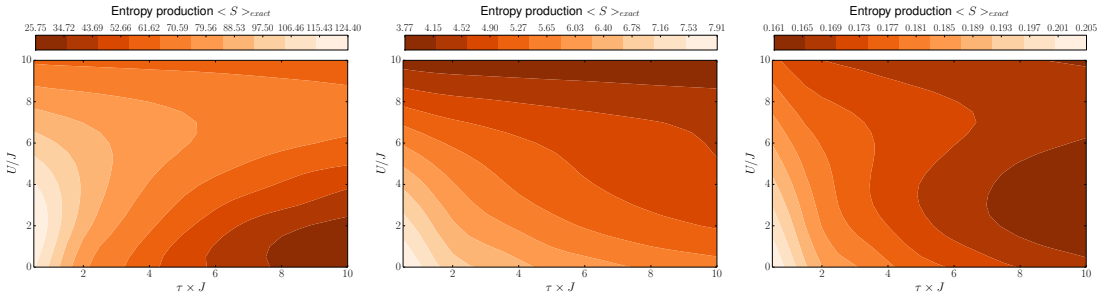

(a) $T = 0.2J/k_B$ (b) $T = 2.5J/k_B$ (c) $T = 20J/k_B$

Figure B.14: Exact entropy for the 6 sites slope at the three temperatures.

B.2 Work with time

Here we show the set of figures displaying the accumulation of average quantum work with time t (x-axis). Each figure shows three temperatures: low temperature $T = 0.2J/k_B$ (top row), medium temperature $T = 2.5J/k_B$ (middle row), and high temperature $T = 20J/k_B$ (bottom row). The columns distinguish between three different driving rates, with the left column as a fast drive, the middle column with a medium drive, and the right column with a slow drive. Each figure shows three different values of U: $U = 0J$ in red, $U = 5J$ in blue, and $U = 10J$ in green.

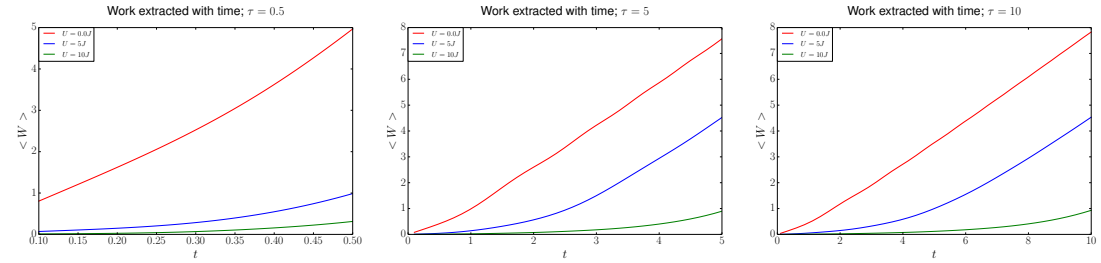

(a) $T = 0.2J/k_B$ $\tau = 0.5$. (b) $T = 0.2J/k_B$ $\tau = 5$. (c) $T = 0.2J/k_B$ $\tau = 10$.

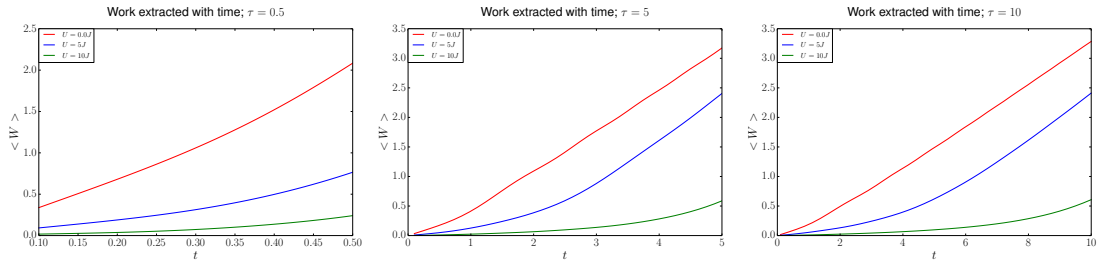

(d) $T = 2.5J/k_B$ $\tau = 0.5$. (e) $T = 2.5J/k_B$ $\tau = 5$. (f) $T = 2.5J/k_B$ $\tau = 10$.

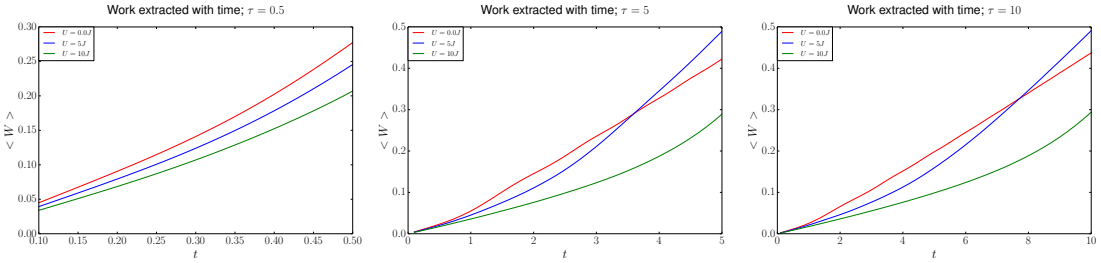

(g) $T = 20J/k_B$ $\tau = 0.5$. (h) $T = 20J/k_B$ $\tau = 5$. (i) $T = 20J/k_B$ $\tau = 10$.

Figure B.15: Average quantum work accumulation in the 2 site system with zigzag potential.

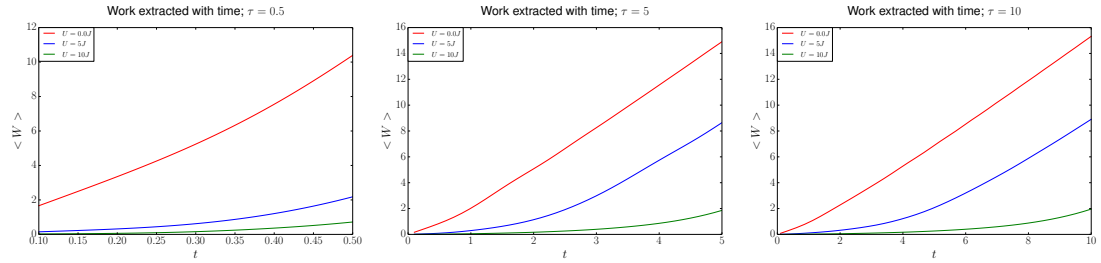

(a) $T = 0.2J/k_B$ $\tau = 0.5$. (b) $T = 0.2J/k_B$ $\tau = 5$. (c) $T = 0.2J/k_B$ $\tau = 10$.

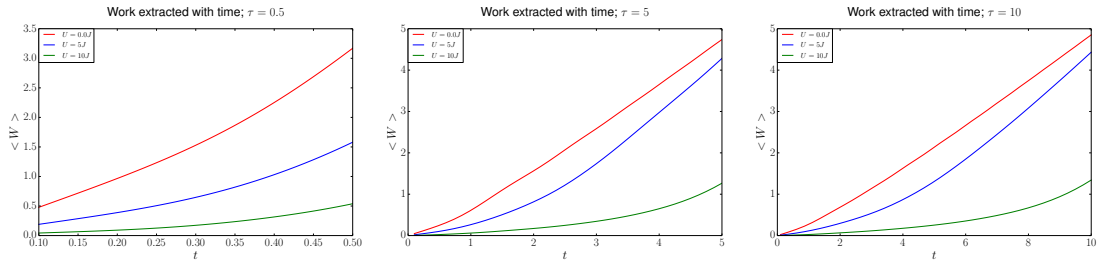

(d) $T = 2.5J/k_B$ $\tau = 0.5$. (e) $T = 2.5J/k_B$ $\tau = 5$. (f) $T = 2.5J/k_B$ $\tau = 10$.

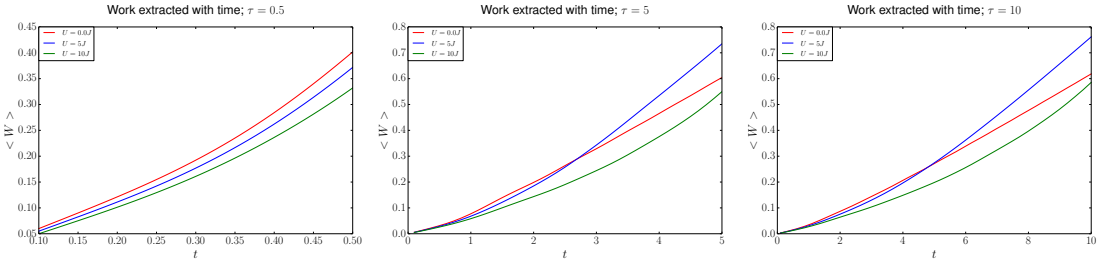

(g) $T = 20J/k_B$ $\tau = 0.5$. (h) $T = 20J/k_B$ $\tau = 5$. (i) $T = 20J/k_B$ $\tau = 10$.

Figure B.16: Average quantum work accumulation in the 4 site system with zigzag potential.

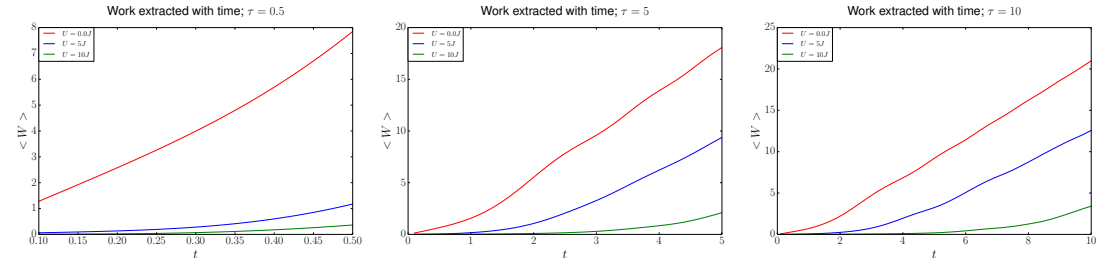

(a) $T = 0.2J/k_B$ $\tau = 0.5$. (b) $T = 0.2J/k_B$ $\tau = 5$. (c) $T = 0.2J/k_B$ $\tau = 10$.

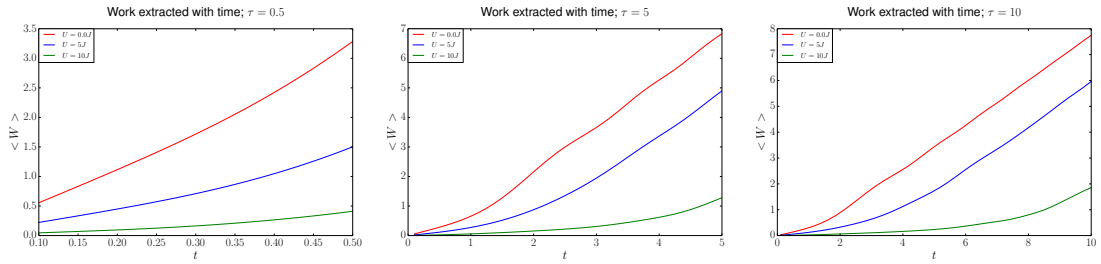

(d) $T = 2.5J/k_B$ $\tau = 0.5$. (e) $T = 2.5J/k_B$ $\tau = 5$. (f) $T = 2.5J/k_B$ $\tau = 10$.

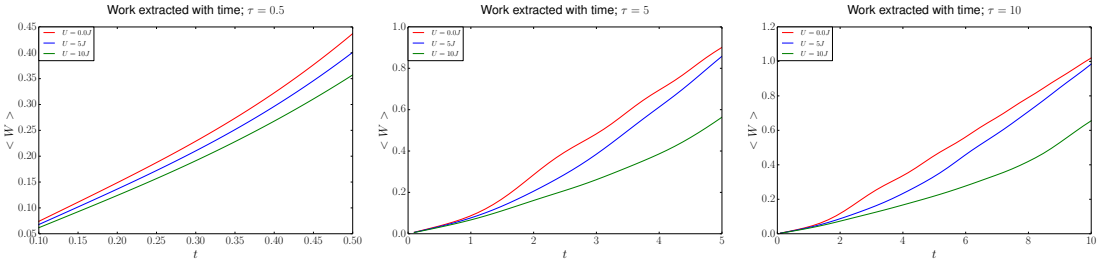

(g) $T = 20J/k_B$ $\tau = 0.5$. (h) $T = 20J/k_B$ $\tau = 5$. (i) $T = 20J/k_B$ $\tau = 10$.

Figure B.17: Average quantum work accumulation in the 4 site system with slope potential.

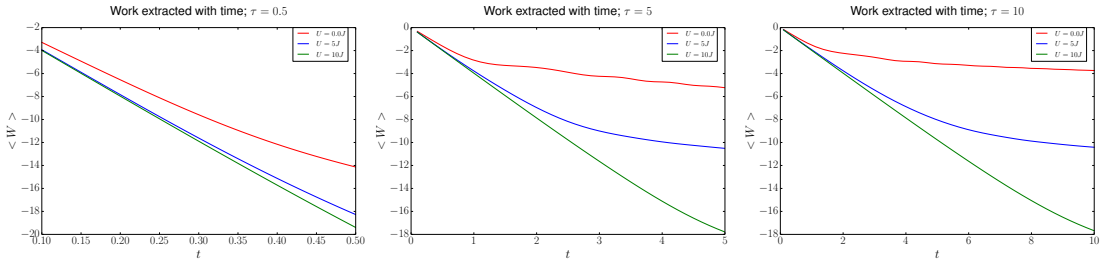

(a) $T = 0.2J/k_B$ $\tau = 0.5$. (b) $T = 0.2J/k_B$ $\tau = 5$. (c) $T = 0.2J/k_B$ $\tau = 10$.

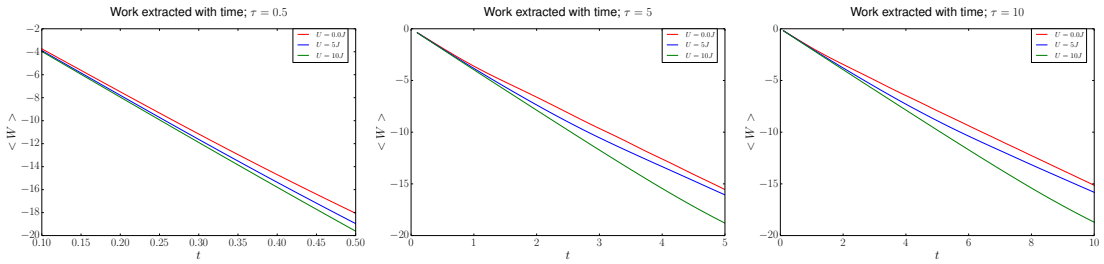

(d) $T = 2.5J/k_B$ $\tau = 0.5$. (e) $T = 2.5J/k_B$ $\tau = 5$. (f) $T = 2.5J/k_B$ $\tau = 10$.

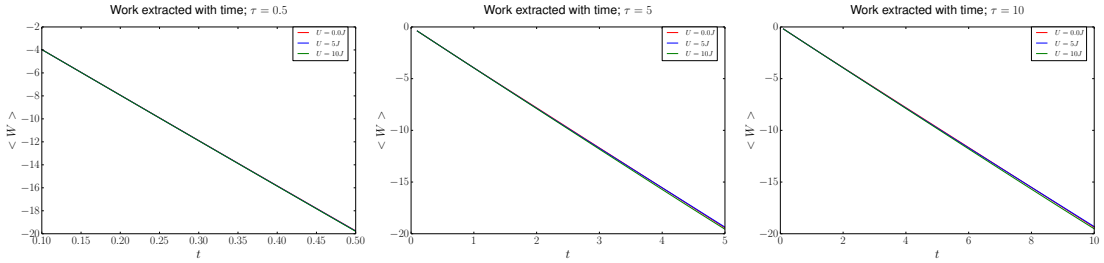

(g) $T = 20J/k_B$ $\tau = 0.5$. (h) $T = 20J/k_B$ $\tau = 5$. (i) $T = 20J/k_B$ $\tau = 10$.

Figure B.18: Average quantum work accumulation in the 4 site system with teeth potential.

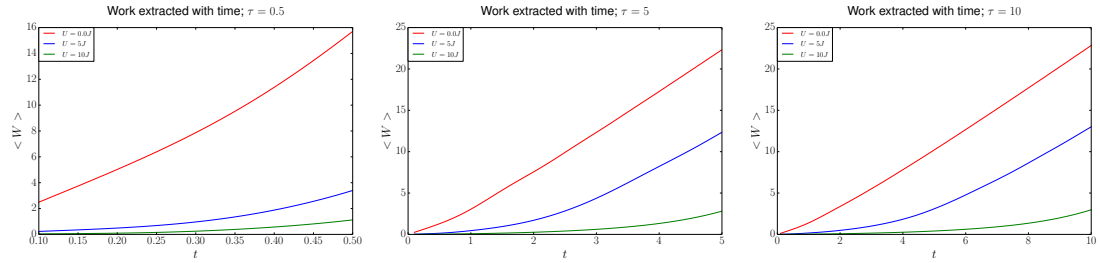

(a) $T = 0.2J/k_B$ $\tau = 0.5$. (b) $T = 0.2J/k_B$ $\tau = 5$. (c) $T = 0.2J/k_B$ $\tau = 10$.

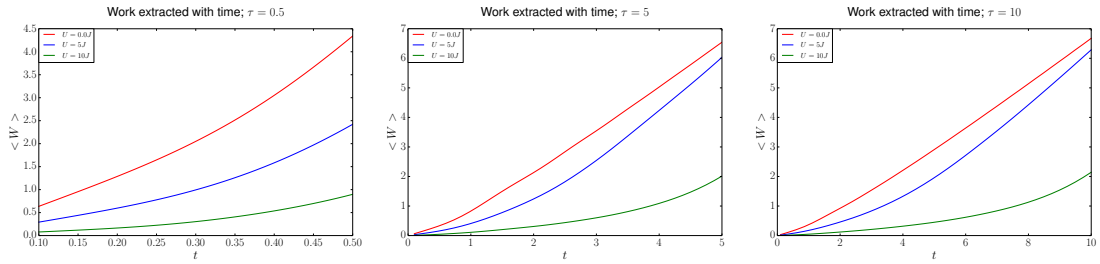

(d) $T = 2.5J/k_B$ $\tau = 0.5$. (e) $T = 2.5J/k_B$ $\tau = 5$. (f) $T = 2.5J/k_B$ $\tau = 10$.

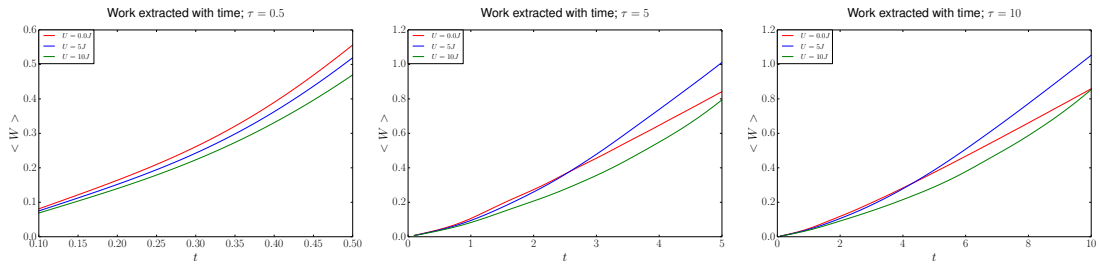

(g) $T = 20J/k_B$ $\tau = 0.5$. (h) $T = 20J/k_B$ $\tau = 5$. (i) $T = 20J/k_B$ $\tau = 10$.

Figure B.19: Average quantum work accumulation in the 6 site system with zigzag potential.

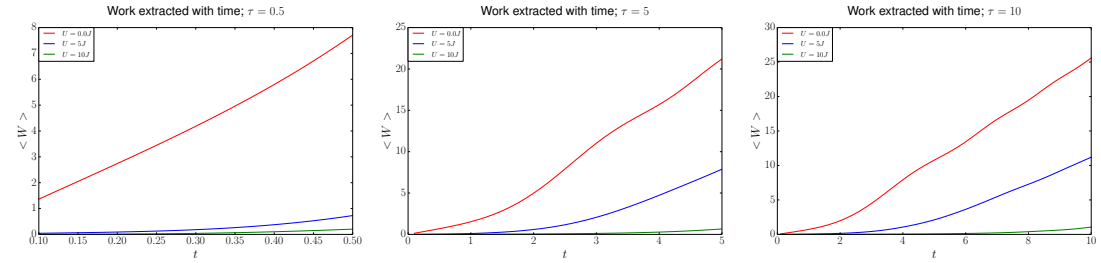

(a) $T = 0.2J/k_B$ $\tau = 0.5$. (b) $T = 0.2J/k_B$ $\tau = 5$. (c) $T = 0.2J/k_B$ $\tau = 10$.

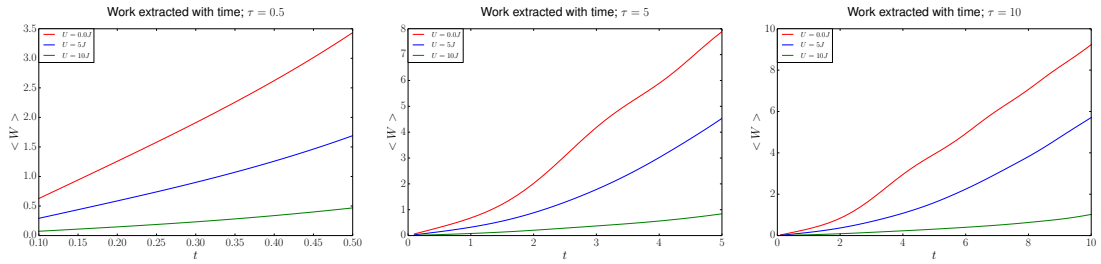

(d) $T = 2.5J/k_B$ $\tau = 0.5$. (e) $T = 2.5J/k_B$ $\tau = 5$. (f) $T = 2.5J/k_B$ $\tau = 10$.

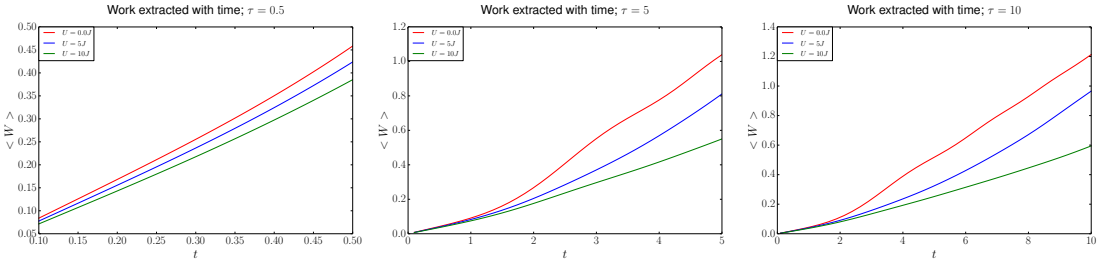

(g) $T = 20J/k_B$ $\tau = 0.5$. (h) $T = 20J/k_B$ $\tau = 5$. (i) $T = 20J/k_B$ $\tau = 10$.

Figure B.20: Average quantum work accumulation in the 6 site system with slope potential.

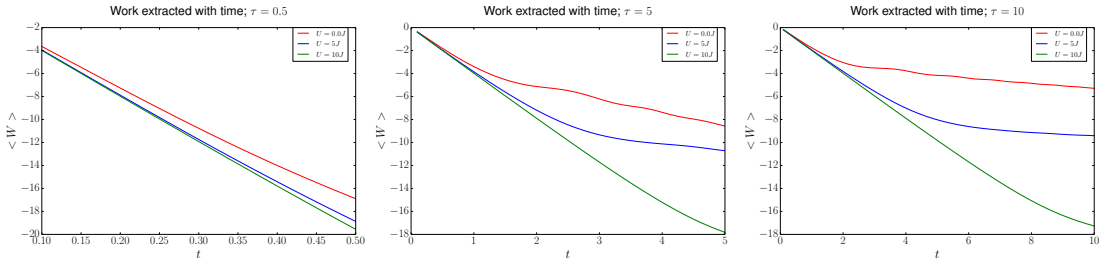

(a) $T = 0.2J/k_B$ $\tau = 0.5$. (b) $T = 0.2J/k_B$ $\tau = 5$. (c) $T = 0.2J/k_B$ $\tau = 10$.

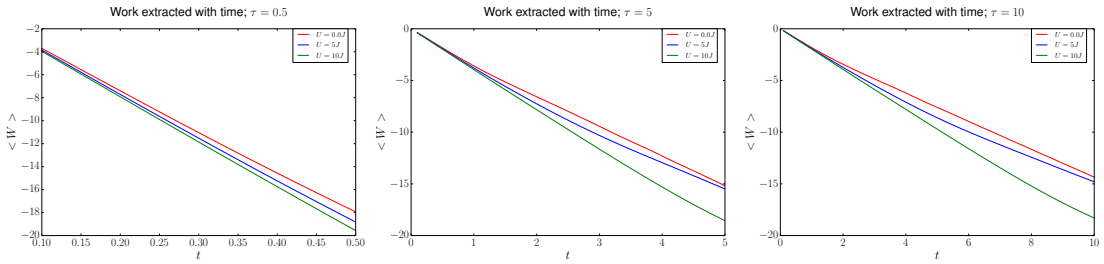

(d) $T = 2.5J/k_B$ $\tau = 0.5$. (e) $T = 2.5J/k_B$ $\tau = 5$. (f) $T = 2.5J/k_B$ $\tau = 10$.

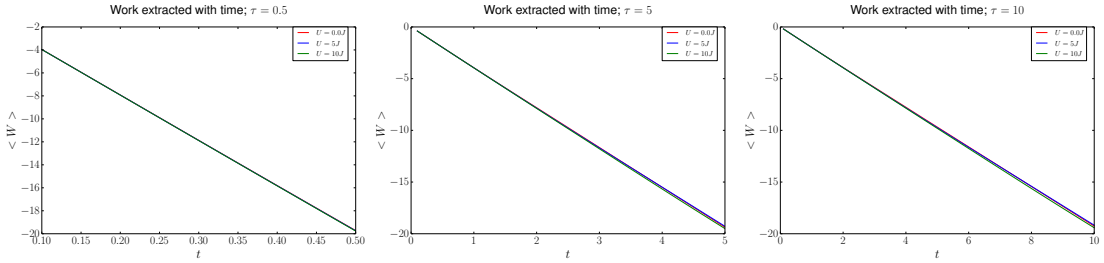

(g) $T = 20J/k_B$ $\tau = 0.5$. (h) $T = 20J/k_B$ $\tau = 5$. (i) $T = 20J/k_B$ $\tau = 10$.

Figure B.21: Average quantum work accumulation in the 6 site system with teeth potential.

C. Testing the variants of the hybrid approximation

The calculation of the quantum work has 6 places where one can use either an approximation or the exact term. These are $\hat{\rho}(0)$, $\hat{H}(0)$, $\hat{\rho}(\tau)$, and $\hat{H}(\tau)$ in the equation of the quantum work (equation 2.76), and then $\hat{\rho}(t)$ and $\hat{H}(t)$ in the evolution from $\hat{\rho}(0)$ to $\hat{\rho}(\tau)$.

When evolving the system, we can choose an approximation for the initial state to be used in $\hat{\rho}(t) = \mathcal{U}\hat{\rho}(0)\mathcal{U}^{\dagger}$, denoted by $\hat{\rho}_0(t)$. However, in this evolution, we can also choose an approximation for $\mathcal{U}$ through the approximation of $\hat{H}(t)$. The mixture of these two approximations gives the approximation of $\hat{\rho}(\tau)$. For example, using the exact initial state for $\hat{\rho}(t)$ but with the non-interacting Hamiltonian for $\mathcal{U}$ will mean $\hat{\rho}(\tau)$ is a combination of the exact and the non-interacting approximations, denoted by $\hat{\rho}^{ex+NI}(\tau)$.

Other than $\hat{\rho}(\tau)$, it is best to keep the approximations of $\hat{\rho}(0)$ and $\hat{\rho}_0(t)$ [the initial state used in the calculation of $\hat{\rho}(t)$] consistent, and likewise with the Hamiltonians, to avoid sudden changes in the constituent terms of the calculation. Because it is the Hamiltonian which includes the many-body interactions during the evolution, it is the Hamiltonian which should be approximated to reduce the complexity of the calculation. As described in chapter 7, the initial state shall be exact to include memory of the interactions in the evolution. However there are several possible combinations of exact and approximated terms in the calculation. We shall use the non-interacting Hamiltonian for the dynamics to demonstrate the variants of applying the hybrid approximation. Table C.1 shows four of these combinations which we studied.

In the following sections we see how each combination is translated into equation 2.76 and what the contour plots of average quantum work look like for 2 sites with zigzag potential at $T = 2.5J/k_B$. We find that the Hamiltonians must have the same approximation throughout the calculation, otherwise the mismatch in eigenstates between $\hat{H}^{ex}$ and $\hat{H}^{NI}$ leads to spurious oscillations

Method	$\hat{\rho}(0)$	$\hat{H}(0)$	$\hat{\rho}_0(t)$	$\hat{H}(t)$	$\hat{\rho}(\tau)$	$\hat{H}(\tau)$
1	ex	ex	ex	NI	ex+NI	ex
2	ex	ex	NI	NI	NI	ex
3	NI	ex	NI	NI	NI	ex
4	ex	NI	ex	NI	ex+NI	NI

Table C.1: A table to summarise where the approximations can be implemented in the average quantum work calculation. Here, "ex" means the exact form is used; "NI" means the non-interacting approximation was used; and "ex+NI" means the final state is obtained using the exact initial state evolved using the non-interacting Hamiltonian.

in the results.

C.1 First method - exact states, exact $\hat{H}(0)$, and exact $\hat{H}(\tau)$, with non-interacting evolution Hamiltonian

The first method looks at only approximating the evolution Hamiltonian, and corresponds to

$$\langle W \rangle = \mathrm{Tr}\left[\hat{\rho}^{ex+NI}(\tau)\hat{H}^{ex}(\tau)\right] - \mathrm{Tr}\left[\hat{\rho}^{ex}(0)\hat{H}^{ex}(0)\right], \tag{C.1}$$

where $\hat{H}^{ex}(0)$ is the exact initial Hamiltonian, $\hat{\rho}^{ex}(0)$ is the exact initial state calculated from $\hat{H}^{ex}(0)$, $\hat{H}^{ex}(\tau)$ is the exact final Hamiltonian, and $\hat{\rho}_\tau^{ex+NI}$ is the final state evolved from the exact initial state through a unitary transformation, U_{NI}, using the non-interacting Hamiltonian $\hat{H}^{NI}$.

Figure C.1 shows the average work extracted and relative error for 2 sites with zigzag potential at the medium temperature for the usual range of correlation strengths and driving times used in this thesis. These results are not as good as one could have hoped for this approximation since we have only approximated the evolution Hamiltonian and nothing else. The oscillations are understood to be arising from the fact that the initial and final eigenstates are not eigenstates of the evolution Hamiltonian.

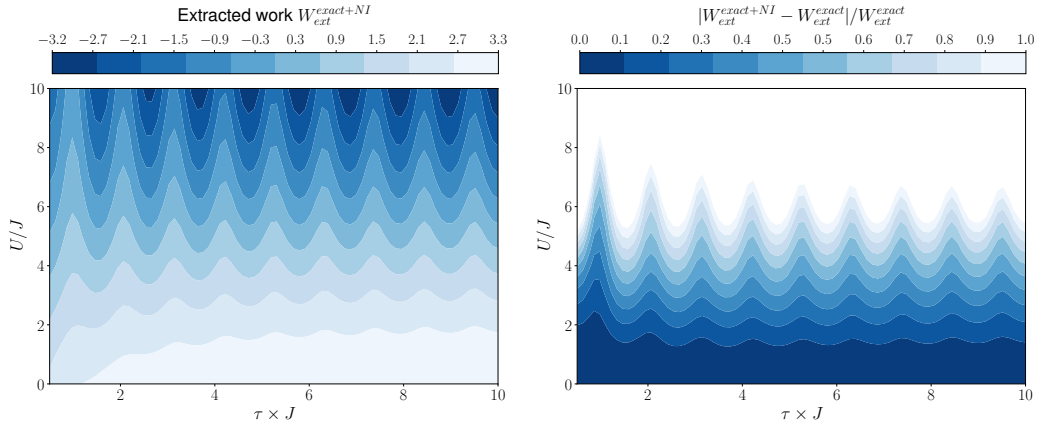

(a) Quantum work

(b) Relative error in quantum work

Figure C.1: Work and relative error for method 1 for a 2 site Hubbard model with zigzag potential at $T = 2.5J/k_B$ over $0 \leq U/J \leq 10$ (y-axis) and $0.5 \leq \tau \times J10$ (x-axis).

C.2 Second method - non-interacting evolution terms

The second method looks at approximating all terms in the evolution to be non-interacting. It is written as

$$\langle W \rangle = \mathrm{Tr}\left[\hat{\rho}^{NI}(\tau)\hat{H}^{ex}(\tau)\right] - \mathrm{Tr}\left[\hat{\rho}^{ex}(0)\hat{H}^{ex}(0)\right], \tag{C.2}$$

where we have used the exact initial state in the calculation of the second term, but then evolved the non-interacting state through the non-interacting evolution to get $\hat{\rho}^{NI}(\tau)$.

Figure C.2 gives the corresponding figures for this calculation, which are mildly better than the previous approximation, however the oscillations are still evident.

C.3 Third method - matching all states

Now we shall look at what happens if we match the initial state approximation with the evolution approximation, i.e. we shall use the non-interacting state for the calculation of the second term as well as the evolution:

$$\langle W \rangle = \mathrm{Tr}\left[\hat{\rho}^{NI}(\tau)\hat{H}^{ex}(\tau)\right] - \mathrm{Tr}\left[\hat{\rho}^{NI}(0)\hat{H}^{ex}(0)\right]. \tag{C.3}$$

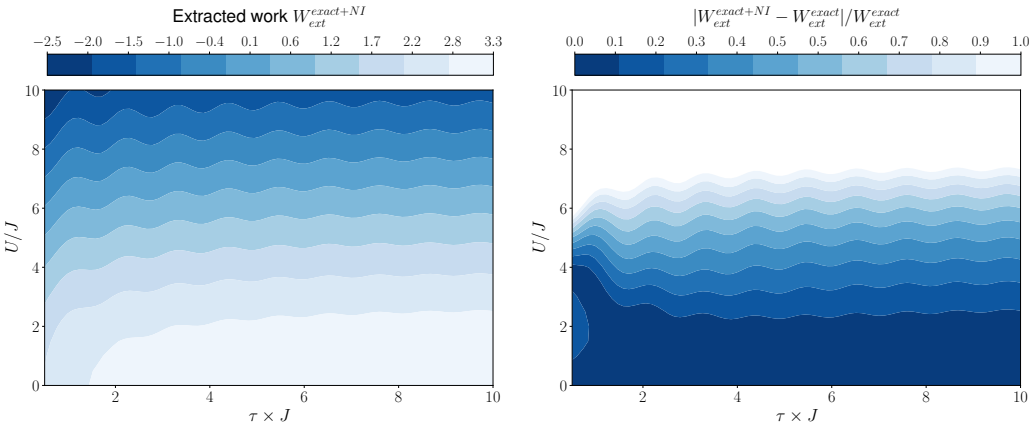

(a) Quantum work (b) Relative error in quantum work

Figure C.2: Work and relative error for method 2 for 2 sites with zigzag potential at $T = 2.5J/k_B$ over $0 \leq U/J \leq 10$ (y-axis) and $0.5 \leq \tau \times J10$ (x-axis).

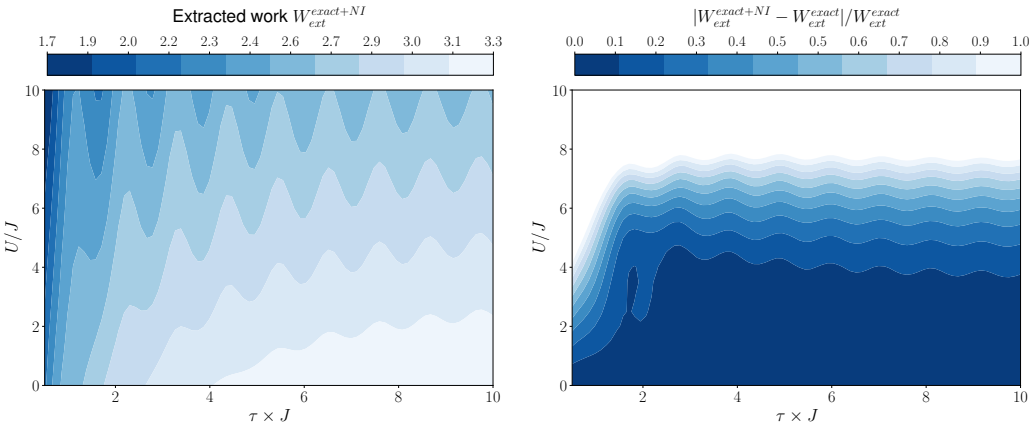

(a) Quantum work (b) Relative error in quantum work

Figure C.3: Work and relative error for method 3 for 2 sites with zigzag potential at $T = 2.5J/k_B$ over $0 \leq U/J \leq 10$ (y-axis) and $0.5 \leq \tau \times J10$ (x-axis).

From the results in figure C.3, we can see how this approximation appears more like the purely non-interacting approximation, with mild improvements, and with improvements in the accuracy compared to methods 1 and 2. However it still suffers from the oscillations.

C.4 Fourth method - matching Hamiltonians

As we can see from table C.1, for methods 1, 2, and 3, the eigenstates from the initial and final (exact) Hamiltonians are not eigenstates of the evolution (non-interacting) Hamiltonian at those times. We now try to match the eigenstates by having a consistent approximation for the Hamiltonians, rather than matching the states.

To do this we shall keep the initial state as exact and keep the evolution as non-interacting, but will make the initial and final Hamiltonians as non-interacting:

$$\langle W \rangle = \mathrm{Tr}\left[\hat{\rho}^{NI+ex}(\tau)\hat{H}^{NI}(\tau)\right] - \mathrm{Tr}\left[\hat{\rho}^{ex}(0)\hat{H}^{NI}(0)\right]. \tag{C.4}$$

The results from this approximation are very promising, as seen in figure C.4, and seem to imply it is more important to ensure the Hamiltonians are consistent (from initial, through evolution, to the final), rather than them being exact. This is physically seems to make sense as the eigenstates should match for the entire evolution, and any mismatch could (and indeed appears to) lead to spurious oscillations in the results.

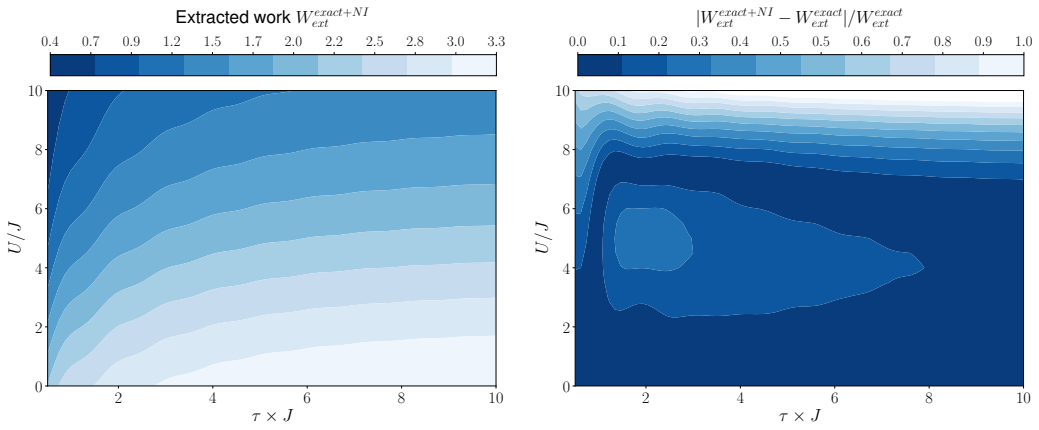

(a) Quantum work

(b) Relative error in quantum work

Figure C.4: Work and relative error for method 4 for 2 sites with zigzag potential at $T = 2.5J/k_B$ over $0 \leq U/J \leq 10$ (y-axis) and $0.5 \leq \tau \times J10$ (x-axis).

D. Complete set of approximated quantum thermodynamic properties

D.1 Non-interacting quantum work and entropy

In this section, we will display the non-interacting (NI) quantum work and entropy production as described in chapter 7 for the complete parameter set (i.e. 2, 4, and 6 sites, with zigzag, teeth, and slope potentials, for $T = 0.2J/k_B$, $T = 2.5J/k_B$, and $T = 20J/k_B$) showing $0 \leq U/J \leq 10$ along the y-axis and $0.5 \leq \tau \times J \leq 10$ along the x-axis.

D.1.1 Non-interacting work

Calculated using $\langle W_{ext}^{NI} \rangle = \mathrm{Tr}\left[\rho^{NI}(0)\hat{H}^{NI}(0)\right] - \mathrm{Tr}\left[\rho^{NI}(\tau)\hat{H}^{NI}(\tau)\right]$ with non-interacting dynamics.

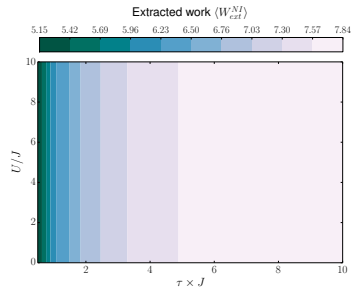

(a) NI quantum work $T = 0.2J/k_B$

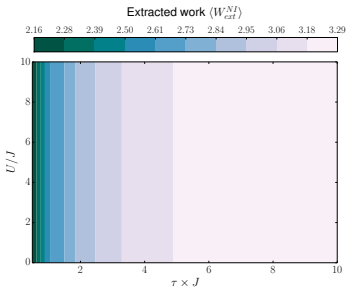

(b) NI quantum work $T = 2.5J/k_B$

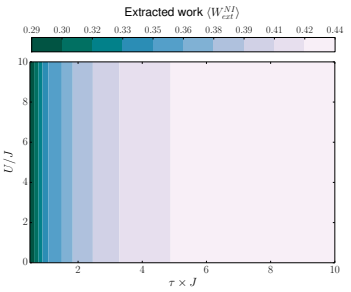

(c) NI quantum work $T = 20J/k_B$

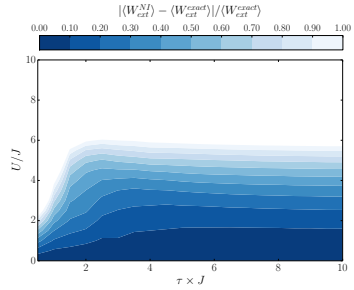

(d) NI quantum work relative error $T = 0.2J/k_B$

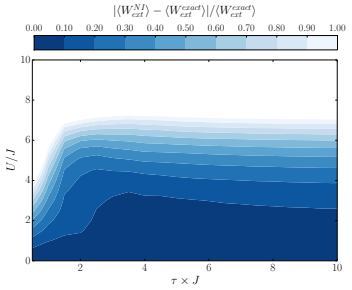

(e) NI quantum work relative error $T = 2.5J/k_B$

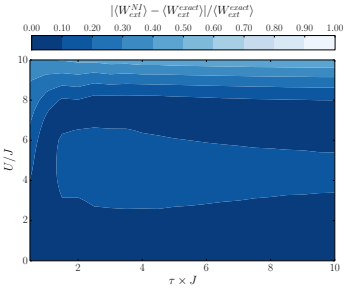

(f) NI quantum work relative error $T = 20J/k_B$

Figure D.1: NI work (top row) and relative error (bottom row) for the 2 sites zigzag at the three temperatures.

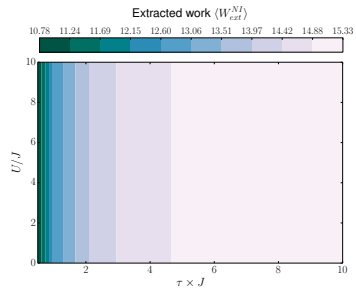

(a) NI quantum work $T = 0.2J/k_B$

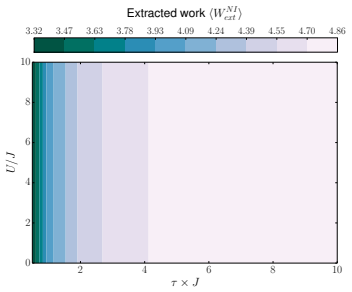

(b) NI quantum work $T = 2.5J/k_B$

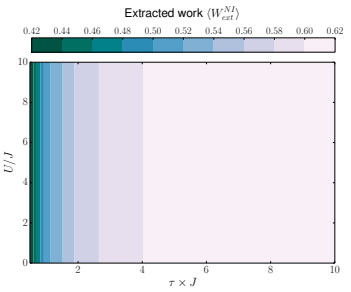

(c) NI quantum work $T = 20J/k_B$

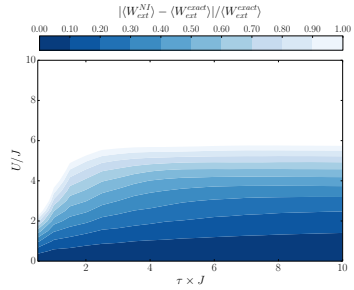

(d) NI quantum work relative error $T = 0.2J/k_B$

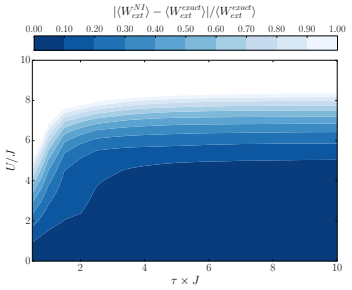

(e) NI quantum work relative error $T = 2.5J/k_B$

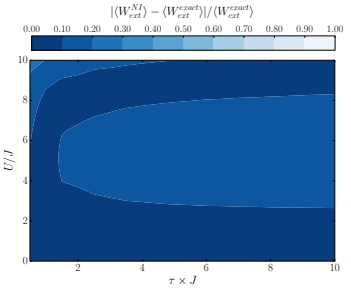

(f) NI quantum work relative error $T = 20J/k_B$

Figure D.2: NI work (top row) and relative error (bottom row) for the 4 sites zigzag at the three temperatures.

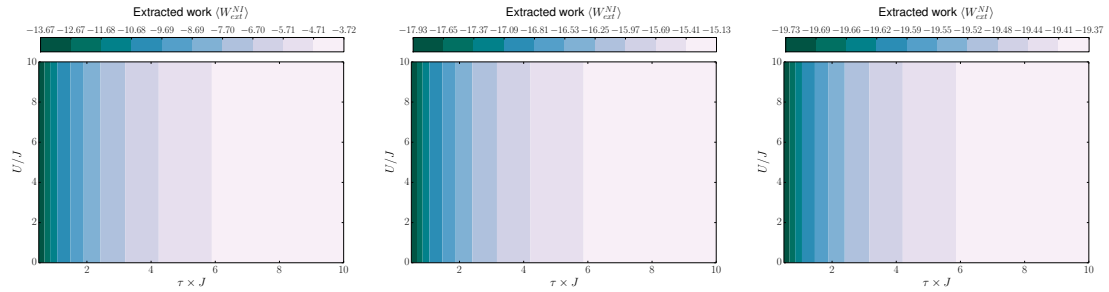

(a) NI quantum work $T = 0.2J/k_B$ (b) NI quantum work $T = 2.5J/k_B$ (c) NI quantum work $T = 20J/k_B$

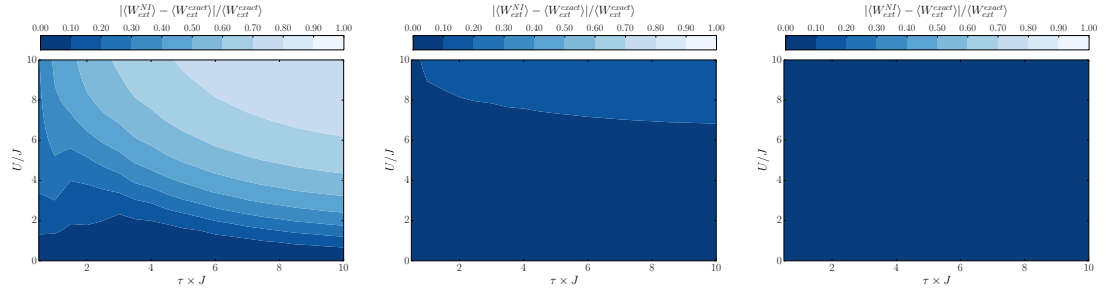

(d) NI quantum work relative error $T = 0.2J/k_B$ (e) NI quantum work relative error $T = 2.5J/k_B$ (f) NI quantum work relative error $T = 20J/k_B$

Figure D.3: NI work (top row) and relative error (bottom row) for the 4 sites teeth at the three temperatures.

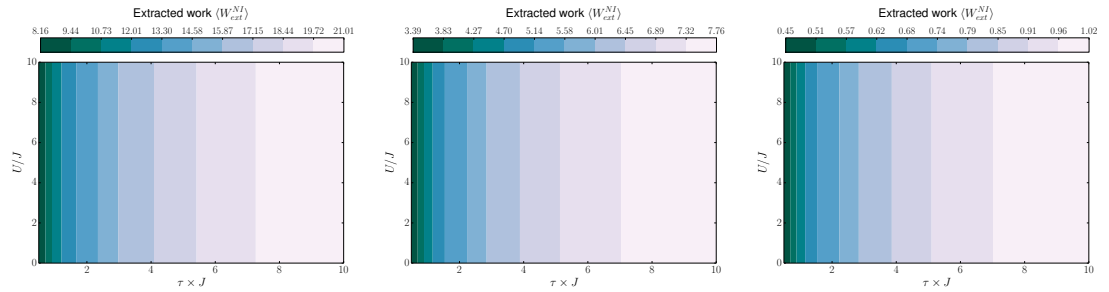

(a) NI quantum work $T = 0.2J/k_B$ (b) NI quantum work $T = 2.5J/k_B$ (c) NI quantum work $T = 20J/k_B$

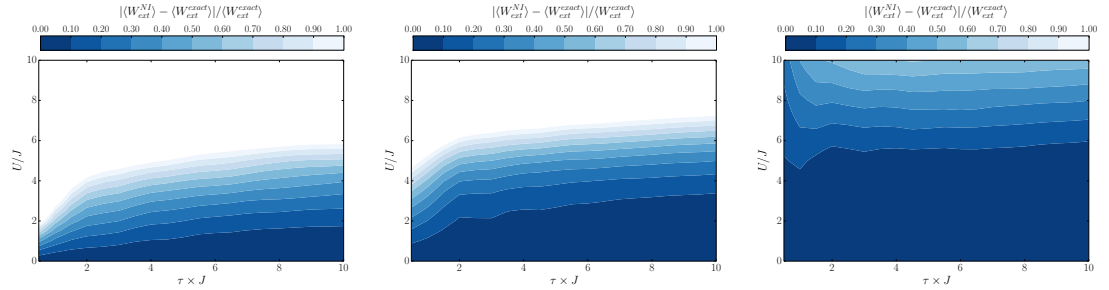

(d) NI quantum work relative error $T = 0.2J/k_B$ (e) NI quantum work relative error $T = 2.5J/k_B$ (f) NI quantum work relative error $T = 20J/k_B$

Figure D.4: NI work (top row) and relative error (bottom row) for the 4 sites slope at the three temperatures.

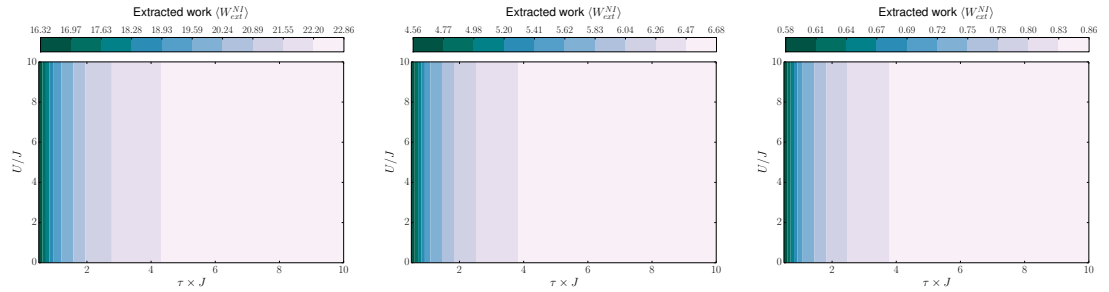

(a) NI quantum work $T = 0.2J/k_B$ (b) NI quantum work $T = 2.5J/k_B$ (c) NI quantum work $T = 20J/k_B$

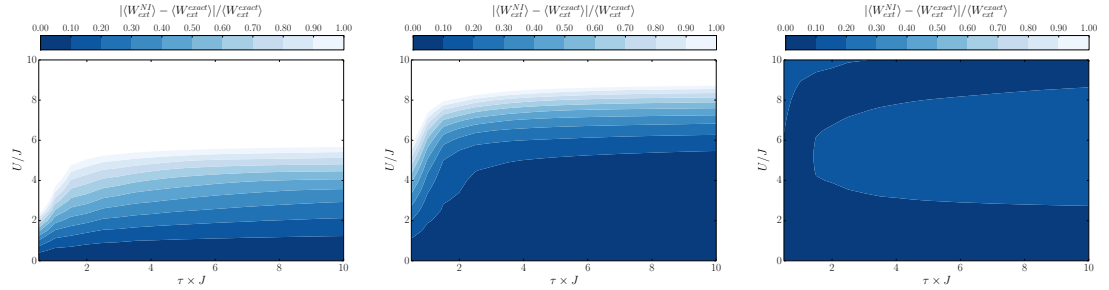

(d) NI quantum work relative error $T = 0.2J/k_B$ (e) NI quantum work relative error $T = 2.5J/k_B$ (f) NI quantum work relative error $T = 20J/k_B$

Figure D.5: NI work (top row) and relative error (bottom row) for the 6 sites zigzag at the three temperatures.

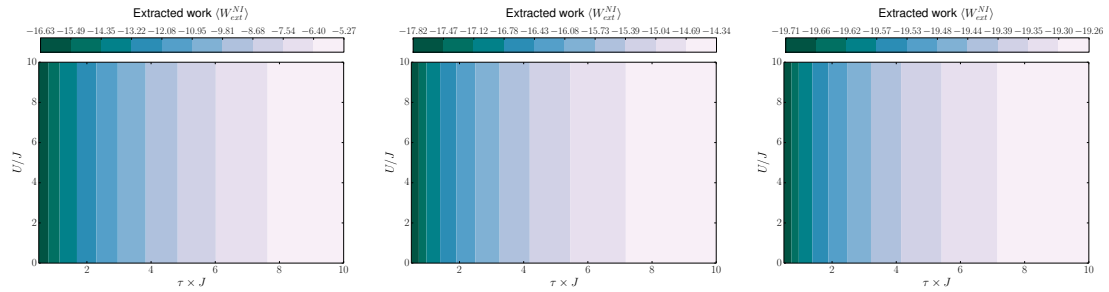

(a) NI quantum work $T = 0.2J/k_B$ (b) NI quantum work $T = 2.5J/k_B$ (c) NI quantum work $T = 20J/k_B$

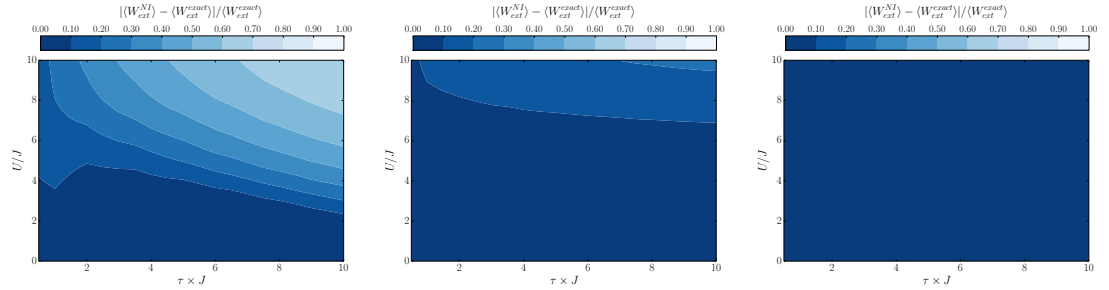

(d) NI quantum work relative error $T = 0.2J/k_B$ (e) NI quantum work relative error $T = 2.5J/k_B$ (f) NI quantum work relative error $T = 20J/k_B$

Figure D.6: NI work (top row) and relative error (bottom row) for the 6 sites teeth at the three temperatures.

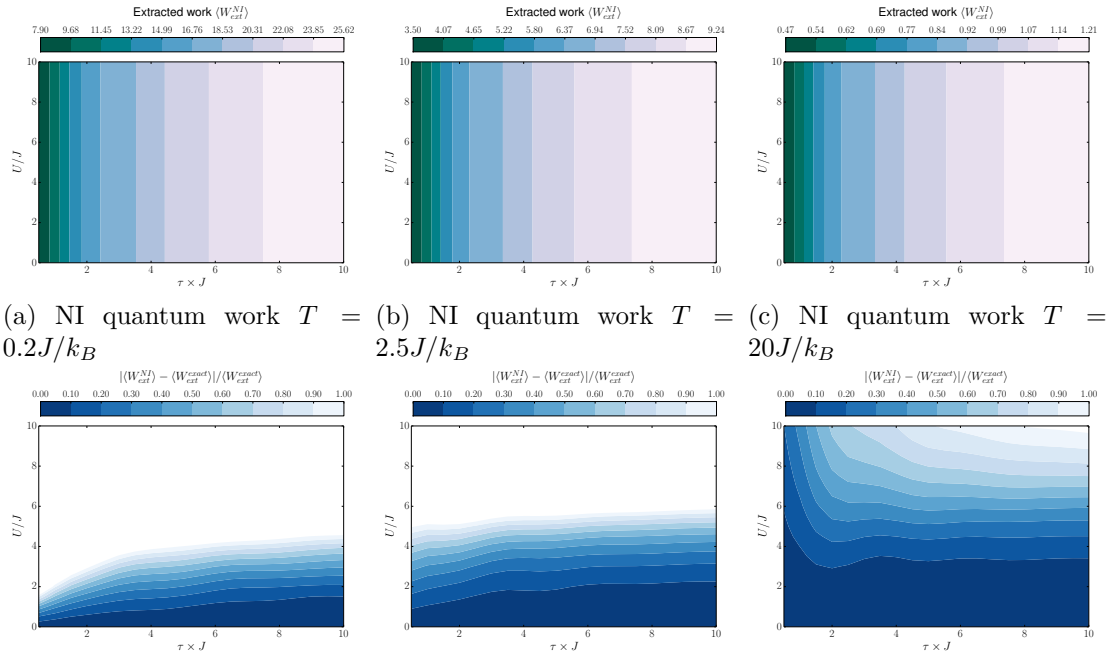

(a) NI quantum work $T = 0.2J/k_B$

(b) NI quantum work $T = 2.5J/k_B$

(c) NI quantum work $T = 20J/k_B$

(d) NI quantum work relative error $T = 0.2J/k_B$

(e) NI quantum work relative error $T = 2.5J/k_B$

(f) NI quantum work relative error $T = 20J/k_B$

Figure D.7: NI work (top row) and relative error (bottom row) for the 6 sites slope at the three temperatures.

D.1.2 NI entropy

The entropy is calculated by $\Delta S_{NI} = \beta \left(\langle W^{NI} \rangle - \Delta F^{NI} \right)$, where $\Delta F^{NI} = -(1/\beta) \ln \left(Z_\tau^{NI} / Z_0^{NI} \right)$.

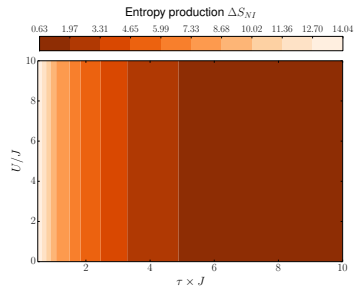

(a) NI entropy $T = 0.2J/k_B$

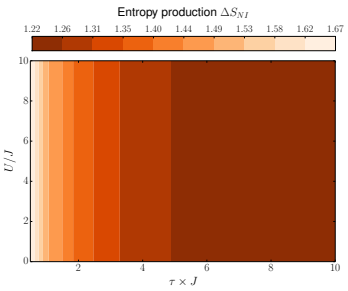

(b) NI entropy $T = 2.5J/k_B$

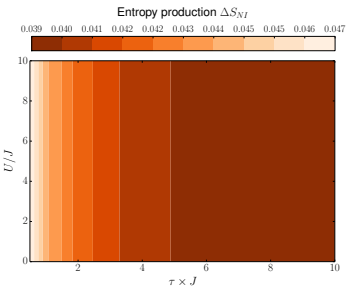

(c) NI entropy $T = 20J/k_B$

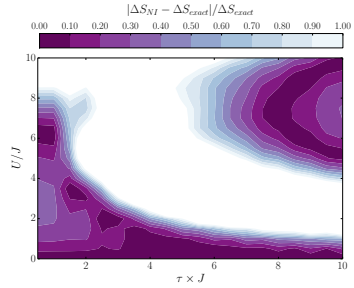

(d) NI entropy relative error $T = 0.2J/k_B$

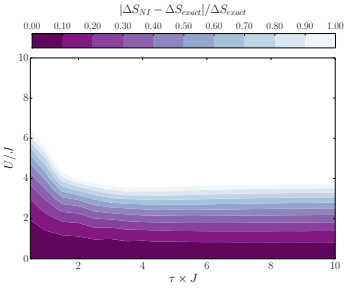

(e) NI entropy relative error $T = 2.5J/k_B$

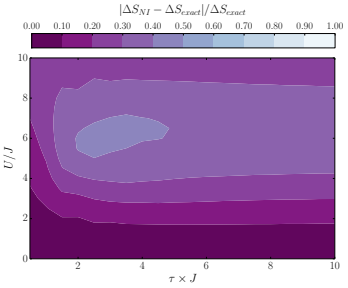

(f) NI entropy relative error $T = 20J/k_B$

Figure D.8: NI entropy (top row) and relative error (bottom row) for the 2 sites zigzag at the three temperatures.

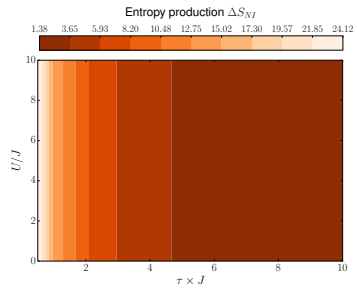

(a) NI entropy $T = 0.2J/k_B$

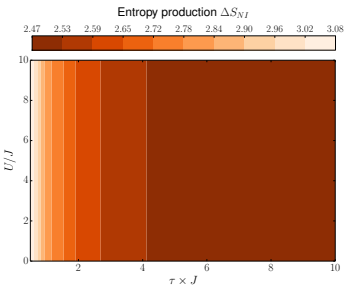

(b) NI entropy $T = 2.5J/k_B$

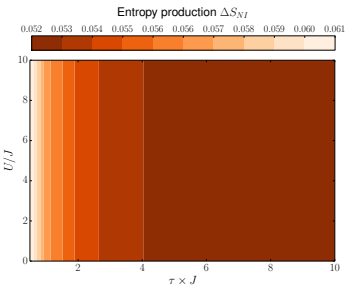

(c) NI entropy $T = 20J/k_B$

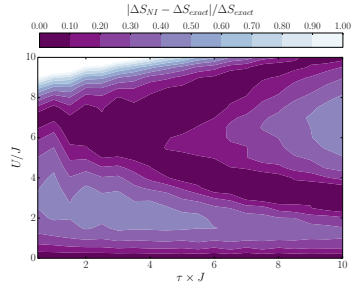

(d) NI entropy relative error $T = 0.2J/k_B$

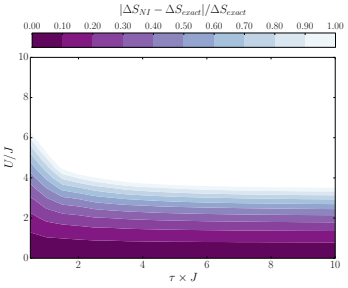

(e) NI entropy relative error $T = 2.5J/k_B$

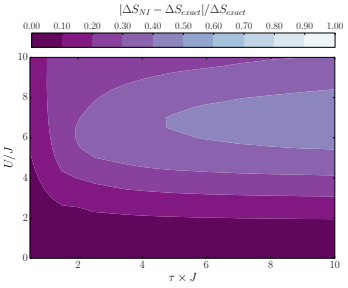

(f) NI entropy relative error $T = 20J/k_B$

Figure D.9: NI entropy (top row) and relative error (bottom row) for the 4 sites zigzag at the three temperatures.

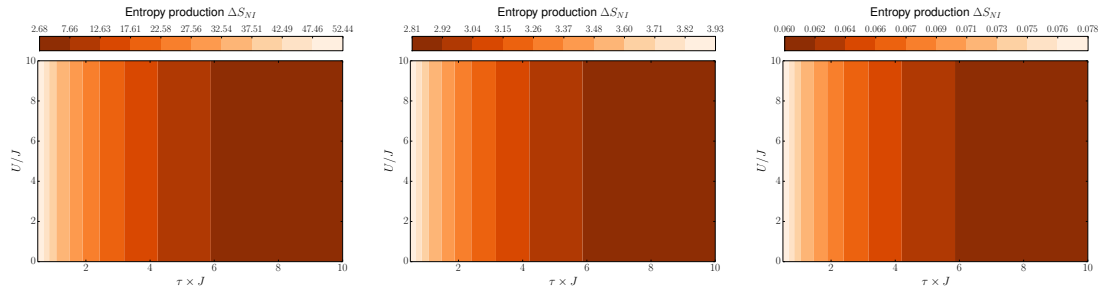

(a) NI entropy $T = 0.2J/k_B$ (b) NI entropy $T = 2.5J/k_B$ (c) NI entropy $T = 20J/k_B$

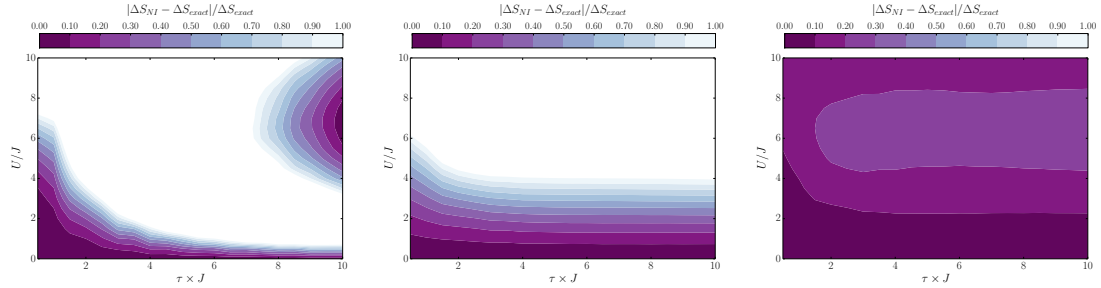

(d) NI entropy relative error $T = 0.2J/k_B$ (e) NI entropy relative error $T = 2.5J/k_B$ (f) NI entropy relative error $T = 20J/k_B$

Figure D.10: NI entropy (top row) and relative error (bottom row) for the 4 sites teeth at the three temperatures.

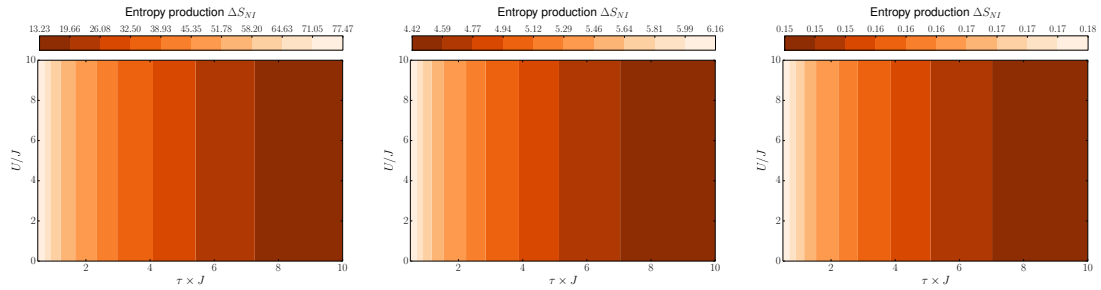

(a) NI entropy $T = 0.2J/k_B$ (b) NI entropy $T = 2.5J/k_B$ (c) NI entropy $T = 20J/k_B$

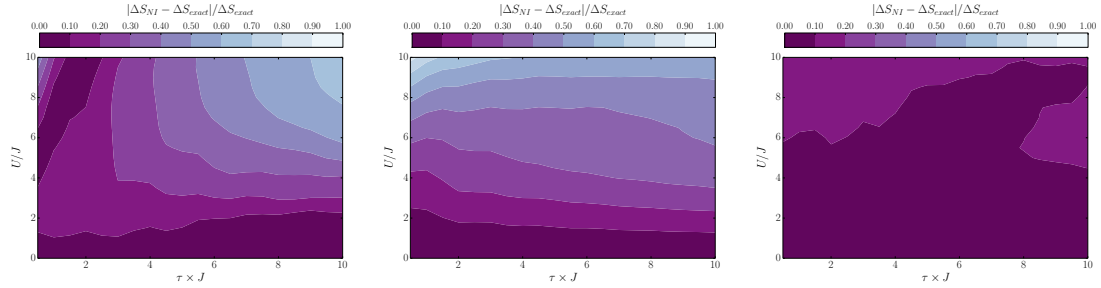

(d) NI entropy relative error $T = 0.2J/k_B$ (e) NI entropy relative error $T = 2.5J/k_B$ (f) NI entropy relative error $T = 20J/k_B$

Figure D.11: NI entropy (top row) and relative error (bottom row) for the 4 sites slope at the three temperatures.

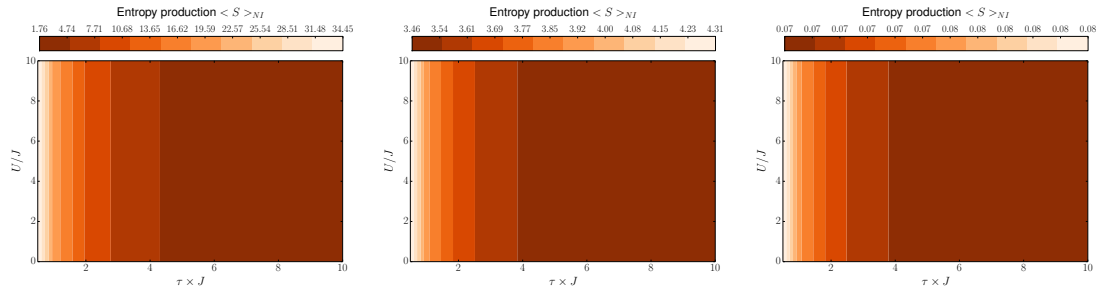

(a) NI entropy $T = 0.2J/k_B$ (b) NI entropy $T = 2.5J/k_B$ (c) NI entropy $T = 20J/k_B$

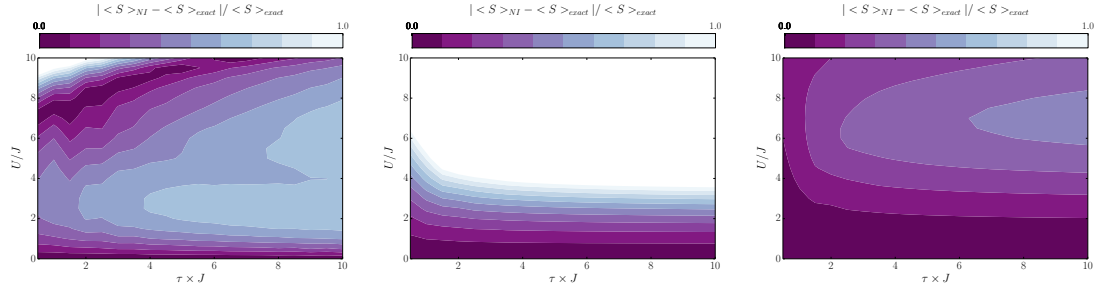

(d) NI entropy relative error $T = 0.2J/k_B$ (e) NI entropy relative error $T = 2.5J/k_B$ (f) NI entropy relative error $T = 20J/k_B$

Figure D.12: NI entropy (top row) and relative error (bottom row) for the 6 sites zigzag at the three temperatures.

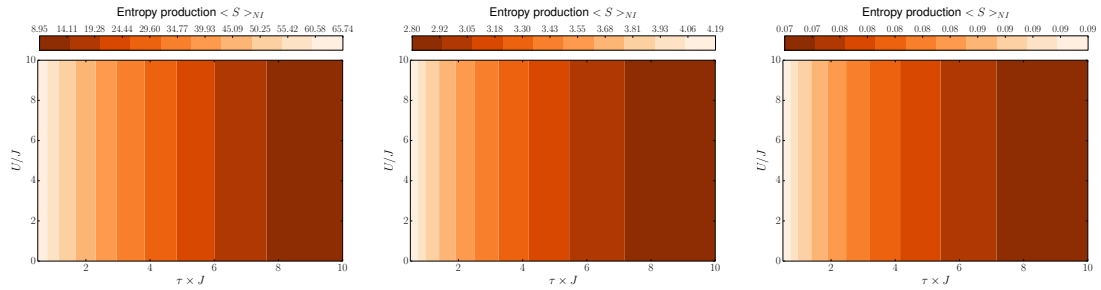

(a) NI entropy $T = 0.2J/k_B$ (b) NI entropy $T = 2.5J/k_B$ (c) NI entropy $T = 20J/k_B$

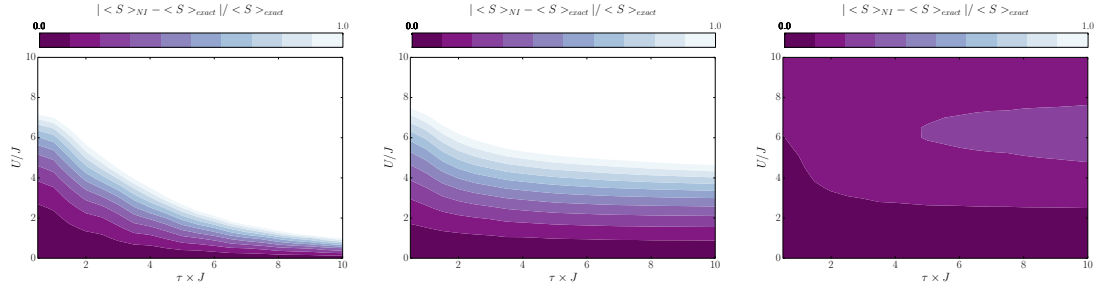

(d) NI entropy relative error $T = 0.2J/k_B$ (e) NI entropy relative error $T = 2.5J/k_B$ (f) NI entropy relative error $T = 20J/k_B$

Figure D.13: NI entropy (top row) and relative error (bottom row) for the 6 sites teeth at the three temperatures.

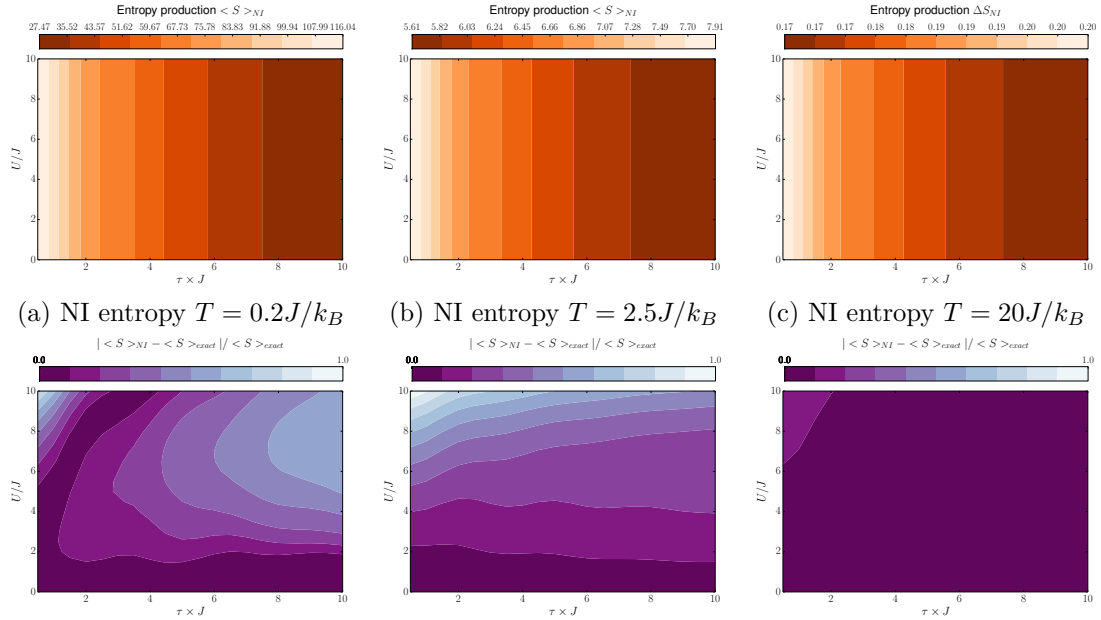

(a) NI entropy $T = 0.2J/k_B$ (b) NI entropy $T = 2.5J/k_B$ (c) NI entropy $T = 20J/k_B$

(d) NI entropy relative error $T = 0.2J/k_B$ (e) NI entropy relative error $T = 2.5J/k_B$ (f) NI entropy relative error $T = 20J/k_B$

Figure D.14: NI entropy (top row) and relative error (bottom row) for the 6 sites slope at the three temperatures.

D.2 'Exact + NI'

This section gives the complete set of quantum work and entropy production results for the 'exact + NI' approximation defined in chapter 7.

D.2.1 'Exact + NI' work

Calculated using $\langle W_{ext}^{exact+NI} \rangle = \mathrm{Tr}\left[\rho^{exact}(0)\hat{H}^{NI}(0)\right] - \mathrm{Tr}\left[\rho^{exact+NI}(\tau)\hat{H}^{NI}(\tau)\right]$ with non-interacting dynamics.

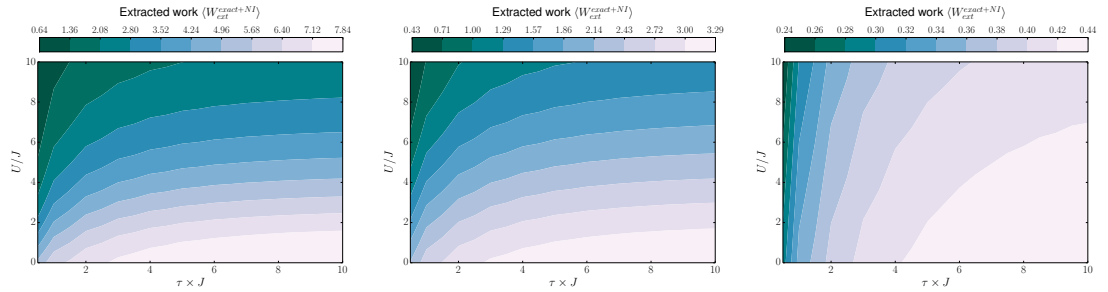

(a) 'Exact + NI' quantum work $T = 0.2J/k_B$

(b) 'Exact + NI' quantum work $T = 2.5J/k_B$

(c) 'Exact + NI' quantum work $T = 20J/k_B$

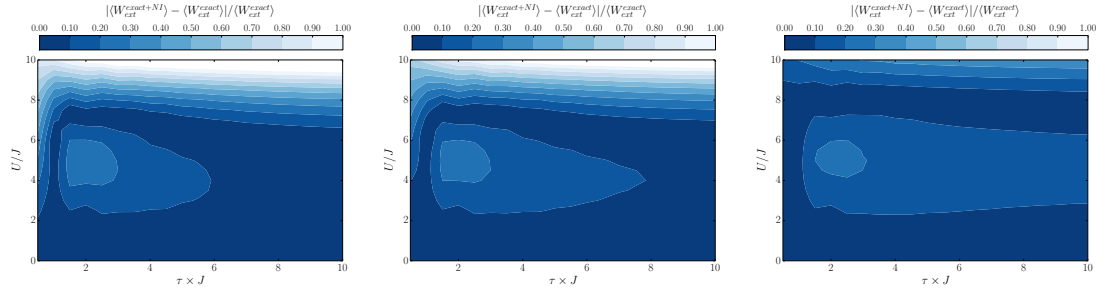

(d) 'Exact + NI' quantum work relative error $T = 0.2J/k_B$

(e) 'Exact + NI' quantum work relative error $T = 2.5J/k_B$

(f) 'Exact + NI' quantum work relative error $T = 20J/k_B$

Figure D.15: 'Exact + NI' work (top row) and relative error (bottom row) for the 2 sites zigzag at the three temperatures.

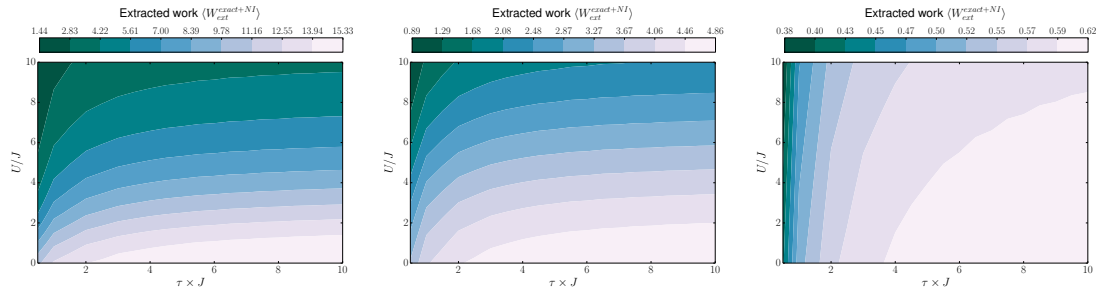

(a) 'Exact + NI' quantum work $T = 0.2J/k_B$

(b) 'Exact + NI' quantum work $T = 2.5J/k_B$

(c) 'Exact + NI' quantum work $T = 20J/k_B$

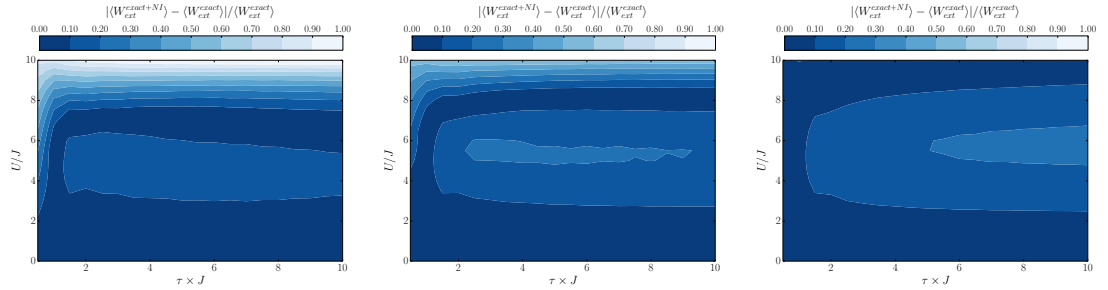

(d) 'Exact + NI' quantum work relative error $T = 0.2J/k_B$

(e) 'Exact + NI' quantum work relative error $T = 2.5J/k_B$

(f) 'Exact + NI' quantum work relative error $T = 20J/k_B$

Figure D.16: 'Exact + NI' work (top row) and relative error (bottom row) for the 4 sites zigzag at the three temperatures.

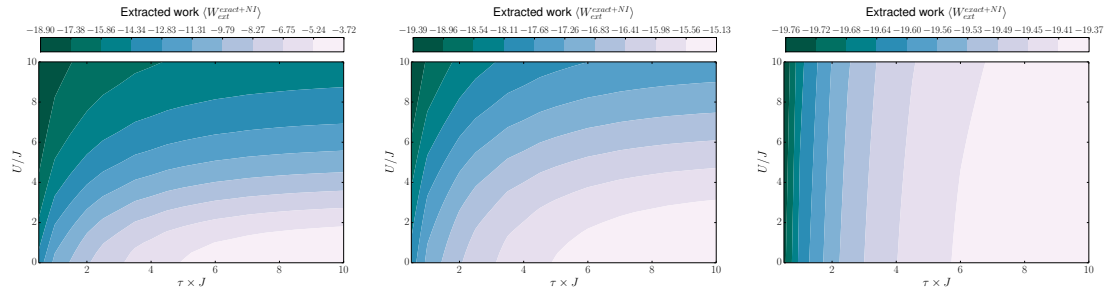

(a) 'Exact + NI' quantum work $T = 0.2J/k_B$ (b) 'Exact + NI' quantum work $T = 2.5J/k_B$ (c) 'Exact + NI' quantum work $T = 20J/k_B$

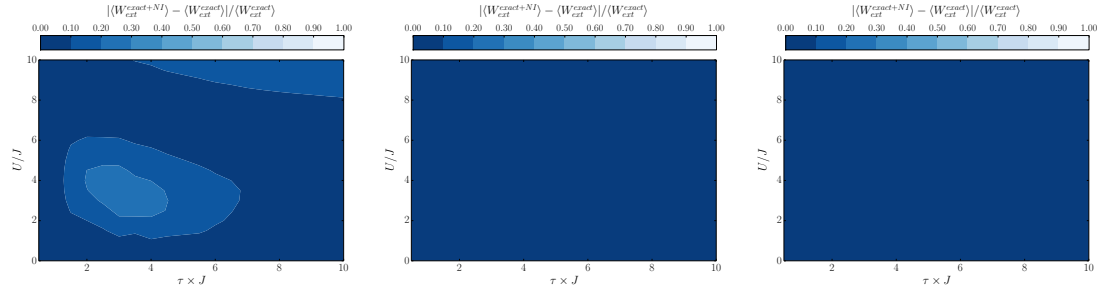

(d) 'Exact + NI' quantum work relative error $T = 0.2J/k_B$ (e) 'Exact + NI' quantum work relative error $T = 2.5J/k_B$ (f) 'Exact + NI' quantum work relative error $T = 20J/k_B$

Figure D.17: 'Exact + NI' work (top row) and relative error (bottom row) for the 4 sites teeth at the three temperatures.

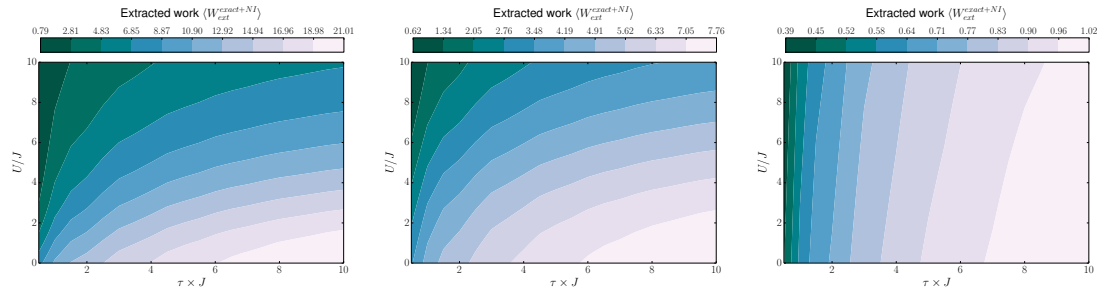

(a) 'Exact + NI' quantum work $T = 0.2J/k_B$ (b) 'Exact + NI' quantum work $T = 2.5J/k_B$ (c) 'Exact + NI' quantum work $T = 20J/k_B$

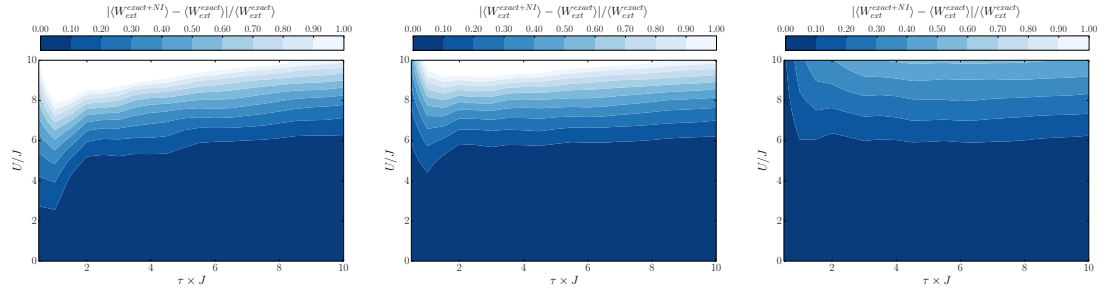

(d) 'Exact + NI' quantum work relative error $T = 0.2J/k_B$ (e) 'Exact + NI' quantum work relative error $T = 2.5J/k_B$ (f) 'Exact + NI' quantum work relative error $T = 20J/k_B$

Figure D.18: 'Exact + NI' work (top row) and relative error (bottom row) for the 4 sites slope at the three temperatures.

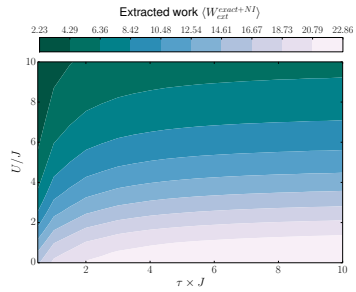

(a) 'Exact + NI' quantum work $T = 0.2J/k_B$

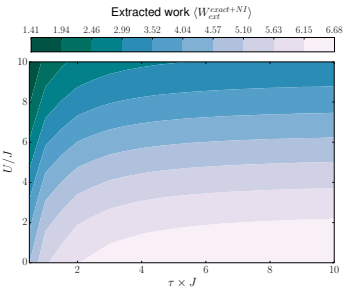

(b) 'Exact + NI' quantum work $T = 2.5J/k_B$

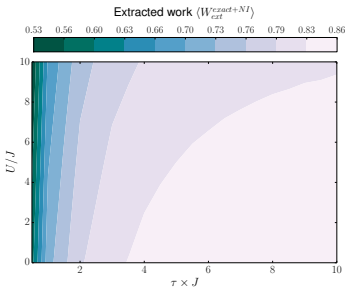

(c) 'Exact + NI' quantum work $T = 20J/k_B$

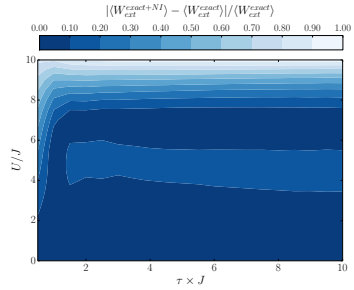

(d) 'Exact + NI' quantum work relative error $T = 0.2J/k_B$

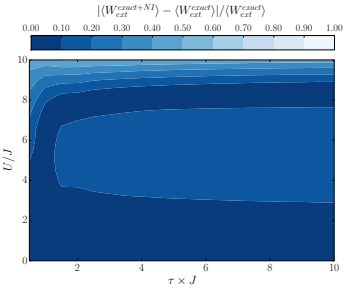

(e) 'Exact + NI' quantum work relative error $T = 2.5J/k_B$

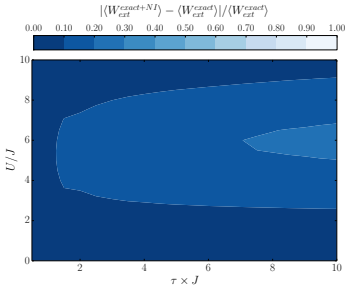

(f) 'Exact + NI' quantum work relative error $T = 20J/k_B$

Figure D.19: 'Exact + NI' work (top row) and relative error (bottom row) for the 6 sites zigzag at the three temperatures.

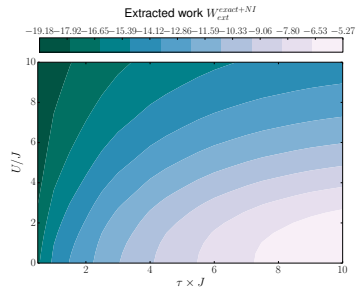

(a) 'Exact + NI' quantum work $T = 0.2J/k_B$

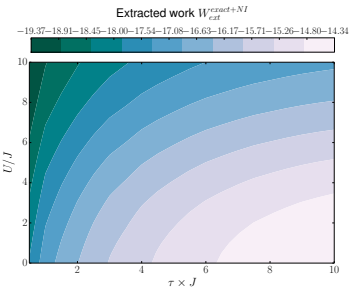

(b) 'Exact + NI' quantum work $T = 2.5J/k_B$

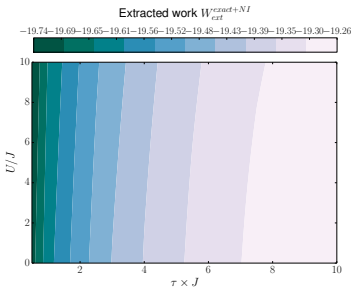

(c) 'Exact + NI' quantum work $T = 20J/k_B$

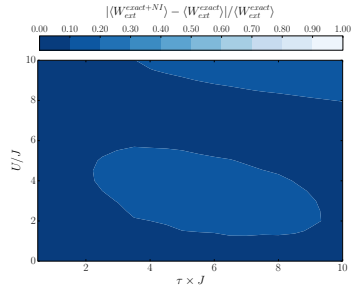

(d) 'Exact + NI' quantum work relative error $T = 0.2J/k_B$

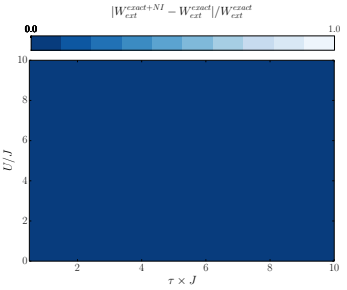

(e) 'Exact + NI' quantum work relative error $T = 2.5J/k_B$

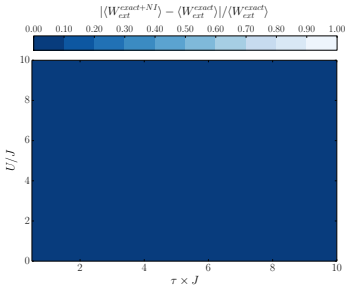

(f) 'Exact + NI' quantum work relative error $T = 20J/k_B$

Figure D.20: 'Exact + NI' work (top row) and relative error (bottom row) for the 6 sites teeth at the three temperatures.

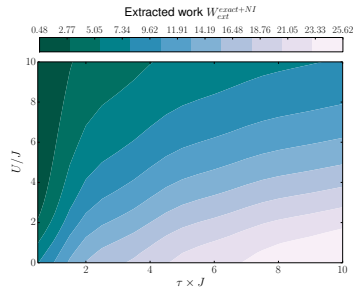

(a) 'Exact + NI' quantum work $T = 0.2J/k_B$

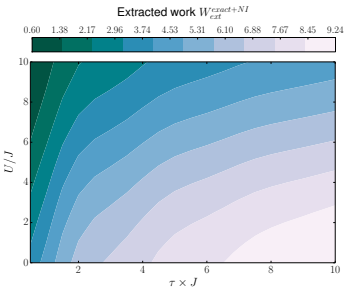

(b) 'Exact + NI' quantum work $T = 2.5J/k_B$

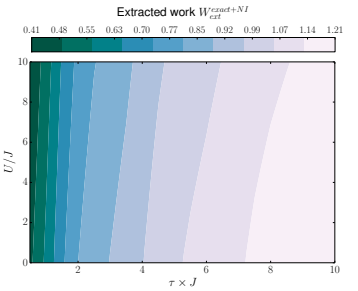

(c) 'Exact + NI' quantum work $T = 20J/k_B$

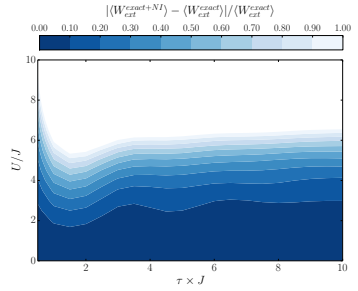

(d) 'Exact + NI' quantum work relative error $T = 0.2J/k_B$

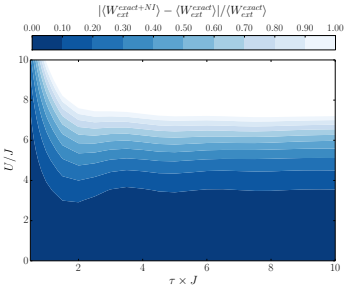

(e) 'Exact + NI' quantum work relative error $T = 2.5J/k_B$

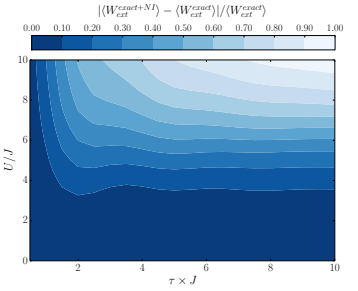

(f) 'Exact + NI' quantum work relative error $T = 20J/k_B$

Figure D.21: 'Exact + NI' work (top row) and relative error (bottom row) for the 6 sites slope at the three temperatures.

D.2.2 'Exact + NI' entropy

The entropy is calculated by $\Delta S_{exact+NI} = \beta \left(\langle W^{exact+NI} \rangle - \Delta F^{exact} \right)$, where $\Delta F^{exact} = -(1/\beta) \ln (Z_\tau^{exact} / Z_0^{exact})$.

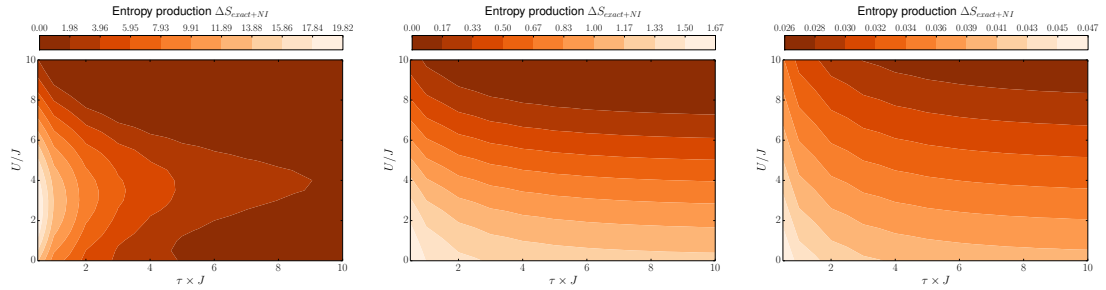

(a) 'Exact + NI' entropy $T = 0.2J/k_B$ (b) 'Exact + NI' entropy $T = 2.5J/k_B$ (c) 'Exact + NI' entropy $T = 20J/k_B$

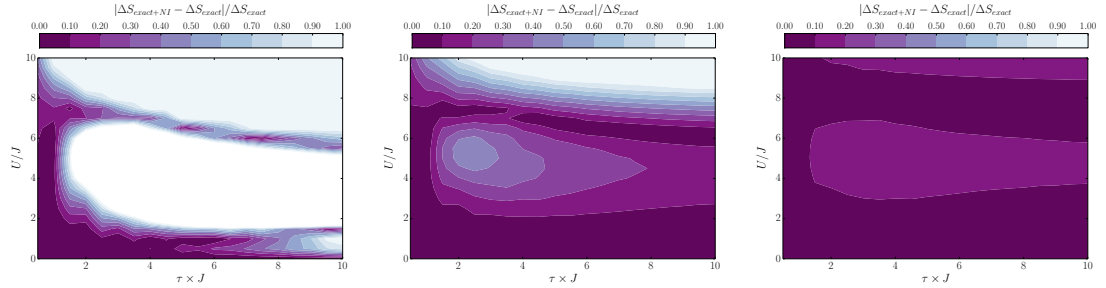

(d) 'Exact + NI' entropy relative error $T = 0.2J/k_B$ (e) 'Exact + NI' entropy relative error $T = 2.5J/k_B$ (f) 'Exact + NI' entropy relative error $T = 20J/k_B$

Figure D.22: 'Exact + NI' entropy (top row) and relative error (bottom row) for the 2 sites zigzag at the three temperatures.

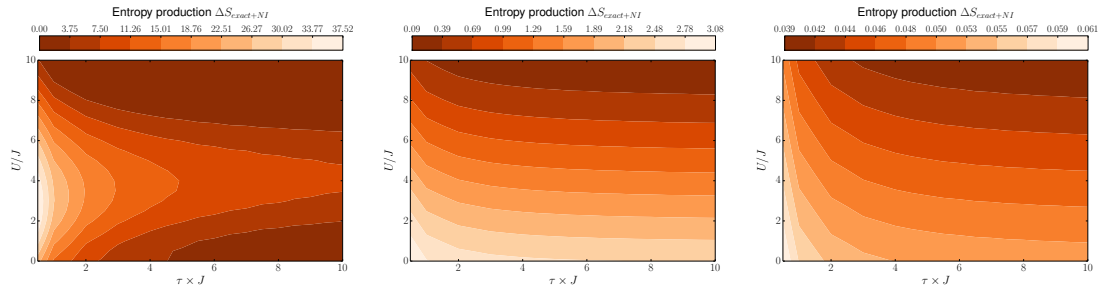

(a) 'Exact + NI' entropy $T = 0.2J/k_B$ (b) 'Exact + NI' entropy $T = 2.5J/k_B$ (c) 'Exact + NI' entropy $T = 20J/k_B$

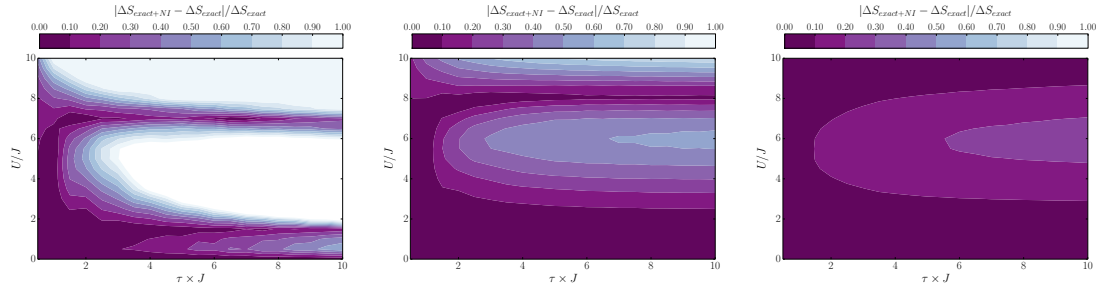

(d) 'Exact + NI' entropy relative error $T = 0.2J/k_B$ (e) 'Exact + NI' entropy relative error $T = 2.5J/k_B$ (f) 'Exact + NI' entropy relative error $T = 20J/k_B$

Figure D.23: 'Exact + NI' entropy (top row) and relative error (bottom row) for the 4 sites zigzag at the three temperatures.

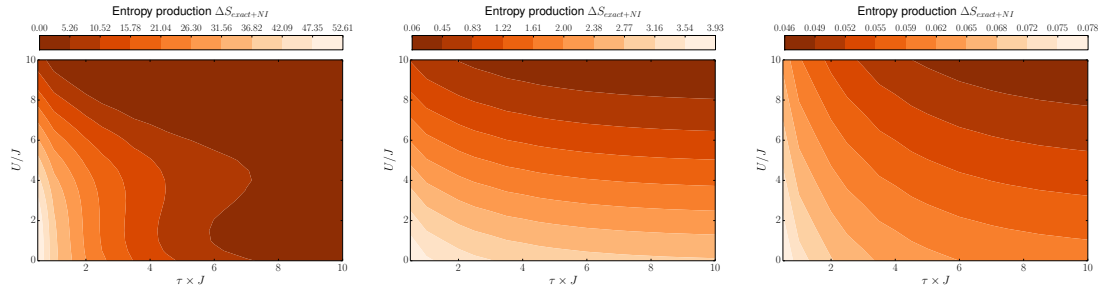

(a) 'Exact + NI' entropy $T = 0.2J/k_B$

(b) 'Exact + NI' entropy $T = 2.5J/k_B$

(c) 'Exact + NI' entropy $T = 20J/k_B$

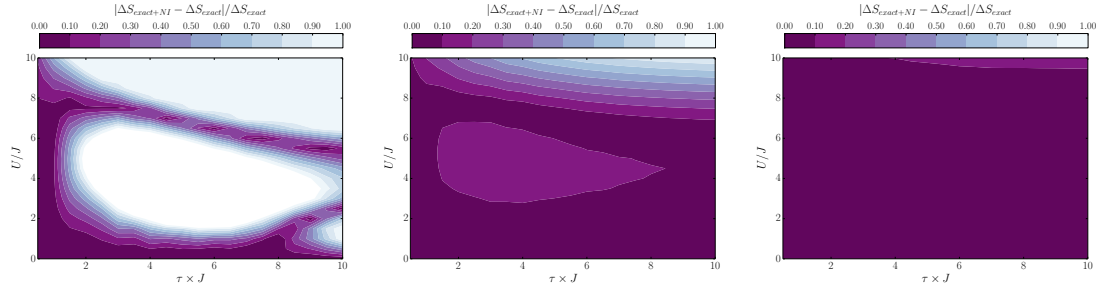

(d) 'Exact + NI' entropy relative error $T = 0.2J/k_B$

(e) 'Exact + NI' entropy relative error $T = 2.5J/k_B$

(f) 'Exact + NI' entropy relative error $T = 20J/k_B$

Figure D.24: 'Exact + NI' entropy (top row) and relative error (bottom row) for the 4 sites teeth at the three temperatures.

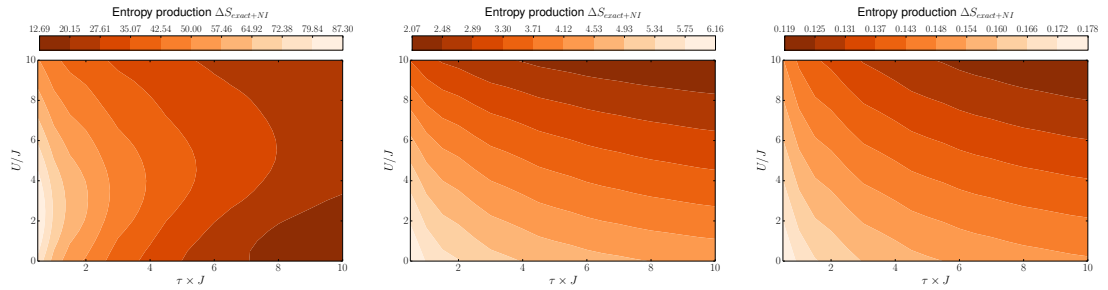

(a) 'Exact + NI' entropy $T = 0.2J/k_B$

(b) 'Exact + NI' entropy $T = 2.5J/k_B$

(c) 'Exact + NI' entropy $T = 20J/k_B$

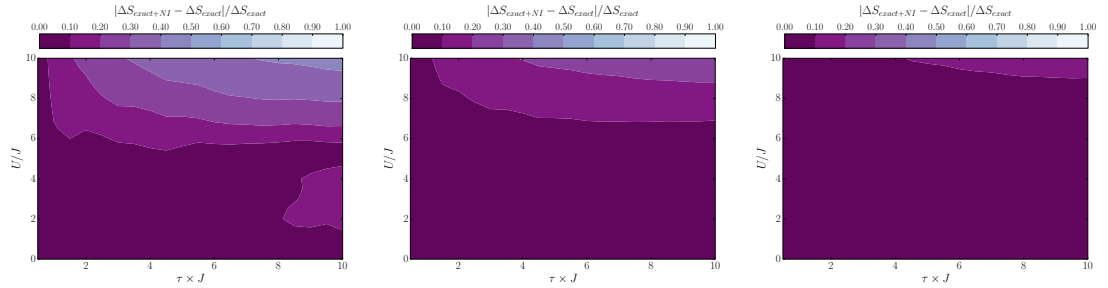

(d) 'Exact + NI' entropy relative error $T = 0.2J/k_B$

(e) 'Exact + NI' entropy relative error $T = 2.5J/k_B$

(f) 'Exact + NI' entropy relative error $T = 20J/k_B$

Figure D.25: 'Exact + NI' entropy (top row) and relative error (bottom row) for the 4 sites slope at the three temperatures.

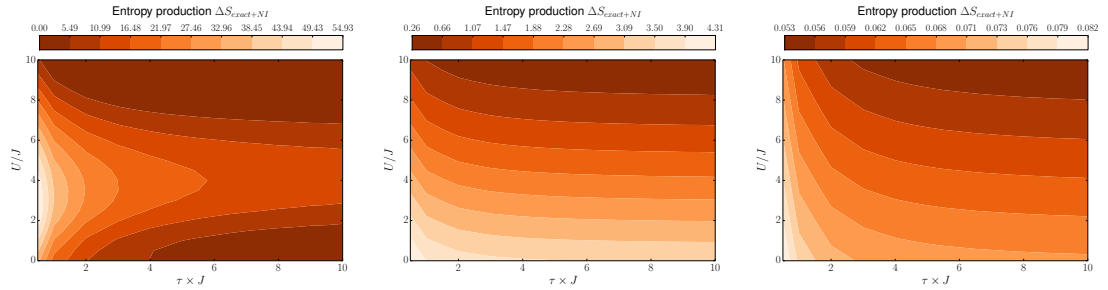

(a) 'Exact + NI' entropy $T = 0.2J/k_B$ (b) 'Exact + NI' entropy $T = 2.5J/k_B$ (c) 'Exact + NI' entropy $T = 20J/k_B$

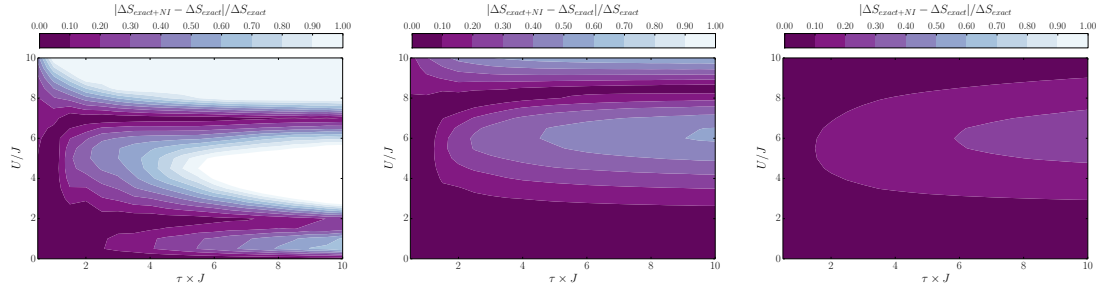

(d) 'Exact + NI' entropy relative error $T = 0.2J/k_B$ (e) 'Exact + NI' entropy relative error $T = 2.5J/k_B$ (f) 'Exact + NI' entropy relative error $T = 20J/k_B$

Figure D.26: 'Exact + NI' entropy (top row) and relative error (bottom row) for the 6 sites zigzag at the three temperatures.

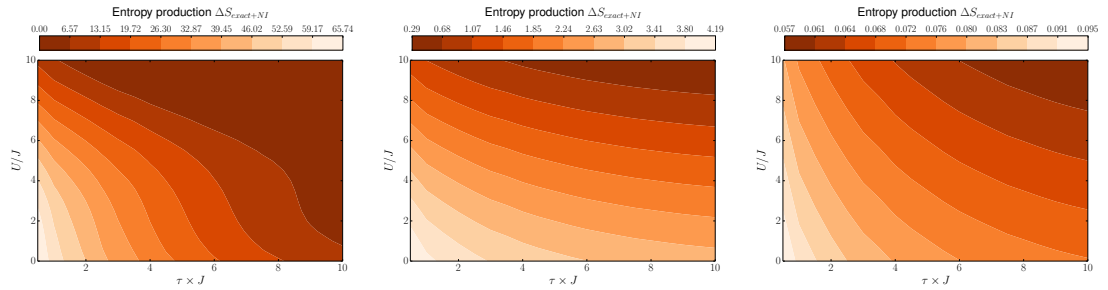

(a) 'Exact + NI' entropy $T = 0.2J/k_B$ (b) 'Exact + NI' entropy $T = 2.5J/k_B$ (c) 'Exact + NI' entropy $T = 20J/k_B$

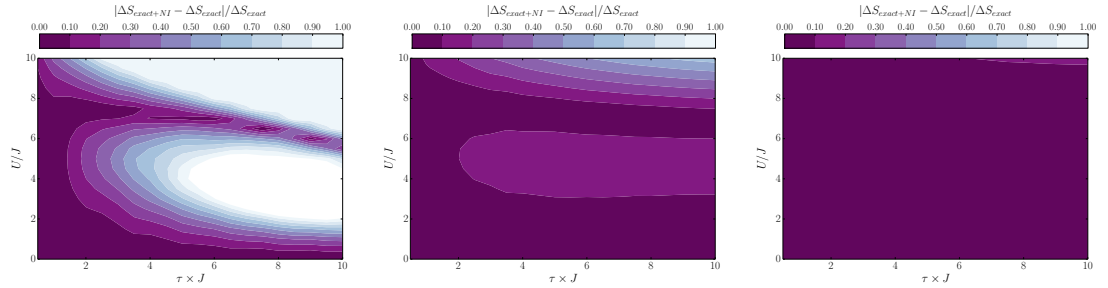

(d) 'Exact + NI' entropy relative error $T = 0.2J/k_B$ (e) 'Exact + NI' entropy relative error $T = 2.5J/k_B$ (f) 'Exact + NI' entropy relative error $T = 20J/k_B$

Figure D.27: 'Exact + NI' entropy (top row) and relative error (bottom row) for the 6 sites teeth at the three temperatures.

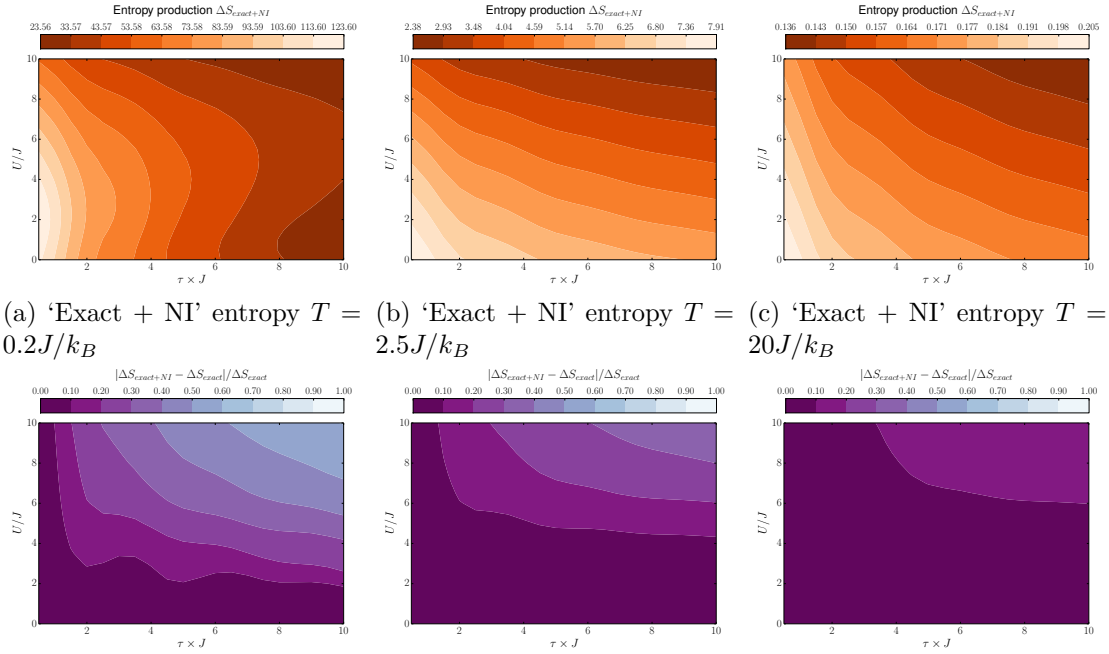

(a) 'Exact + NI' entropy $T = 0.2J/k_B$

(b) 'Exact + NI' entropy $T = 2.5J/k_B$

(c) 'Exact + NI' entropy $T = 20J/k_B$

(d) 'Exact + NI' entropy relative error $T = 0.2J/k_B$

(e) 'Exact + NI' entropy relative error $T = 2.5J/k_B$

(f) 'Exact + NI' entropy relative error $T = 20J/k_B$

Figure D.28: 'Exact + NI' entropy (top row) and relative error (bottom row) for the 6 sites slope at the three temperatures.

D.3 'BALDA'-based approximation

This section shows the complete set of results based on the parameter set outlined in section 6.2.2 for the 'BALDA' approximation defined in chapter 8.

D.3.1 'BALDA' work

Calculated using $\langle W_{ext}^{BALDA} \rangle = \mathrm{Tr}\left[\rho^{BALDA}(0)\hat{H}^{BALDA}(0)\right] - \mathrm{Tr}\left[\rho^{BALDA}(\tau)\hat{H}^{BALDA}(\tau)\right]$ with $\hat{H}_{\mathrm{evo}}$ approximated using BALDA at $t = 0$.

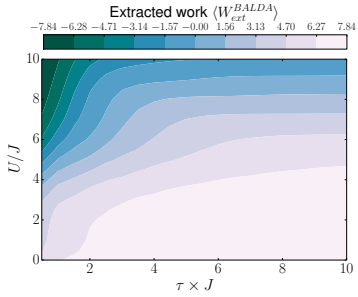

(a) 'BALDA' quantum work $T = 0.2J/k_B$

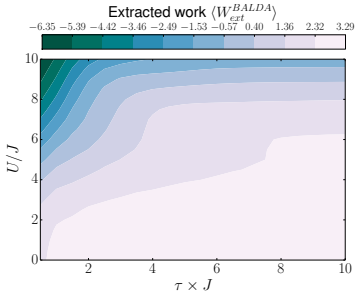

(b) 'BALDA' quantum work $T = 2.5J/k_B$

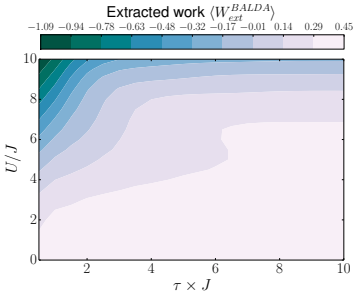

(c) 'BALDA' quantum work $T = 20J/k_B$

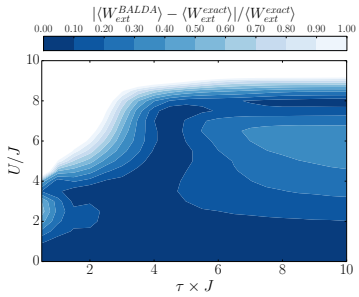

(d) 'BALDA' quantum work relative error $T = 0.2J/k_B$

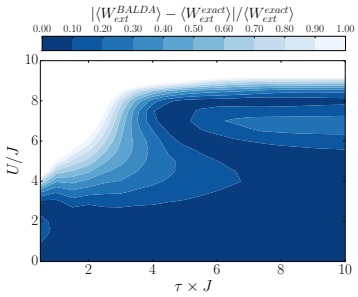

(e) 'BALDA' quantum work relative error $T = 2.5J/k_B$

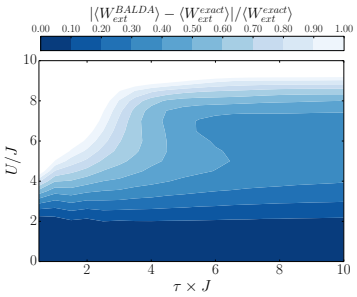

(f) 'BALDA' quantum work relative error $T = 20J/k_B$

Figure D.29: 'BALDA' work (top row) and relative error (bottom row) for the 2 sites zigzag at the three temperatures.

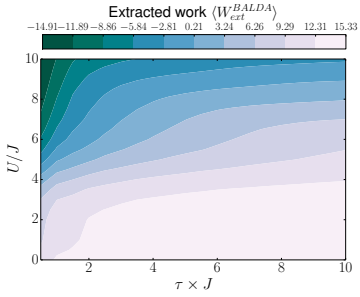

(a) 'BALDA' quantum work $T = 0.2J/k_B$

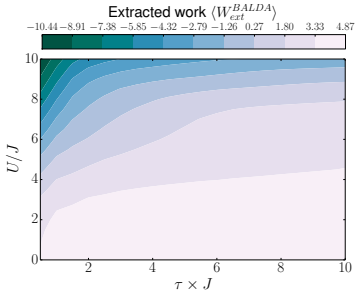

(b) 'BALDA' quantum work $T = 2.5J/k_B$

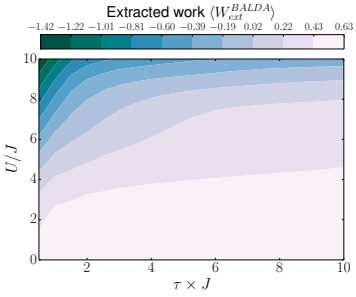

(c) 'BALDA' quantum work $T = 20J/k_B$

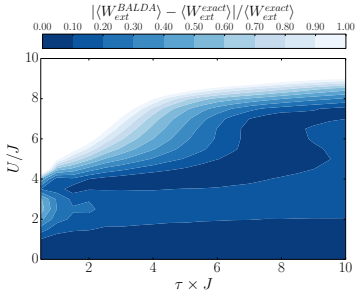

(d) 'BALDA' quantum work relative error $T = 0.2J/k_B$

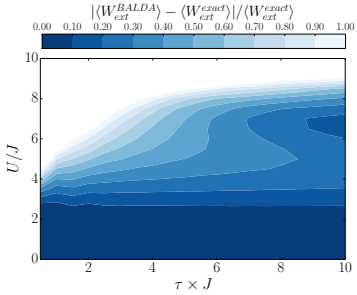

(e) 'BALDA' quantum work relative error $T = 2.5J/k_B$

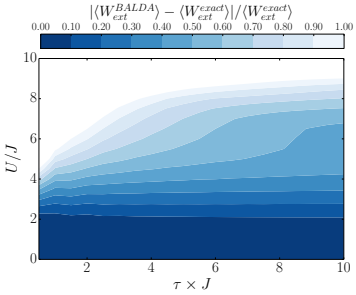

(f) 'BALDA' quantum work relative error $T = 20J/k_B$

Figure D.30: 'BALDA' work (top row) and relative error (bottom row) for the 4 sites zigzag at the three temperatures.

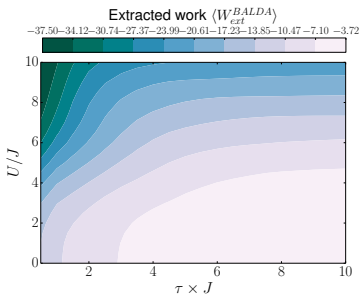

(a) 'BALDA' quantum work $T = 0.2J/k_B$

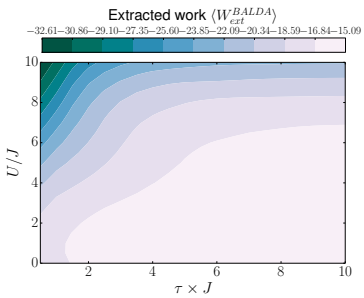

(b) 'BALDA' quantum work $T = 2.5J/k_B$

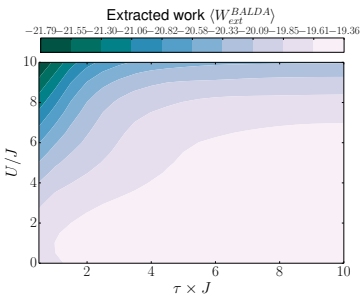

(c) 'BALDA' quantum work $T = 20J/k_B$

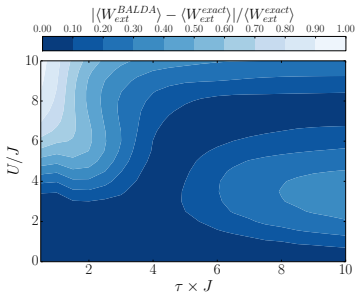

(d) 'BALDA' quantum work relative error $T = 0.2J/k_B$

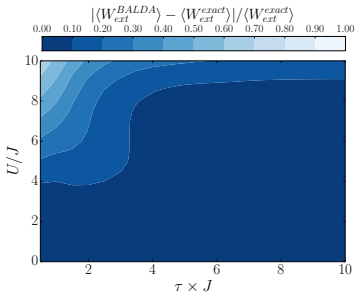

(e) 'BALDA' quantum work relative error $T = 2.5J/k_B$

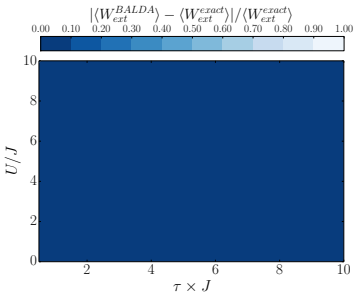

(f) 'BALDA' quantum work relative error $T = 20J/k_B$

Figure D.31: 'BALDA' work (top row) and relative error (bottom row) for the 4 sites teeth at the three temperatures.

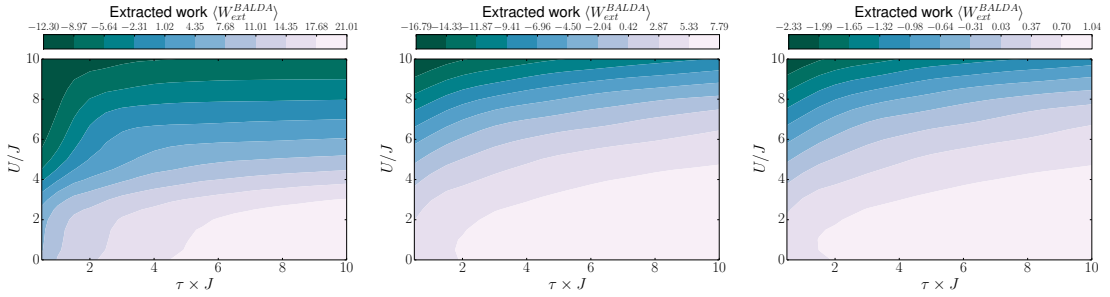

(a) 'BALDA' quantum work $T = 0.2J/k_B$ (b) 'BALDA' quantum work $T = 2.5J/k_B$ (c) 'BALDA' quantum work $T = 20J/k_B$

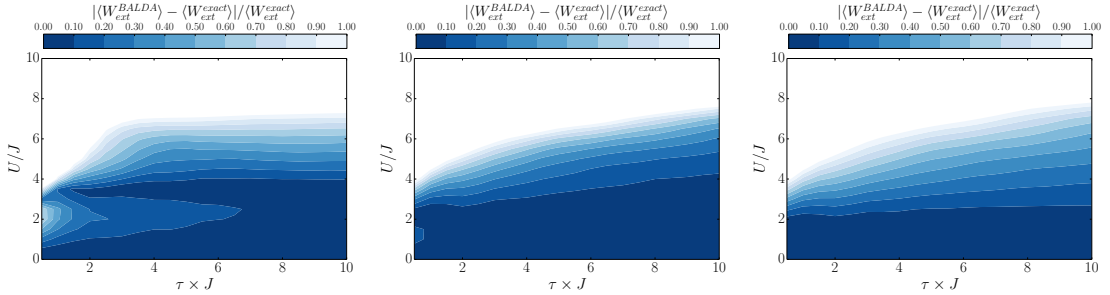

(d) 'BALDA' quantum work relative error $T = 0.2J/k_B$ (e) 'BALDA' quantum work relative error $T = 2.5J/k_B$ (f) 'BALDA' quantum work relative error $T = 20J/k_B$

Figure D.32: 'BALDA' work (top row) and relative error (bottom row) for the 4 sites slope at the three temperatures.

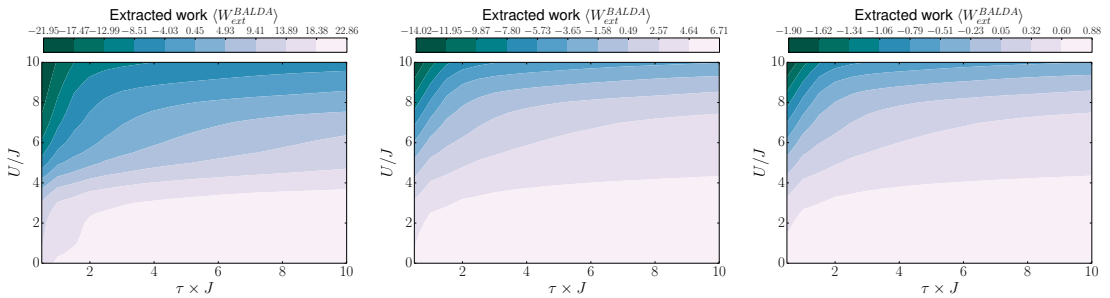

(a) 'BALDA' quantum work $T = 0.2J/k_B$ (b) 'BALDA' quantum work $T = 2.5J/k_B$ (c) 'BALDA' quantum work $T = 20J/k_B$

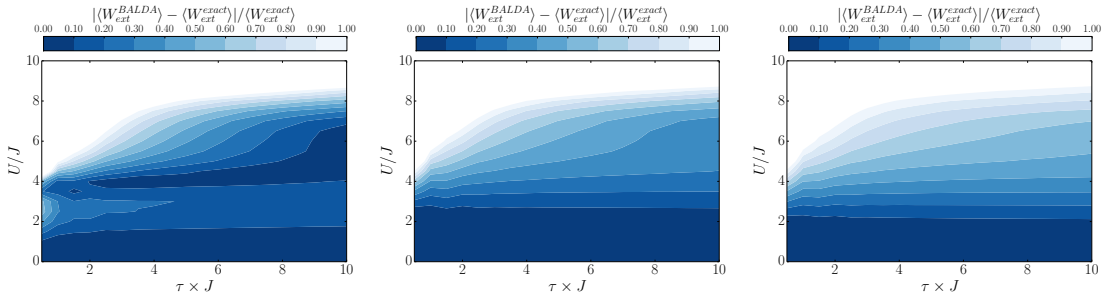

(d) 'BALDA' quantum work relative error $T = 0.2J/k_B$ (e) 'BALDA' quantum work relative error $T = 2.5J/k_B$ (f) 'BALDA' quantum work relative error $T = 20J/k_B$

Figure D.33: 'BALDA' work (top row) and relative error (bottom row) for the 6 sites zigzag at the three temperatures.

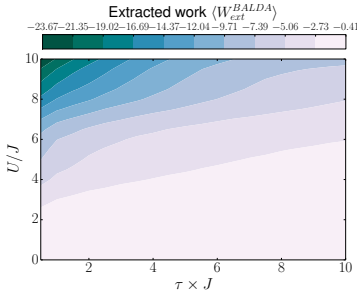

(a) 'BALDA' quantum work $T = 0.2J/k_B$

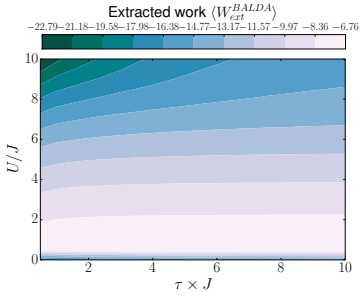

(b) 'BALDA' quantum work $T = 2.5J/k_B$

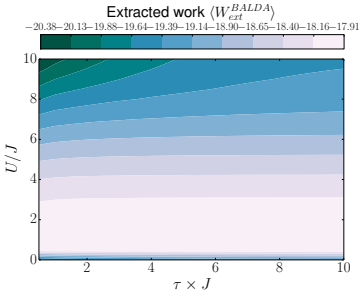

(c) 'BALDA' quantum work $T = 20J/k_B$

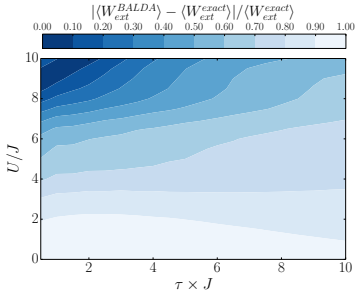

(d) 'BALDA' quantum work relative error $T = 0.2J/k_B$

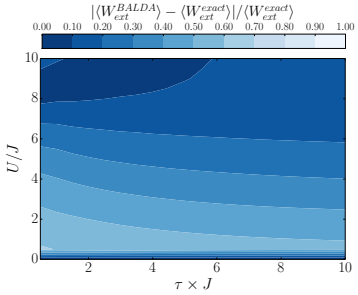

(e) 'BALDA' quantum work relative error $T = 2.5J/k_B$

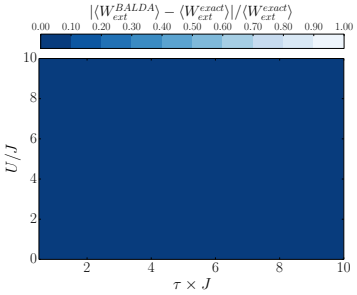

(f) 'BALDA' quantum work relative error $T = 20J/k_B$

Figure D.34: 'BALDA' work (top row) and relative error (bottom row) for the 6 sites teeth at the three temperatures.

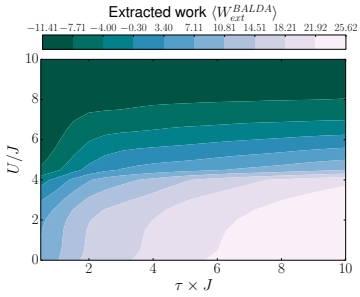

(a) 'BALDA' quantum work $T = 0.2J/k_B$

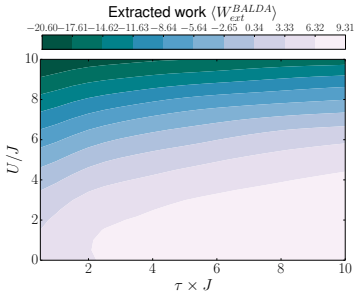

(b) 'BALDA' quantum work $T = 2.5J/k_B$

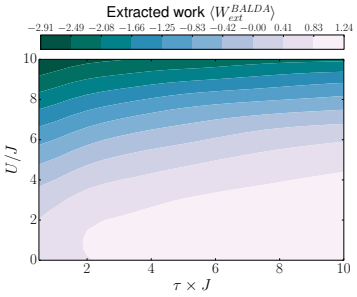

(c) 'BALDA' quantum work $T = 20J/k_B$

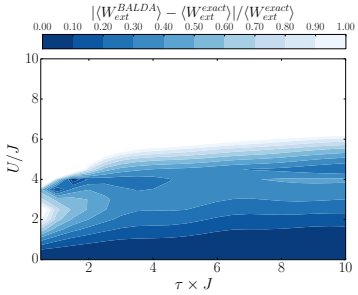

(d) 'BALDA' quantum work relative error $T = 0.2J/k_B$

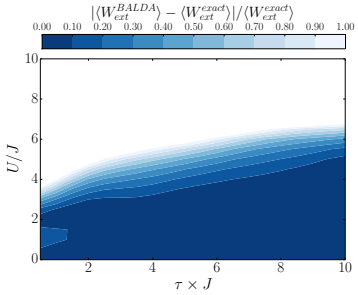

(e) 'BALDA' quantum work relative error $T = 2.5J/k_B$

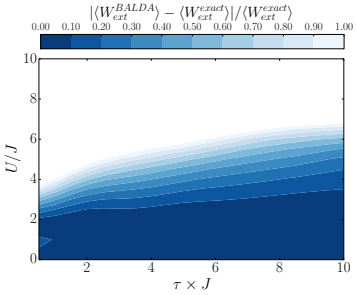

(f) 'BALDA' quantum work relative error $T = 20J/k_B$

Figure D.35: 'BALDA' work (top row) and relative error (bottom row) for the 6 sites slope at the three temperatures.

D.3.2 'BALDA' entropy

The entropy is calculated by $\Delta S_{BALDA} = \beta \left(\langle W^{BALDA} \rangle - \Delta F^{BALDA} \right)$, where $\Delta F^{BALDA} = -\left(1/\beta\right) \ln \left(Z_{\tau}^{BALDA} / Z_{0}^{BALDA} \right)$.

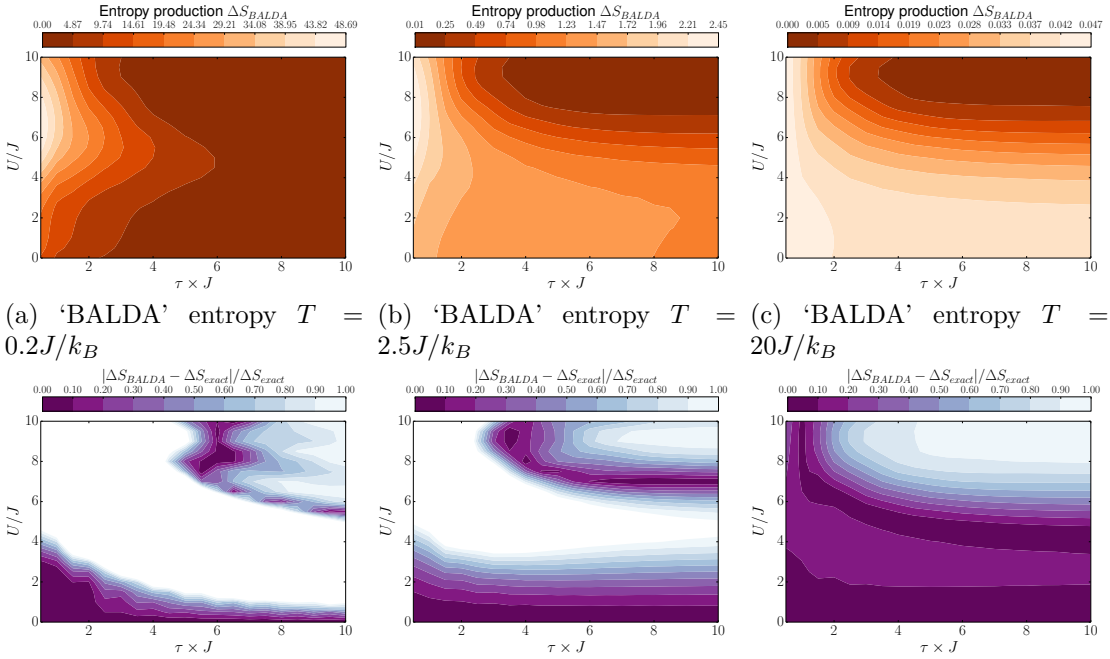

(a) 'BALDA' entropy $T = 0.2J/k_B$

(b) 'BALDA' entropy $T = 2.5J/k_B$

(c) 'BALDA' entropy $T = 20J/k_B$

(d) 'BALDA' entropy relative error $T = 0.2J/k_B$

(e) 'BALDA' entropy relative error $T = 2.5J/k_B$

(f) 'BALDA' entropy relative error $T = 20J/k_B$

Figure D.36: 'BALDA' entropy (top row) and relative error (bottom row) for the 2 sites zigzag at the three temperatures.

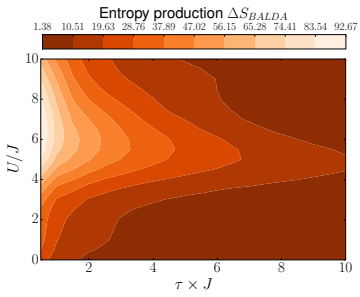

(a) 'BALDA' entropy $T = 0.2J/k_B$

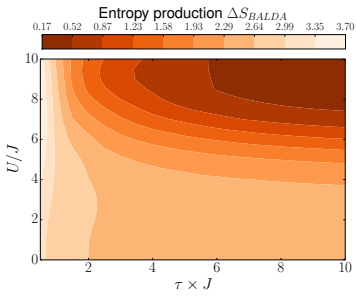

(b) 'BALDA' entropy $T = 2.5J/k_B$

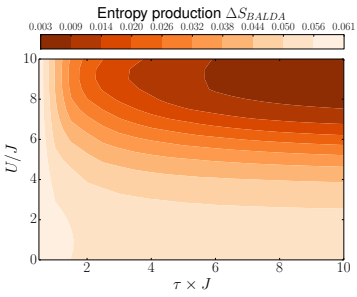

(c) 'BALDA' entropy $T = 20J/k_B$

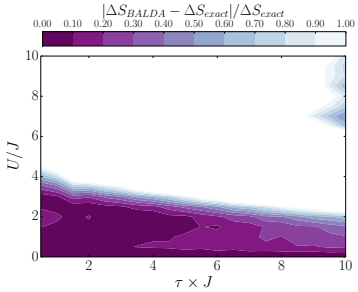

(d) 'BALDA' entropy relative error $T = 0.2J/k_B$

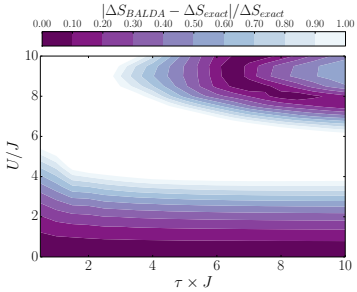

(e) 'BALDA' entropy relative error $T = 2.5J/k_B$

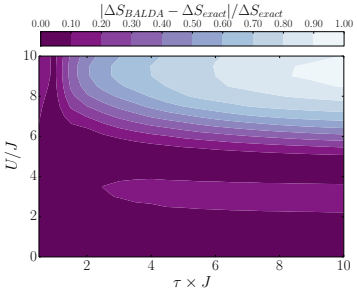

(f) 'BALDA' entropy relative error $T = 20J/k_B$

Figure D.37: 'BALDA' entropy (top row) and relative error (bottom row) for the 4 sites zigzag at the three temperatures.

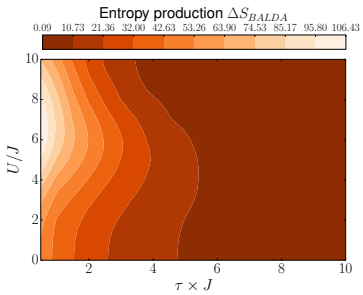

(a) 'BALDA' entropy $T = 0.2J/k_B$

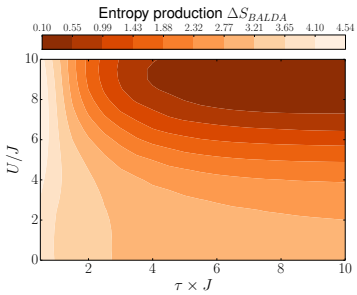

(b) 'BALDA' entropy $T = 2.5J/k_B$

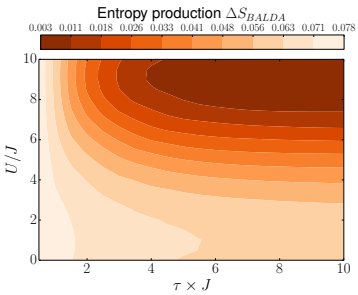

(c) 'BALDA' entropy $T = 20J/k_B$

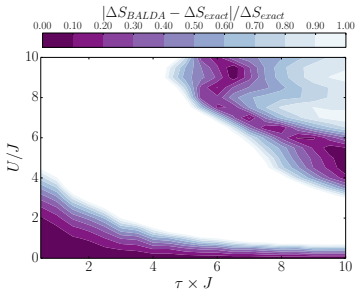

(d) 'BALDA' entropy relative error $T = 0.2J/k_B$

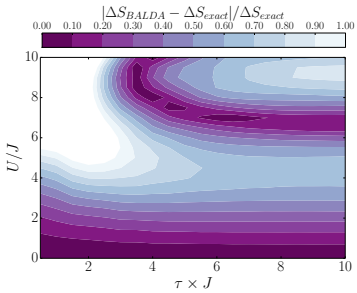

(e) 'BALDA' entropy relative error $T = 2.5J/k_B$

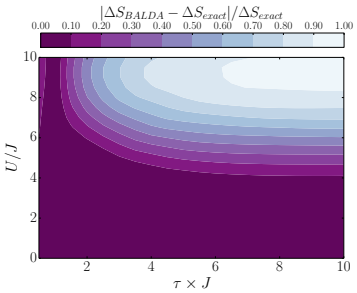

(f) 'BALDA' entropy relative error $T = 20J/k_B$

Figure D.38: 'BALDA' entropy (top row) and relative error (bottom row) for the 4 sites teeth at the three temperatures.

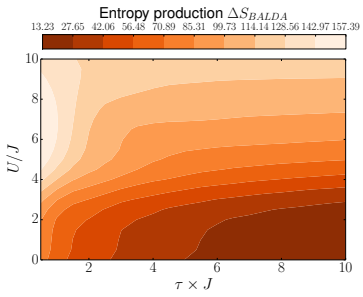

(a) 'BALDA' entropy $T = 0.2J/k_B$

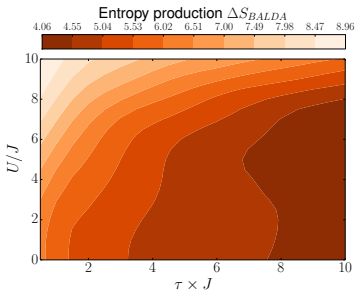

(b) 'BALDA' entropy $T = 2.5J/k_B$

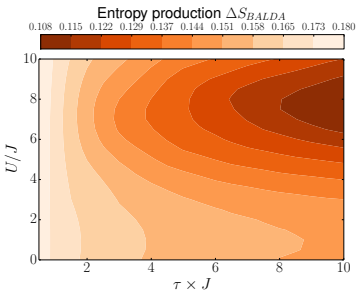

(c) 'BALDA' entropy $T = 20J/k_B$

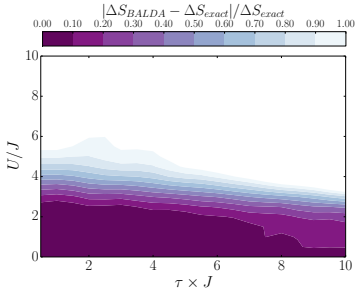

(d) 'BALDA' entropy relative error $T = 0.2J/k_B$

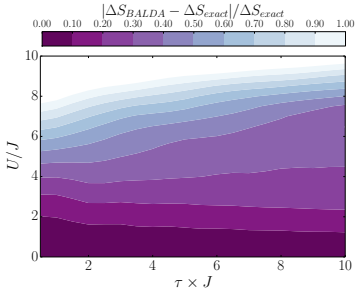

(e) 'BALDA' entropy relative error $T = 2.5J/k_B$

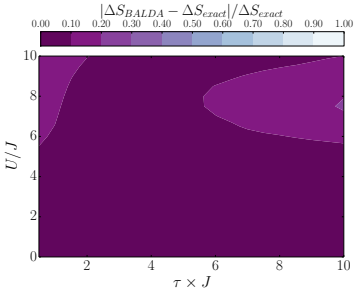

(f) 'BALDA' entropy relative error $T = 20J/k_B$

Figure D.39: 'BALDA' entropy (top row) and relative error (bottom row) for the 4 sites slope at the three temperatures.

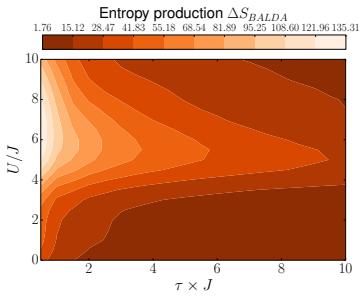

(a) 'BALDA' entropy $T = 0.2J/k_B$

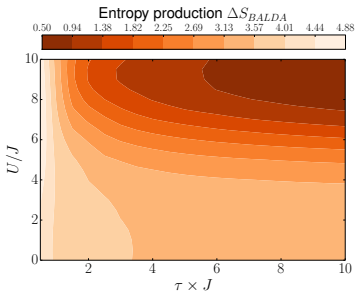

(b) 'BALDA' entropy $T = 2.5J/k_B$

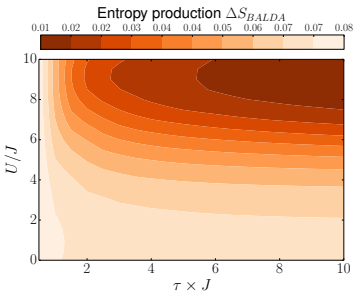

(c) 'BALDA' entropy $T = 20J/k_B$

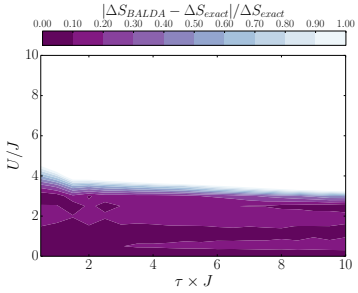

(d) 'BALDA' entropy relative error $T = 0.2J/k_B$

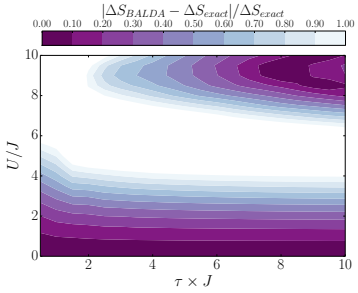

(e) 'BALDA' entropy relative error $T = 2.5J/k_B$

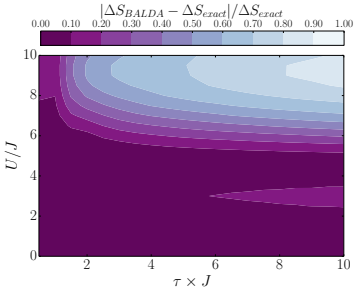

(f) 'BALDA' entropy relative error $T = 20J/k_B$

Figure D.40: 'BALDA' entropy (top row) and relative error (bottom row) for the 6 sites zigzag at the three temperatures.

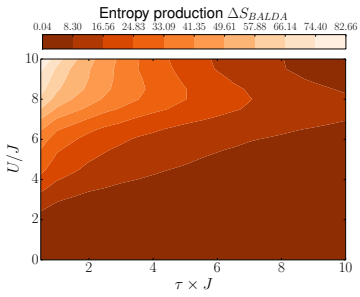

(a) 'BALDA' entropy $T = 0.2J/k_B$

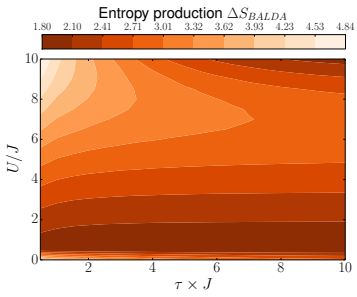

(b) 'BALDA' entropy $T = 2.5J/k_B$

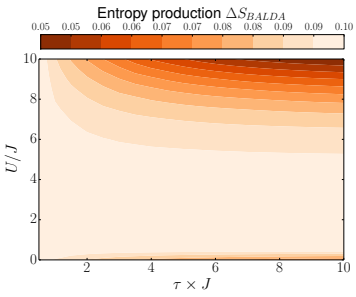

(c) 'BALDA' entropy $T = 20J/k_B$

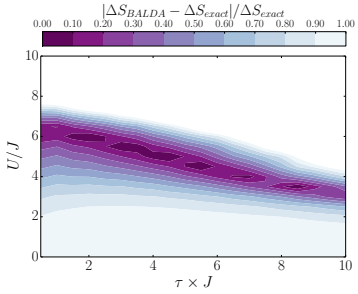

(d) 'BALDA' entropy relative error $T = 0.2J/k_B$

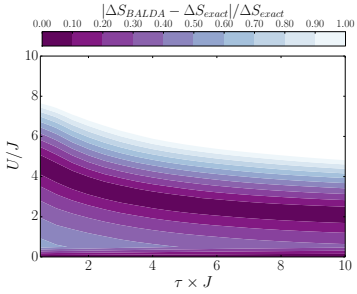

(e) 'BALDA' entropy relative error $T = 2.5J/k_B$

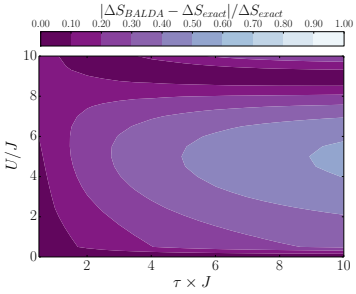

(f) 'BALDA' entropy relative error $T = 20J/k_B$

Figure D.41: 'BALDA' entropy (top row) and relative error (bottom row) for the 6 sites teeth at the three temperatures.

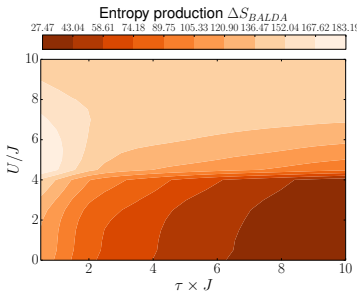

(a) 'BALDA' entropy $T = 0.2J/k_B$

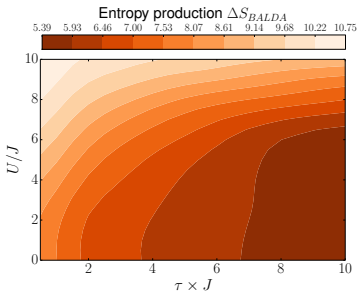

(b) 'BALDA' entropy $T = 2.5J/k_B$

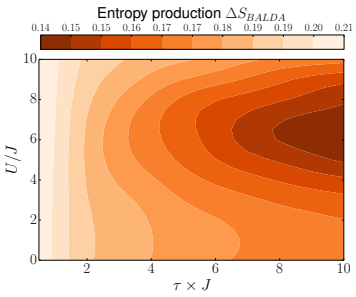

(c) 'BALDA' entropy $T = 20J/k_B$

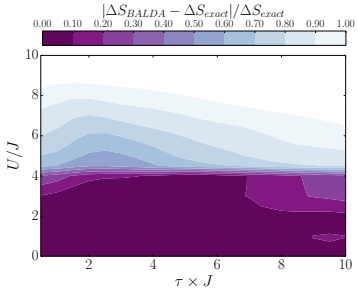

(d) 'BALDA' entropy relative error $T = 0.2J/k_B$

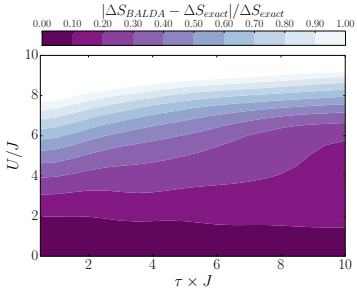

(e) 'BALDA' entropy relative error $T = 2.5J/k_B$

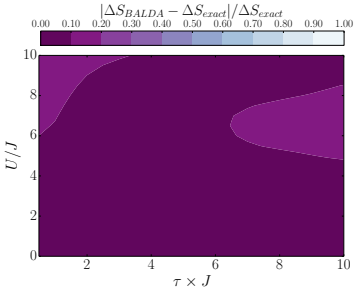

(f) 'BALDA' entropy relative error $T = 20J/k_B$

Figure D.42: 'BALDA' entropy (top row) and relative error (bottom row) for the 6 sites slope at the three temperatures.

D.4 'Exact + BALDA'

This section shows the complete set of results based on the parameter set outlined in section 6.2.2 for the 'exact + BALDA' approximation defined in chapter 8.

D.4.1 'Exact + BALDA' work

Calculated using $\langle W_{ext}^{ex+BALDA} \rangle = \mathrm{Tr}\left[\rho^{ex}(0)\hat{H}^{BALDA}(0)\right] - \mathrm{Tr}\left[\rho^{ex+BALDA}(\tau)\hat{H}^{BALDA}(\tau)\right]$ with $\hat{H}_{\mathrm{evo}}$ approximated using BALDA at $t = 0$.

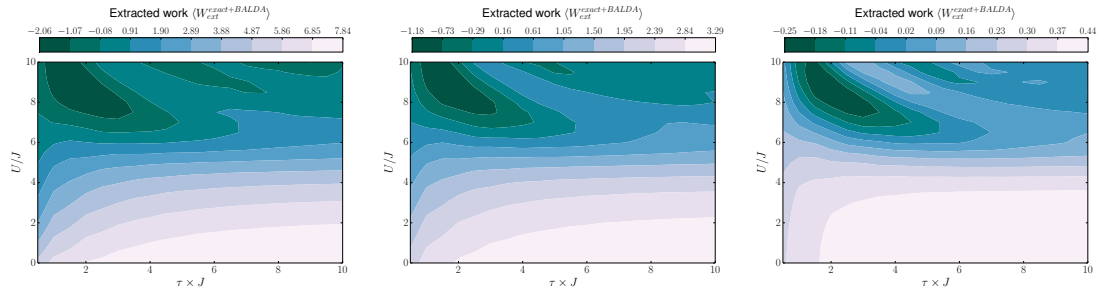

(a) 'Exact + BALDA' quantum work $T = 0.2J/k_B$

(b) 'Exact + BALDA' quantum work $T = 2.5J/k_B$

(c) 'Exact + BALDA' quantum work $T = 20J/k_B$

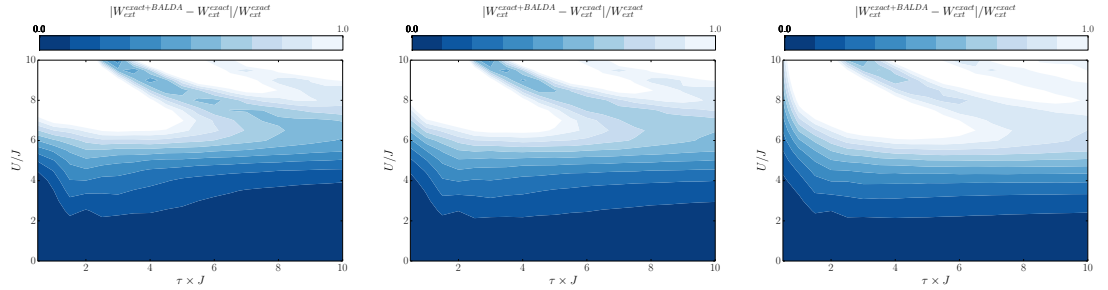

(d) 'Exact + BALDA' quantum work relative error $T = 0.2J/k_B$

(e) 'Exact + BALDA' quantum work relative error $T = 2.5J/k_B$

(f) 'Exact + BALDA' quantum work relative error $T = 20J/k_B$

Figure D.43: 'Exact + BALDA' work (top row) and relative error (bottom row) for the 2 sites zigzag at the three temperatures.

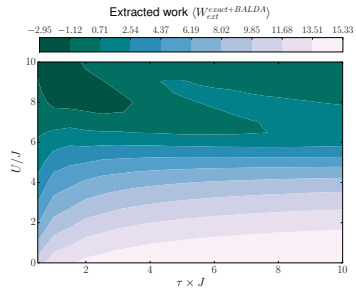

(a) 'Exact + BALDA' quantum work $T = 0.2J/k_B$

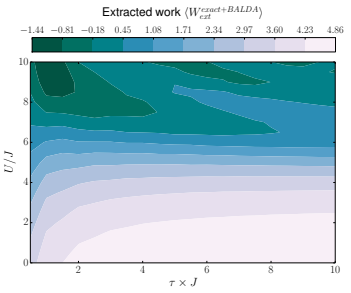

(b) 'Exact + BALDA' quantum work $T = 2.5J/k_B$

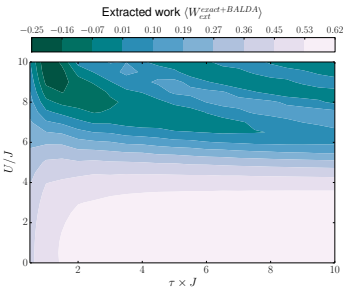

(c) 'Exact + BALDA' quantum work $T = 20J/k_B$

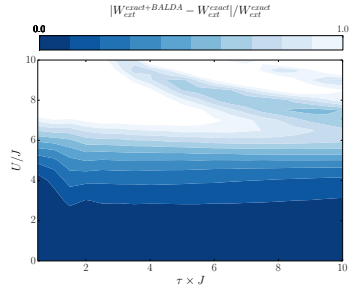

(d) 'Exact + BALDA' quantum work relative error $T = 0.2J/k_B$

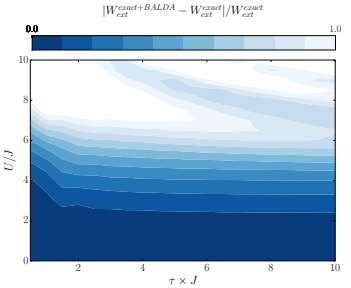

(e) 'Exact + BALDA' quantum work relative error $T = 2.5J/k_B$

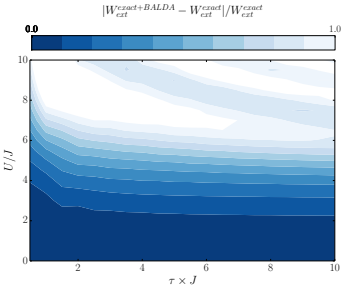

(f) 'Exact + BALDA' quantum work relative error $T = 20J/k_B$

Figure D.44: 'Exact + BALDA' work (top row) and relative error (bottom row) for the 4 sites zigzag at the three temperatures.

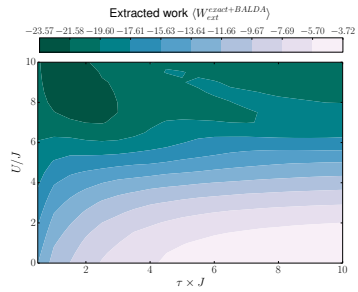

(a) 'Exact + BALDA' quantum work $T = 0.2J/k_B$

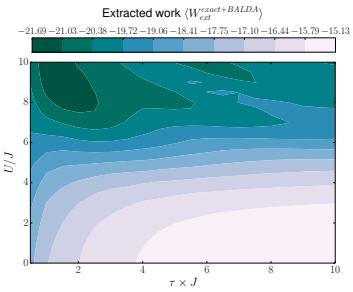

(b) 'Exact + BALDA' quantum work $T = 2.5J/k_B$

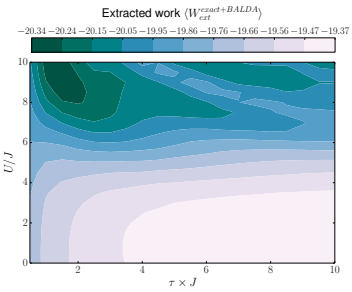

(c) 'Exact + BALDA' quantum work $T = 20J/k_B$

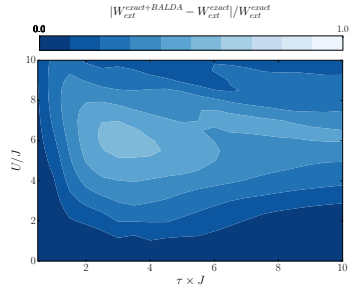

(d) 'Exact + BALDA' quantum work relative error $T = 0.2J/k_B$

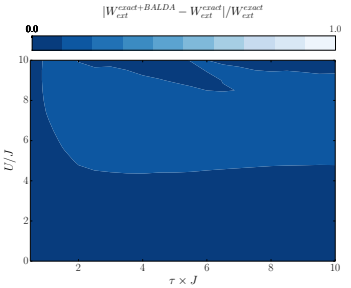

(e) 'Exact + BALDA' quantum work relative error $T = 2.5J/k_B$

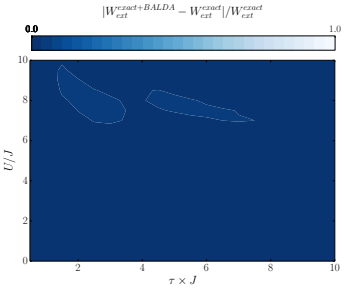

(f) 'Exact + BALDA' quantum work relative error $T = 20J/k_B$

Figure D.45: 'Exact + BALDA' work (top row) and relative error (bottom row) for the 4 sites teeth at the three temperatures.

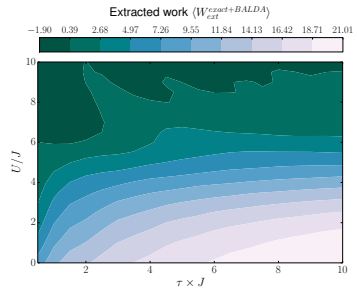

(a) 'Exact + BALDA' quantum work $T = 0.2J/k_B$

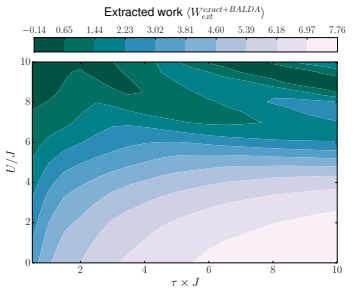

(b) 'Exact + BALDA' quantum work $T = 2.5J/k_B$

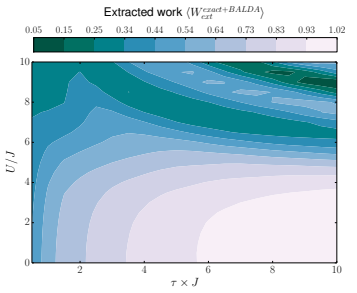

(c) 'Exact + BALDA' quantum work $T = 20J/k_B$

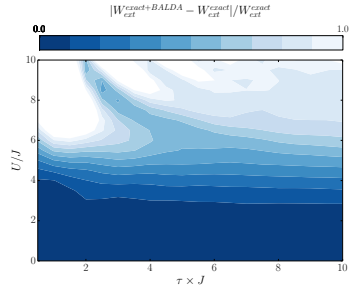

(d) 'Exact + BALDA' quantum work relative error $T = 0.2J/k_B$

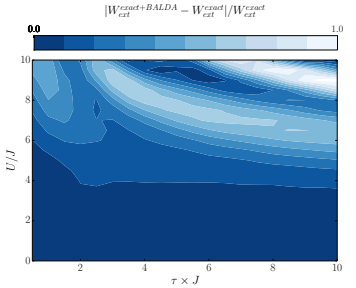

(e) 'Exact + BALDA' quantum work relative error $T = 2.5J/k_B$

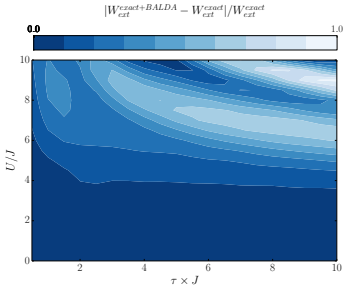

(f) 'Exact + BALDA' quantum work relative error $T = 20J/k_B$

Figure D.46: 'Exact + BALDA' work (top row) and relative error (bottom row) for the 4 sites slope at the three temperatures.

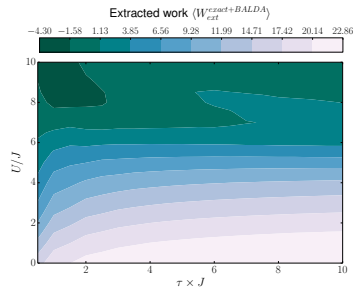

(a) 'Exact + BALDA' quantum work $T = 0.2J/k_B$

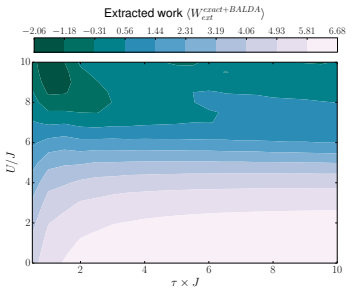

(b) 'Exact + BALDA' quantum work $T = 2.5J/k_B$

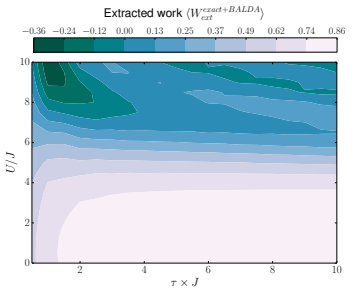

(c) 'Exact + BALDA' quantum work $T = 20J/k_B$

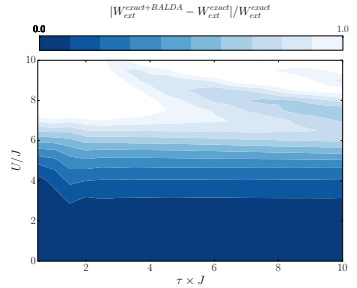

(d) 'Exact + BALDA' quantum work relative error $T = 0.2J/k_B$

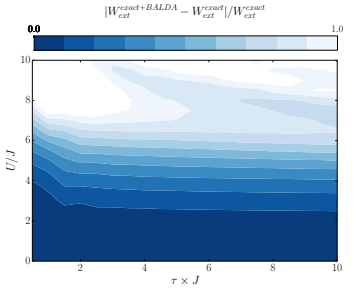

(e) 'Exact + BALDA' quantum work relative error $T = 2.5J/k_B$

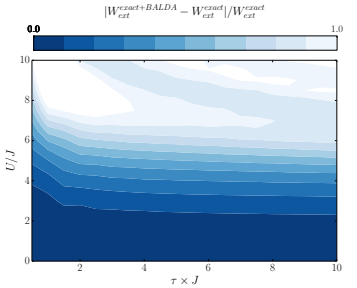

(f) 'Exact + BALDA' quantum work relative error $T = 20J/k_B$

Figure D.47: 'Exact + BALDA' work (top row) and relative error (bottom row) for the 6 sites zigzag at the three temperatures.

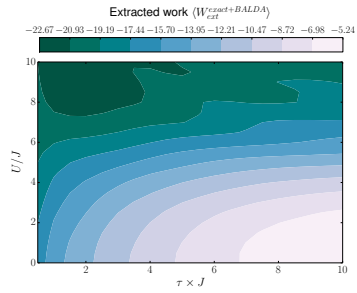

(a) 'Exact + BALDA' quantum work $T = 0.2J/k_B$

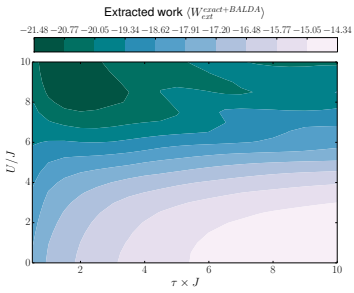

(b) 'Exact + BALDA' quantum work $T = 2.5J/k_B$

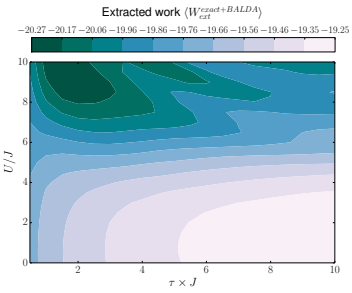

(c) 'Exact + BALDA' quantum work $T = 20J/k_B$

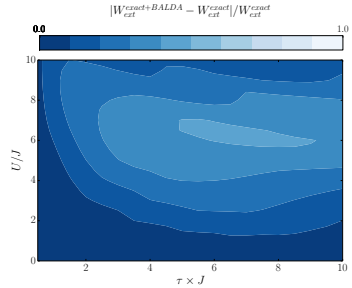

(d) 'Exact + BALDA' quantum work relative error $T = 0.2J/k_B$

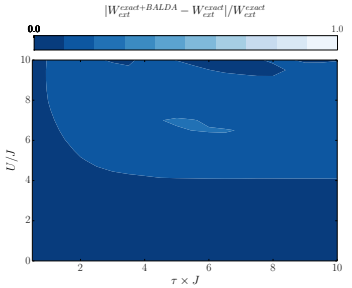

(e) 'Exact + BALDA' quantum work relative error $T = 2.5J/k_B$

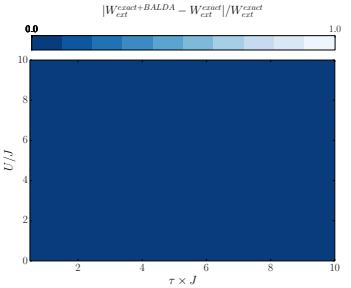

(f) 'Exact + BALDA' quantum work relative error $T = 20J/k_B$

Figure D.48: 'Exact + BALDA' work (top row) and relative error (bottom row) for the 6 sites teeth at the three temperatures.

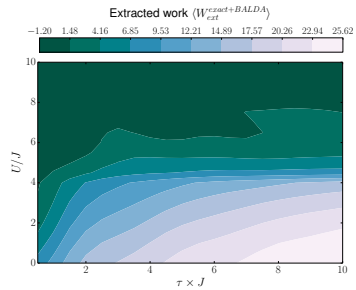

(a) 'Exact + BALDA' quantum work $T = 0.2J/k_B$

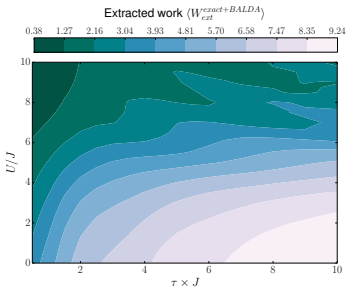

(b) 'Exact + BALDA' quantum work $T = 2.5J/k_B$

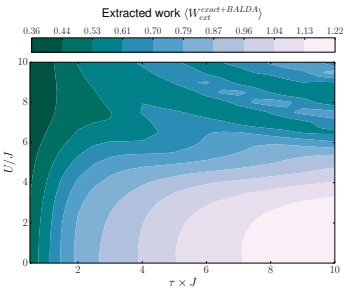

(c) 'Exact + BALDA' quantum work $T = 20J/k_B$

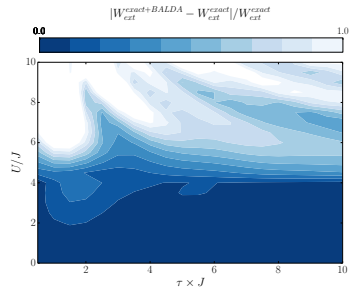

(d) 'Exact + BALDA' quantum work relative error $T = 0.2J/k_B$

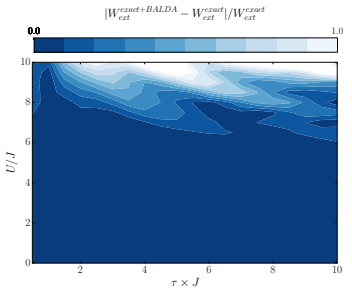

(e) 'Exact + BALDA' quantum work relative error $T = 2.5J/k_B$

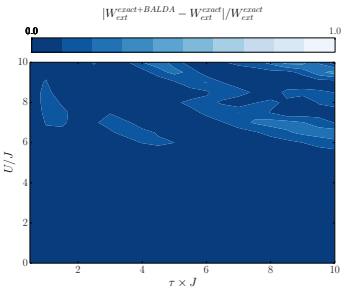

(f) 'Exact + BALDA' quantum work relative error $T = 20J/k_B$

Figure D.49: 'Exact + BALDA' work (top row) and relative error (bottom row) for the 6 sites slope at the three temperatures.

D.4.2 'Exact + BALDA' entropy

The entropy is calculated by $\Delta S_{exact+BALDA} = \beta \left(\langle W^{exact+BALDA} \rangle - \Delta F^{exact} \right)$, where $\Delta F^{exact} = -\left(1/\beta\right) \ln \left(Z_{\tau}^{exact} / Z_{0}^{exact} \right)$.

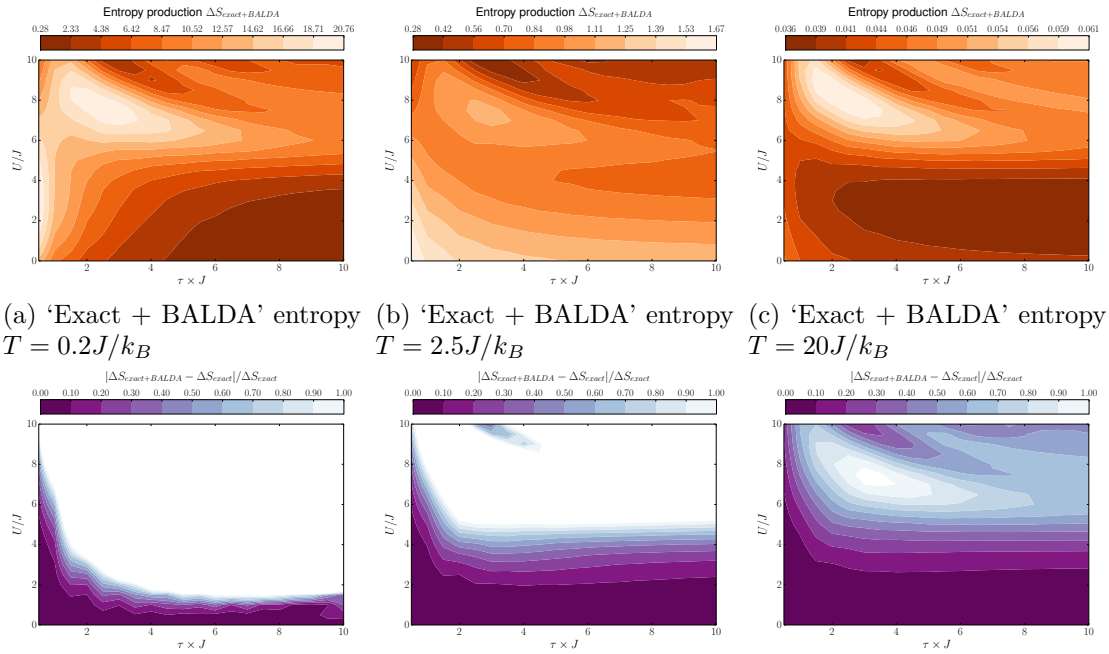

(a) 'Exact + BALDA' entropy $T = 0.2J/k_B$

(b) 'Exact + BALDA' entropy $T = 2.5J/k_B$

(c) 'Exact + BALDA' entropy $T = 20J/k_B$

(d) 'Exact + BALDA' entropy relative error $T = 0.2J/k_B$

(e) 'Exact + BALDA' entropy relative error $T = 2.5J/k_B$

(f) 'Exact + BALDA' entropy relative error $T = 20J/k_B$

Figure D.50: 'Exact + BALDA' entropy (top row) and relative error (bottom row) for the 2 sites zigzag at the three temperatures.

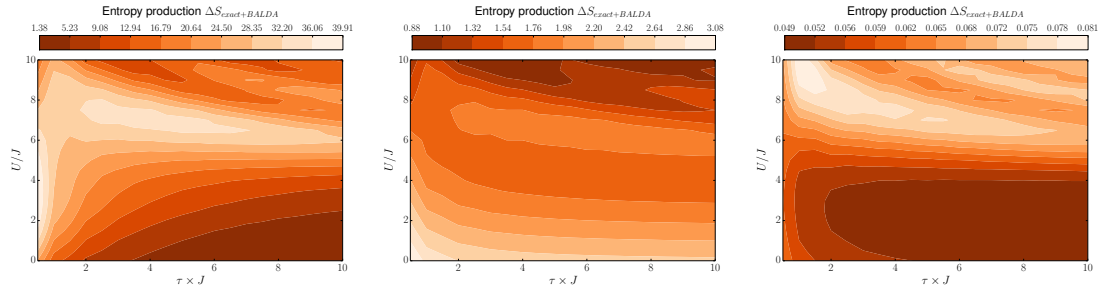

(a) 'Exact + BALDA' entropy $T = 0.2J/k_B$ (b) 'Exact + BALDA' entropy $T = 2.5J/k_B$ (c) 'Exact + BALDA' entropy $T = 20J/k_B$

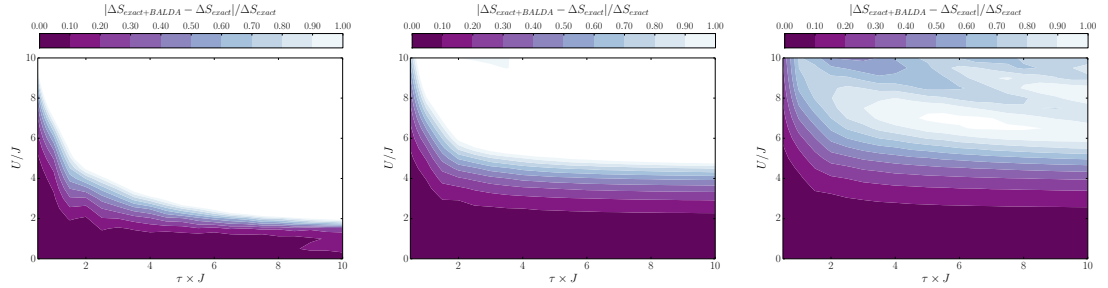

(d) 'Exact + BALDA' entropy relative error $T = 0.2J/k_B$ (e) 'Exact + BALDA' entropy relative error $T = 2.5J/k_B$ (f) 'Exact + BALDA' entropy relative error $T = 20J/k_B$

Figure D.51: 'Exact + BALDA' entropy (top row) and relative error (bottom row) for the 4 sites zigzag at the three temperatures.

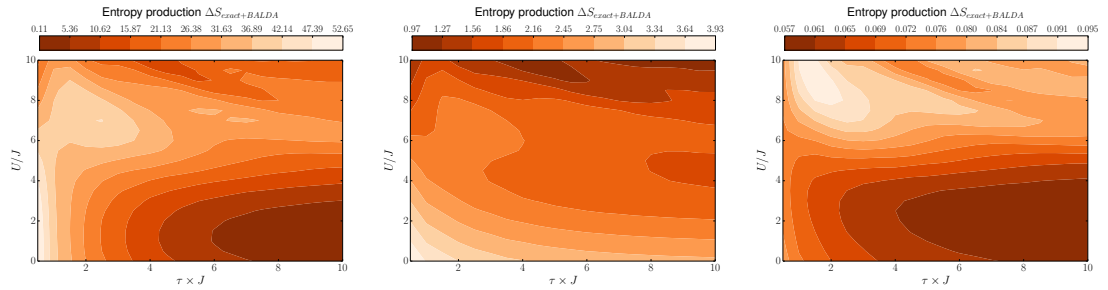

(a) 'Exact + BALDA' entropy $T = 0.2J/k_B$ (b) 'Exact + BALDA' entropy $T = 2.5J/k_B$ (c) 'Exact + BALDA' entropy $T = 20J/k_B$

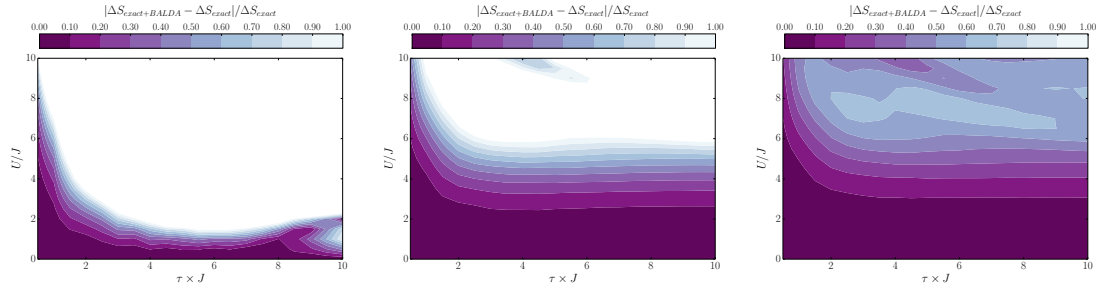

(d) 'Exact + BALDA' entropy relative error $T = 0.2J/k_B$ (e) 'Exact + BALDA' entropy relative error $T = 2.5J/k_B$ (f) 'Exact + BALDA' entropy relative error $T = 20J/k_B$

Figure D.52: 'Exact + BALDA' entropy (top row) and relative error (bottom row) for the 4 sites teeth at the three temperatures.

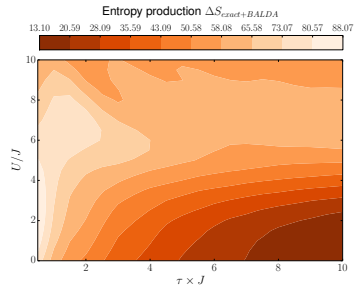

(a) 'Exact + BALDA' entropy $T = 0.2J/k_B$

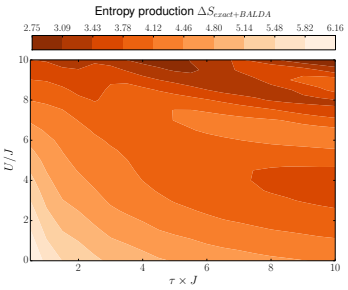

(b) 'Exact + BALDA' entropy $T = 2.5J/k_B$

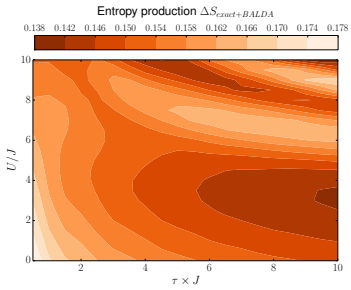

(c) 'Exact + BALDA' entropy $T = 20J/k_B$

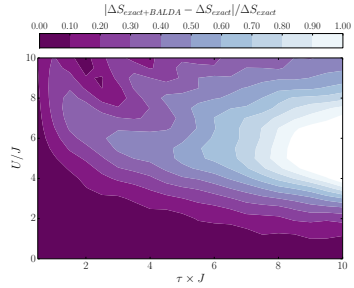

(d) 'Exact + BALDA' entropy relative error $T = 0.2J/k_B$

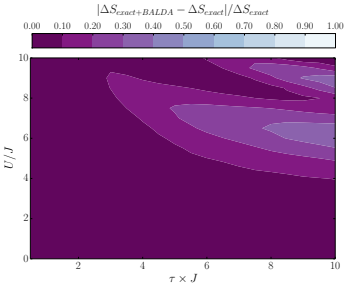

(e) 'Exact + BALDA' entropy relative error $T = 2.5J/k_B$

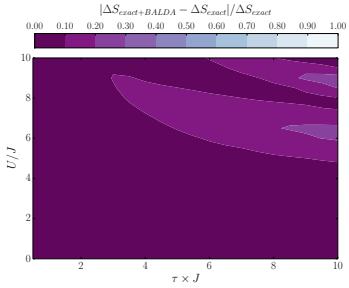

(f) 'Exact + BALDA' entropy relative error $T = 20J/k_B$

Figure D.53: 'Exact + BALDA' entropy (top row) and relative error (bottom row) for the 4 sites slope at the three temperatures.

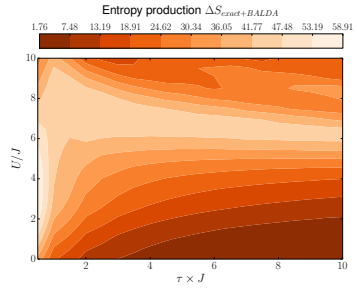

(a) 'Exact + BALDA' entropy $T = 0.2J/k_B$

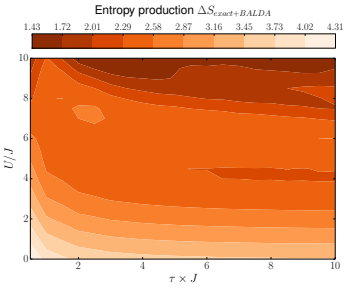

(b) 'Exact + BALDA' entropy $T = 2.5J/k_B$

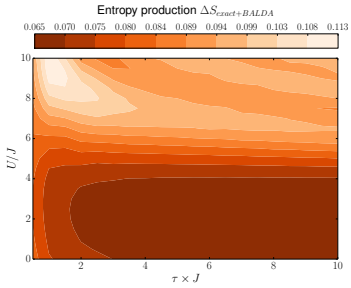

(c) 'Exact + BALDA' entropy $T = 20J/k_B$

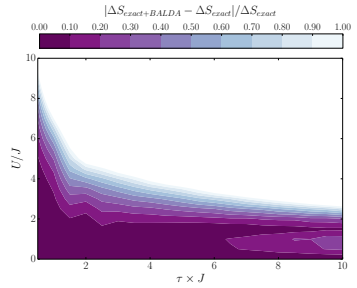

(d) 'Exact + BALDA' entropy relative error $T = 0.2J/k_B$

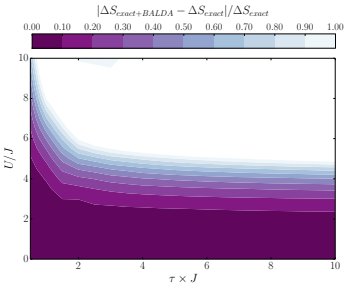

(e) 'Exact + BALDA' entropy relative error $T = 2.5J/k_B$

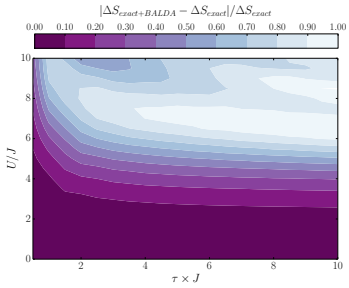

(f) 'Exact + BALDA' entropy relative error $T = 20J/k_B$

Figure D.54: 'Exact + BALDA' entropy (top row) and relative error (bottom row) for the 6 sites zigzag at the three temperatures.

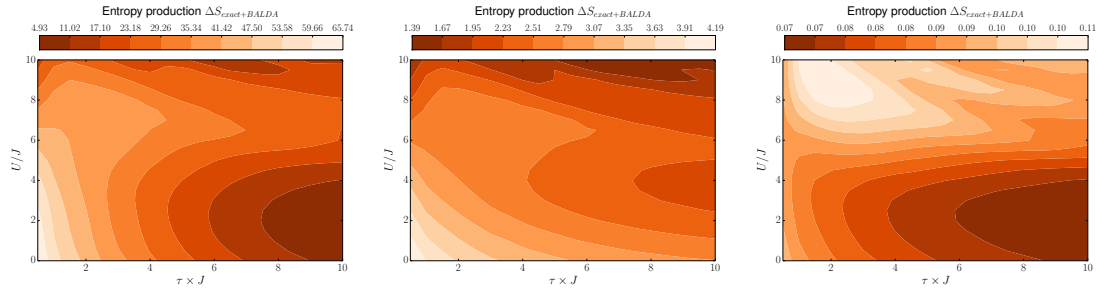

(a) 'Exact + BALDA' entropy $T = 0.2J/k_B$ (b) 'Exact + BALDA' entropy $T = 2.5J/k_B$ (c) 'Exact + BALDA' entropy $T = 20J/k_B$

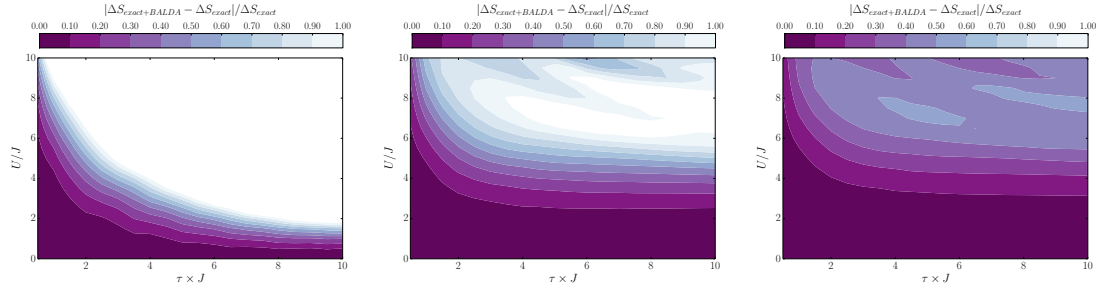

(d) 'Exact + BALDA' entropy relative error $T = 0.2J/k_B$ (e) 'Exact + BALDA' entropy relative error $T = 2.5J/k_B$ (f) 'Exact + BALDA' entropy relative error $T = 20J/k_B$

Figure D.55: 'Exact + BALDA' entropy (top row) and relative error (bottom row) for the 6 sites teeth at the three temperatures.

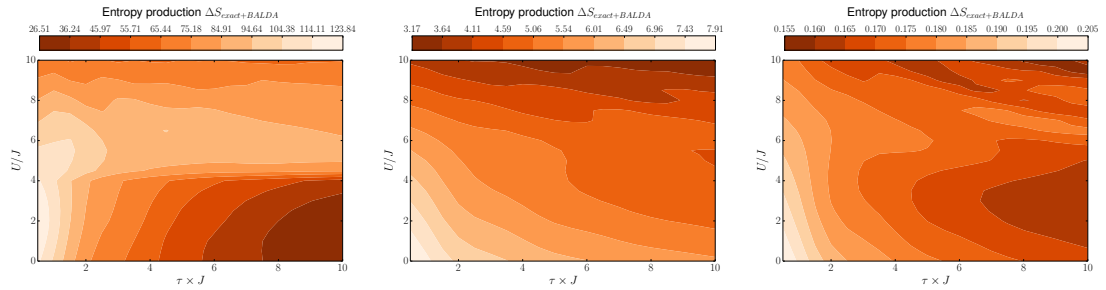

(a) 'Exact + BALDA' entropy $T = 0.2J/k_B$ (b) 'Exact + BALDA' entropy $T = 2.5J/k_B$ (c) 'Exact + BALDA' entropy $T = 20J/k_B$

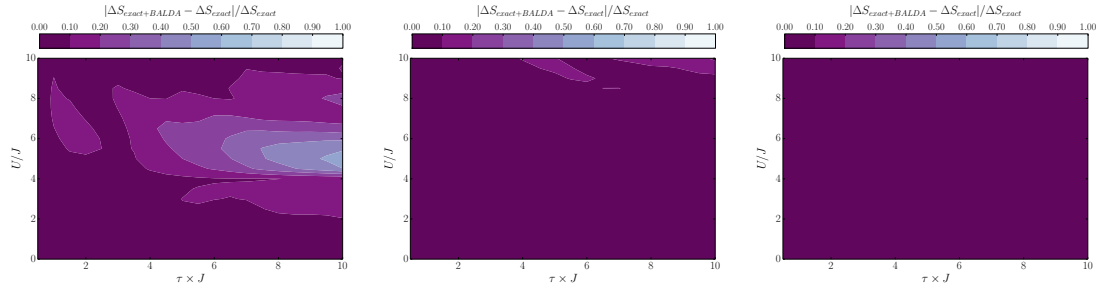

(d) 'Exact + BALDA' entropy relative error $T = 0.2J/k_B$ (e) 'Exact + BALDA' entropy relative error $T = 2.5J/k_B$ (f) 'Exact + BALDA' entropy relative error $T = 20J/k_B$

Figure D.56: 'Exact + BALDA' entropy (top row) and relative error (bottom row) for the 6 sites slope at the three temperatures.

D.5 Approximation based on the exact ground state exchange-correlation potential, 'v_{xc}'

This section shows the complete set of results based on the parameter set outlined in section 6.2.2 for the 'v_{xc}' approximation defined in chapter 8. Note that for 6 sites the teeth potential is absent. This is because the nature of the system at $t = 0$ (all sites having extremely similar energies) means it is too challenging to achieve an accurate inversion of the density.

D.5.1 Exact ground state exchange-correlation potential 'v_{xc}' work

Calculated using $\langle W_{ext}^{v_{xc}} \rangle = \mathrm{Tr}\left[\rho^{v_{xc}}(0)\hat{H}^{v_{xc}}(0)\right] - \mathrm{Tr}\left[\rho^{v_{xc}}(\tau)\hat{H}^{v_{xc}}(\tau)\right]$ with $\hat{H}_{\mathrm{evo}}$ approximated using the exact ground state v_{xc} at $t = 0$.

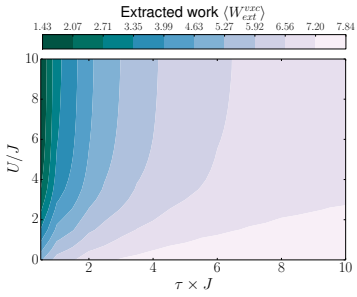

(a) 'v_{xc}' quantum work $T = 0.2J/k_B$

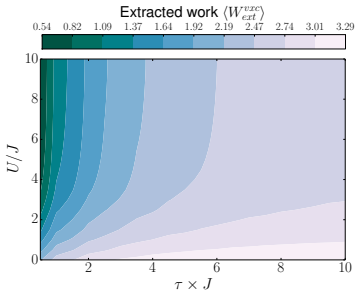

(b) 'v_{xc}' quantum work $T = 2.5J/k_B$

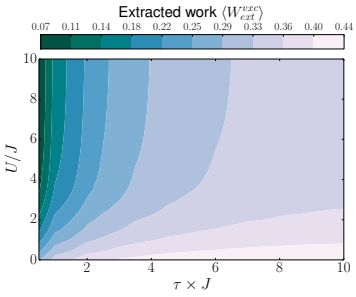

(c) 'v_{xc}' quantum work $T = 20J/k_B$

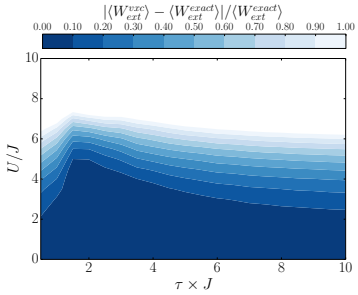

(d) 'v_{xc}' quantum work relative error $T = 0.2J/k_B$

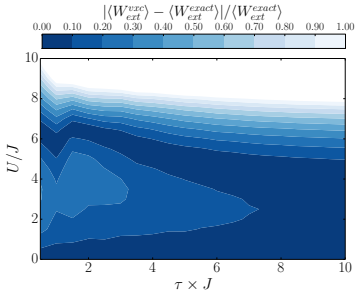

(e) 'v_{xc}' quantum work relative error $T = 2.5J/k_B$

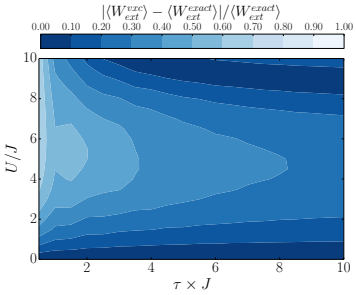

(f) 'v_{xc}' quantum work relative error $T = 20J/k_B$

Figure D.57: 'v_{xc}' work (top row) and relative error (bottom row) for the 2 sites zigzag at the three temperatures.

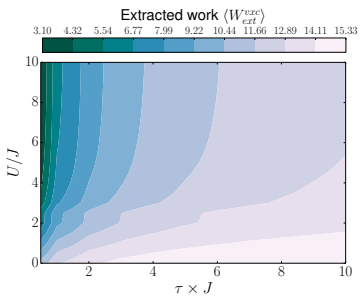

(a) 'v_{xc}' quantum work $T = 0.2J/k_B$

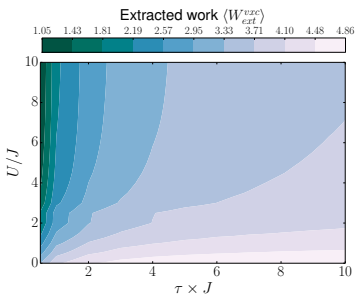

(b) 'v_{xc}' quantum work $T = 2.5J/k_B$

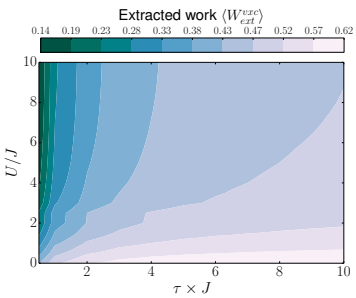

(c) 'v_{xc}' quantum work $T = 20J/k_B$

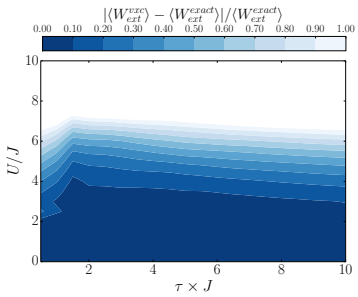

(d) 'v_{xc}' quantum work relative error $T = 0.2J/k_B$

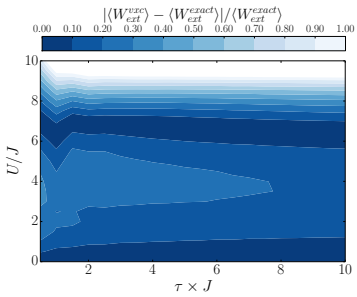

(e) 'v_{xc}' quantum work relative error $T = 2.5J/k_B$

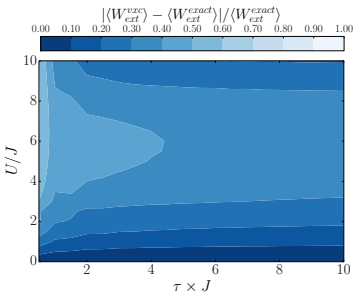

(f) 'v_{xc}' quantum work relative error $T = 20J/k_B$

Figure D.58: 'v_{xc}' work (top row) and relative error (bottom row) for the 4 sites zigzag at the three temperatures.

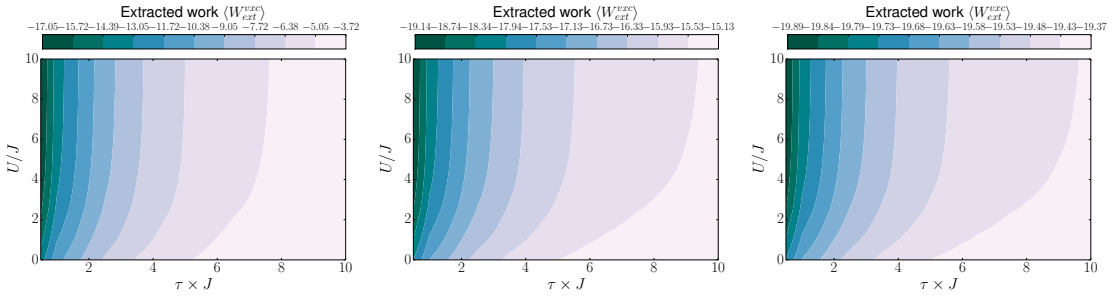

(a) 'v_{xc}' quantum work $T = 0.2J/k_B$ (b) 'v_{xc}' quantum work $T = 2.5J/k_B$ (c) 'v_{xc}' quantum work $T = 20J/k_B$

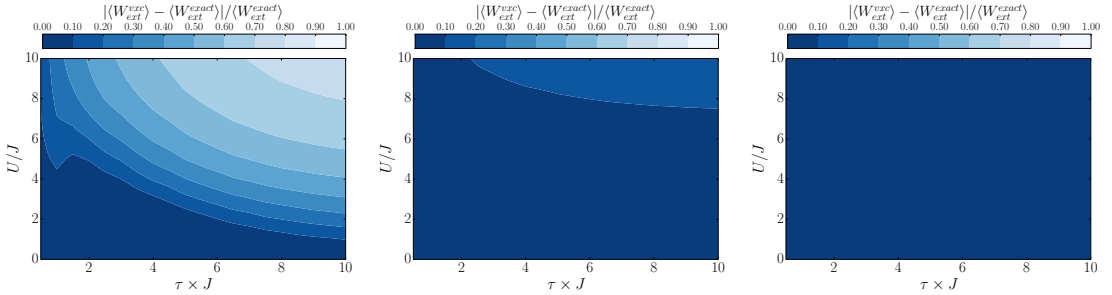

(d) 'v_{xc}' quantum work relative error $T = 0.2J/k_B$ (e) 'v_{xc}' quantum work relative error $T = 2.5J/k_B$ (f) 'v_{xc}' quantum work relative error $T = 20J/k_B$

Figure D.59: 'v_{xc}' work (top row) and relative error (bottom row) for the 4 sites teeth at the three temperatures.

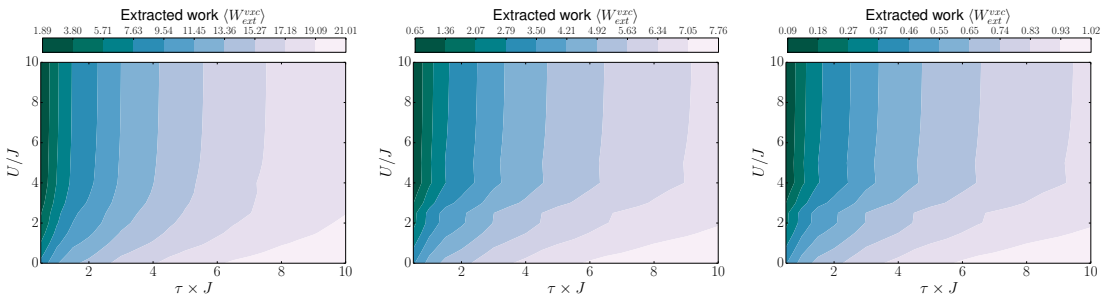

(a) 'v_{xc}' quantum work $T = 0.2J/k_B$ (b) 'v_{xc}' quantum work $T = 2.5J/k_B$ (c) 'v_{xc}' quantum work $T = 20J/k_B$

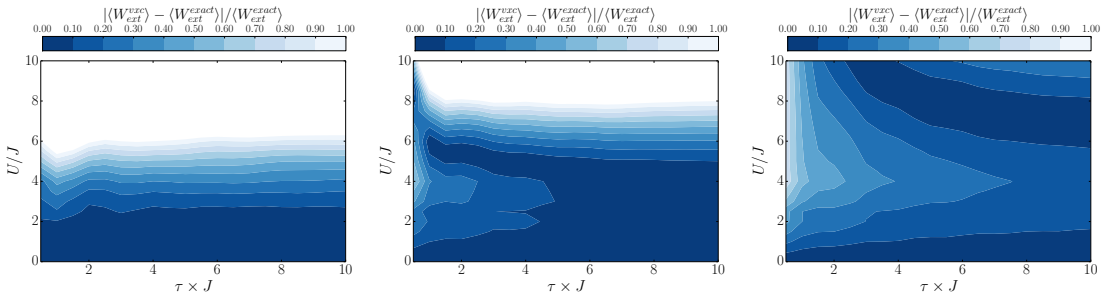

(d) 'v_{xc}' quantum work relative error $T = 0.2J/k_B$ (e) 'v_{xc}' quantum work relative error $T = 2.5J/k_B$ (f) 'v_{xc}' quantum work relative error $T = 20J/k_B$

Figure D.60: 'v_{xc}' work (top row) and relative error (bottom row) for the 4 sites slope at the three temperatures.

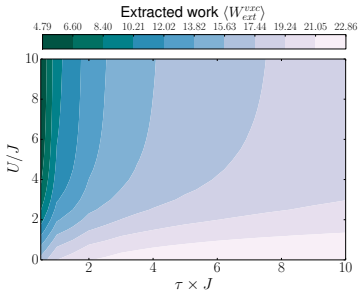

(a) 'v_{xc}' quantum work $T = 0.2J/k_B$

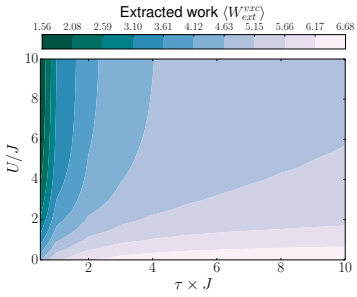

(b) 'v_{xc}' quantum work $T = 2.5J/k_B$

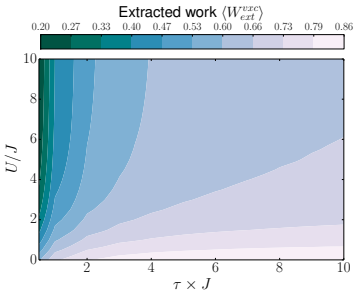

(c) 'v_{xc}' quantum work $T = 20J/k_B$

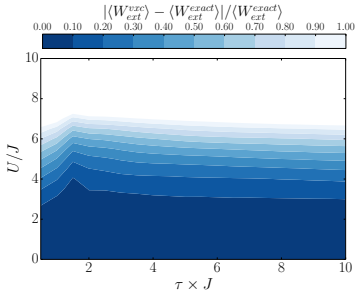

(d) 'v_{xc}' quantum work relative error $T = 0.2J/k_B$

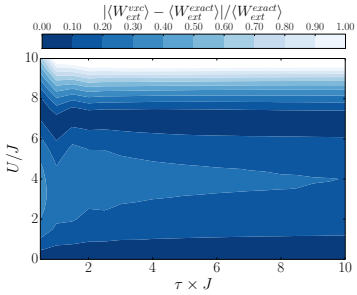

(e) 'v_{xc}' quantum work relative error $T = 2.5J/k_B$

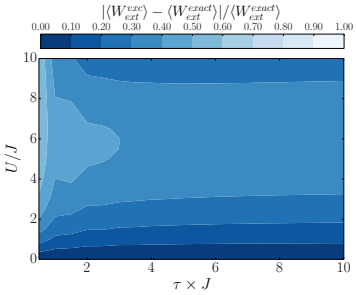

(f) 'v_{xc}' quantum work relative error $T = 20J/k_B$

Figure D.61: 'v_{xc}' work (top row) and relative error (bottom row) for the 6 sites zigzag at the three temperatures.

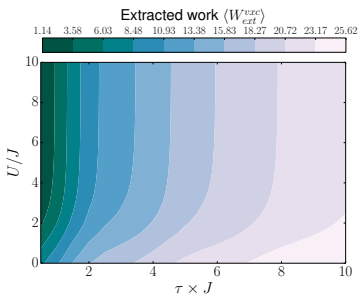

(a) 'v_{xc}' quantum work $T = 0.2J/k_B$

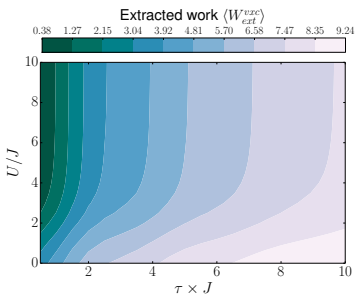

(b) 'v_{xc}' quantum work $T = 2.5J/k_B$

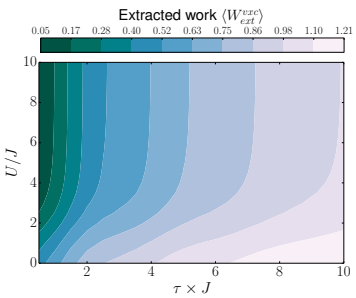

(c) 'v_{xc}' quantum work $T = 20J/k_B$

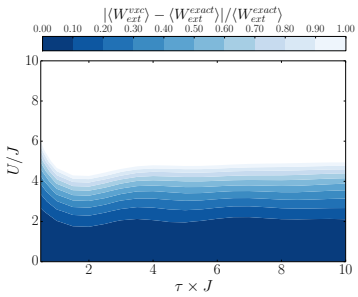

(d) 'v_{xc}' quantum work relative error $T = 0.2J/k_B$

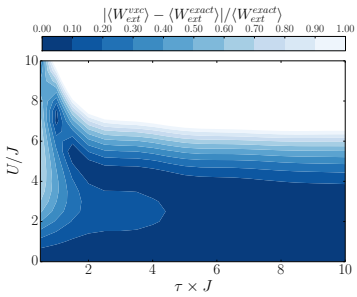

(e) 'v_{xc}' quantum work relative error $T = 2.5J/k_B$

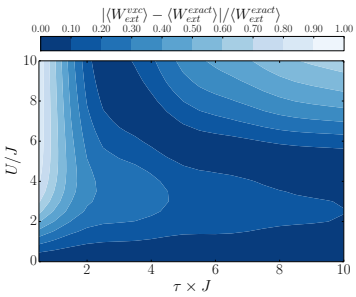

(f) 'v_{xc}' quantum work relative error $T = 20J/k_B$

Figure D.62: 'v_{xc}' work (top row) and relative error (bottom row) for the 6 sites slope at the three temperatures.

D.5.2 'v_{xc}' entropy

The entropy is calculated by $\Delta S_{v_{xc}} = \beta\left(\langle W^{v_{xc}}\rangle - \Delta F^{v_{xc}}\right)$, where $\Delta F^{v_{xc}} = -\left(1/\beta\right)\ln\left(Z_{\tau}^{v_{xc}}/Z_{0}^{v_{xc}}\right)$.

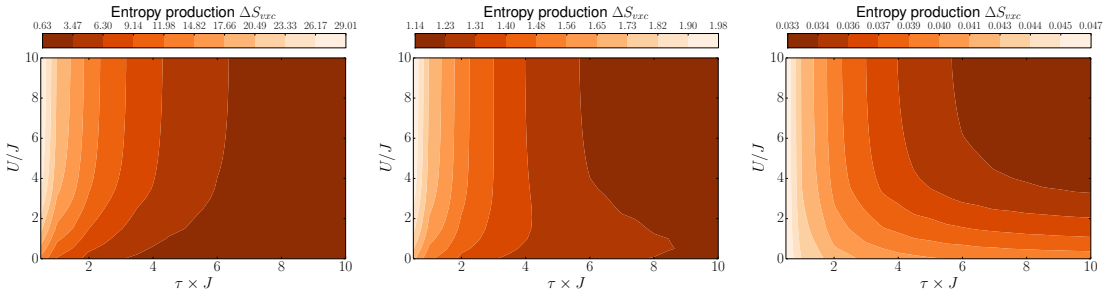

(a) 'v_{xc}' entropy $T = 0.2J/k_B$ (b) 'v_{xc}' entropy $T = 2.5J/k_B$ (c) 'v_{xc}' entropy $T = 20J/k_B$

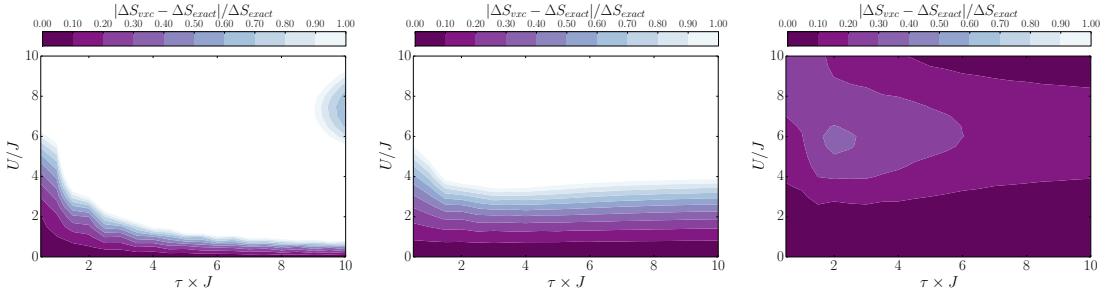

(d) 'v_{xc}' entropy relative error $T = 0.2J/k_B$ (e) 'v_{xc}' entropy relative error $T = 2.5J/k_B$ (f) 'v_{xc}' entropy relative error $T = 20J/k_B$

Figure D.63: 'v_{xc}' entropy (top row) and relative error (bottom row) for the 2 sites zigzag at the three temperatures.

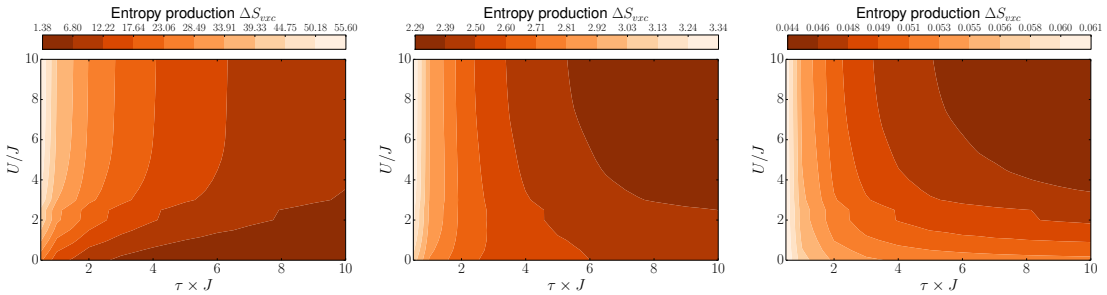

(a) 'v_{xc}' entropy $T = 0.2J/k_B$ (b) 'v_{xc}' entropy $T = 2.5J/k_B$ (c) 'v_{xc}' entropy $T = 20J/k_B$

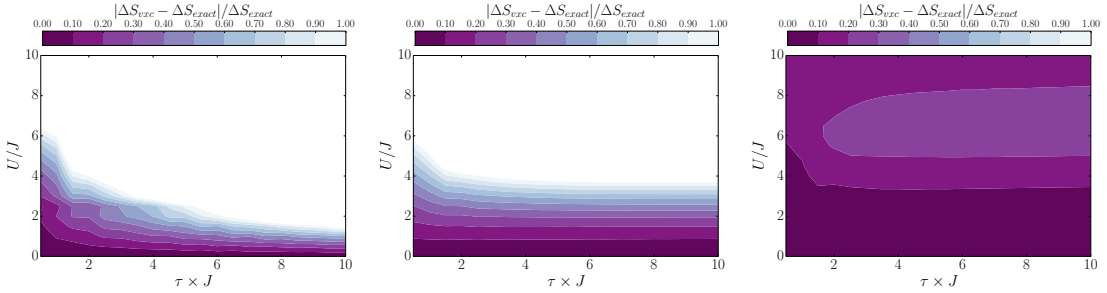

(d) 'v_{xc}' entropy relative error $T = 0.2J/k_B$ (e) 'v_{xc}' entropy relative error $T = 2.5J/k_B$ (f) 'v_{xc}' entropy relative error $T = 20J/k_B$

Figure D.64: 'v_{xc}' entropy (top row) and relative error (bottom row) for the 4 sites zigzag at the three temperatures.

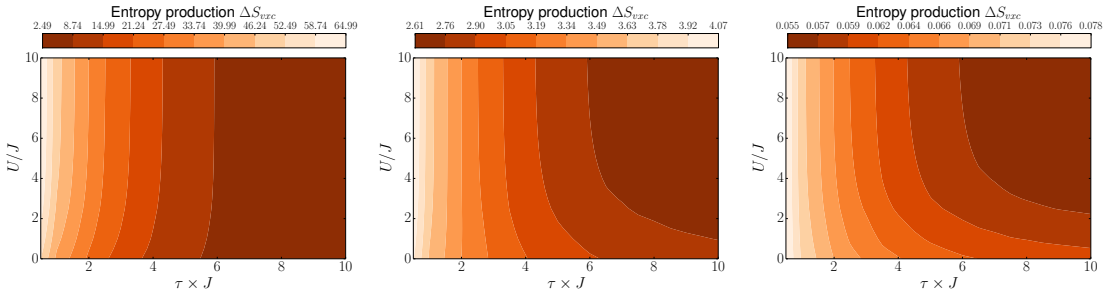

(a) 'v_{xc}' entropy $T = 0.2J/k_B$ (b) 'v_{xc}' entropy $T = 2.5J/k_B$ (c) 'v_{xc}' entropy $T = 20J/k_B$

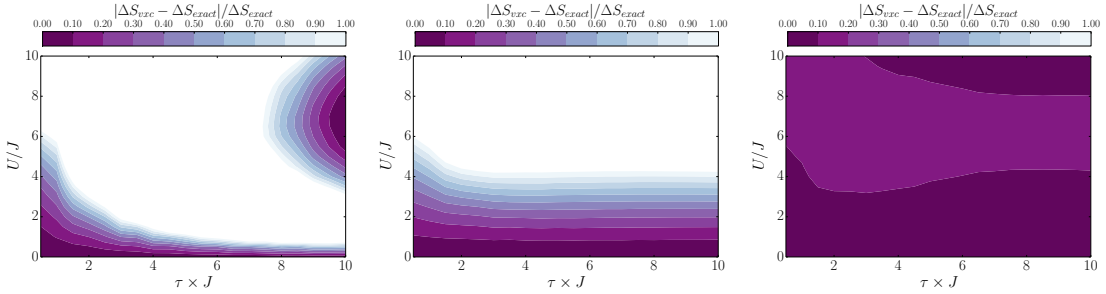

(d) 'v_{xc}' entropy relative error $T = 0.2J/k_B$ (e) 'v_{xc}' entropy relative error $T = 2.5J/k_B$ (f) 'v_{xc}' entropy relative error $T = 20J/k_B$

Figure D.65: 'v_{xc}' entropy (top row) and relative error (bottom row) for the 4 sites teeth at the three temperatures.

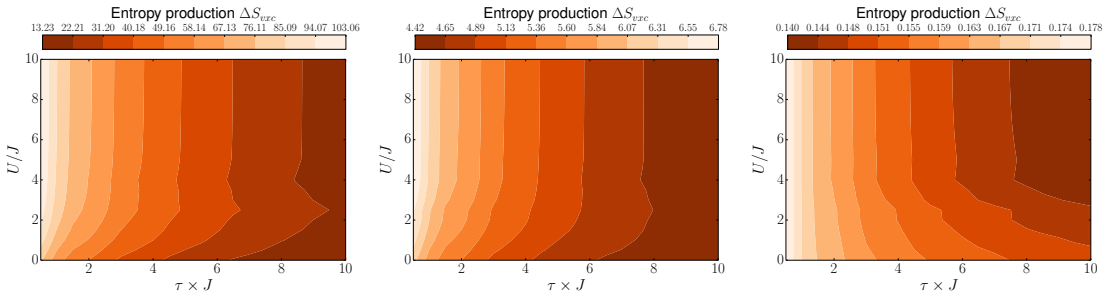

(a) 'v_{xc}' entropy $T = 0.2J/k_B$ (b) 'v_{xc}' entropy $T = 2.5J/k_B$ (c) 'v_{xc}' entropy $T = 20J/k_B$

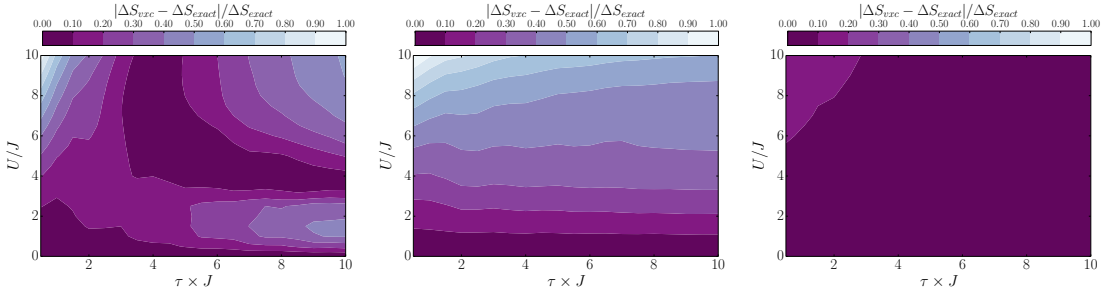

(d) 'v_{xc}' entropy relative error $T = 0.2J/k_B$ (e) 'v_{xc}' entropy relative error $T = 2.5J/k_B$ (f) 'v_{xc}' entropy relative error $T = 20J/k_B$

Figure D.66: 'v_{xc}' entropy (top row) and relative error (bottom row) for the 4 sites slope at the three temperatures.

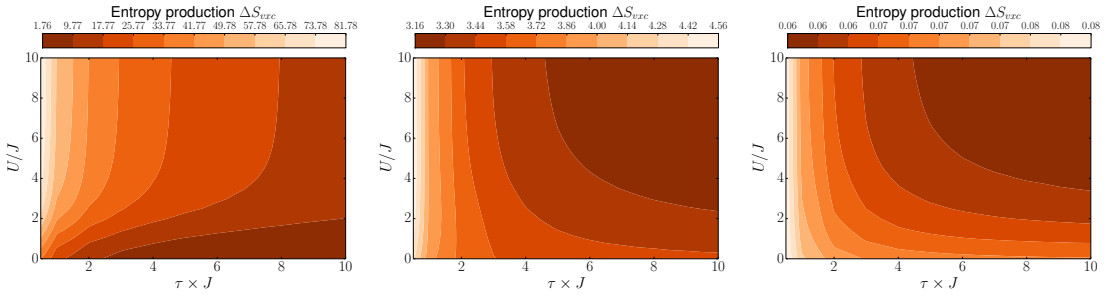

(a) 'v_{xc}' entropy $T = 0.2J/k_B$ (b) 'v_{xc}' entropy $T = 2.5J/k_B$ (c) 'v_{xc}' entropy $T = 20J/k_B$

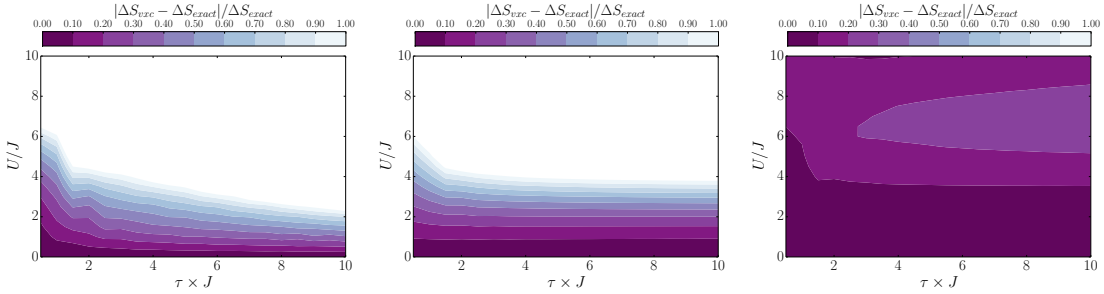

(d) 'v_{xc}' entropy relative error $T = 0.2J/k_B$ (e) 'v_{xc}' entropy relative error $T = 2.5J/k_B$ (f) 'v_{xc}' entropy relative error $T = 20J/k_B$

Figure D.67: 'v_{xc}' entropy (top row) and relative error (bottom row) for the 6 sites zigzag at the three temperatures.

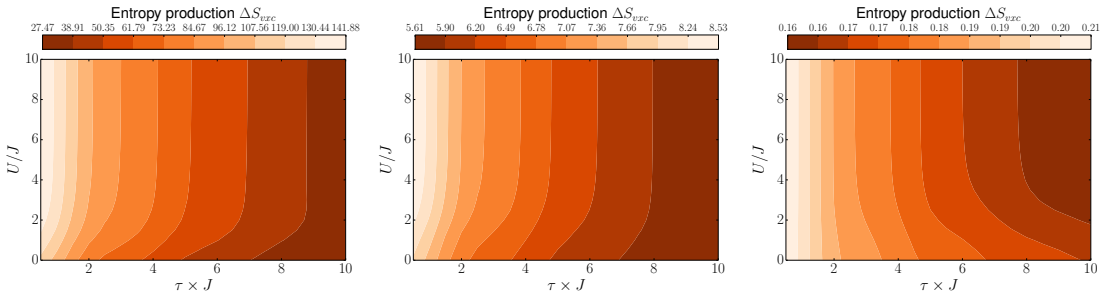

(a) 'v_{xc}' entropy $T = 0.2J/k_B$ (b) 'v_{xc}' entropy $T = 2.5J/k_B$ (c) 'v_{xc}' entropy $T = 20J/k_B$

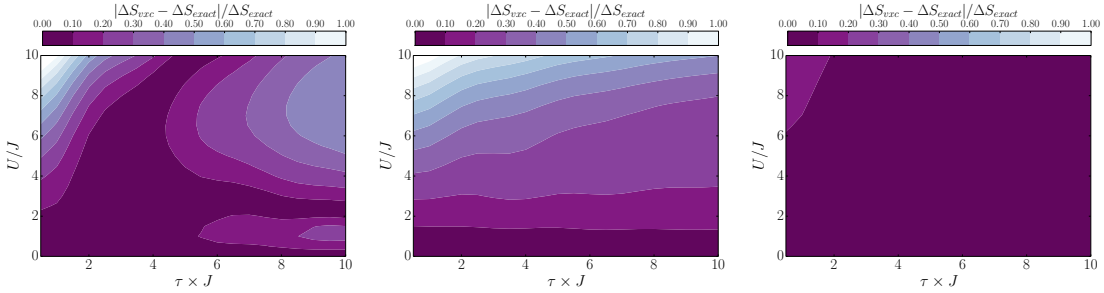

(d) 'v_{xc}' entropy relative error $T = 0.2J/k_B$ (e) 'v_{xc}' entropy relative error $T = 2.5J/k_B$ (f) 'v_{xc}' entropy relative error $T = 20J/k_B$

Figure D.68: 'v_{xc}' entropy (top row) and relative error (bottom row) for the 6 sites slope at the three temperatures.

D.6 'Exact + v_{xc}'

This section shows the complete set of results based on the parameter set outlined in section 6.2.2 for the 'exact + v_{xc}' approximation defined in chapter 8. Once again the 6 site teeth results are absent, for the same reason as described previously.

D.6.1 'Exact + v_{xc}' work

Calculated using $\langle W_{ext}^{ex+v_{xc}} \rangle = \mathrm{Tr}\left[\rho^{ex}(0)\hat{H}^{v_{xc}}(0)\right] - \mathrm{Tr}\left[\rho^{ex+v_{xc}}(\tau)\hat{H}^{v_{xc}}(\tau)\right]$ with $\hat{H}_{\mathrm{evo}}$ approximated using the exact ground state v_{xc} at $t = 0$.

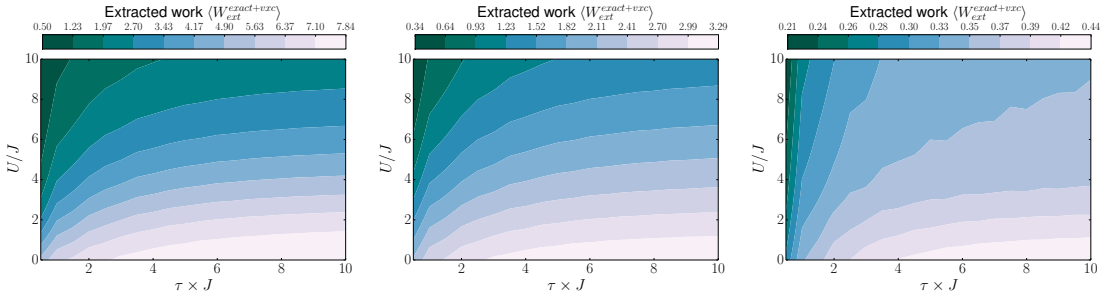

(a) 'Exact + v_{xc}' quantum work $T = 0.2J/k_B$

(b) 'Exact + v_{xc}' quantum work $T = 2.5J/k_B$

(c) 'Exact + v_{xc}' quantum work $T = 20J/k_B$

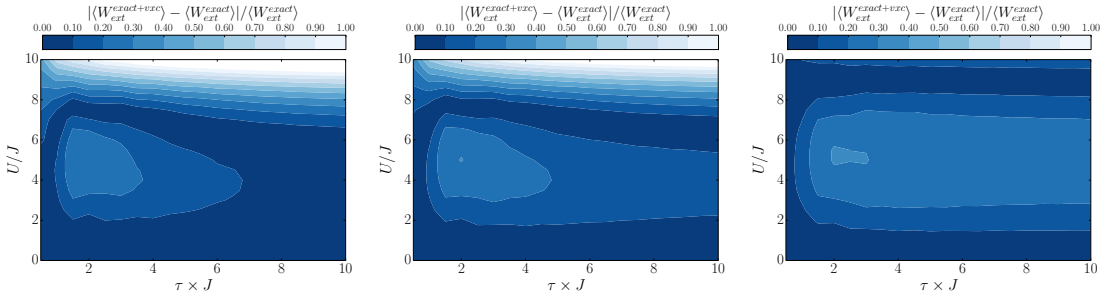

(d) 'Exact + v_{xc}' quantum work relative error $T = 0.2J/k_B$

(e) 'Exact + v_{xc}' quantum work relative error $T = 2.5J/k_B$

(f) 'Exact + v_{xc}' quantum work relative error $T = 20J/k_B$

Figure D.69: 'Exact + v_{xc}' work (top row) and relative error (bottom row) for the 2 sites zigzag at the three temperatures.

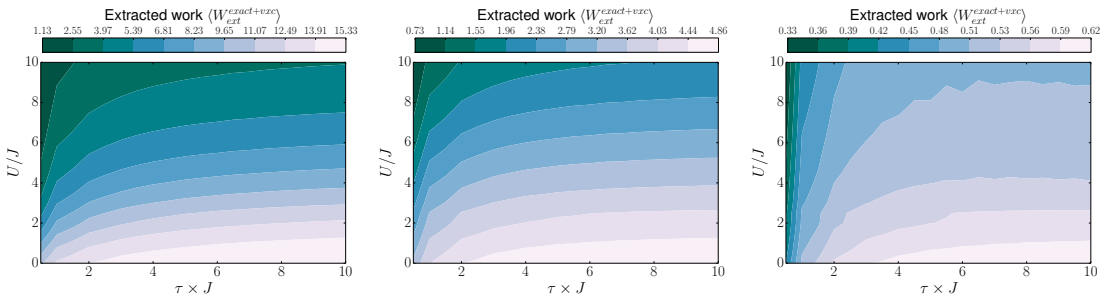

(a) 'Exact + v_{xc}' quantum work $T = 0.2J/k_B$

(b) 'Exact + v_{xc}' quantum work $T = 2.5J/k_B$

(c) 'Exact + v_{xc}' quantum work $T = 20J/k_B$

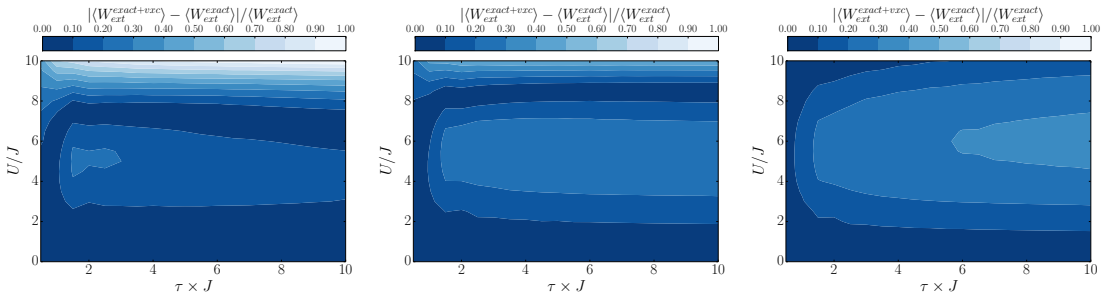

(d) 'Exact + v_{xc}' quantum work relative error $T = 0.2J/k_B$

(e) 'Exact + v_{xc}' quantum work relative error $T = 2.5J/k_B$

(f) 'Exact + v_{xc}' quantum work relative error $T = 20J/k_B$

Figure D.70: 'Exact + v_{xc}' work (top row) and relative error (bottom row) for the 4 sites zigzag at the three temperatures.

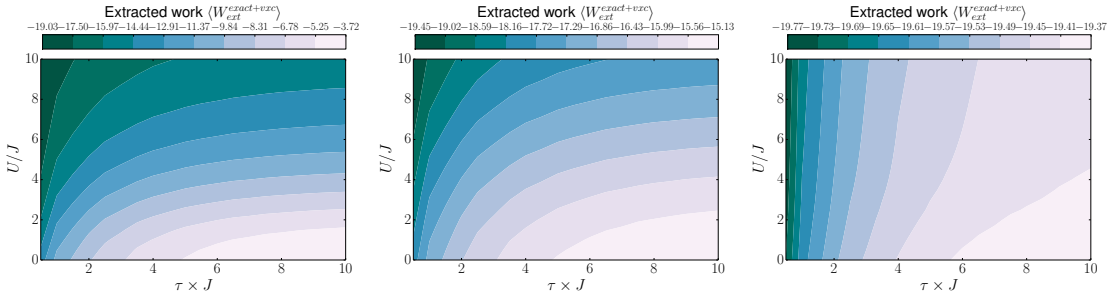

(a) 'Exact + v_{xc}' quantum work $T = 0.2J/k_B$ (b) 'Exact + v_{xc}' quantum work $T = 2.5J/k_B$ (c) 'Exact + v_{xc}' quantum work $T = 20J/k_B$

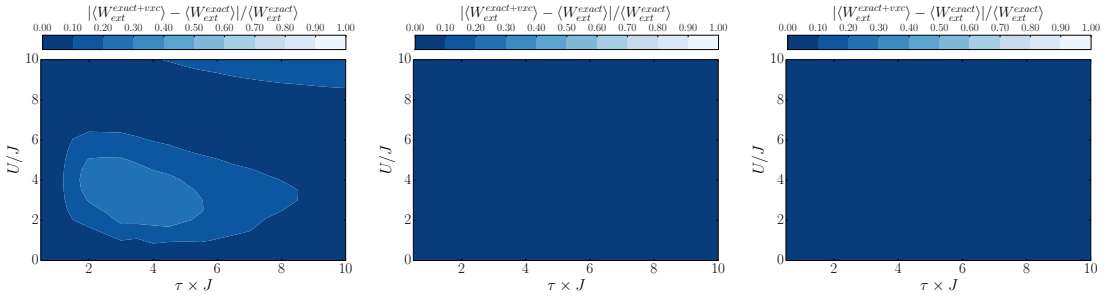

(d) 'Exact + v_{xc}' quantum work relative error $T = 0.2J/k_B$ (e) 'Exact + v_{xc}' quantum work relative error $T = 2.5J/k_B$ (f) 'Exact + v_{xc}' quantum work relative error $T = 20J/k_B$

Figure D.71: 'Exact + v_{xc}' work (top row) and relative error (bottom row) for the 4 sites teeth at the three temperatures.

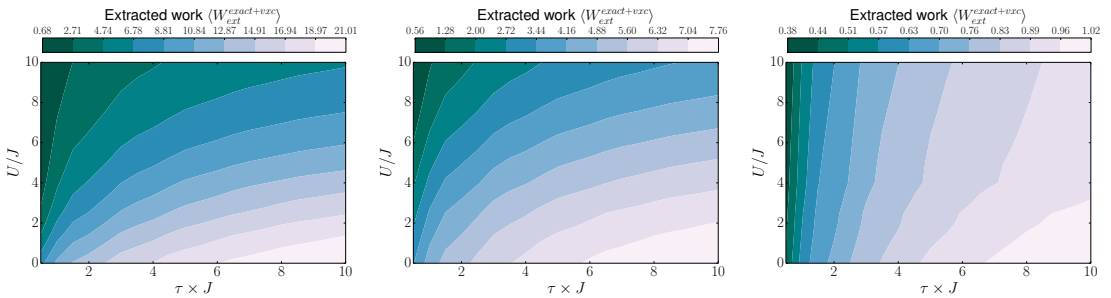

(a) 'Exact + v_{xc}' quantum work $T = 0.2J/k_B$ (b) 'Exact + v_{xc}' quantum work $T = 2.5J/k_B$ (c) 'Exact + v_{xc}' quantum work $T = 20J/k_B$

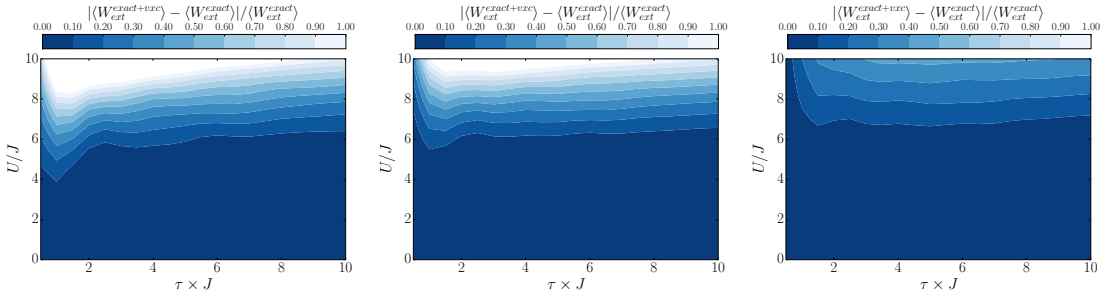

(d) 'Exact + v_{xc}' quantum work relative error $T = 0.2J/k_B$ (e) 'Exact + v_{xc}' quantum work relative error $T = 2.5J/k_B$ (f) 'Exact + v_{xc}' quantum work relative error $T = 20J/k_B$

Figure D.72: 'Exact + v_{xc}' work (top row) and relative error (bottom row) for the 4 sites slope at the three temperatures.

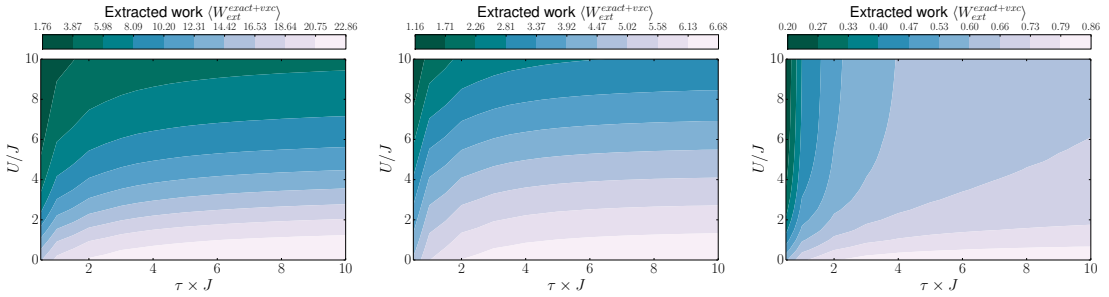

(a) 'Exact + v_{xc}' quantum work $T = 0.2J/k_B$

(b) 'Exact + v_{xc}' quantum work $T = 2.5J/k_B$

(c) 'Exact + v_{xc}' quantum work $T = 20J/k_B$

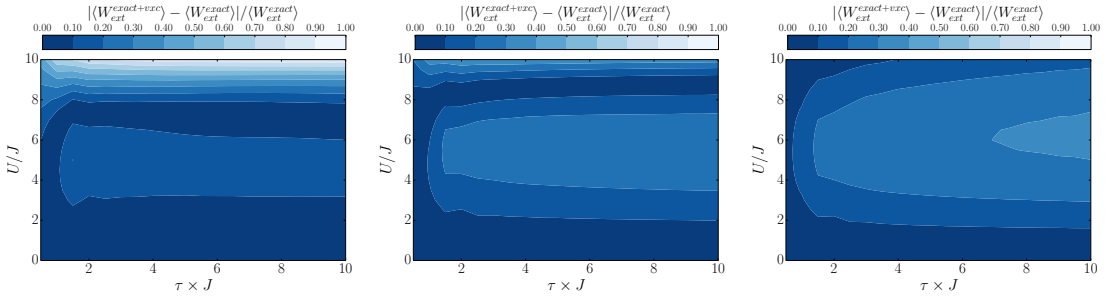

(d) 'Exact + v_{xc}' quantum work relative error $T = 0.2J/k_B$

(e) 'Exact + v_{xc}' quantum work relative error $T = 2.5J/k_B$

(f) 'Exact + v_{xc}' quantum work relative error $T = 20J/k_B$

Figure D.73: 'Exact + v_{xc}' work (top row) and relative error (bottom row) for the 6 sites zigzag at the three temperatures.

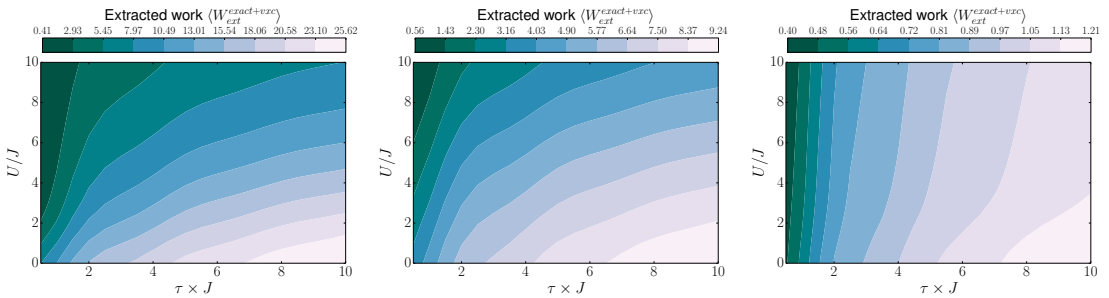

(a) 'Exact + v_{xc}' quantum work $T = 0.2J/k_B$

(b) 'Exact + v_{xc}' quantum work $T = 2.5J/k_B$

(c) 'Exact + v_{xc}' quantum work $T = 20J/k_B$

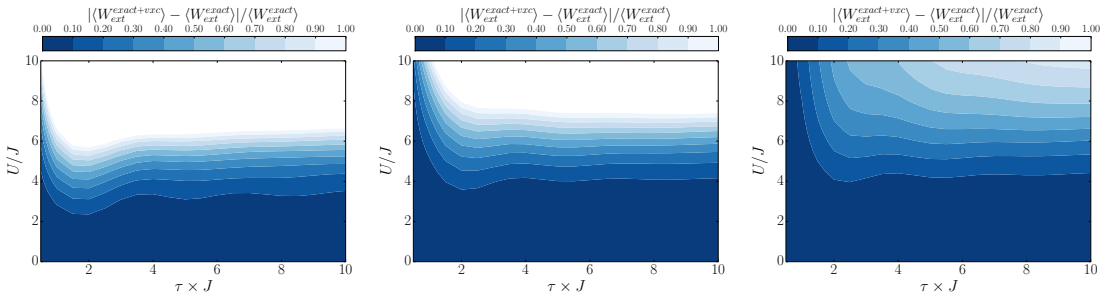

(d) 'Exact + v_{xc}' quantum work relative error $T = 0.2J/k_B$

(e) 'Exact + v_{xc}' quantum work relative error $T = 2.5J/k_B$

(f) 'Exact + v_{xc}' quantum work relative error $T = 20J/k_B$

Figure D.74: 'Exact + v_{xc}' work (top row) and relative error (bottom row) for the 6 sites slope at the three temperatures.

D.6.2 'Exact + v_{xc}' entropy

The entropy is calculated by $\Delta S_{exact+v_{xc}} = \beta\left(\langle W^{exact+v_{xc}}\rangle - \Delta F^{exact}\right)$, where $\Delta F^{exact} = -\left(1/\beta\right)\ln\left(Z_{\tau}^{exact}/Z_{0}^{exact}\right)$.

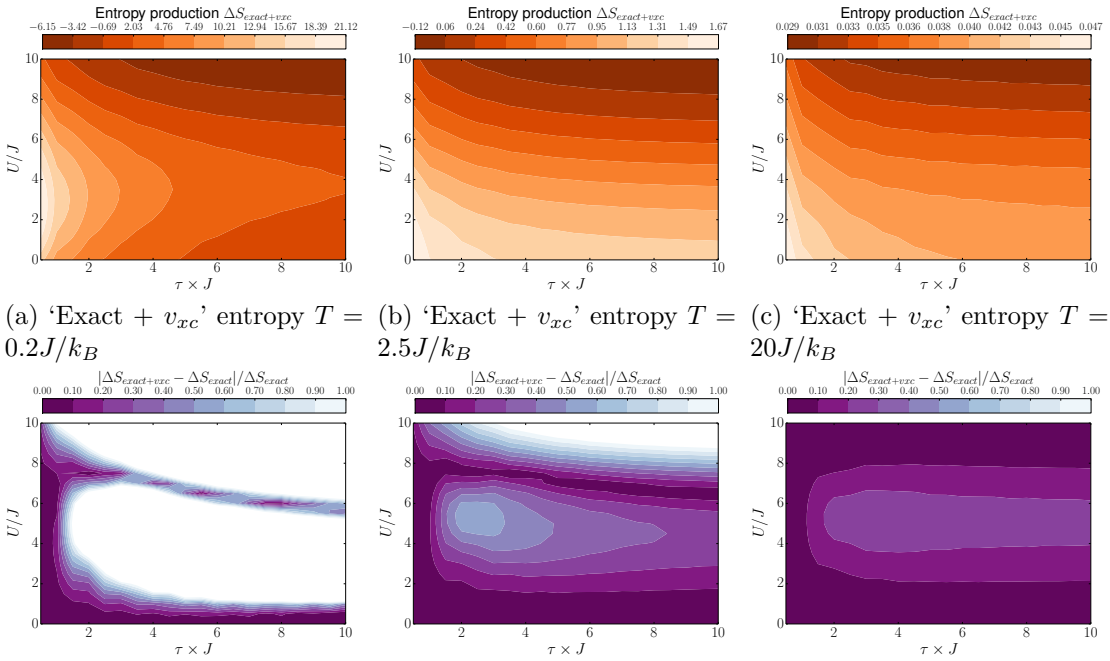

(a) 'Exact + v_{xc}' entropy $T = 0.2J/k_B$ (b) 'Exact + v_{xc}' entropy $T = 2.5J/k_B$ (c) 'Exact + v_{xc}' entropy $T = 20J/k_B$

(d) 'Exact + v_{xc}' entropy relative error $T = 0.2J/k_B$ (e) 'Exact + v_{xc}' entropy relative error $T = 2.5J/k_B$ (f) 'Exact + v_{xc}' entropy relative error $T = 20J/k_B$

Figure D.75: 'Exact + v_{xc}' entropy (top row) and relative error (bottom row) for the 2 sites zigzag at the three temperatures.

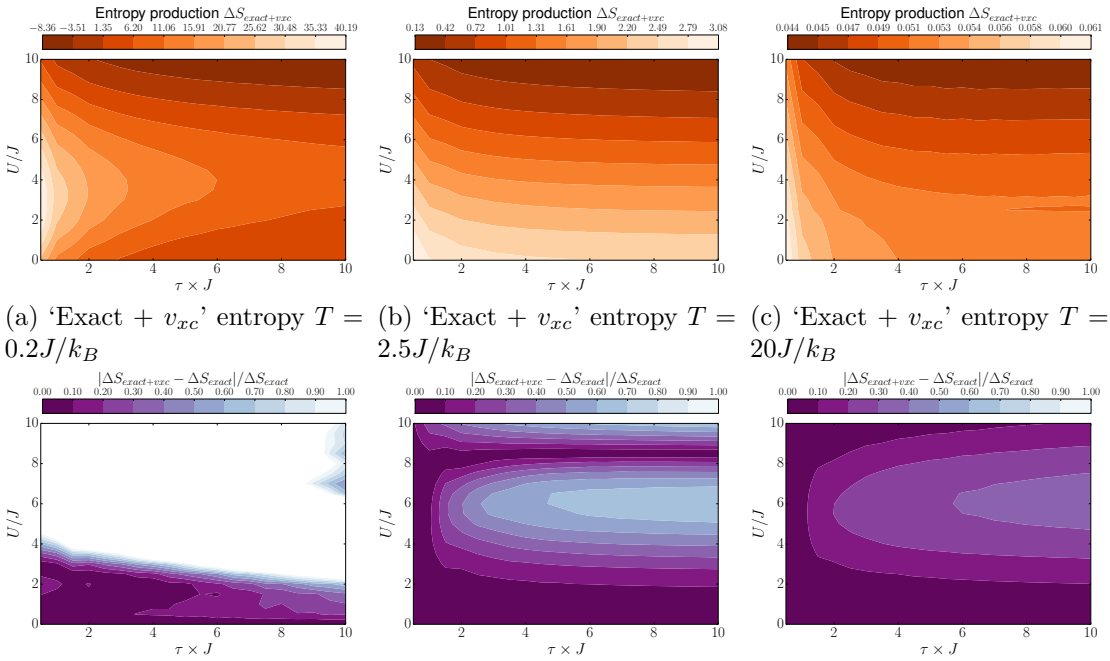

(a) 'Exact + v_{xc}' entropy $T = 0.2J/k_B$ (b) 'Exact + v_{xc}' entropy $T = 2.5J/k_B$ (c) 'Exact + v_{xc}' entropy $T = 20J/k_B$

(d) 'Exact + v_{xc}' entropy relative error $T = 0.2J/k_B$ (e) 'Exact + v_{xc}' entropy relative error $T = 2.5J/k_B$ (f) 'Exact + v_{xc}' entropy relative error $T = 20J/k_B$

Figure D.76: 'Exact + v_{xc}' entropy (top row) and relative error (bottom row) for the 4 sites zigzag at the three temperatures.

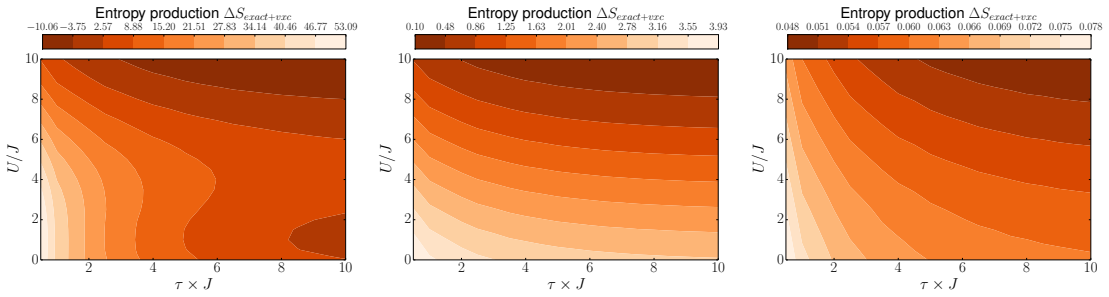

(a) 'Exact + v_{xc}' entropy $T = 0.2J/k_B$

(b) 'Exact + v_{xc}' entropy $T = 2.5J/k_B$

(c) 'Exact + v_{xc}' entropy $T = 20J/k_B$

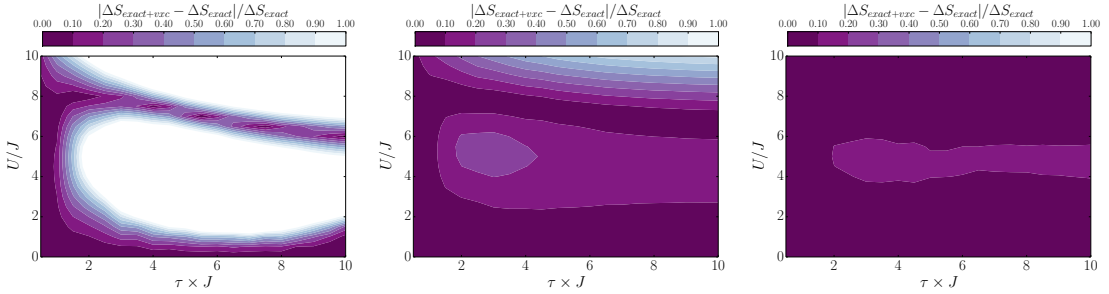

(d) 'Exact + v_{xc}' entropy relative error $T = 0.2J/k_B$

(e) 'Exact + v_{xc}' entropy relative error $T = 2.5J/k_B$

(f) 'Exact + v_{xc}' entropy relative error $T = 20J/k_B$

Figure D.77: 'Exact + v_{xc}' entropy (top row) and relative error (bottom row) for the 4 sites teeth at the three temperatures.

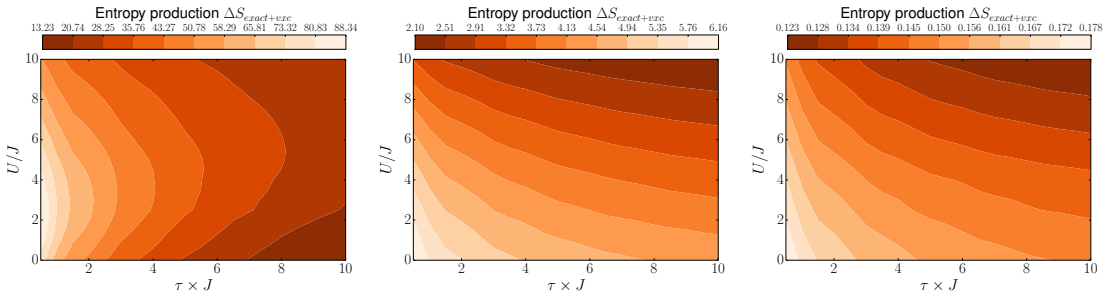

(a) 'Exact + v_{xc}' entropy $T = 0.2J/k_B$

(b) 'Exact + v_{xc}' entropy $T = 2.5J/k_B$

(c) 'Exact + v_{xc}' entropy $T = 20J/k_B$

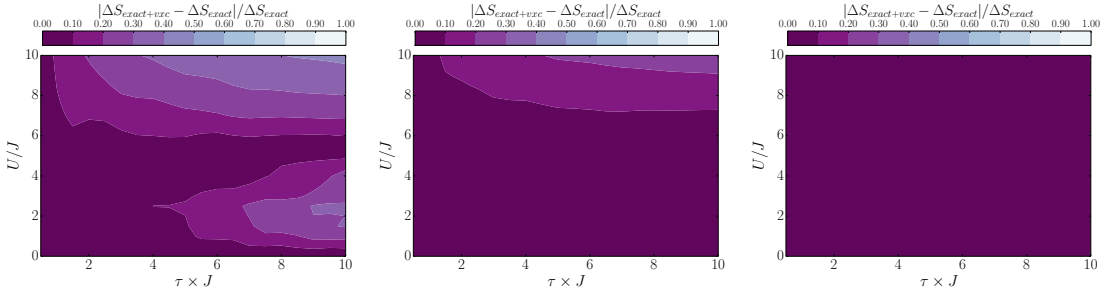

(d) 'Exact + v_{xc}' entropy relative error $T = 0.2J/k_B$

(e) 'Exact + v_{xc}' entropy relative error $T = 2.5J/k_B$

(f) 'Exact + v_{xc}' entropy relative error $T = 20J/k_B$

Figure D.78: 'Exact + v_{xc}' entropy (top row) and relative error (bottom row) for the 4 sites slope at the three temperatures.

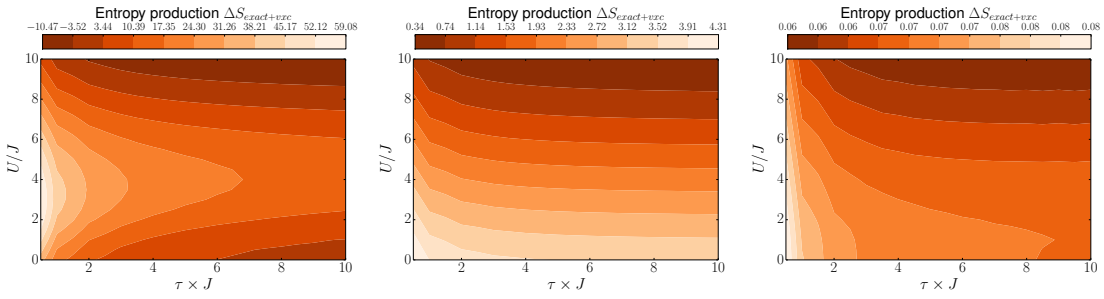

(a) 'Exact + v_{xc}' entropy $T = 0.2J/k_B$

(b) 'Exact + v_{xc}' entropy $T = 2.5J/k_B$

(c) 'Exact + v_{xc}' entropy $T = 20J/k_B$

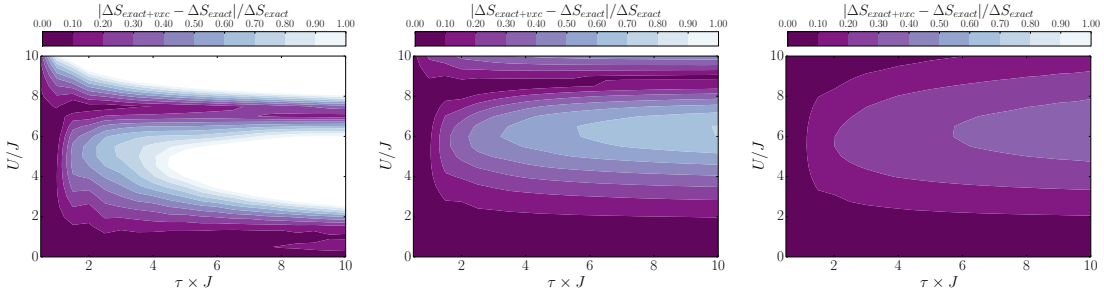

(d) 'Exact + v_{xc}' entropy relative error $T = 0.2J/k_B$

(e) 'Exact + v_{xc}' entropy relative error $T = 2.5J/k_B$

(f) 'Exact + v_{xc}' entropy relative error $T = 20J/k_B$

Figure D.79: 'Exact + v_{xc}' entropy (top row) and relative error (bottom row) for the 6 sites zigzag at the three temperatures.

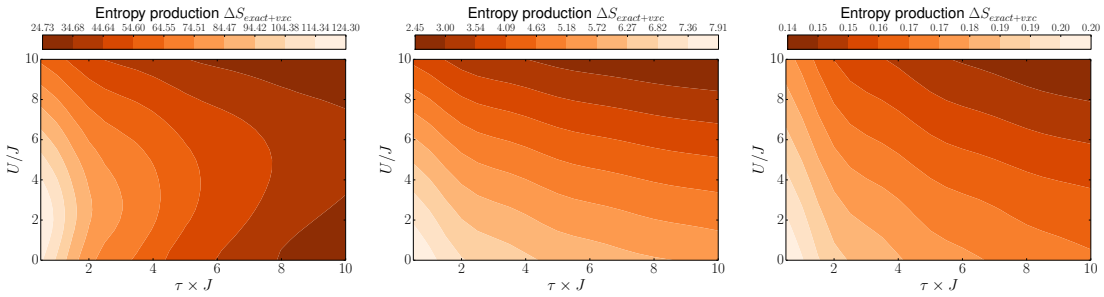

(a) 'Exact + v_{xc}' entropy $T = 0.2J/k_B$

(b) 'Exact + v_{xc}' entropy $T = 2.5J/k_B$

(c) 'Exact + v_{xc}' entropy $T = 20J/k_B$

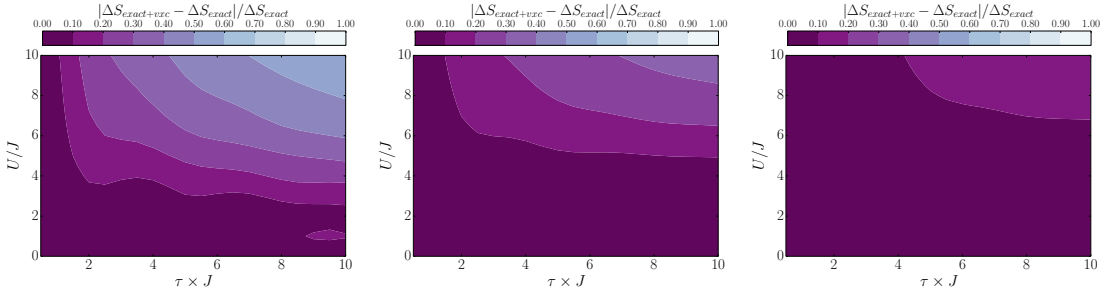

(d) 'Exact + v_{xc}' entropy relative error $T = 0.2J/k_B$

(e) 'Exact + v_{xc}' entropy relative error $T = 2.5J/k_B$

(f) 'Exact + v_{xc}' entropy relative error $T = 20J/k_B$

Figure D.80: 'Exact + v_{xc}' entropy (top row) and relative error (bottom row) for the 6 sites slope at the three temperatures.

Bibliography

[1] Andrew Steane. "Quantum computing". In: *Reports on Progress in Physics* 61.2 (Feb. 1998), pp. 117–173.

[2] Johannes Roßnagel et al. "A single-atom heat engine". In: *Science* 352.6283 (2016), pp. 325–329.

[3] Gleb Maslennikov et al. "Quantum absorption refrigerator with trapped ions". In: *Nature Communications* 10.202 (2019).

[4] T. B. Batalhão et al. "Irreversibility and the Arrow of Time in a Quenched Quantum System". In: *Phys. Rev. Lett.* 115.190601 (19 Nov. 2015).

[5] Sadi Carnot. *Réflexions sur la puissance motrice du feu et sur les machines propres à développer cette puissance*. Paris, France: Bachelier, 1824.

[6] American Society of Mechanical Engineers. Internal Combustion Engine Division. Technical Conference et al. *History of the internal combustion engine: presented at the Eleventh Annual Fall Technical Conference of the ASME Internal Combustion Engine Division, Dearborn, Michigan, October 15-18, 1989*. Ice (Series), V. 8. American Society of Mechanical Engineers, 1989.

[7] Robert M. Wald. "The Thermodynamics of Black Holes". In: *Living Reviews in Relativity* 4.6 (2001).

[8] Frank H. Verhoek. "Thermodynamics and rocket propulsion". In: *Journal of Chemical Education* 46.3 (1969), p. 140.

[9] NASA. *Hubble's deepest view of the universe unveils bewildering galaxies across billions of years*. 1996. URL: `https://hubblesite.org/contents/news-releases/1996/news-1996-01.html` (visited on 03/05/2020).

[10] Sai Vinjanampathy and Janet Anders. “Quantum thermodynamics”. In: *Contemporary Physics* 57.545 (2016).

[11] J. Goold et al. “The role of quantum information in thermodynamics - A topical review”. In: *J. Phys. A* 49.143001 (2016).

[12] Janet Anders and Massimiliano Esposito. “Focus on quantum thermodynamics”. In: *New J. Phys.* 19.010201 (2017).

[13] J. Millen and A. Xuereb. “Perspective on quantum thermodynamics”. In: *New J. Phys.* 18.011002 (2016).

[14] J. M. R. Parrondo, J. M. Horowitz, and T. Sagawa. “Thermodynamics of information”. In: *Nat. Phys.* 11.131 (2015).

[15] P. Luizzo-Scorpo et al. “Thermodynamics of quantum feedback cooling”. In: *Entropy* 18.48 (2016).

[16] Wolfgang Niedenzu, Marcus Huber, and Erez Boukobza. “Concepts of work in autonomous quantum heat engines”. In: *Quantum* 3.195 (Oct. 2019).

[17] Ronnie Kosloff and Amikam Levy. “Quantum Heat Engines and Refrigerators: Continuous Devices”. In: *Annual Review of Physical Chemistry* 65.1 (2014), pp. 365–393.

[18] Felix C Binder et al. In: 17.7 (July 2015), p. 075015.

[19] Mischa P. Woods, Nelly Huei Ying Ng, and Stephanie Wehner. “The maximum efficiency of nano heat engines depends on more than temperature”. In: *Quantum* 3.177 (Aug. 2019).

[20] Michał Horodecki and Jonathan Oppenheim. “Fundamental limitations for quantum and nanoscale thermodynamics”. In: *Nature Communications* 4.2059 (2013).

[21] Álvaro M. Alhambra et al. “Work and reversibility in quantum thermodynamics”. In: *Phys. Rev. A* 97.062114 (6 June 2018).

[22] Pasquale Calabrese, John Cardy, and Benjamin Doyon. “Entanglement entropy in extended quantum systems”. In: *Journal of Physics A: Mathematical and Theoretical* 42.50 (Dec. 2009), p. 500301.

[23] Tameem Albash and Daniel A. Lidar. “Adiabatic quantum computation”. In: *Rev. Mod. Phys.* 90.015002 (1 Jan. 2018).

[24] E. Farhi et al. “A quantum adiabatic evolution algorithm applied to random instances of an NP-complete problem”. In: *Science* 292.472 (2001).

[25] Murray Gell-Mann and Francis Low. “Bound States in Quantum Field Theory”. In: *Phys. Rev.* 84 (2 Oct. 1951), pp. 350–354.

[26] Dave Bacon and Steven T. Flammia. “Adiabatic Gate Teleportation”. In: *Phys. Rev. Lett.* 103.120504 (12 Sept. 2009).

[27] Itay Hen. “Quantum gates with controlled adiabatic evolutions”. In: *Phys. Rev. A* 91.022309 (2 Feb. 2015).

[28] Alan C. Santos, Raphael D. Silva, and Marcelo S. Sarandy. “Shortcut to adiabatic gate teleportation”. In: *Phys. Rev. A* 93.012311 (1 Jan. 2016).

[29] O. Abah and E. Lutz. “Energy efficient quantum machines”. In: *Eur. Lett. (EPL)* 118.40005 (2017).

[30] Jizhou He, Jincan Chen, and Ben Hua. “Quantum refrigeration cycles using spin-$\frac{1}{2}$ systems as the working substance”. In: *Phys. Rev. E* 65.036145 (3 Mar. 2002).

[31] Chang-Kang Hu et al. “Validation of quantum adiabaticity through non-inertial frames and its trapped-ion realization”. In: *Scientific Reports* 9.10449 (2019).

[32] M. Herrera, R. M. Serra, and I. D’Amico. “DFT-inspired methods for quantum thermodynamics”. In: *Scientific Reports* 7.4655 (2017).

[33] J. Roland and N. J. Cerf. “Quantum search by local adiabatic evolution”. In: *Phys. Rev. A* 65.042308 (2002).

[34] S. Das, R. Kobes, and G. Kunstatter. “Adiabatic quantum computation and Deutsch’s algorithm”. In: *Phys. Rev. A* 65.062310 (2002).

[35] F. Plastina et al. “Irreversible work and inner friction in quantum thermodynamic processes”. In: *Phys. Rev. Lett.* 113.260601 (2014).

[36] Marcela Herrera et al. “Nonadiabatic quantum state engineering driven by fast quench dynamics”. In: *Phys. Rev. A* 89.022323 (2 Feb. 2014).

[37] S. Bachmann, W. De Roeck, and M. Fraas. “Adiabatic theorem for quantum spin systems”. In: *Phys. Rev. Lett.* 119.060201 (2017).

[38] M. W. Johnson et al. “Quantum annealing with manufactured spin”. In: *Nature* 473.194 (2011).

[39] E. Gibney. “D-wave upgrade: How scientists are using the world’s most controversial quantum computer”. In: *Nature* 541.447 (2017).

[40] E. Fahri et al. *Quantum Computation by Adiabatic Evolution*. Version 1. Jan. 28, 2000. arXiv: `arXiv:quant-ph/0001106 [cs.DS]`.

[41] Sabine Jansen, Mary-Beth Ruskai, and Ruedi Seiler. "Bounds for the adiabatic approximation with applications to quantum computation". In: *Journal of Mathematical Physics* 48.102111 (2007).

[42] K.-P. Marzlin and B. C. Sanders. "Inconsistency in the application of the adiabatic theorem". In: *Phys. Rev. Lett.* 93.160408 (2004).

[43] J. Ortigoso. "Quantum adiabatic theorem in light of the Marzlin-Sanders inconsistency". In: *Phys. Rev. A* 86.032121 (2012).

[44] Kavan Modi. "Quantum many-body physics in a nutshell". In: *Contemporary Physics* 60.2 (2019), pp. 197–197.

[45] Thao P. Le et al. "Spin-chain model of a many-body quantum battery". In: *Phys. Rev. A* 97.022106 (2 Feb. 2018).

[46] Srijit Goswami et al. "Controllable valley splitting in silicon quantum devices". In: *Nature Physics* 3.41 (2007).

[47] R. J. Lewis-Swan et al. "Dynamics of quantum information". In: *Nature Reviews Physics* 1 (2019), pp. 627–634.

[48] Antonio Acín et al. "The quantum technologies roadmap: a European community view". In: *New Journal of Physics* 20.8 (Aug. 2018), p. 080201.

[49] A. Silva. "Statistics of the work done on a quantum critical system by quenching a control parameter." In: *Phys. Rev. Lett.* 101.120603 (2008).

[50] R. Dorner et al. "Emergent Thermodynamics in a Quenched Quantum Many-Body System". In: *Phys. Rev. Letters* 109.160601 (2012).

[51] D. Joshi and M. Campisi. "Quantum Hertz entropy increase in a quenched spin chain". In: *Eur. Phys. J. B.* 86.157 (2013).

[52] E. Mascarenhas. "Work and quantum phase transitions: Quantum latency". In: *Phys. Rev. E* 89.062103 (2014).

[53] A. Sindona. "Statistics of the work distribution for a quenched Fermi gas". In: *New J. Phys.* 16.045013 (2014).

[54] L. Fusco et al. "Assessing the Nonequilibrium Thermodynamics in a Quenched Quantum Many-Body System via Single Projective Measurements". In: *Phys. Rev. X* 4.031029 (2014).

[55] M. Zhong and P. Tong. “Work done and irreversible entropy production in a suddenly quenched quantum spin chain with asymmetrical excitation spectra”. In: *Phys. Rev. E* 91.032137 (2015).

[56] J. Eisert, M. Friesdorf, and C. Gogolin. “Quantum many-body systems out of equilibrium”. In: *Nat. Phys.* 11.124 (2015).

[57] A. Bayat et al. “Nonequilibrium critical scaling in quantum thermodynamics”. In: *Phys. Rev. B* 93.201106(R) (2016).

[58] E. Solano-Carrillo and A. J. Millis. “Theory of entropy production in quantum many-body systems”. In: *Phys. Rev. B* 93.224305 (2016).

[59] M. Herrera, K. Zawadzki, and I. D’Amico. “Melting a Hubbard dimer: benchmarks of ‘ALDA’ for quantum thermodynamics”. In: *The European Physical Journal B* 91.248 (2018).

[60] J. C. Smith, A. Pribram-Jones, and K. Burke. “Exact thermal density functional theory for a model system: Correlation components and accuracy of the zero-temperature exchange-correlation approximation”. In: *Phys. Rev. B* 93.245131 (24 June 2016).

[61] K. Capelle. “A bird’s-eye view of density-functional theory”. In: *Braz. J. Phys.* 36.4a (2006).

[62] D. J. Carrascal et al. “The Hubbard dimer: a density functional case study of a many-body problem”. In: *J. Phys. Cond. Mat.* 27(39).393001 (2015).

[63] Klaus Capelle and Vivaldo L. Campo. “Density functionals and model Hamiltonians: Pillars of many-particle physics”. In: *Physics Reports* 528.3 (2013), pp. 91–159.

[64] Carsten A. Ullrich. *Time-Dependent Density-Functional Theory: Concepts and Applications.* Oxford University Press, 2013.

[65] G. Vignale and Mark Rasolt. “Density-functional theory in strong magnetic fields”. In: *Phys. Rev. Lett.* 59 (20 Nov. 1987), pp. 2360–2363.

[66] Jorge M. Seminario. “An introduction to density functional theory in chemistry”. In: *Modern Density Functional Theory.* Ed. by J.M. Seminario and P. Politzer. Vol. 2. Theoretical and Computational Chemistry. Elsevier, 1995, pp. 1–27.

[67] Axel D. Becke. “Perspective: Fifty years of density-functional theory in chemical physics”. In: *The Journal of Chemical Physics* 140.18 (2014), 18A301.

[68] Daniel J Cole and Nicholas D M Hine. “Applications of large-scale density functional theory in biology”. In: *Journal of Physics: Condensed Matter* 28.39 (Aug. 2016), p. 393001.

[69] Wanda Andreoni. “Density-Functional Theory and Molecular Dynamics: A New Perspective for Simulations of Biological Systems”. In: *3D QSAR in Drug Design: Ligand-Protein Interactions and Molecular Similarity*. Ed. by Hugo Kubinyi, Gerd Folkers, and Yvonne C. Martin. Dordrecht: Springer Netherlands, 1998, pp. 161–167. ISBN: 978-0-306-46857-5.

[70] Justin C. Smith, Francisca Sagredo, and Kieron Burke. “Warming Up Density Functional Theory”. In: *Frontiers of Quantum Chemistry*. Ed. by Marek J. Wójcik et al. Singapore: Springer Singapore, 2018, pp. 249–271. ISBN: 978-981-10-5651-2.

[71] E. Runge and E. K. U. Gross. “Density-Functional Theory for Time-Dependent Systems”. In: *Phys. Rev. Lett.* 52.997 (1984).

[72] N. A. Lima et al. “Density Functionals Not Based on the Electron Gas: Local-Density Approximation for a Luttinger Liquid”. In: *Phys. Rev. Lett.* 90.146402 (14 Apr. 2003).

[73] O. Gunnarsson and K. Schönhammer. “Density-Functional Treatment of an Exactly Solvable Semiconductor Model”. In: *Phys. Rev. Lett.* 56 (18 May 1986), pp. 1968–1971.

[74] P. Hohenberg and W. Kohn. “Inhomogeneous Electron Gas”. In: *Physical Review* 136 (3B) (1964), B864–B871.

[75] D. J. Griffiths. *Introduction to Quantum Mechanics*. New Jersey, USA: Prentice Hall, 1995.

[76] W. Kohn and L. J. Sham. “Self-Consistent Equations Including Exchange and Correlation Effects”. In: *Phys. Rev.* 140.A1133 (1965).

[77] I. D’Amico et al. “Quantum Mechanics in Metric Space: Wave Functions and Their Densities”. In: *Phys. Rev. Lett.* 106.050401 (2011).

[78] P. M. Sharp and I. D’Amico. “Metric space formulation of quantum mechanical conservation laws”. In: *Phys. Rev. B* 89.115137 (2014).

[79] P. M. Sharp and I. D’Amico. “Metric space analysis of systems immersed in a magnetic field”. In: *Phys. Rev. A* 92.032509 (2015).

[80] D. Spehner et al. “Geometric Measures of Quantum Correlations with Bures and Hellinger Distances”. In: *Lectures on General Quantum Correlations and their Applications*. Ed. by Felipe Fernandes Fanchini, Diogo de Oliveira Soares Pinto, and Gerardo Adesso. Cham: Springer International Publishing, 2017, pp. 105–157. ISBN: 978-3-319-53412-1.

[81] Damian Markham et al. “Quantum state discrimination: A geometric approach”. In: *Phys. Rev. A* 77.042111 (4 Apr. 2008).

[82] I. Bengtsson and K. Życzkowski. *Geometry of Quantum States: An Introduction to Quantum Entanglement*. Cambridge, England: Cambridge University Press, 2006.

[83] T. de Picoli, I. D’Amico, and V. V. França. “Metric-Space Approach for Distinguishing Quantum Phase Transitions in Spin-Imbalanced Systems”. In: *Brazilian Journal of Physics* 48.5 (Oct. 2018), pp. 472–476.

[84] T. M. Osán and Lamberti P. W. “Purification-based metric to measure the distance between quantum states and processes”. In: *Phys. Rev. A* 87.062319 (2013).

[85] A. H. Skelt, R. W. Godby, and I. D’Amico. “Metrics for Two Electron Random Potential Systems”. In: *Brazilian Journal of Physics* 48.5 (Oct. 2018), pp. 467–471.

[86] Simone Marocchi, Stefano Pittalis, and Irene D’Amico. “Fermionic correlations as metric distances: A useful tool for materials science”. In: *Phys. Rev. Materials* 1.043801 (4 Sept. 2017).

[87] Gh.-S. Paraoanu and Horia Scutaru. “Bures distance between two displaced thermal states”. In: *Phys. Rev. A* 58 (2 Aug. 1998), pp. 869–871.

[88] C. A. Fuchs and J. van de Graaf. “Cryptographic distinguishability measures for quantum-mechanical states”. In: *IEEE Transactions on Information Theory* 45.4 (May 1999), pp. 1216–1227.

[89] Berthold-Georg Englert. “Fringe Visibility and Which-Way Information: An Inequality”. In: *Phys. Rev. Lett.* 77 (11 Sept. 1996), pp. 2154–2157.

[90] Paulina Marian and Tudor A. Marian. “Bures distance as a measure of entanglement for symmetric two-mode Gaussian states”. In: *Phys. Rev. A* 77.062319 (6 June 2008).

[91] I. Nagy and I. Aldazabal. “Metric measures of interparticle interaction in an exactly solvable two-electron model atom”. In: *Phys. Rev. A* 84.032516 (3 Sept. 2011).

[92] W. Sutherland. *Introduction to Metric and Topological Spaces*. Oxford: Oxford University Press, 2009.

[93] A. H. Skelt, R. W. Godby, and I. D’Amico. “Measuring adiabaticity in nonequilibrium quantum systems”. In: *Phys. Rev. A* 98.012104 (1 July 2018).

[94] Donald Bures. “An Extension of Kakutani’s Theorem on Infinite Product Measures to the Tensor Product of Semifinite w*-Algebras”. In: *Transactions of the American Mathematical Society* 135 (1969), pp. 199–212.

[95] Mark M. Wilde. *Quantum Information Theory*. Cambridge University Press, 2013. Chap. 9.

[96] M. Born and V. A. Fock. “Beweis des Adiabatensatzes”. In: *Z. Phys. A* 51 (1928), pp. 165–180.

[97] J. E. Avron and A. Elgart. “Adiabatic Theorem without a Gap Condition”. In: *Communications in Mathematical Physics* 203 (1999), pp. 445–463.

[98] D. M. Tong et al. “Quantitative Conditions Do Not Guarantee the Validity of the Adiabatic Approximation”. In: *Phys. Rev. Lett.* 95.110407 (2005).

[99] D. Comparat. “General conditions for quantum adiabatic evolution”. In: *Phys. Rev. A* 80.012106 (2009).

[100] D. Li. “Invalidity of the quantitative adiabatic condition and general conditions for adiabatic approximations”. In: *Laser Phys. Lett.* 13.055203 (2016).

[101] Jiangfeng Du et al. “Experimental study of the validity of quantitative conditions in the quantum adiabatic theorem”. In: *Phys. Rev. Lett.* 101.060403 (2008).

[102] M. H. S. Amin. “Consistency of the adiabatic theorem”. In: *Phys. Rev. Lett.* 102.220401 (2009).

[103] Oleg Lychkovskiy, Oleksandr Gamayun, and Vadim Cheianov. “Necessary and sufficient condition for quantum adiabaticity in a driven one-dimensional impurity-fluid system”. In: *Phys. Rev. B* 98.024307 (2 July 2018).

[104] P. Talkner, E. Lutz, and P. Hänggi. “Fluctuation theorems: Work is not an observable”. In: *Phys. Rev. E* 75.050102 (2007).

[105] Fernando Brandão et al. “The second laws of quantum thermodynamics”. In: *Proceedings of the National Academy of Sciences* 112.11 (2015), pp. 3275–3279.

[106] Álvaro M. Alhambra et al. “Fluctuating Work: From Quantum Thermodynamical Identities to a Second Law Equality”. In: *Phys. Rev. X* 6.041017 (4 Oct. 2016).

[107] Christopher Jarzynski. “Equalities and Inequalities: Irreversibility and the Second Law of Thermodynamics at the Nanoscale”. In: *Annual Review of Condensed Matter Physics* 2.1 (2011), pp. 329–351.

[108] J M Deutsch. “Thermodynamic entropy of a many-body energy eigenstate”. In: *New Journal of Physics* 12.7 (July 2010), p. 075021.

[109] V. V. França and K. Capelle. “Entanglement of strongly interacting low-dimensional fermions in metallic, superfluid, and antiferromagnetic insulating systems”. In: *Phys. Rev. A* 74.042325 (4 Oct. 2006).

[110] Vivian V. França, Dominik Hörndlein, and Andreas Buchleitner. “Fulde-Ferrell-Larkin-Ovchinnikov critical polarization in one-dimensional fermionic optical lattices”. In: *Phys. Rev. A* 86.033622 (3 Sept. 2012).

[111] F.H.L. Essler et al. *The One-Dimensional Hubbard Model*. Cambridge University Press, 2005. ISBN: 9781139441582.

[112] Hal Tasaki. “The Hubbard model - an introduction and selected rigorous results”. In: *Journal of Physics: Condensed Matter* 10.20 (May 1998), pp. 4353–4378.

[113] J. P. Coe, V. V. França, and I. D’Amico. “Hubbard model as an approximation to the entanglement in nanostructures”. In: *Phys. Rev. A* 81.052321 (5 May 2010).

[114] Shuo Yang, Xin Wang, and S. Das Sarma. “Generic Hubbard model description of semiconductor quantum-dot spin qubits”. In: *Phys. Rev. B* 83.161301 (16 Apr. 2011).

[115] Simon Murmann et al. “Two Fermions in a Double Well: Exploring a Fundamental Building Block of the Hubbard Model”. In: *Phys. Rev. Lett.* 114.080402 (8 Feb. 2015).

[116] J. P. Coe, V. V. França, and I. D’Amico. “Feasibility of approximating spatial and local entanglement in long-range interacting systems using the extended Hubbard model”. In: *EPL (Europhysics Letters)* 93.1 (Jan. 2011), p. 10001.

[117] Peter T. Brown et al. “Bad metallic transport in a cold atom Fermi-Hubbard system”. In: *Science* 363.6425 (2019), pp. 379–382.

[118] Matthew A. Nichols et al. “Spin transport in a Mott insulator of ultracold fermions”. In: *Science* 363.6425 (2019), pp. 383–387.

[119] Elliott H. Lieb and F. Y. Wu. “Absence of Mott Transition in an Exact Solution of the Short-Range, One-Band Model in One Dimension”. In: *Phys. Rev. Lett.* 21 (3 July 1968), pp. 192–192.

[120] J. I. Fuks and N. T. Maitra. “Challenging adiabatic time-dependent density functional theory with a Hubbard dimer: the case of time-resolved long-range charge transfer”. In: *Phys. Chem. Chem. Phys.* 16(28).14504 (2014).

[121] S. R. Manmana et al. “Quantum critical behavior of the one-dimensional ionic Hubbard model”. In: *Phys. Rev. B* 70.155115 (15 Oct. 2004).

[122] A P Kampf et al. “Nature of the insulating phases in the half-filled ionic Hubbard model”. In: *Journal of Physics: Condensed Matter* 15.34 (Aug. 2003), pp. 5895–5907.

[123] Michele Fabrizio, Alexander O. Gogolin, and Alexander A. Nersesyan. “From Band Insulator to Mott Insulator in One Dimension”. In: *Phys. Rev. Lett.* 83 (10 Sept. 1999), pp. 2014–2017.

[124] Heng-Fu Lin et al. “Phase transitions of the ionic Hubbard model on the honeycomb lattice”. In: *Scientific Reports* 5.9810 (2015).

[125] A. A. Aligia and C. D. Batista. “Dimerized phase of ionic Hubbard models”. In: *Phys. Rev. B* 71 (12 Mar. 2005), p. 125110. DOI: 10.1103/PhysRevB.71.125110. URL: https://link.aps.org/doi/10.1103/PhysRevB.71.125110.

[126] Rupan Preet Kaur, Ravinder Singh Sawhney, and Derick Engles. “Quantum tunneling through aromatic molecular junctions for molecular devices: A review”. In: *Chinese Journal of Physics* 56.5 (2018), pp. 2226–2234.

[127] Michael Thoss and Ferdinand Evers. “Perspective: Theory of quantum transport in molecular junctions”. In: *The Journal of Chemical Physics* 148.3 (2018), p. 030901.

[128] M. J. P. Hodgson et al. “Exact time-dependent density-functional potentials for strongly correlated tunneling electrons”. In: *Phys. Rev. B* 88.241102(R) (2013).

[129] J.R. Johansson, P.D. Nation, and Franco Nori. “QuTiP: An open-source Python framework for the dynamics of open quantum systems”. In: *Computer Physics Communications* 183.8 (2012), pp. 1760–1772.

[130] J.R. Johansson, P.D. Nation, and Franco Nori. “QuTiP 2: A Python framework for the dynamics of open quantum systems”. In: *Computer Physics Communications* 184.4 (2013), pp. 1234–1240.

[131] J. Crank and P. Nicholson. “A practical method for numerical evaluation of solutions of partial differential equations of the heat-conduction type”. In: *Mathematical Proceedings of the Cambridge Philosophical Society* 43(1) (1947), pp. 50–67.

[132] J. P. Coe, I. D’Amico, and V. V. França. “Uniqueness of density-to-potential mapping for fermionic lattice systems”. In: *EPL (Europhysics Letters)* 110.6 (2015), p. 63001.

[133] Gustavo Rigolin and Gerardo Ortiz. “Adiabatic theorem for quantum systems with spectral degeneracy”. In: *Phys. Rev. A* 85.062111 (6 June 2012).

[134] A. H. Skelt. *The Metric Space Approach to Many-Body Quantum Mechanics*. Master’s thesis. Department of Physics, University of York. 2016.

[135] Oleg Lychkovskiy, Oleksandr Gamayun, and Vadim Cheianov. “Time Scale for Adiabaticity Breakdown in Driven Many-Body Systems and Orthogonality Catastrophe”. In: *Phys. Rev. Lett.* 119.200401 (2017).

[136] John F. Dobson. “Harmonic-Potential Theorem: Implications for Approximate Many-Body Theories”. In: *Phys. Rev. Lett.* 73 (16 Oct. 1994), pp. 2244–2247.

[137] Amy H. Skelt and Irene D'Amico. "Characterizing Adiabaticity in Quantum Many-Body Systems at Finite Temperature". In: *Advanced Quantum Technologies* 3.7 (2020), p. 1900139. DOI: 10.1002/qute.201900139.

[138] A H Skelt, K Zawadzki, and I D'Amico. "Many-body effects on the thermodynamics of closed quantum systems". In: *Journal of Physics A: Mathematical and Theoretical* 52.48 (Nov. 2019), p. 485304.

[139] M. V. Berry. "Transitionless quantum driving". In: *Journal of Physics A* 42.36 (2009).

[140] Ingemar Bengtsson and Karol Zyczkowski. *Geometry of Quantum States: An Introduction to Quantum Entanglement*. Cambridge University Press, 2006.

[141] V. V. França, J. P. Coe, and I. D'Amico. "Testing density-functional approximations on a lattice and the applicability of the related Hohenberg-Kohn-like theorem". In: *Scientific Reports* 8.664 (2018).

[142] Claudio Verdozzi. "Time-Dependent Density-Functional Theory and Strongly Correlated Systems: Insight from Numerical Studies". In: *Phys. Rev. Lett.* 101.166401 (16 Oct. 2008).

[143] Aurora Pribram-Jones et al. "Thermal Density Functional Theory in Context". In: *Frontiers and Challenges in Warm Dense Matter*. Ed. by Frank Graziani et al. Cham: Springer International Publishing, 2014, pp. 25–60. ISBN: 978-3-319-04912-0.

[144] Aurora Pribram-Jones, Paul E. Grabowski, and Kieron Burke. "Thermal Density Functional Theory: Time-Dependent Linear Response and Approximate Functionals from the Fluctuation-Dissipation Theorem". In: *Phys. Rev. Lett.* 116 (23 June 2016), p. 233001. DOI: 10.1103/PhysRevLett.116.233001. URL: https://link.aps.org/doi/10.1103/PhysRevLett.116.233001.

[145] K. Zawadzki, I. D'Amico, and L.N. Oliveira. "Symmetries and Boundary Conditions with a Twist". In: *Brazilian Journal of Physics* 47.488 (2017).

[146] D. M. Tong. "Quantitative Condition is Necessary in Guaranteeing the Validity of the Adiabatic Approximation". In: *Phys. Rev. Lett.* 104 (12 Mar. 2010), p. 120401. DOI: 10.1103/PhysRevLett.104.120401.

[147] K. Bergmann, H. Theuer, and B. Shore. “Coherent population transfer among quantum states of atoms and molecules”. In: *Rev. Mod. Phys.* 70.1003 (1998).

[148] M. J. Hartmann. “Quantum simulation with interacting photons”. In: *J. Opt.* 18.104005 (2016).

[149] T. B. Batalhão et al. “Experimental Reconstruction of Work Distribution and Study of Fluctuation Relations in a Closed Quantum System”. In: *Phys. Rev. Lett.* 113.140601 (2014).

[150] R. Kosloff. “Quantum thermodynamics: A dynamical viewpoint”. In: *Entropy* 15.2100 (2013).

[151] Neil Qiang Su and Xin Xu. “Development of New Density Functional Approximations”. In: *Annual Review of Physical Chemistry* 68.1 (2017), pp. 155–182.

[152] Narbe Mardirossian and Martin Head-Gordon. “Thirty years of density functional theory in computational chemistry: an overview and extensive assessment of 200 density functionals”. In: *Molecular Physics* 115.19 (2017), pp. 2315–2372.

[153] M. T. Entwistle et al. “Local density approximations from finite systems”. In: *Phys. Rev. B* 94.205134 (20 Nov. 2016).

[154] Lucas O. Wagner et al. “Kohn-Sham calculations with the exact functional”. In: *Phys. Rev. B* 90.045109 (4 July 2014).

[155] John J. Rehra and Joshua J. Kas. “Exchange and correlation in finite-temperature TDDFT”. In: *Eur. Phys. J. B* 91.153 (2018).

[156] S. Pittalis et al. “Exact Conditions in Finite-Temperature Density-Functional Theory”. In: *Phys. Rev. Lett.* 107.163001 (16 Oct. 2011).

[157] Kieron Burke, John P. Perdew, and Yue Wang. “Derivation of a Generalized Gradient Approximation: The PW91 Density Functional”. In: *Electronic Density Functional Theory: Recent Progress and New Directions*. Ed. by John F. Dobson, Giovanni Vignale, and Mukunda P. Das. Boston, MA: Springer US, 1998, pp. 81–111. ISBN: 978-1-4899-0316-7.

[158] J. P. Coe, K. Capelle, and I. D’Amico. “Reverse engineering in many-body quantum physics: Correspondence between many-body systems and effective single-particle equations”. In: *Phys. Rev. A* 79.032504 (3 Mar. 2009).

[159] N. David Mermin. “Thermal Properties of the Inhomogeneous Electron Gas”. In: *Phys. Rev.* 137 (5A Mar. 1965), A1441–A1443.